INFLUENCES OF SEAWATER FLOWS ON THE DEGRADATION OF ORGANIC COATINGS APPLIED ON OFFSHORE WIND TURBINES

A Dissertation
Submitted to the Graduate Faculty
of the
North Dakota State University
of Agriculture and Applied Science

By

Amin Vedadi

In Partial Fulfillment of the Requirements
for the Degree of
DOCTOR OF PHILOSOPHY

Major Department:
Mechanical Engineering

March 2022

Fargo, North Dakota

North Dakota State University
Graduate School

Title

INFLUENCES OF SEAWATER FLOWS ON THE DEGRADATION OF ORGANIC COATINGS APPLIED ON OFFSHORE WIND TURBINES

By

Amin Vedadi

The Supervisory Committee certifies that this ***disquisition*** complies with North Dakota State University's regulations and meets the accepted standards for the degree of

DOCTOR OF PHILOSOPHY

SUPERVISORY COMMITTEE:

Dr. Yechun Wang
Chair

Dr. Jordi Estevadeordal

Dr. Yildirim Bora Suzen

Dr. Zhibin Lin

Approved:

April 19, 2022
Date

Dr. Alan Kallmeyer
Department Chair

ABSTRACT

The regular protection methods of offshore wind structures consist of the application of two or three layers of epoxy-based coatings with a polyurethane topcoat. The coating systems of offshore wind turbines are mostly tested on-site, where different coated samples are exposed to the sea water at the specific locations planned for the installations of the turbines. Despite several advantages of laboratory testing, the majority of laboratory-based tests have been limited to the exposure of coated or unprotected metals to stationary electrolytic solutions, while the flow-induced corrosion measurements have not received enough attention until recently. The focus of our work is to investigate the influence of applied mechanical stresses due to the water flow on the degradation of organic coatings. In order to resemble the condition of coated monopile structures in shallow water flow, an impingement chamber device and a wave tank were designed and constructed. The Electrochemical Impedance Stereoscopy (EIS) method was utilized for monitoring the electrochemical processes occurred during the degradation of coatings. Computational Fluid Dynamic (CFD) method, as well as Particle Image Velocimetry (PIV) tests were utilized in order to calculate the magnitude of applied stresses on the coating surfaces. Atomic Force Microscopy method (AFM) was employed for characterizations of coating' surfaces. The theory of thermo-activated processes in combination with the thermoelasticity equations were derived in a way to calculate the influence of applied stresses on different electrochemical parameters of the coatings' degradation. The afore-mentioned experimental methods and the developed analytical procedure can potentially predict the behavior of organic coatings applied on offshore wind turbines at different exposure zones with respect to the sea water flow.

ACKNOWLEDGMENTS

I want to express my gratitude toward Dr. Yechun Wang for her very kind and generous support during my PhD studies. She has provided all the means necessary for my research projects and without her professional guidance nothing could have been accomplished.

I deeply appreciate Dr. Estevadeordal's generous financial support to work on my research project for two summers. I am very grateful for his professional reviews and inputs on my research papers. He also kindly provided me access to the PIV device in his lab to improve the quality of my research work.

I am thankful to Dr. Xinan Wang for his unconditional support alongside with his previous graduate student, Mr. Parvej, on conducting the AFM measurements for the projects.

Special thanks to Dr. Lin for providing us the coatings materials and the coating application device.

I am thankful to Dr. Xingyu Wang for helping me to prepare coated samples.

I would like to thank Eric van Gulijk, Alex Johnson, Jacob Fietek, and Michael Stoddard for their help in the design and setup of the test chamber.

I would like to thank Ashley Jacobson, Marius Cobb, Marek Cobb, Ian Blair, and Jaffery Ayub for their help in the design and setup of the wave tank.

I am very thankful to Dr. Al Habib Ullah and PhD. Candidate Charles Fabijanic for their help provided for the setup, conduction, and analysis of PIV tests.

Finally, I am extremely thankful to the Mechanical Engineering department of NDSU and its' chair Dr. Alan Kallmeyer, for the generous support during my PhD studies.

DEDICATION

To my love, my wife, Nadia, who has been my guardian angel on every step of this long journey.

To my dear parents, Mina and Javad, who sacrificed everything they owned to make the dream come true.

To my brother, Ahmad, whom I missed a lot and count every second to see him again.

TABLE OF CONTENTS

LIST OF TABLES

LIST OF FIGURES

LIST OF ABBREVIATIONS

AFM.....Atomic Force Microscopy.

CFD.....Computational Fluid Dynamic.

EIS……..Electrochemical Impedance Spectroscopy.

ENM.....Electrochemical Noise Measurement.

IEA.....International Energy Agency.

LCOE.....Levelized Cost Of Energy.

NREL…….National Renewable Energy Laboratory.

PIV .....Particle Image Velocimetry.

TBC.....Thermal Barrier Coating.

WFO.....World Forum Offshore Wind.

LIST OF SYMBOLS

Symbol	Parameter	Unit (SI)
A	Surface area	cm^2
C	Polarizability (film capacitance)	$\mu F.cm^2$
C_0	Intact coating capacitance	$\mu F.cm^2$
C_c	Coating capacitance	$\mu F.cm^2$
C_{dl}	Double layer capacitance	$\mu F.cm^2$
D	Diffusion coefficient	$m^2.s^{-1}$
d	Depth of water from free surface/ diameter of water molecule	m
E_a	Activation energy	$J.mol^{-1}$
E_k	Kinetic energy	J
F	Force	N
G	Gibbs free energy	J
H	Wave height	m
ΔH	Enthalpy change	J
h	Planck's constant	$m^2.kg.s^{-1}$
K	Reaction rate constant	s^{-1}
k	Wave number	-
k_B	Boltzmann constant	$J.K^{-1}$
L	Wave length	m
l	Thickness of the coating	μm
M_t	Total amount of diffusing fluid	g
P	Pressure	atm

Q	Volume flow rate	cm^3s^{-1}
R	Gas constant	$J.mol^{-1}.K^{-1}$
S	Stroke length	m
ΔS	Entropy change	$J.kg^{-1}.K^{-1}$
T	Absolute temperature/ Wave period	K/ s
t	time	*hours or sec*
U	Wave speed	$m.s^{-1}$
ΔU	Internal energy	J
V	Velocity	$m.s^{-1}$
V_a	Activation volume	m^3
α	Ratio of the film's capacitance constant	-
Γ	Pre-exponential factor	-
ε_f	Dielectric constant of the fluid	-
ε_0	Absolute permittivity	$\mu F.cm^{-1}$
ε_c	Dielectric constant of the coating	-
ρ	Density	$g.cm^{-3}$
σ	Normal stress	Pa
σ_R	Average total stress	Pa
ϕ	Volume fraction of absorbed fluid	-
ξ	Transmission coefficient	-
ψ	Helmholtz free energy	J
ω	Wave frequency	$Rad.s^{-1}$
μ	Dynamic viscosity	$Pa.s$

η	Displacement of the water surface	m
τ	Shear stress	Pa

1. INTRODUCTION

Offshore wind turbines are considered as one of the most reliable sources of electricity generation among renewable energy sources. There are several problems with the on-shore wind turbines including being considered as an eyesore and source of noise for the nearby residences, its threat against the birds and bats (an estimation death toll of 57 million a year [1]), and being fed by the poor wind speed with high fluctuation due to the physical wind blockages of buildings and hills. On the other hand, offshore wind installations have the advantages of vast energy potential due to inexpensive enormous offshore spaces, strong and relatively constant wind speed, and unlimited height of wind constructions in contrast to the limits imposed by urban rules for onshore installations [2]. Based on the recent report of World Forum Offshore Wind (WFO) [3], by the end of the year 2020, the total installed capacity of offshore wind will reach 30 GW. To the author's best knowledge, about 5800 offshore wind turbines have been installed all around the globe, while 1220 more offshore wind turbines are under constructions that will be finished within next three years. International Energy Agency (IEA) [4] reported under conservative estimation that the installation of offshore wind turbines will increase up to 350 GW, while a sustainable development scenario estimates the growth up to 550 GW, covering almost 5.5% of electricity supply share by the year 2040. IEA pointed out in the same report that the sustainable development scenario is only possible if the offshore wind reaches a competitive price in comparison with the other energy resources. Based on National Renewable Energy Laboratory (NREL) report of 2018 [5], the levelized cost of energy (LCOE) for fixed offshore wind turbines estimated as $89/MWh, while for onshore installations LCOE stood for $42/MWh. The LCOE calculations consist of two main expenditure categories, capital and maintenance costs, which both include several subcategories. Based on the report, the maintenance costs of

the offshore wind turbines were more than 2.5 times greater than onshore ($30.3, and $12.1 per MWh, respectively). One of the main reasons of such high maintenance costs is the degradation of the coatings applied on the wind turbine constructions. Based on regular wind turbine installations in Europe, today, the cost of coating structures ranges 15–25 €/m^2 (18–31 \$/m^2 or 1.7–2.9 \$/ft^2) (depending on the structure, process and coating system). The cost of coating repair work performed on-site on offshore structures is approximately 5–10 times higher than initial coating [6]. In general, the regular financial investments on offshore wind installations have an amortization period of 20 years [5], [6], indicating the offshore wind structures should be kept operative in an extremely corrosive environment for at least 20 years. The highest percentage of the offshore wind structures in the world are monopiles (74% by 2011) [7], while the share of offshore monopiles in Europe was 81.9% by the year 2019 [8]. Monopile is a circular hollow steel tube that is embedded into the seabed and extends above sea level where it interfaces through a transition piece with the offshore wind turbine tower [9]. The monopile offshore wind turbines are primarily installed in shallow water depths (10 – 30 m) [10], while the extra-large monopiles are installed in intermediate water depths (30 – 40 m) [11]. The offshore wind structures must be designed to withstand the corrosive and harsh nature of the marine environment [6], [12]–[15] .

Almost all monopile structures are made of steel, which usually protected by multi-layer of different types of coatings. The type and severity of corrosion on the offshore wind structures are highly subjected to the different zones defined by the different conditions in which the structure exposed to the corrosive environment. Except for the part of structure which is buried in the soil, four main zones are considered including the underwater zone where the structure is completely submerged and is under constant influence of the water flow, the tidal zone where the

cyclic wave loads attacking the structure, the splash zone which is subjected to the continuous wet-dry cycles (the most vulnerable zone) and atmospheric zone where is not affected by the sea water directly (see Figure 1) [14], [16]. The corrosion rate is not the same at different zones, for example the corrosion rate at the splash zone is much higher than the under-water zone due to the cyclic wet-dry procedure which leads to attachment of dried salt on the structure [6], [14]. Momber [17] compared the corrosion rates of unprotected mild steel at different zones as shown in Table 1.

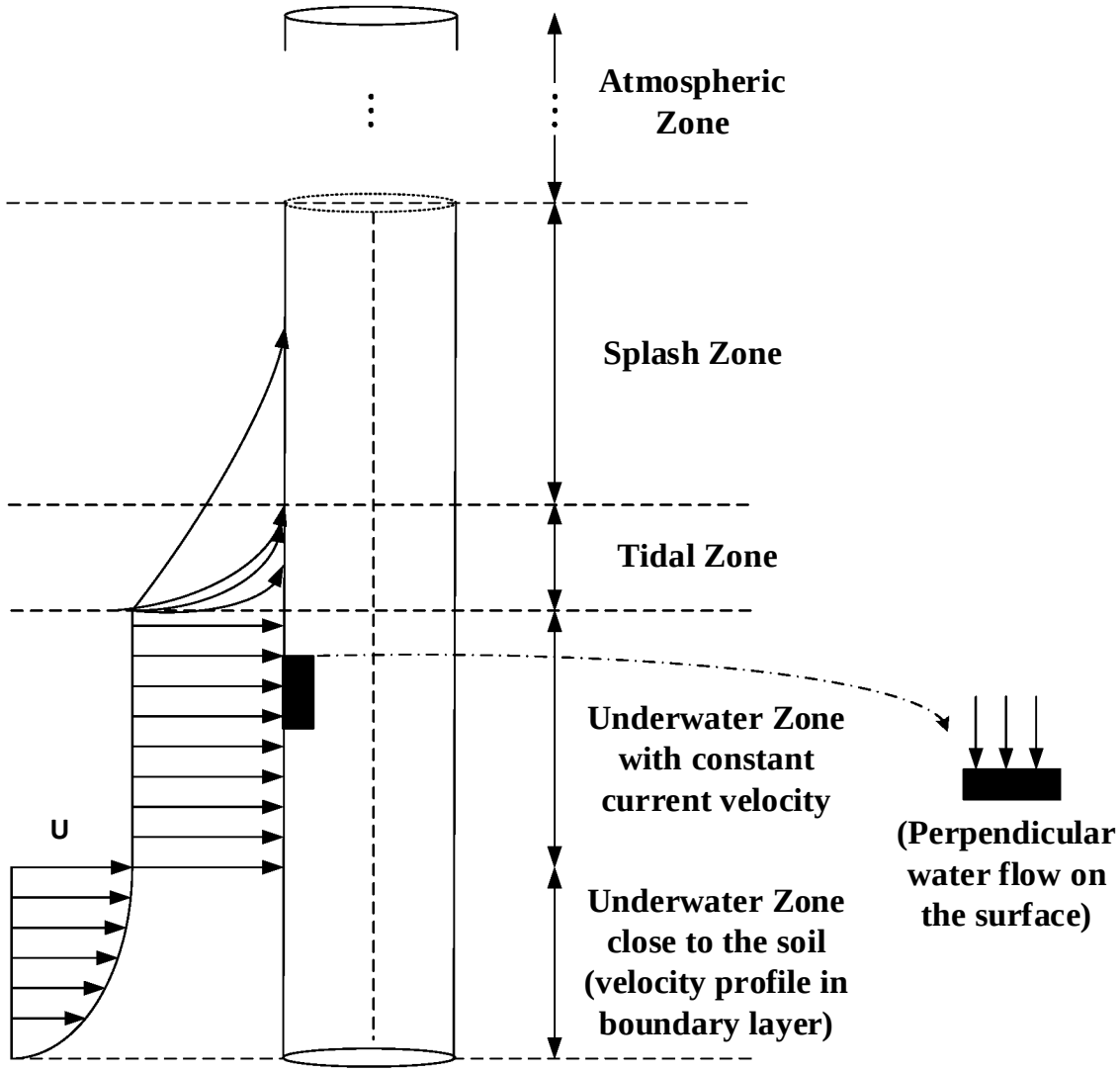

Figure 1.Schematic of the velocity profile of seawater flow on monopile structure in underwater zone with specified region of study for lab-scale experimental measurements.

Table 1. Corrosion rates of unprotected mild steel with respect to the different zones of the structure of offshore wind turbines [17].

Zones	**Corrosion rate of unprotected steel in µm/year**
Atmospheric zone	50 to 75
Splash zone	230 to 400
Tidal zone	50 to 230
Under-water zone	130 to 200
Buried in soil zone	60 to 130

Application of coatings on metals is the most common method of corrosion protection; however, in order to select the right type of coating, the number of layer of applications, in addition to the thickness of each layer, it is important to know about the dominance and influence of each corrosive factor with respect to the environment where the exposure takes place. For example, for most of the agricultural machines and devices the chemicals in the soil and animal waste are the most destructive factors [18], [19], while in the case of the automobile industry salt content of the small puddles on the roads and UV lights are the most vital corrosive factors [20]. For offshore structures identifying the participation level of each corrosive factor is very difficult since the combination of multiple factors with high level of severity corrodes the structures. The corrosive factors include UV lights, high speed moisturized air in atmosphere, salt, temperature, and bacterial content of water, in addition to the cyclic loads applied by ice, water motion and wind around the structure [15], [21]–[25]. Cyclic loading results in crack initiation and consequent fatigue which ultimately leads to failure of the structure [26].

The regular protection methods of offshore wind structures consist of the application of two or three layers of epoxy-based coatings with a polyurethane topcoat coupled with the cathodic protection especially for under-water zone [6], [27], [28]. For the monopile structures, the condition of the wind turbine structure is identical to any other vertical cylindrical structure like offshore oil constructions, bridge pier etc., which are placed in shallow waters. Based on

different available standards (EN ISO 12944, ISO 20340, etc.) the number of layers and the thickness of applied organic coatings (generally epoxy based) in underwater zone varies corresponding to the location of the offshore installations. In general, the number of layers is between one to five with the total dry film thickness of 350 to 800 µm [16], [29], [30]. The coating systems of offshore wind turbine are mostly tested on-site, where different coated samples exposed to the sea water at the specific locations planned for the installations of the turbines. The main advantage of on-site testing is that all the corrosive factors affect the coated samples simultaneously and therefore the protection rates of coatings can be evaluated with high certainty. However, the on-site testing is subjected to some disadvantages such as the duration of tests which regularly take between one and three years, the limitation of the validity of the results to the location of testing, and lack of measurement methods and devices to distinguish between the effects of each destructive factor.

There are different types of laboratory tests including salt spray assessment, static and cyclic accelerated assessments, and immersion in electrolytic solutions, while Electrochemical Impedance Spectroscopy (EIS) measurements monitor and characterize the degradation process of both metals and applied coatings. Although the laboratory tests are subjected to some disadvantages like the difficulty to correlate with naturally weathered samples, the main advantages include the widely proven reliable EIS results to detect the onset of coating failure, the universality of results, the far less expenses in comparison with on-site, and the shorter assessment durations compared to natural environments in accelerated tests. Despite the several advantages of laboratory EIS testing, the majority of the tests have been limited to the exposure of coated or unprotected metals to electrolytic solutions, while the flow-induced corrosion measurements have not received enough attention until recently [31]–[36].

Among all participating corrosive factors in the environment of offshore wind turbines, the focus of our work is on the influence of mechanical stresses due to the water flow on the degradation of organic coatings. Organic coatings are usually applied as an outer layer of multi-layer system of coatings. The outer layer works as a primary protective layer between the rest of the coated layers and the corrosive environment.

In our study, the influence of sea water flows on the degradation of the organic coatings was investigated in the underwater zone. In the underwater zone, water currents flow continuously at constant velocity with respect to the time of the day and year, and their distance to the water level (wave zone) and the seabed. In order to resemble the condition of coated monopile structures to such a water flow, an impingement chamber device was designed. Different flow rates were applied on the steel coated samples for a week for each flow rate. EIS was utilized for monitoring the change of barrier properties of coatings occurred during the exposure. An elcometer was utilized to measure the thickness of coatings before and after the exposure of samples to the electrolyte (3.5 wt. % NaCl solution) flow. Computational fluid dynamic (CFD) method, in addition to Particle Image Velocimetry (PIV) tests were utilized to calculate the magnitude of applied stresses on the coating surfaces. Atomic Force Microscopy method (AFM) was employed to study the influence of flow on the surface properties of the coating samples. Having analyzed both the EIS results, and the applied stresses, the theory of thermo-activated processes in combination with the thermoelasticity equations were derived in a way to calculate the influence of applied stresses on the change of dialectic constant of the coating (ε_c), activation volume (V_a), volume fraction (ϕ), amount of fluid uptake (M_t) and the diffusion coefficient (D) of the coatings. Considering the calculated parameters, the equilibrium

values of volume fraction, amount of fluid uptake and capacitance were obtained and related to the influence of impingement flow and the rate of the flow.

Secondly, the effects of freely suspended particles, which may exist in seawater that monopiles encounter, was investigated. The same impingement chamber device, and the same measurement techniques as mentioned for underwater zone, were utilized for this purpose. The suspended particles could have destructive effects on the coatings of offshore wind structures. Such effects can be categorized into chemical and physical effects. The high concentration of suspended particles including living species in the vicinity of the offshore structure could change the PH of the sea water, the oxygen content, and other mineral and organic contents of water, which could promote the severity of the corrosive environment for the coatings. However, the focus of our work was on the physical effects, which relates applied stresses on the coatings due to the kinetic energy of the suspended solid particles in water currents to the changes of the barrier properties of the coatings.

Finally, to investigate the influence of cyclic loads of waves on the degradation of organic coatings (the wave zone), a wave tank was designed and configurated. The wave tank designed in a way to apply very low to medium range of stresses on the surface of coating samples. Such stresses helped to study the gradual degradation of coatings rather than witnessing the fatigue damage. The velocity of the water flow in addition to the stresses were measured with the Particle Image Velocimetry method. Moreover, the Electrochemical Impedance Spectroscopy method was utilized to monitor the deterioration of coatings. Figure 2 shows the schematic of how the variety of methods have been employed to investigate the effect of stresses on the degradation of organic coatings.

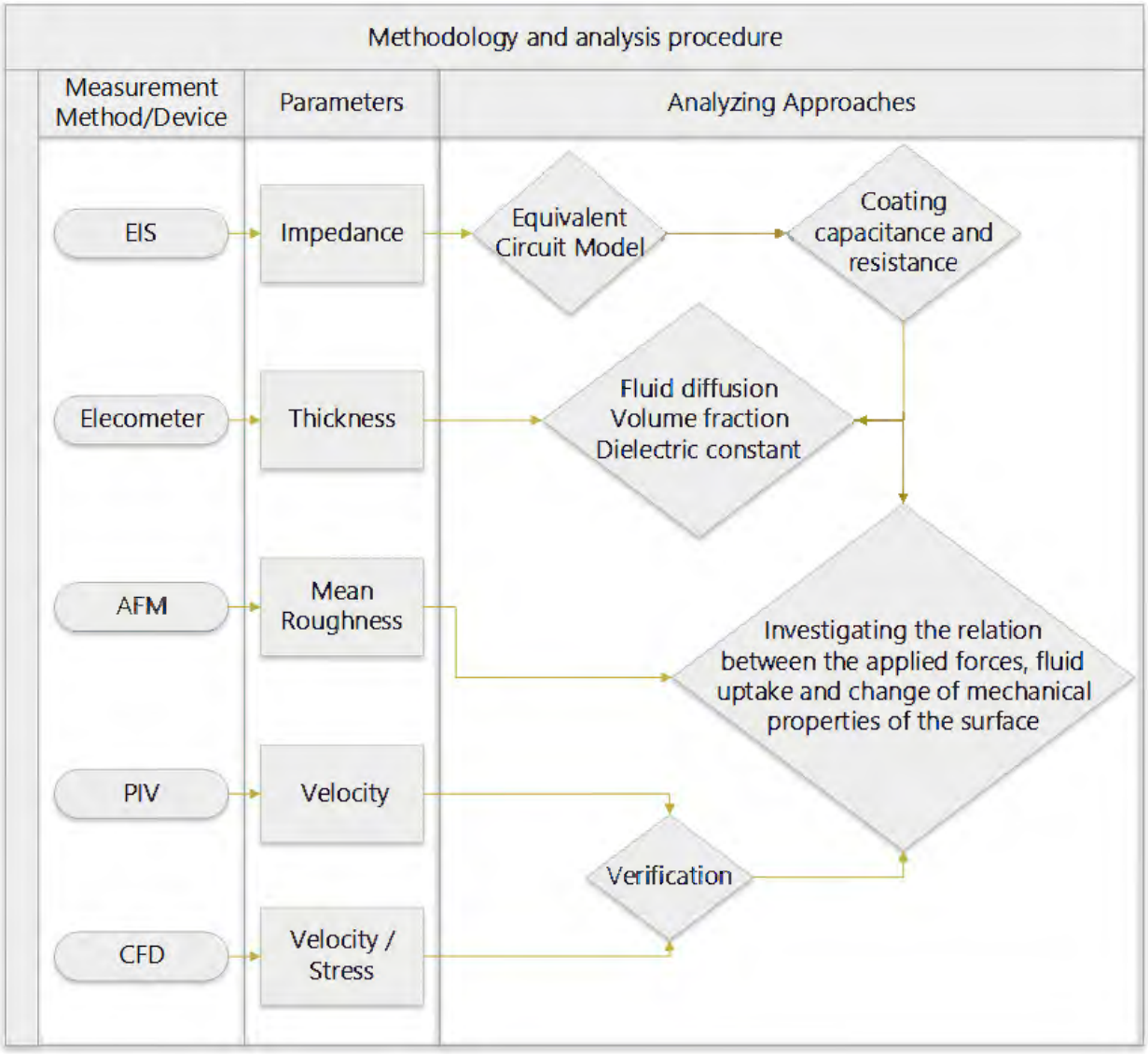

Figure 2. The methods and processes, which are employed to investigate the effect of applied stresses due to water flow on the degradation of organic coatings.

To investigate the influence of applied stresses due to the water flows on the degradation of organic coatings, a set of experimental approaches were needed to be designed. The experiments provided raw EIS data, which were utilized to track and analyze the coatings' degradations with respect to the electrical elements of the equivalent circuit models. Moreover, CFD and PIV methods were utilized to calculate the applied stresses on the surface of the coatings. A set of equations were derived and utilized in order to specify the direct influence of

the applied stresses on the electrochemical parameters. The summary of the objectives that are accomplished in this dissertation are listed as follows:

- Investigating the effect of an impingement flow of 3.5 wt. % NaCl solution on the degradation of organic coating as compared with that of a stationary condition.
- Investigating the influence of the different flow rates of the impingement flow on degradation of organic coatings using EIS.
- Topography characterization of exposed coating surfaces under different flow rates using AFM.
- Investigating the influence of particles contained in the 3.5 wt. % NaCl solution on the degradation of organic coatings using EIS.
- Investigating the influence of cyclic loads resulted from lab-scale simulated waves of salt water on the degradation of organic coatings using EIS.
- Modeling and verifying the magnitude of applied fluid stresses on the coated samples with CFD and PIV.
- Identifying and analyzing the effect of applied stresses due to the fluid flow on the electrochemical reactions using thermal activation theory, thermal elasticity laws, thermodynamics relations, in addition to the Fick's laws.

2. DEGRADATION OF EPOXY COATINGS EXPOSED TO IMPINGEMENT FLOW

2.1. Introduction

Metal corrosion has been a serious challenge in engineering equipment associated with marine technologies, medical and biomedical devices [37], [38], oil and gas industry, offshore wind turbines etc. In general, corrosion on metals is caused by redox reaction and could be promoted by the movement of fluid flow on the metal surface [39], [40], Organic coatings are widely used for the corrosion protection of metal substrates. Many corrosion protective coatings are under the influence of fluid flow. The offshore wind turbine structures are impacted by the flow of seawater at a variety of speed and angle of attack [41], [42]. Similar phenomena can be found on the bridge structures and offshore oil drilling rigs, where the degradation of corrosion protective coating is promoted by the continuous impingement attacks of fluid flow on the structures [21]–[23], [25]. Currently, the studies of coating degradation have been mostly limited to the exposure of coated samples to a stationary electrolytic solution, e.g. Refs [43]–[49]. Few studies have been contributed to understand the influence of the fluid flow on the degradation of organic coatings. Bierwagen's group [48], [50] first conducted experiments to study the influence of both open flow and a controlled laminar flow of a 3.5-wt% NaCl solution on the degradation of organic coatings. Electrochemical Impedance Spectroscopy (EIS) method was used to monitor the degradation of coating. Wang and Bierwagen [50] observed that the barrier properties of the coating measured electrochemically decreased with the increasing flow rate. Zhou et al. [45], [51] compared the influence of two different working fluids (DI water versus 3.5 wt. % NaCl solution) on organic coating degradation as characterized by EIS measurements. They concluded that the barrier property of coatings decrease with the immersion time and the decrease was more substantial for flowing fluid at higher flow rate disregard of the

fluid type. They also found that the decay of relative impedance modulus was larger for the organic coatings immersed in DI water. In another study, Zhou et al. [52] investigated the influence of the shear stresses on clear coat caused by laminar flow of 3.5 wt % NaCl solution at different flow rates. They concluded that the thickness of the coated samples increases due to the water penetration and blistering when the samples exposed to stationary or low velocity fluids, while with high velocity flow in laminar regime, the thickness of the coated sample decreases due to fluid shear.

So far to the authors' knowledge, no fundamental work has been reported on the influence of impingement flow on the degradation of organic coatings, although a plethora of existing studies were concentrated on the impingement-flow-induced corrosion on bare metals and metal alloys in direct contact with the electrolytic solution [33]–[36]. Cheng et al. [31] studied the erosion–corrosion characteristics of casing and tubing steels in oil fields. They performed experiments with a jet flow of 2-wt % NaCl solution at different impingement angles and flow velocities. They concluded that the corrosion rates of those steel samples increase with the rise of the flow rate, and the variations in the impact angles have a noticeable effect on the corrosion rates. Meng et al. [32] investigated the erosion–corrosion performance of two stainless steels under liquid–solid impingement conditions in 3.5-wt% NaCl solution. They concluded that material loss can be represented as a function of flow velocity. Zheng et al. [33] investigated the influence of the velocity of an impingement flow on steel using a 3.5 wt.% NaCl solution with a sand concentration of 2 wt%. They observed during the exposure the mass loss rate and change of surface roughness remain constant up to the velocity of 6 ms^{-1}, and then both mass loss rate and roughness increase rapidly with the increase of velocity up to 20 ms^{-1}. Wharton and Wood [34] studied the influence of the impingement flow for a wide range of flow rates on 304

stainless steel pipe using the electrochemical noise measurement (ENM) method. They discovered a critical velocity above which the fluid penetrates across the surface of the exposed metal causing the growth of stable pits. Melchers and Jeffrey [36] exposed steel samples to coastal tidal water flows with the velocity up to 1 ms^{-1} and measured the corresponsive corrosion rates with the weight loss method. They concluded that although the corrosion rate increased proportionally to the increase of the water flow, the relation between corrosion rate and the velocity of water was not linear. They also concluded with sufficient protection, the direct effect of water flow on the corrosion rate of steel could be negligible.

In this study, a laboratory-scale device has been designed and employed to investigate the influence of impingement flow on the electrochemical barrier properties of epoxy coatings on steel samples. In the current work, coatings are exposed to a vertical impingement flow of a 3.5 wt. % NaCl solution with a variety of flow rates. EIS has been incorporated in the device and employed to characterize the changes in coating properties inline during exposure. Moreover, Atomic Force Microscopy method (AFM) was employed to study the influence of flow on the surface properties of the coating samples.

2.2. Materials and sample preparation

The monopiles can be modeled as two-dimensional, because their diameter is much larger than its wall thickness. The diameter of monopile structures is between 5 and 10 m, with the wall thickness of 70–100, and usually coated with multilayer of coatings with average thickness of 350 μm [6], [53], [54]. Steel panels (Q-Panel, S-612 Lab Products) were used as the metal substrate. The panels are known in SAE Material Designation with the code 1008/1010 and based on ASTM Material Specifications as A1008. One side of the panels are originally polished by grinding and the mill surfaces are completely removed. The polished surface

generally gives better adhesion results when the coating applies. The properties of the steel substrates can be found in Ref. [55]. The coating sample was formulated by base component, 31.65 wt. % epoxy resin (EPON Resin 828, Miller-Stephenson), 43.04 wt. % curing agent, EPI-CURE 3164, and 25.31 wt. % xylene. The weight ratio of curing agent to EPON Resin 828 was 1.36 and no pigment was added in the coating system. The coating was applied on the polished surface of the steel substrates by draw-down method covering an area of 155 mm ×152 mm (see Figure 3). The samples were left to cure at room temperature for 48 hours. A circular area with a diameter of 80 mm on each coated sample was exposed to the electrolyte solution. The thickness of the coated samples was measured inside the circular exposure area using a coating thickness gauge (Elcometer 415). AFM measurements have been performed to explore the surface feature of the coated samples. All AFM images and results were obtained in air and collected over a scan size of 10×10 μm. The AFM measurements were taken approximately at the center of the exposed area (Point A in Figure 3) and two other locations between the center and the edge of the exposed area, with approximately 15 mm from each other (points B and C in Figure 4).

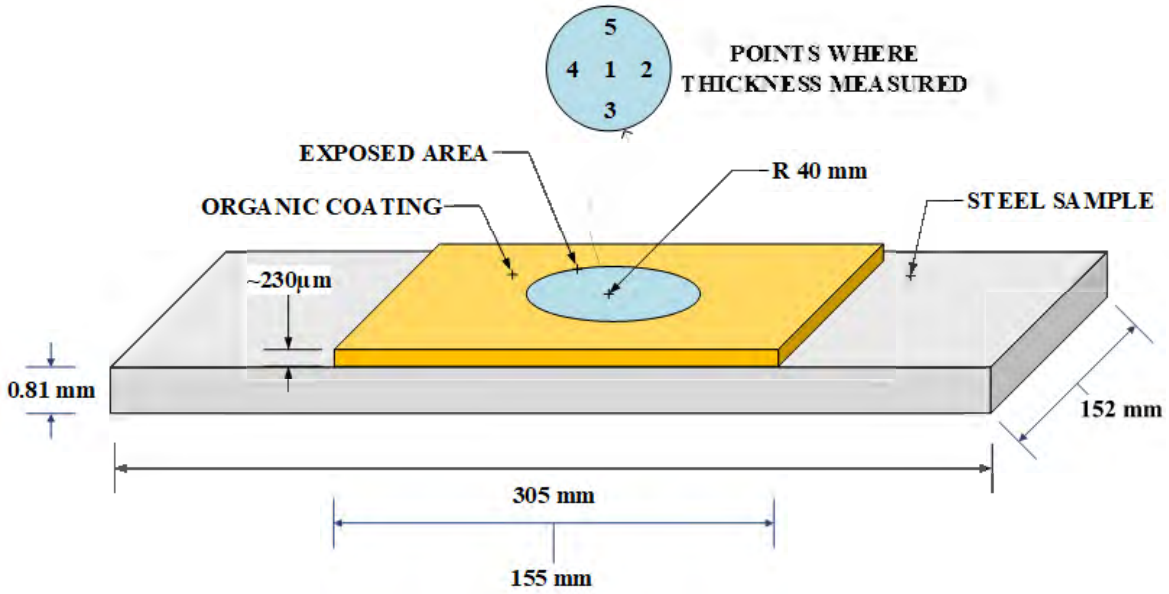

Figure 3.The schematic of the coating sample for impingement flow experiments, and the locations where the thickness measurements were performed.

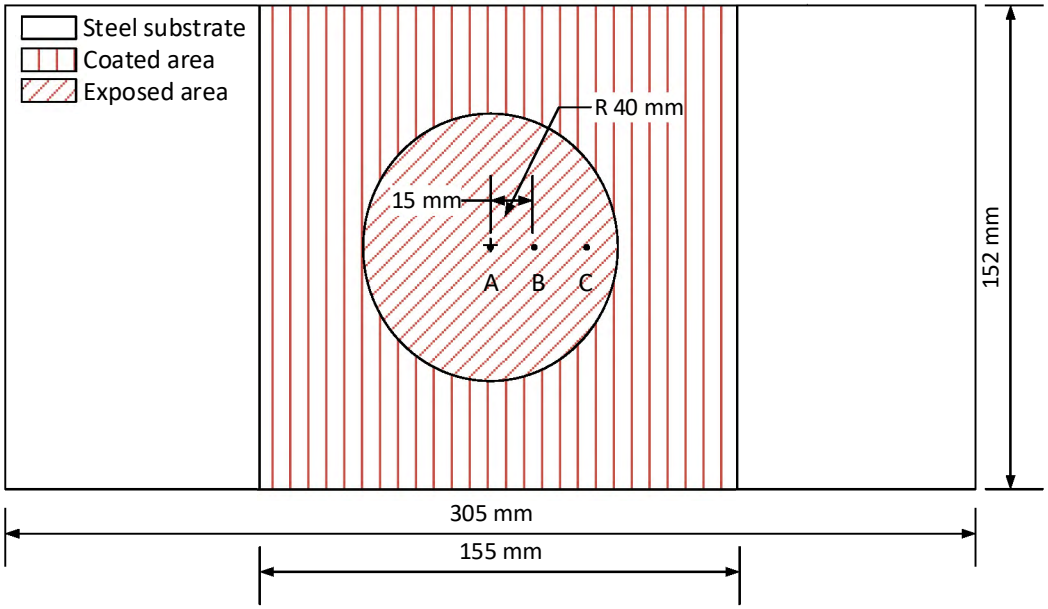

Figure 4. Schematic diagram of the coated area, exposure area, and approximate locations where AFM measurements were taken.

2.3. Test chamber

A test chamber has been designed and fabricated which is able to create vertical impingement flow on the sample surface, while EIS data could be collected simultaneously to monitor the coating degradation. A schematic of the test chamber is shown in Figure 4. The design consists of aluminum top and bottom plates as well as supports to ensure a rigid structure. The sample s sandwiched between a tube-like upper adapter (F) and a lower adapter (H). Both adapters are made by acrylic. An O-ring (E) is used to seal the upper adaptor and the reservoir (D) to the working fluid. There are no two different metals in direct contact with each other preventing galvanic corrosion. The flow inlet is placed at the top of the fixture (A) and the flow outlets are located on the sides of F. The test chamber is also equipped with a reference electrode, a counter electrode, and working electrode for EIS measurements. An internal tube is placed in the reservoir to ensure the flow is not disturbed by the electrodes. The test chamber is placed in a Faraday cage when EIS data is collected.

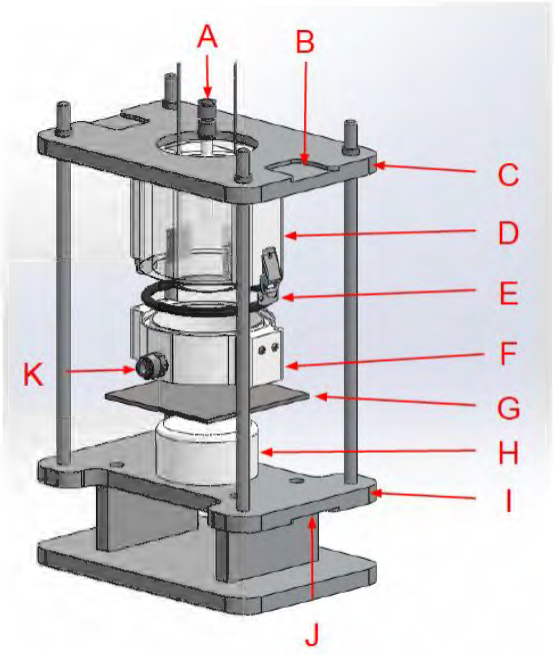

A. Inlet Orifice
B. Upper Clamping Location
C. Upper Fixture Plate
D. Saline Reservoir
E. O-Ring
F. Upper Adapter
G. Test Sample
H. Lower Adapter
I. Lower Fixture Plate
J. Lower Clamping Location
K. Exit Orifice

Figure 5. Schematic diagram of the test chamber.

2.4. Fluid circulation system

Figure 6 shows the schematic of the complete circulation system. The working fluid was fed into the chamber through the inlet orifice with an inner diameter of 5 mm by a peristaltic pump. The distance between the inlet nozzle and the coating surface is maintained at 7.5 cm. The inlet flow rate was controllable by adjusting the speed of the pump and was measured by a flow meter which were placed between the pump and the inlet orifice. In order to investigate the influence of the impingement flow on the degradation of coated samples, three different flow rates of Q = 0.1, 0.2 and 0.3 gpm (i.e. 6.31, 12.62 and 18.93 cm^3s^{-1}) applied on coated samples for a week on each test. Since the diameter of inlet nozzle was 5 mm, the velocities at the nozzle exit were V = 0.3214, 0.6427, 0.9641 ms^{-1}. The maximum applied velocity is approximately the average velocity of seawater in shallow regions of the ocean and seas (up to 30 m) where the majority of monopole offshore wind turbines are installed. In addition, selecting the mentioned applied velocities was to maintain the stability of the fluid flow inside the impingement chamber for the duration sample immersion. An air diffuser was connected to the reservoir and used to

saturate the solution with air. The working fluid was discharged through the two exit orifices (K in Figure *5*) by the gravity toward a reservoir container. A steady circulation of the fluid in the system was maintained. Each coating sample was immersed in an impinging 3.5 wt. % NaCl solution for a week. The samples were placed between the lower and upper adaptors (as shown in Figure *6*) at the bottom of the test chamber. The working fluid was pumped from the fluid reservoir at room temperature to the chamber section, and then recycled back to the reservoir through the exit orifices by gravity. A rotameter was used to measure the flow rate for each test. The area of each sample that was exposed to the working fluid was 50.26 cm^2.

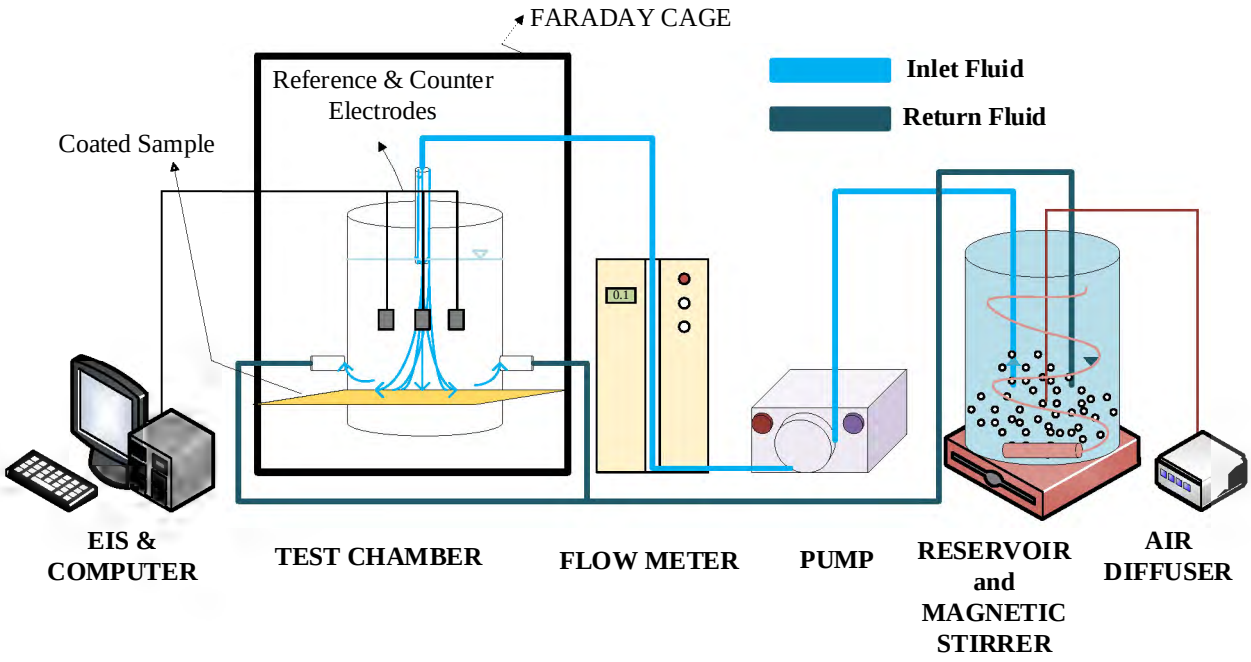

Figure 6. Schematic diagram of the particulate flow circulating from the reservoir to the impingement flow chamber while the degradation of coatings monitored by EIS.

2.5. Electrochemical Impedance Spectroscopy (EIS) measurements

For the EIS test, the working electrode was connected to the stainless-steel substrate, while two platinum electrodes were used as counter electrodes located in symmetry on the left and right sides of the sample. Another platinum electrode was used as the reference electrode, which was immersed in the solution just above the sample. A Reference 600 Potentiostat by

Gamry Instruments was employed to collect the EIS data. Measurements were taken over a frequency range of 10^{-2} to 10^{5} Hz with ten points per decade using 15 mV AC perturbation coupled with the open circuit potential. In order to filter the noise and disturbances influencing the EIS results, the impingement flow chamber was located in a Faraday cage.

2.6. Measurement of the barrier properties of coatings and corresponding analysis

EIS measurements have been carried out to monitor the changes in the barrier properties of the epoxy coating samples. Experiments are designed to fulfill two comparisons. The first is to reveal the effect of impingement flow in contrast to stationary immersion. The second comparison is regarding the EIS results among different flow rates.

2.6.1. Comparison between impingement flow and stationary immersion

2.6.1.1. EIS results

Figure 7 shows the Bode plot of EIS data for coating samples under stationary condition and flow rate Q = 18.93 cm^3s^{-1} respectively. Figure 8 shows the corresponding phase angle behaviors. The low frequency impedance modulus decreases with the increase of the immersion time for both cases. The rate of change of the impedance modulus is more significant at the initial hours of exposure, followed by a relatively slower decrease. This behavior demonstrates that the barrier property of organic coatings was deteriorated during a week of the exposure to the working fluid. The impedance modulus of EIS spectra at low frequency serves as a strong indicator of the corrosion resistance of coating samples; therefore, the impedance modulus at 0.01 Hz as a function of immersion time is plotted in Figure 9. To make a comparison between the low-frequency impedance modulus, the initial value of impedance for each test has been used as the base to normalize all low-frequency data for the same flow rate. Considering both Figure 9 and Figure 10, we observe that the rate of decrease of the impedance modulus for Q = 18.93

cm^3s^{-1} was higher than the stationary condition, especially during the first 24 hours. This indicates the fluid flow may have promoted the percolation of water into the coated samples.

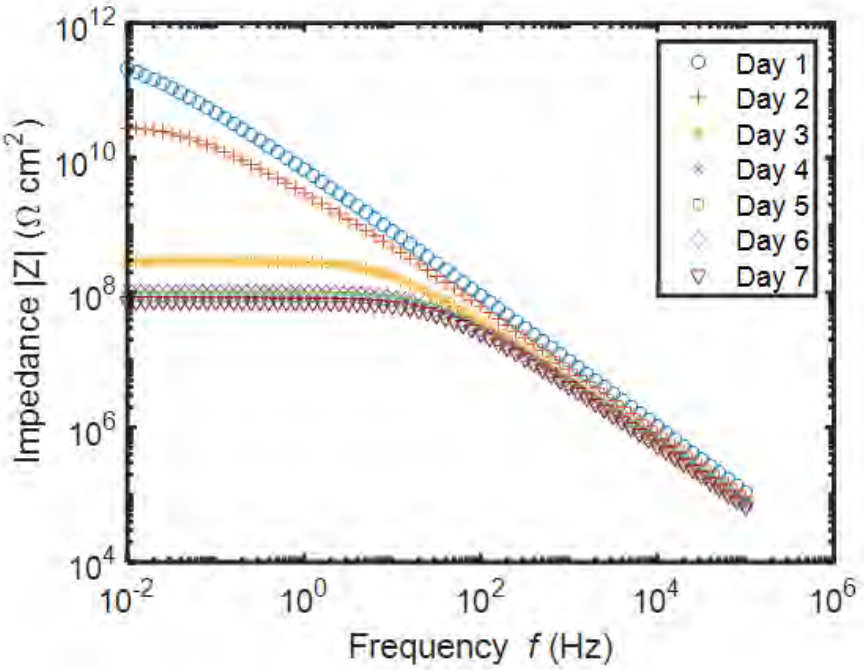

(a)

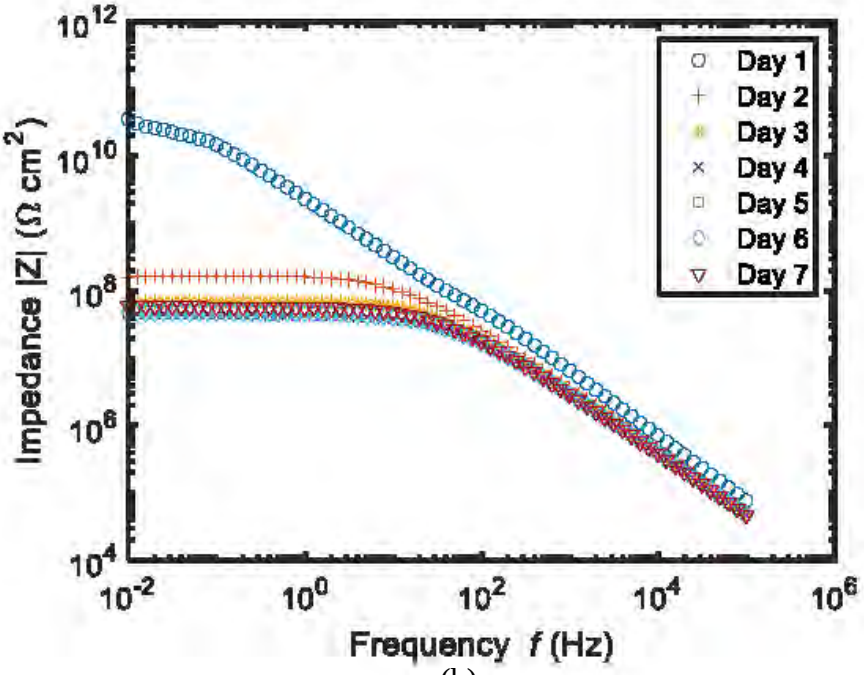

(b)

Figure 7. Impedance modulus as a function of frequency (Bode diagram) for coating samples exposed to a 3.5 wt. % NaCl solution for (a) Stationary, (b) Q=0.3 gpm (18.93 cm^3s^{-1}).

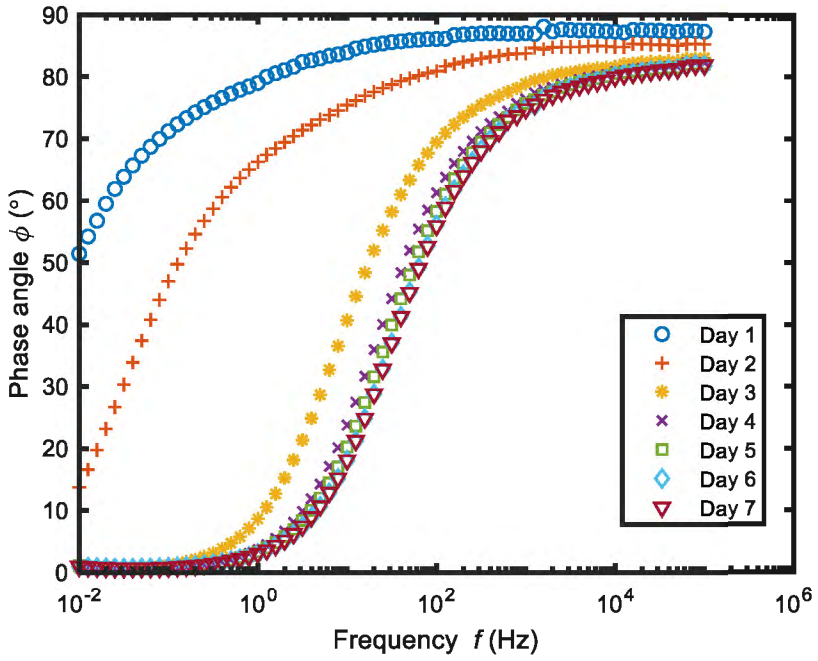

(a)

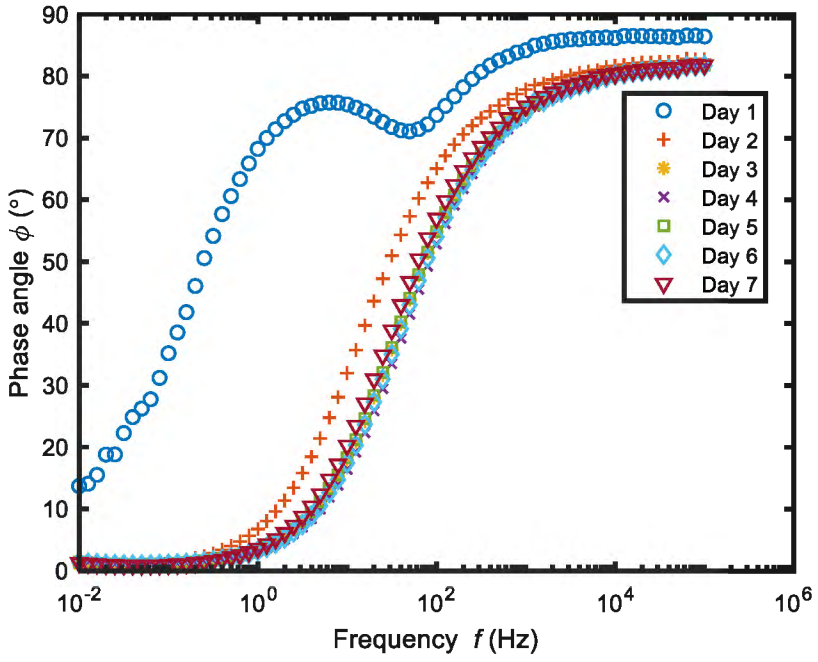

(b)

Figure 8. The phase angle as a function of frequency (Bode diagram) for coating samples exposed to a 3.5 wt. % NaCl solution for (a) Stationary, (b) Q=0.3 gpm (18.93 cm^3s^{-1}).

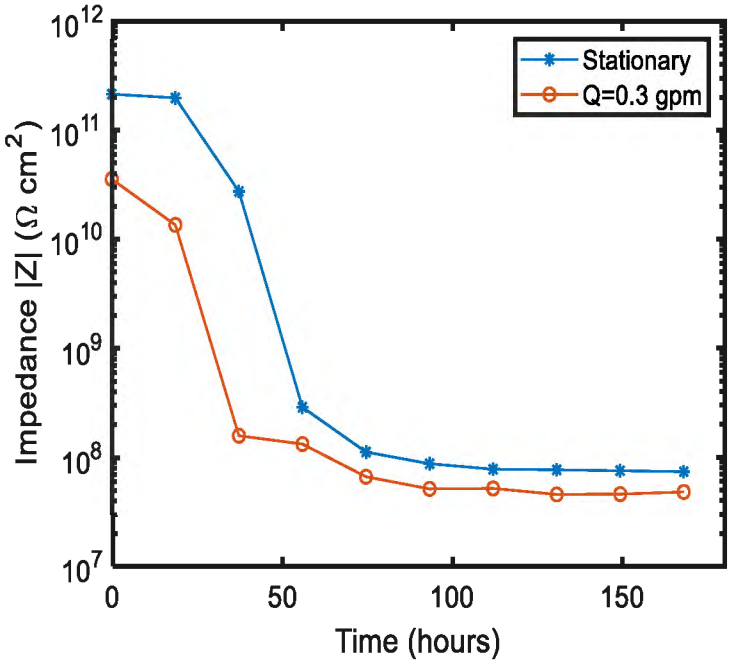

Figure 9. Impedance modulus at 0.01 Hz as a function of time for stationary immersion and an applied flow rate of Q = 0.3 gpm.

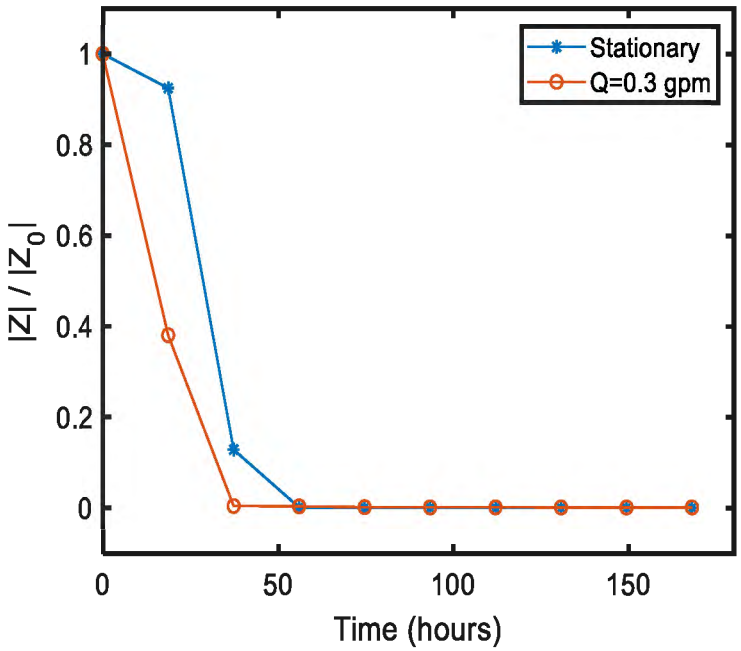

Figure 10. Relative impedance modulus as a function of time for stationary immersion and applied flow rate of Q = 0.3 gpm.

2.6.1.2. Equivalent circuit modeling

Figure 11 shows two different equivalent circuit models that have been used to analyze the EIS data. ZsimpWin3.6 has been employed in the process. The best fitted equivalent circuit model was selected by fitting to the Nyquist graphs of EIS data and the values of χ^2 were compared. Ideally the value of χ^2 should be between 10^{-5} and 10^{-3} to be regarded as an acceptable circuit model [56]. As an example of the model selection, Figure *12* shows a Nyquist diagram of the experimental data of one of the samples that was exposed to the flow rate of Q = 18.93 cm^3s^{-1}, the circles indicate the experimental data, while the dashed line represents the calculated impedance modulus for degraded coating model 1 and the solid line illustrates model 2. Figure 12 shows that model 2 was fitted the best to the experimental data with $\chi^2 = 1.7\times10^{-4}$. While equivalent circuit models for ideal dielectric materials involve lumped resistive (R) and capacitive (C) components [57], for most realistic cases where the impedance data cannot be represented by lumped circuit elements, such as the current case, distributed elements or constant phase elements (CPE) are employed [58]. Evidence could be found in Figure *8* for the complicated behavior of phase angles. Figure 8 shows the phase angle as a function of frequency as the immersion time increases. The maximum values of phase angles for all experiments were less than 90°. Theoretically, a phase angle of 0° represents complete resistance, and 90° complete capacitance; therefore, the values below 90° represent the existence of non-perfect capacitance. In this case a constant phase angle element (CPE) is suitable to be used. A CPE is a mathematical realization of a system in which the phase angle between applied AC voltage and resulting current remains independent of the frequency. CPE is usually employed in a model to replace a capacitor to simulate the non-homogeneity of the system. The CPE element is formulated as follows,

$$Y_{CPE} = Y_o(j\omega)^n \tag{1}$$

where ω is the radial frequency, Y_0 is a factor of proportionality. As the exponent, *n* defines the character of frequency dependence *(-1 ≤ n ≤ 1)* [56]. For integer values of n (*n = 1, 0, −1*), the *CPE* characterizes *C* (capacitance), *R* (resistance), and *L* (inductance), respectively. The values of n are associated with the non-uniform distribution of the current due to materials non-homogeneities, such as the adsorption of inhibitors, formation of porous layers and the variations in properties or composition of surface layers [59]. Y_{CPE1} and Y_{CPE2} are employed in the second model for the interface between the coating surface and solution, and that for the metal-coating interface respectively. To better understand the coating behavior, *CPE* is converted into capacitance with the following equation [40], [60]:

$$C = (R^{1-n} \cdot Y_{CPE})^{\frac{1}{n}} \tag{2}$$

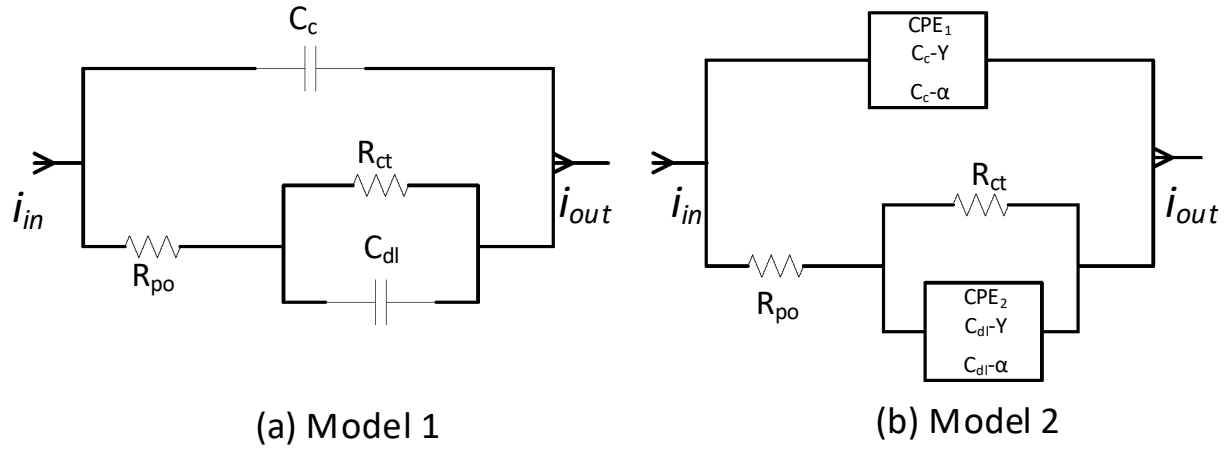

Figure 11. Different equivalent circuit models used in analysis. R_{po} is the coating resistance. R_{ct} is the resistance of the coating-substrate interface, C_c and C_{dl} are coating capacitance and double layer capacitance respectively, CPE_1 and CPE_2 are the constant phase element between coating-solution and coating-metal interfaces respectively.

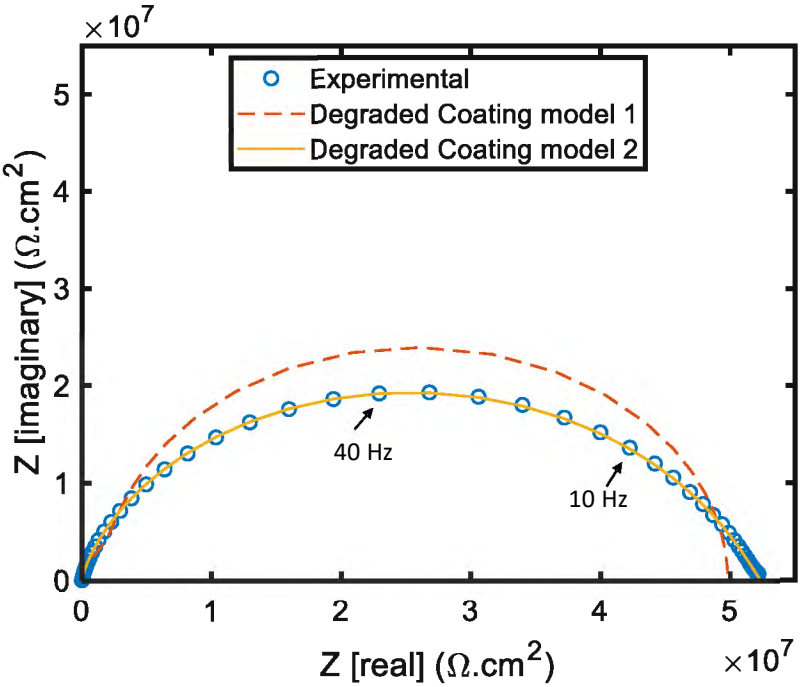

Figure 12. A comparison between fitting curves of the Nyquist diagram of two different equivalent circuit models, degraded coating models 1 and 2.

Figure 13 shows the behavior of the coating capacitance C_c of the equivalent circuit model. The coating capacitance increases as immersion time increases for both cases, indicating the reduction in the corrosion rate toward the end of the exposure time. It is also observed that the coating capacitance increases more rapidly for the presence of fluid flow within the first hours of exposure. The phenomenon may be explained by the increased percolation of solution into the coatings promoted by applied flow rate. The value of the double layer capacitance depends on many variables including electrode potential, temperature, ionic concentrations, types of ions, oxide layers, electrode roughness, impurity adsorption, etc; however, the fluctuations of C_{dl} values are within a small range for both cases (Figure 14), which provides not obvious difference between the two conditions.

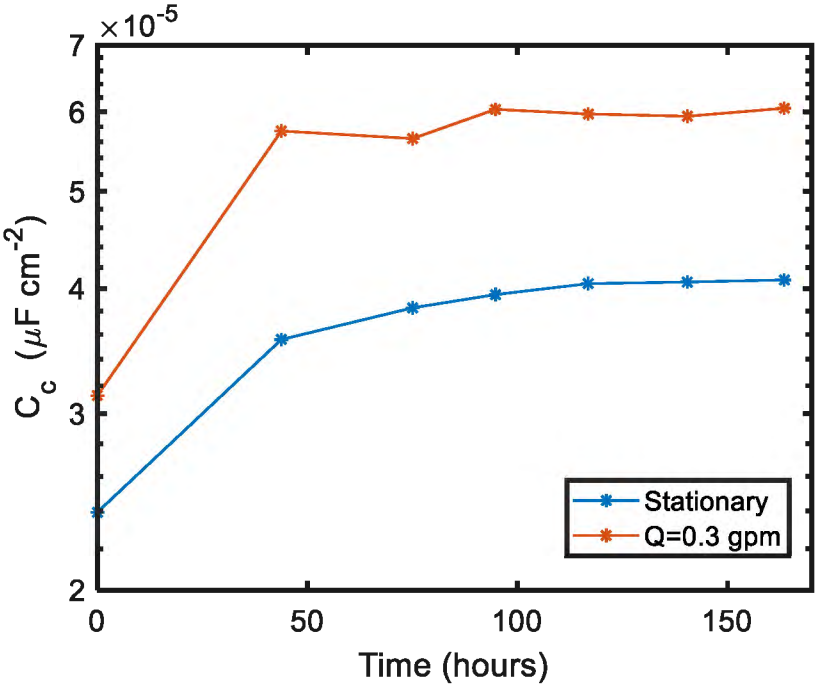

(a)

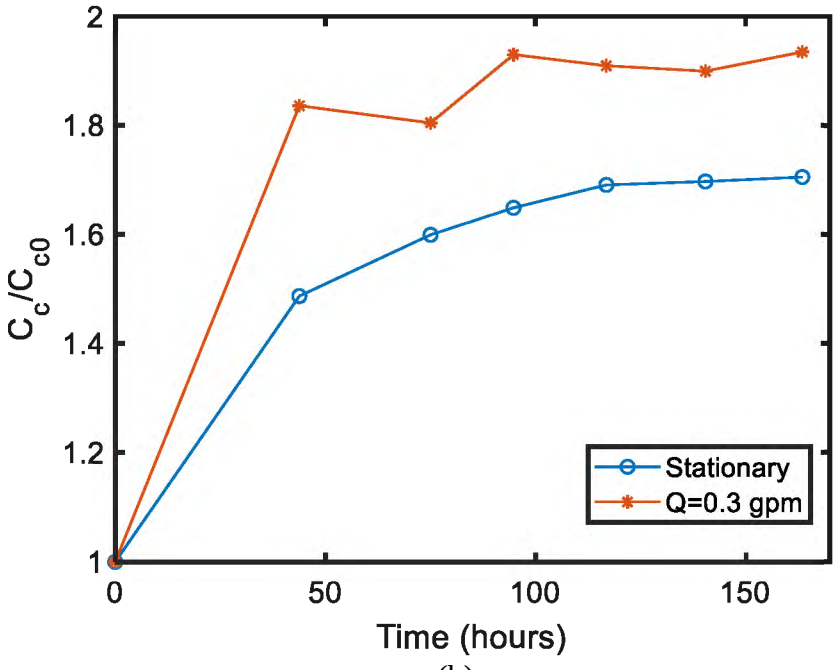

(b)

Figure 13. The absolute (a) and normalized (b) coating capacitance (C_c) of the equivalent circuit model as a function of immersion time for stationary condition and 0.3 gpm.

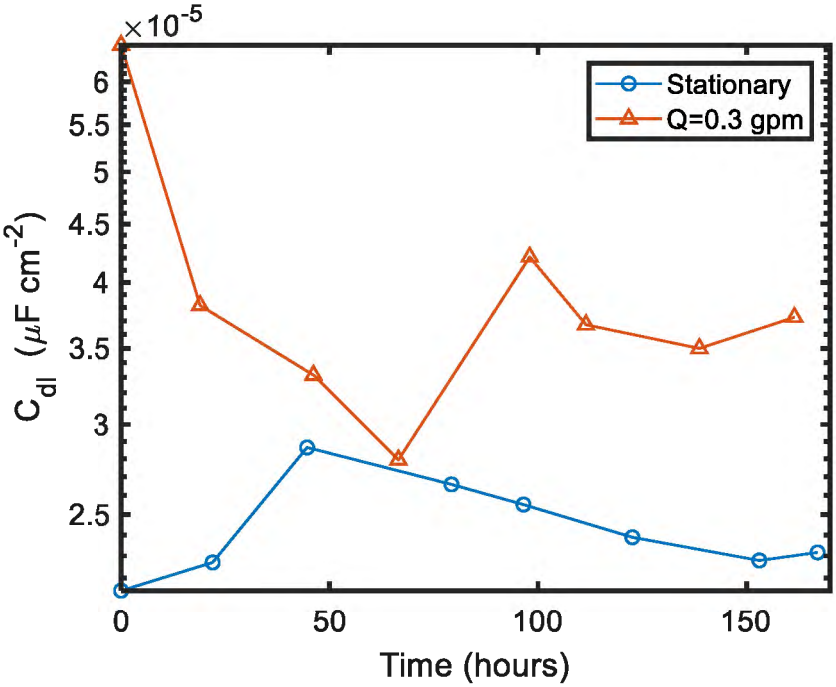

Figure 14. Double layer capacitance (C_{dl}) of the equivalent circuit model as a function of immersion time for stationary condition and flow rate of Q = 0.3 gpm.

Figure 15 shows the pore resistance (R_{PO}) and its normalized value as a function of immersion time. The value of R_{PO} indicates the amount of ion conducting pathways that develop in the coating. The overall trends indicate that the R_{PO} values decrease over time for both cases; however, the decline rate of pore resistance is much higher for the exposure to the impingement flow especially during the first 24 hours. Indicating a higher rate of water penetration beneath the coating.

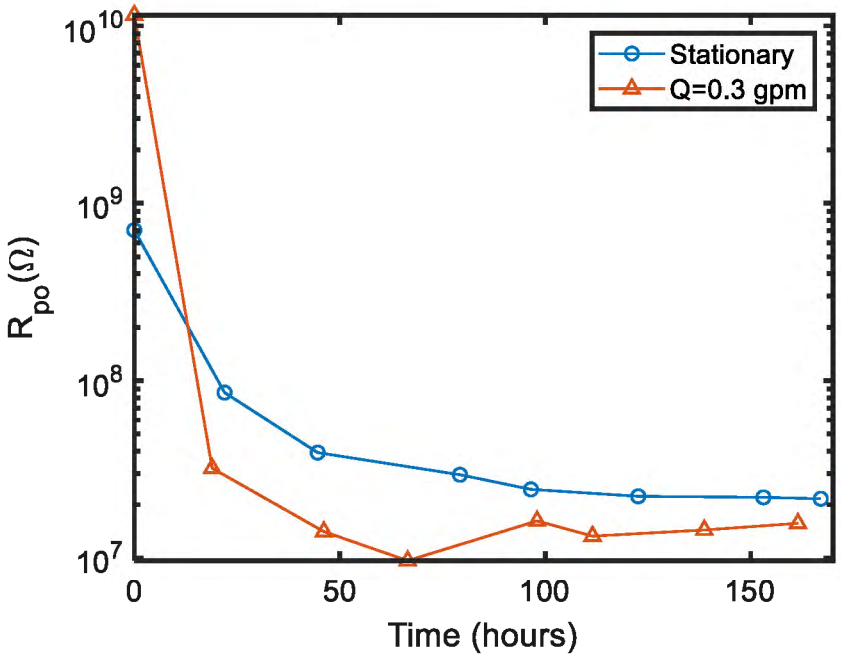

(a)

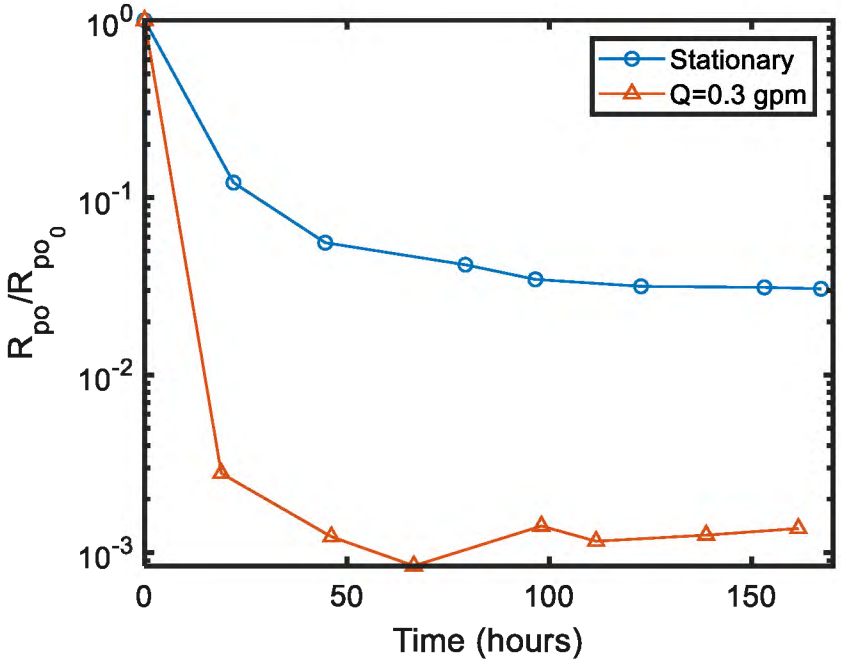

(b)

Figure 15. Pore resistance (R_{PO}) of the equivalent circuit model as a function of the immersion time for (a) the absolute values of R_{PO}, (b) the normalized values of R_{PO}.

Figure 16 illustrates the charge transfer resistance (R_{ct}) of the equivalent circuit model as a function of immersion time. When an electrode is polarized, it can cause the current to flow via

electrochemical reactions that occur on the electrode surface. The amount of current is controlled by the kinetics of the reactions as well as the diffusion of reactants/products towards/away from the electrode. During immersion, the R_{ct} values decrease as immersion time increases for both cases and the decline rate is almost the same during the whole tests' period.

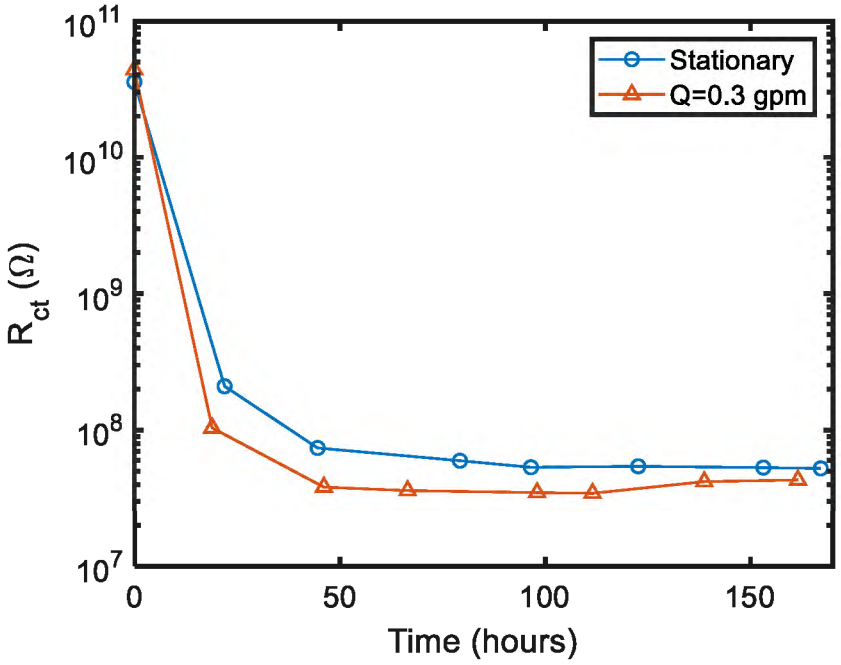

(a)

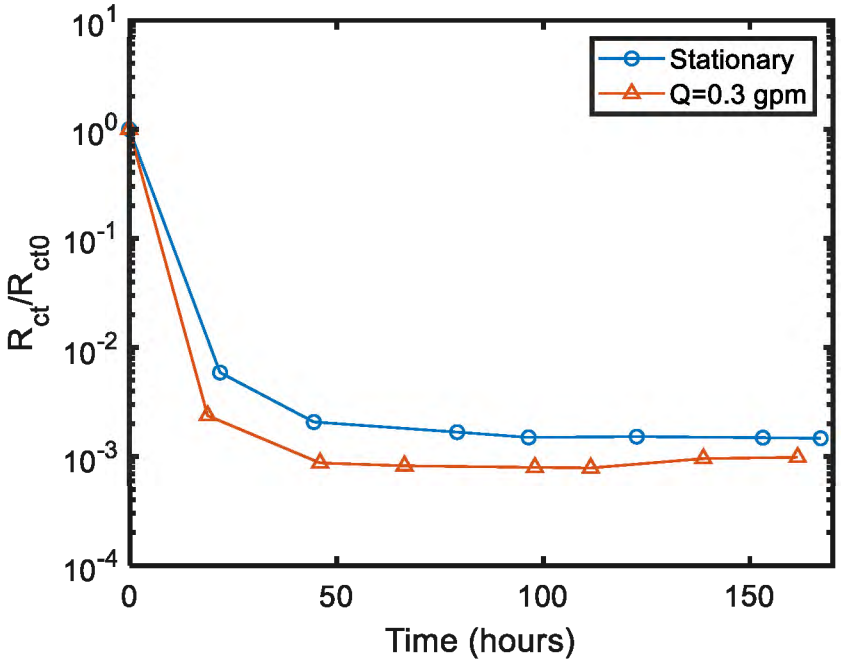

(b)

Figure 16. Polarization resistance (R_{ct}) of the equivalent circuit model as a function of the immersion time for a) the absolute values of R_{ct} and (b) the normalized values of R_{ct}.

2.6.1.3. Topography characterization

The thickness of the coating samples was measured within a radius of 4 cm from the center of the coating samples, where the coatings were exposed to the fluid. The mean values for each sample were taken into comparison. Figure 17 shows the values of coating thickness before and after the immersion. We observe that for the stationary test the thickness of the coating slightly increases after immersion. We believe the coating swelling was dominating in this case, which was caused by the solution that percolates through the coating layers. For the samples exposed to impingement flow, the coating thickness was reduced after the immersion. In those cases, due to the increase of the applied flow rate and the associated elevated fluid shear, coating samples experienced more substantial abrasion on their surfaces that may lead to significant decline of the thickness.

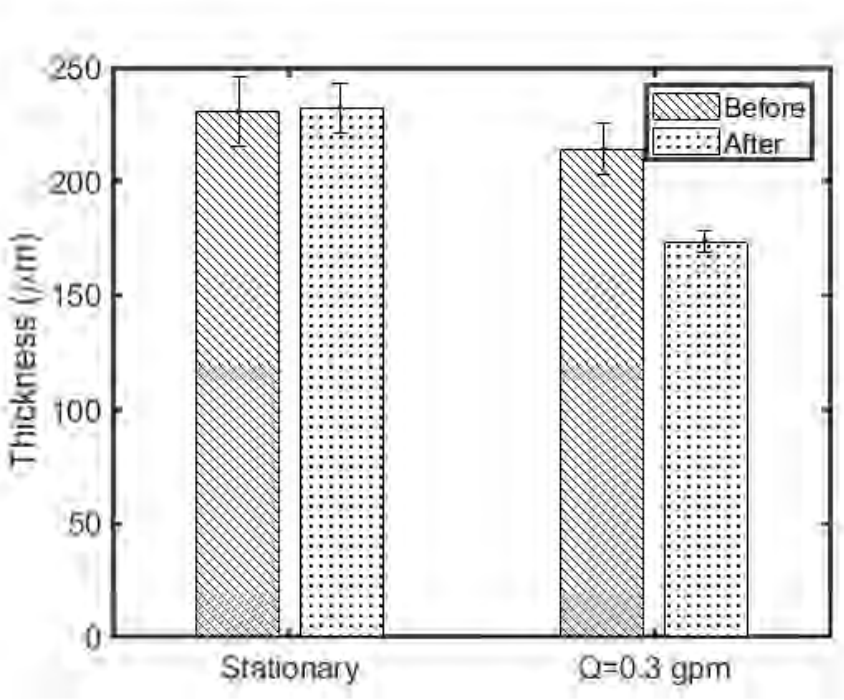

Figure 17. Coating thickness before and after the immersion for stationary condition and applied flow rate of Q = 0.3 gpm.

To examine the influence of fluid flow on the surface features of the coating samples, we obtained the AFM images before and after immersion as shown in Figure 18. The images shown were all taken from the center points of the samples. The coating surfaces were smooth before the exposure. More protuberances were observed on the coating surface after the immersion and larger surface features could be found for higher flow rates. As shown in Figure 19, we plot the roughness of the coating samples obtained from AFM analysis before and after the immersion. The Samples exposed to a flow rate of Q = 0.3 gpm exhibit a more substantial increase in its roughness comparing to smaller flow rates. The error bars in Figure 19 indicate that the variation in measured roughness data is also greater for higher flow rates. As the fluid flow impacts coating surface, materials get removed from the coating surface, and more bumps and dimples are formed on the surface which leads to the increase of the mean roughness and the variations in roughness.

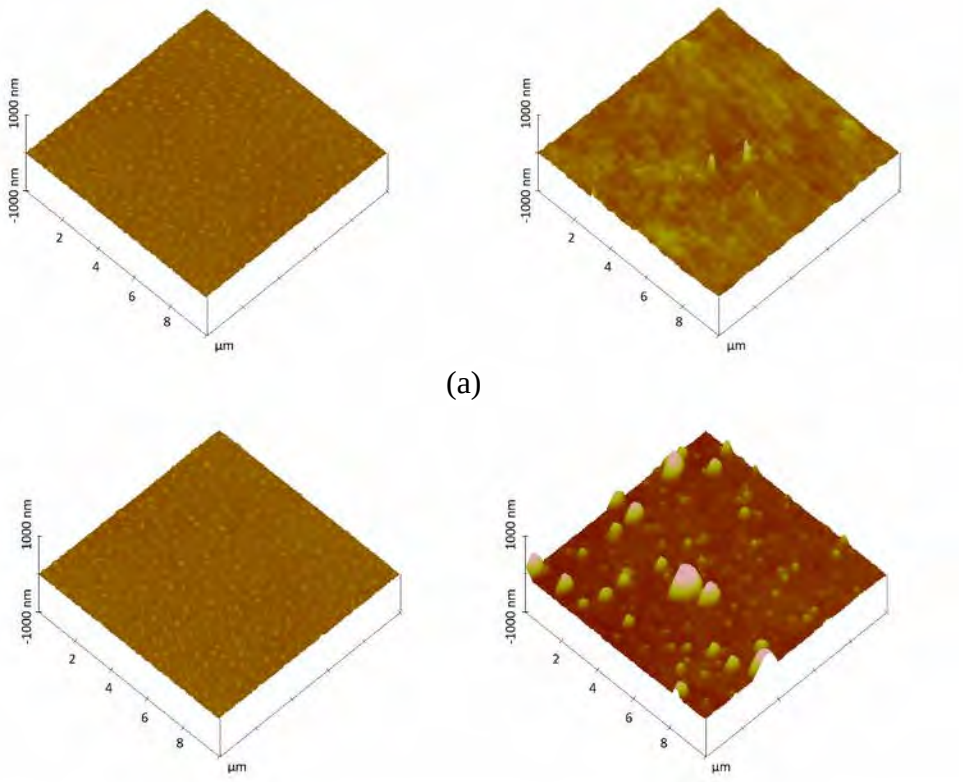

Figure 18. AFM images for the coated surface before (left) and after (right) exposure (a) stationary immersion (b) impingement flow rate of Q = 0.3 gpm.

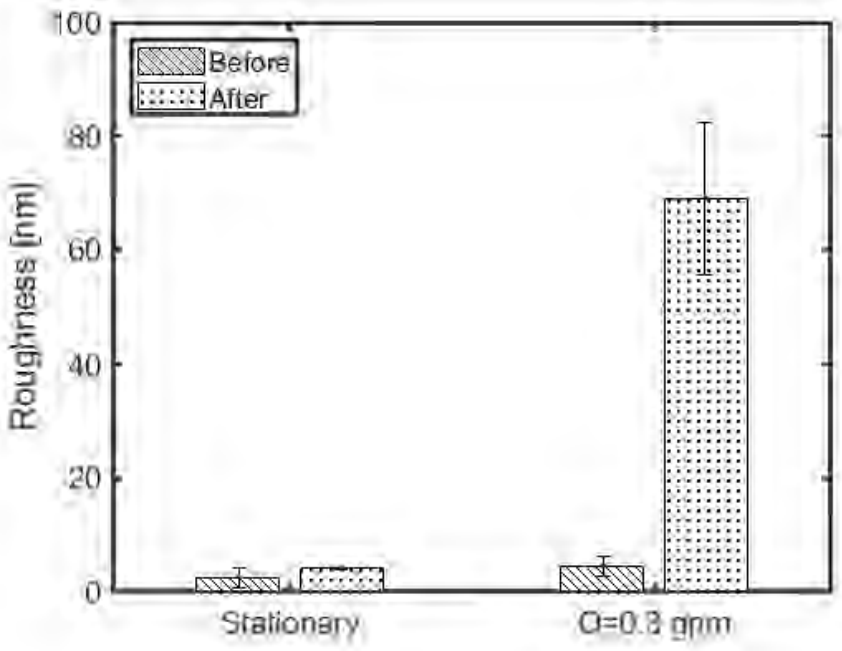

Figure 19. Roughness of the coating surface before and after the immersion for stationary condition and applied flow rate of Q = 0.3 gpm.

2.6.1.4. Discussion

This study compared the degradation behavior of an epoxy coating exposed to an impingement flow of 3.5 wt. % NaCl solution and the stationary immersion of the same solution. The analysis of EIS data and equivalent circuit models revealed the changes in coatings' barrier property, while measuring the thickness and mean roughness of the coated surfaces enabled us to study the physical effects of stresses caused by the fluid flow on the samples. For all the measured and calculated criteria except the thickness and mean roughness which were measured at the beginning and the end of the tests, the influence of the fluid flow was very significant during the first 24 hours for both cases, while the decline rate of the low frequency impedance modulus and pore and polarization resistances were relatively higher for the exposure to the impingement flow. Those help us to understand that the applied flow rate promoted the percolation of working fluids and the transport of the oxygen and ions into coatings with a higher

rate. Impingement flow produces shear stresses on the surface of the coating samples causing abrasion of the coated materials. That is why the reduction of the coating's thickness and increase of the mean roughness were significant in comparison to the stationary condition.

The comparison between stationary submersion and flowing situation shows that although in short term the stationary test could provide a close estimate of the barrier properties of the coating, it does not capture the promoted rate of water percolation in the coating layers, nor would it account for the accelerated loss of coating materials during fluid abrasion.

2.6.2. Comparing the influence of different applied flow rates

2.6.2.1. EIS results

The Bode plot and phase diagrams are shown in Figure 20 for EIS measurements of samples subject to impingement flow with flow rates Q = 6.31, 12.62 and 18.93 cm^3s^{-1}. For all cases, the low frequency impedance modulus decreases with the increase of the immersion time. The rate of change of the impedance modulus is more significant at the initial hours of exposure to the flow, followed by a relatively slower decrease. This behavior demonstrates that the barrier property of organic coatings was deteriorated during a week of the exposure to the impingement flow of the working fluid. The fact that the value of the low-frequency impedance modulus for all cases were between 107 and 108 $\Omega.cm^2$ on the last day of immersion indicates that the coating did not completely fail during the experiment. The impedance modulus at 0.01 Hz as a function of immersion time is plotted in Figure *21*. In Figure 21, it is observed that the rate of decrease of the impedance modulus for flow rates Q = 12.62 cm^3s^{-1} and Q = 18.93 cm^3s^{-1} were relatively higher than the lower flow rate (Q = 6.31 cm^3s^{-1}), especially during the first 24 hours.

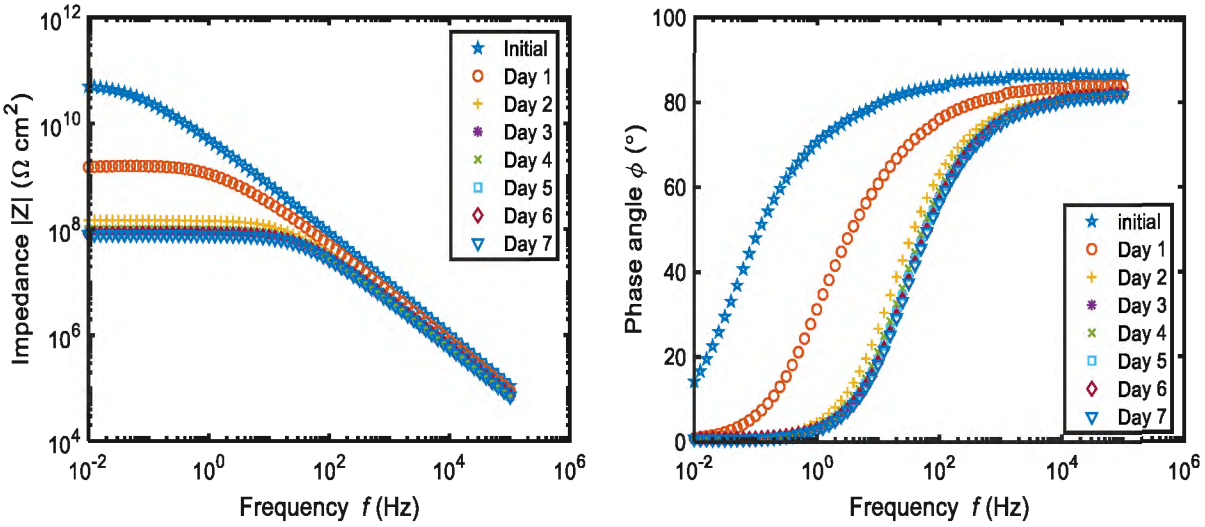

(a) Q=6.31 cm^3s^{-1}

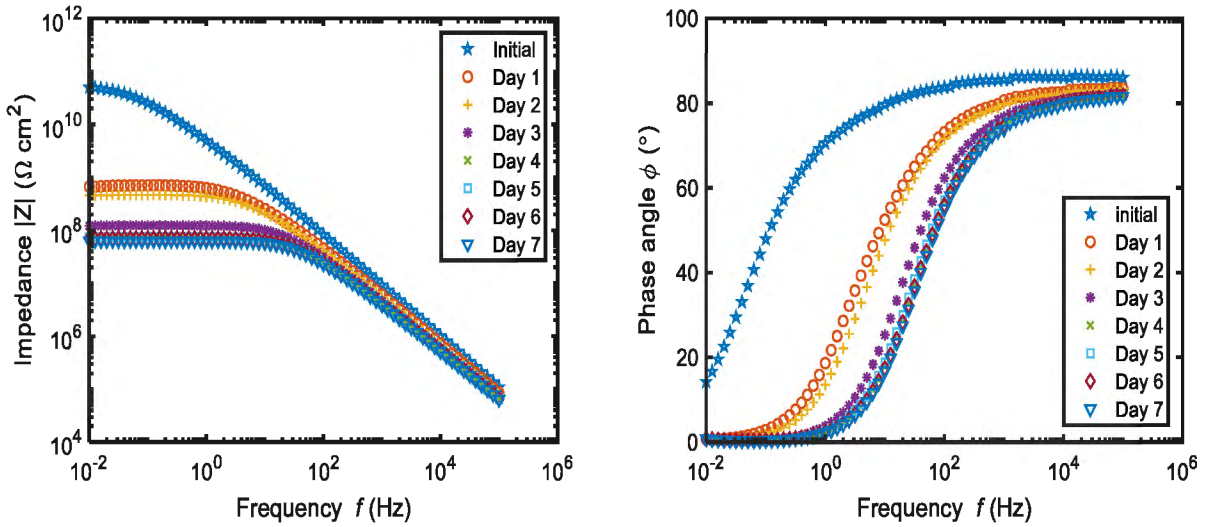

(b) Q=12.62 cm^3s^{-1}

Figure 20. Impedance modulus and phase angle as a function of the frequency for the coatings exposed to 3.5 wt. % NaCl solution for (a) Q=6.31 cm^3s^{-1}, (b) Q=12.62 cm^3s^{-1}.

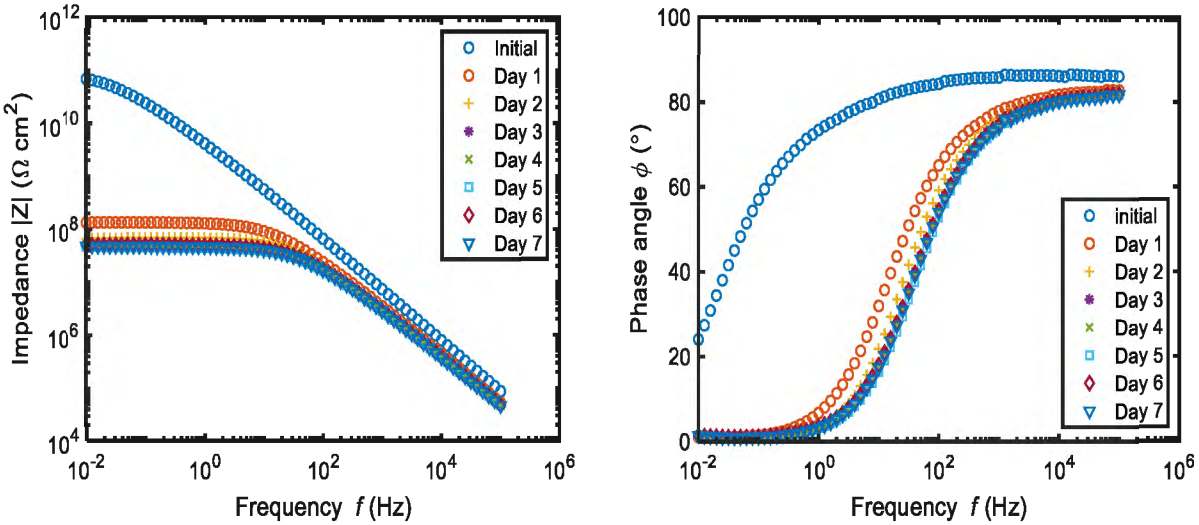

(c) Q=18.93 cm^3s^{-1}

Figure 20. Impedance modulus and phase angle as a function of the frequency for the coatings exposed to 3.5 wt. % NaCl solution for (a) Q=6.31 cm^3s^{-1}, (b) Q=12.62 cm^3s^{-1}, and (c) Q=18.93 cm^3s^{-1} (continued).

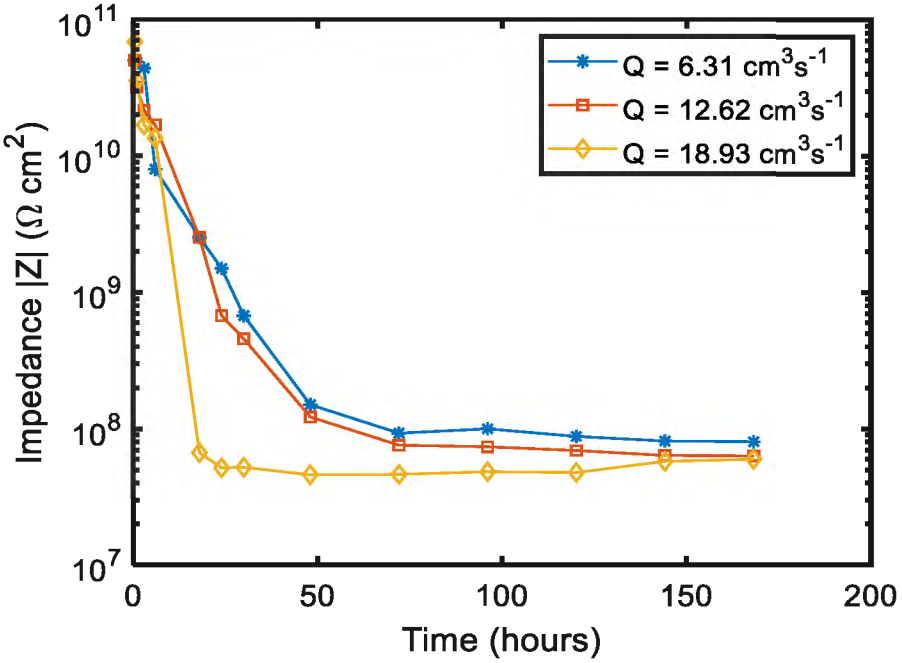

Figure 21. Impedance modulus as a function of immersion time at 0.01 Hz for different flow rates, while 3.5 wt. % NaCl solution was the working fluid.

2.6.2.2. Equivalent circuit modeling

The equivalent circuit model for the applied flow rates is shown in Figure 11. Figure 22 shows the behavior of the coating capacitance C_c during the immersion in the impingement flow at different flow rates. Figure 22 also plots the capacitance values normalized by the capacitance at initial immersion for comparison purpose. The coating capacitance increases as immersion time increases. It is also observed that the coating capacitance increases more rapidly for higher flow rates. The phenomenon may be explained by the increased percolation of solution into the coatings promoted by higher flow rates. We plot the double layer capacitance (C_{dl}) as a function of immersion time in Figure 23 for different flow rates. The value of the double layer capacitance depends on many variables including electrode potential, temperature, ionic concentrations, types of ions, oxide layers, electrode roughness, impurity adsorption, etc. There is no obvious tendency observed with respect to the immersion time and the flow rate, as may be caused by a model artifact.

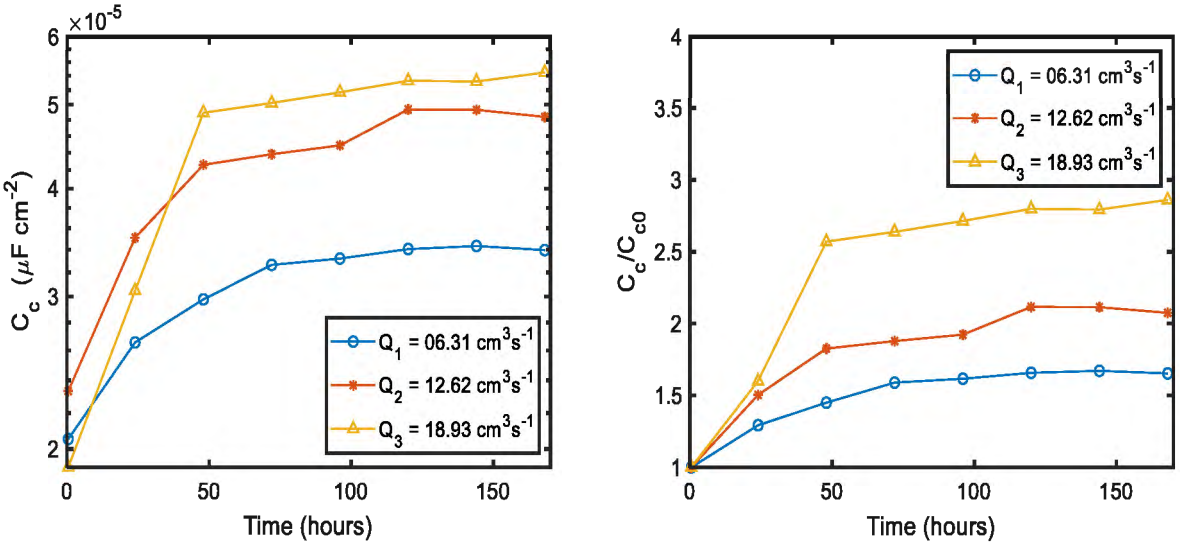

Figure 22. Coating capacitance (Cc) of the equivalent circuit model as a function of immersion time for different flow rates: (left) absolute values of capacity in one week, (right) the normalized values of the capacitance.

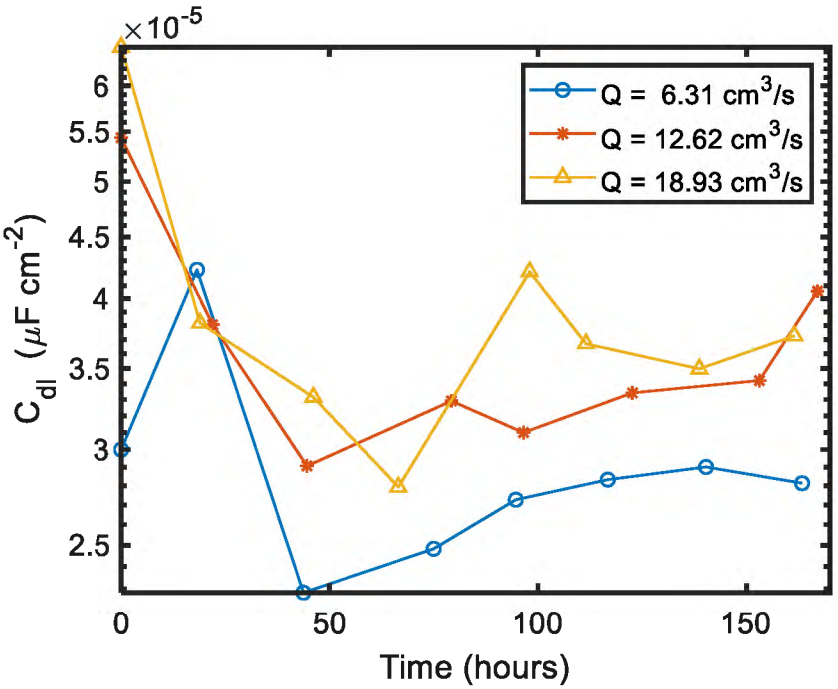

Figure 23. Double layer capacitance (C_{dl}) of the equivalent circuit model as a function of immersion time for different flow rates.

Figure 24 shows the pore resistance (R_{PO}) and its normalized value as a function of immersion time. The value of R_{PO} indicates the amount of ion conducting pathways that develop in the coating. The decline of the value of pore resistance indicates the increase in the amount of conducting pathways and the deterioration of the coating's barrier properties against corrosion. The overall trends indicate that the R_{PO} values decrease over time for all samples, and the higher the applied flow rate is, the greater decrease R_{PO} value exhibits.

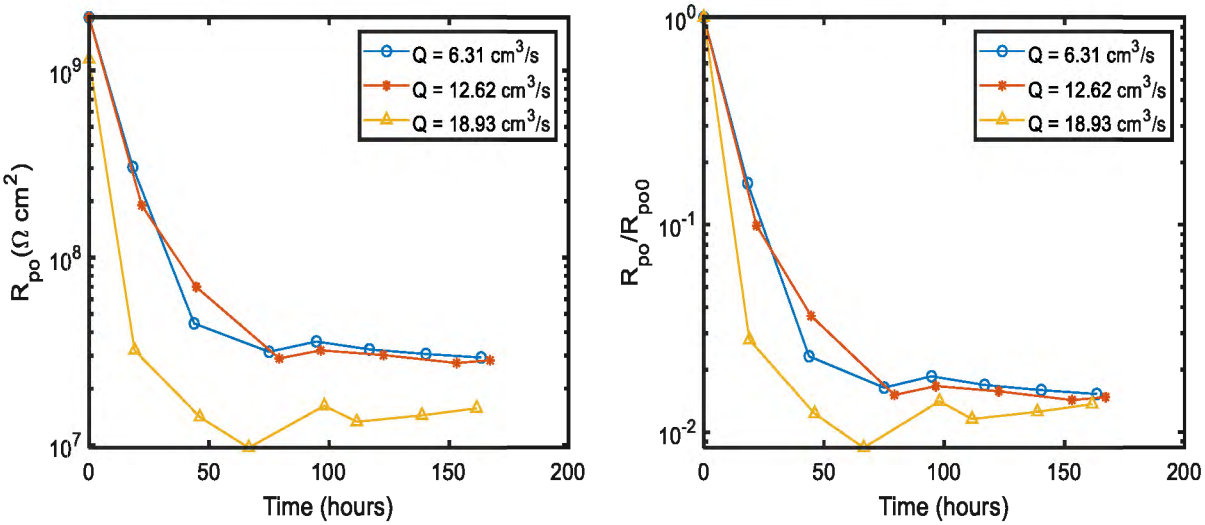

Figure 24. The magnitude and normalized graphs of pore resistance (R_{po}) of the equivalent circuit model as a function of the immersion time for the non- particulate 3.5 wt.% NaCl solution flow.

Figure 25 illustrates the polarization resistance (R_{ct}) of the equivalent circuit model as a function of immersion time. When an electrode is polarized, it can cause the current to flow via electrochemical reactions that occur on the electrode surface. The amount of current is controlled by the kinetics of the reactions as well as the diffusion of reactants/products towards/away from the electrode. During immersion, for all samples R_{ct} values decrease as immersion time increases. We observe in Figure 25 that R_{ct} exhibits a more rapid decay for Q = 18.93 cm^3s^{-1}, owing to a faster diffusion rate promoted by higher flow velocities of the working fluid.

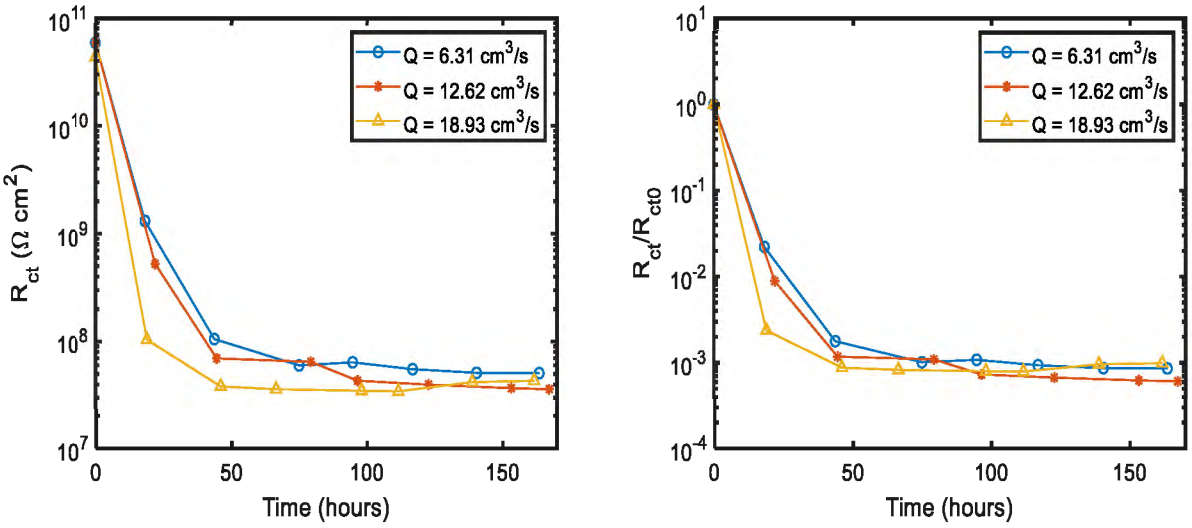

Figure 25. The magnitude and normalized graphs of charge transfer resistance (Rct) of the equivalent circuit model as a function of the immersion time for the non- particulate 3.5 wt.% NaCl solution flow.

2.6.2.3. Topography characterization

The thickness of the coating samples was measured within a radius of 4 cm from the center of the coating samples, where the coatings were exposed to the impingement flow. The mean values for each sample were taken into comparison. Figure 26 shows the values of coating thickness before and after the immersion. We observe that for Q = 6.31 cm^3s^{-1}, the thickness of the coating slightly increases after immersion. We believe the coating swelling was dominating in this case, which was caused by the solution that percolates through the coating layers. For samples immersed in higher flow rates, the coating thickness was reduced after the immersion. In those cases, due to the increase of the applied flow rate and the associated elevated fluid shear, coating samples experienced more substantial abrasion on their surfaces that may lead to significant decline of the thickness. To examine the influence of fluid flow on the surface features of the coating samples, we obtained the AFM images before and after immersion as shown in Figure 27. The images shown were all taken from the center points of the samples. The coating surfaces were smooth before the exposure. More protuberances were observed on the

coating surface after the immersion and larger surface features could be found for higher flow rates. As shown in Figure 28, we plot the roughness of the coating samples obtained from AFM analysis before and after the immersion. All roughness values were measured significantly higher after the samples were immersed in the impingement flow. Samples exposed to a flow rate of Q = 18.93 cm^3s^{-1} exhibit a more substantial increase in its roughness comparing to smaller flow rates. The error bars in Figure 28 indicate that the variation in measured roughness data is also greater for higher flow rates. As the fluid flow impacts coating surface, materials get removed from the coating surface, and more bumps and dimples are formed on the surface which leads to the increase of the mean roughness and the variations in roughness.

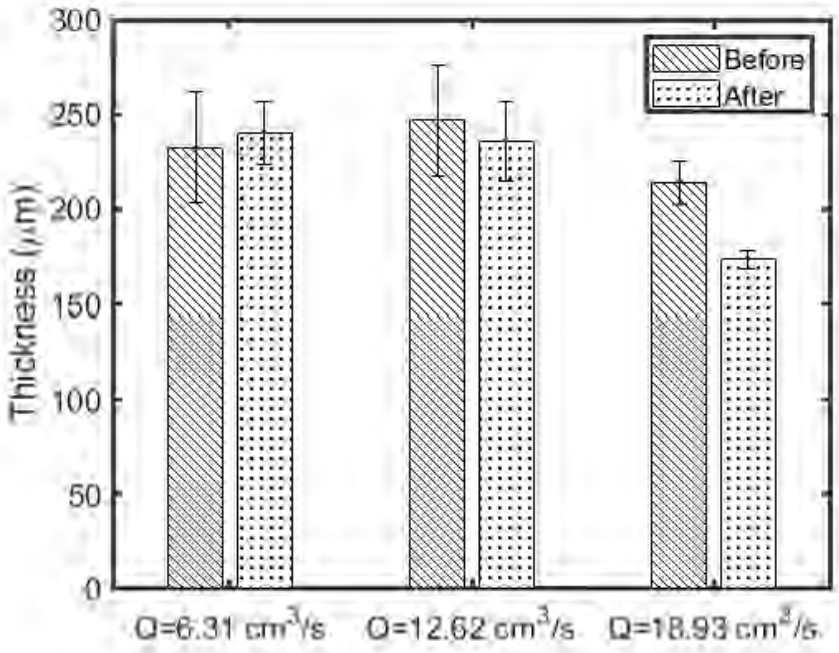

Figure 26. Coating thickness before and after the immersion in the impingement flow.

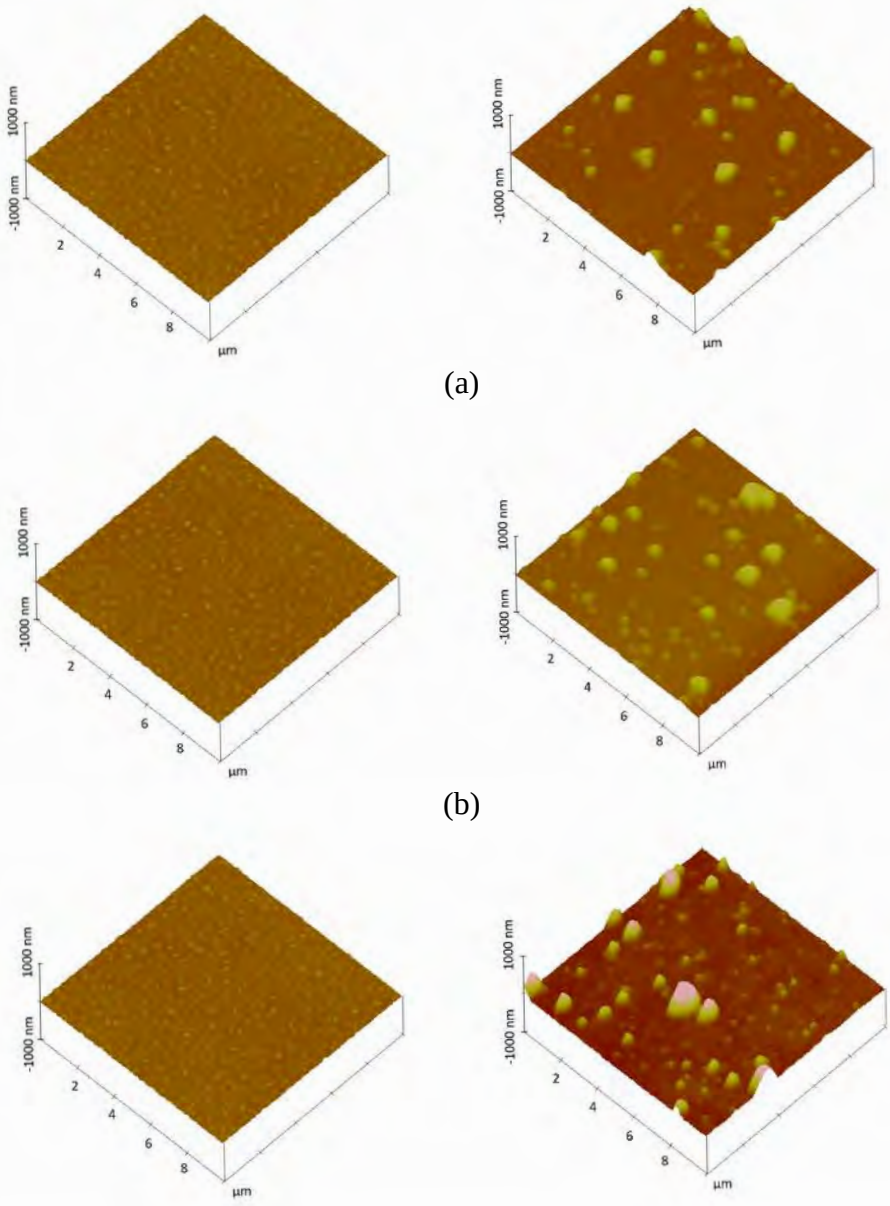

Figure 27. AFM images for the coated surface before (left) and after (right) exposure to the impingement flow: (a) Q=6.31 cm^3s^{-1}, (b) Q=12.62 cm^3s^{-1}, and (c) Q=18.93 cm^3s^{-1}.

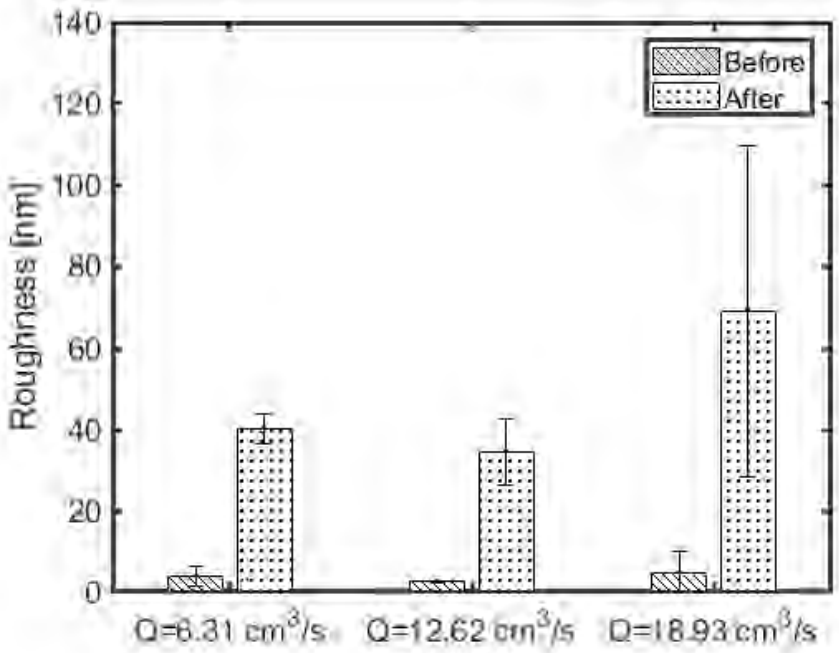

Figure 28. Roughness of the coating surface before and after the immersion for different flow rates.

2.6.2.4. Discussion

This study investigated the degradation behavior of an epoxy coating exposed to an impingement flow of 3.5 wt. % NaCl solution at different flow rates. The analysis of EIS data and equivalent circuit models revealed the changes in coatings' barrier property. We observed that the impedance modulus experiences a more significant decrease after its immersion in higher flow rates. Assisted by equivalent circuit models, we discovered that under the influence of impingement flow, higher flow rates result in a more substantial decrease in polarization resistance and double layer capacitance. The coating capacitance value also shows significant increase as the flow rate increases. Those help us to understand that the higher flow rates promote the percolation of working fluids and the transport of the oxygen and ions into coatings. For higher flow rates larger shear stresses were produced on the surface of the coating samples causing abrasion of the coated materials. Moreover, the variations in the coatings thickness are resulted from two contradicting behaviors of the working fluids: i) the swelling process during

the absorption of working fluids into the coatings and ii) the abrasion created by fluid shear. Calculations also reveal increased volume fraction of water uptake in coatings under higher flow rates. The AFM results show that the mean roughness of the samples increases as we increase the flow rates. The changes in surface feature are more substantial for higher flow rates. Overall, we conclude that the higher flow rates of impinging working fluids not only promote the transport rate of ion and oxygen and water penetration, but also expedite the degradation of the organic coating via water update and abrasion from fluid shear.

3. DEGRADATION OF EPOXY COATINGS EXPOSED TO SAND PARTICULATE IMPINGEMENT FLOW

3.1. Introduction

There are several types of suspended solid particles in the oceans. The size and concentration ratio of suspended solids depend on several natural factors. The type of solids suspending and drifting in the oceans water varies from sediment, silt, and sand to plankton and algae. The small organic particles like animals' decay and plants are contributing to the different types of suspending particles in the oceans [61]. The size of algae particles varies between 0.2 and 5.5 µm [62]. Clay as the smallest soil particle has the average diameter of 1.95 µm, while silt particles are in the range of 4.9 to 47 µm, and the size of sand particles are between100 µm and 1.5 mm [63].

The flow velocity, temperature, sea depth, salinity, and the amount and density of submerged living plants also influence the size and concentration of particles in seawater. The higher the velocity of the flow, the larger the particles that can be suspended [64]. Particles larger than 0.5 mm usually agglomerate at the seabed as water flow decreases [64]. Although the direct influence of the temperature on the concentration of the suspended solids in oceans is not known, the on-site observations indicate huge differences between the concentration of solids in different seasons. For example, the obtained data from 6 different offshore sites in England [65] demonstrated that the concentration of suspended solid particles were between 15 and 80 mgl-1 in January, while that rage reduced gradually down to 5 to 10 mgl^{-1} in June, and then increased again towards December to be in range of 10 to 40 mgl^{-1}. The reason for such a significant difference could be the existence of several factors including the various number of sediments supplied from riverine during different seasons, the intensity of water evaporation due to the sun

light, and the change of the water temperature itself. The investigation of the same group [65] also indicated that the concentration of suspended solids was 20 to 40 % higher at water surface in comparison with the deeper areas close to the seabed. The salinity of the ocean increases the aggregation of suspended particles, and consequently increase the weight of particles and cause them to settle on the seabed [66]. In general, the concentration of suspended solid particles in the shallow water of oceans (up to 50 m) can be estimated between 20 and 50 mgl^{-1} [64].

In addition, the human activities such as the installation of offshore structures also contributes to the change of the type, size, and concentration of suspended particles in the vicinity of the structures. The installations of offshore wind farms, especially the monopile structures, increase the number of suspended particles too. Vanhellemont et. al. [67] observed the turbid wakes associated with one monopile offshore wind turbine were 30 to 150 m wide and several kilometers in length. They argued that the turbid wakes could significantly impact sediment transport and the concentration of suspended solids around the offshore wind structures. In another study, Baeye et. al. [68] figured that the total suspended particulate matters in water increased five times in the wake of offshore wind turbines. Other investigations revealed that the installation of offshore wind turbines in Rhode Island attracted more benthic communities (species living on or in the seabed) to reside in the vicinity of the offshore wind foundation [69]. The abundance of living creatures around the structures increases the number of fishes and other species [70], which leads to more decays from animals and increase in the concentration of suspended particles. One investigation on an offshore windfarm in Denmark reported 50 to 150 times increase in benthic animals and biomass compared with the time prior to the windfarm development [26].

The destructive influence of solid particles on the erosion-corrosion of metals have been studied comprehensively in historical literatures [71]–[77]. In these studies, a combination of experimental and analytical approaches was accomplished to address the impact of solid particles on metal surfaces. The degradation of metals was investigated by considering the mechanical properties of the metals including hardness, toughness, and elastic modulus, as well as the shape, size, velocity, elastic modulus, and impact angles of particles suspended in working fluids. The erosion rate of the metals, the depth of the formed crates (volume of created hole due to the particles' impact), and the formation of raised lips on the metals were calculated. Moreover, the boost of oil industry in last decades and the high corrosion rates of gas and oil slurry pipelines attracted the attention of many scientists to study the influence of slurry sand flows on erosion-corrosion of metals [77]–[82], where concurrent destructive influence of both liquid (mostly saline fluid) and solid particles on metals were investigated. However, for slurry flows, generally a high concentration of solid content is considered (10 to 20 wt. % of the liquid). Stack et al. [83] mapped the transition boundaries from corrosion to erosion-corrosion of metals with respect to the vertical impingement fluid flow of a 3 wt. % NaCl solution with a velocity varying between 0.1 and 100 ms^{-1}, and sand particles' concentration between 0 and 40 wt. %. They concluded that by increasing the particles' concentrations, the erosion rate of the metals increased. Moreover, they showed that by increasing the velocity of the fluids the erosion-corrosion rate increased. By recent progress in electrochemical techniques, Electrochemical Impedance Spectroscopy (EIS) has been employed in the study of the erosion-corrosion of metals due to particulate flows [84]–[87]. Jiang et al. [84] studied the effects of parallel rotational flow of 3 wt. % NaCl solution with 0.2 wt. % sand on steel samples with EIS method. They concluded that the increase of flow velocities decreased the impedance modulus, and therefore, increased the rate of

the metal corrosion. They also compared the existence and absence of particles in their fluid flow and reported that the existence of the sand particles increased the corrosion rate of steel samples significantly. They concluded the higher corrosion rate of the particulate flow was due to the destruction of steels' passive film. Niu and Cheng [85] made similar conclusions regarding the wear of passive film for the Aluminum samples due to the impact of particles. Zhao et al. [86] investigated the influence of high-velocity (20.5 ms^{-1}) impingement jet of a 3.5 wt. % NaCl solution with 0.21 wt. % silica and sea sand on wear of AISI 316 stainless steel with EIS method. They conducted their experiment with three different impingement angles (20°, 60°, and 75°) and concluded that the erosion rates were higher for the smaller impact angle due to the dominant applied shear stresses. They also reported the fluid flow with sea sand appeared to be more corrosive than the silica sand. Moreover, they observed that the weight losses of the steel samples caused mainly by the smallest sand particles. The influence of the size and shape of solid particles, in addition to the magnitude and direction of applied stresses on erosion-corrosion of the steel samples were revealed.

In contrast to the abundance of studies on solid particles' impact on metals, there have been very few works that addressed the influence of particle impacts on degradation of organic coatings. Matthewson [88] provided an in-depth theory and mathematical model for indentation of a soft, thin coating by rigid solid particles. The provided theories by Matthewson covered a wide range of the mechanical behavior and characteristics of the coatings including the movement of the coating material from its unloaded position, the viscoelastic behavior of the coatings subjected to particle impacts and calculation of applied stresses at the contact point of solid and coating. Pool et al. [89] then further developed theoretical and experimental models for the wear of polymeric composites and coatings affected by particles. Wood [90] formulated the

erosive rate of the coatings with respect to the sand impact velocities between 10 and 30 ms^{-1} with jet angles of 30° and 90°. Tan et al. [91] investigated the influence of particle impact on the erosion-corrosion of HVOF coatings using electrochemical current measurements and gravimetric analysis. Papini and Spelt [92]–[94], and Zouari and Touratier [95] investigated the removal of organic coatings by particle impact by utilizing spherical particles in air flow jets with very high applied velocities (between 50 and 150 ms^{-1}). To the best knowledge of the authors, most studies on the influence of the particulate flow on the coatings have been limited to the high velocity particulate air flows [96], [97]. Recently, Zeng et al. [98] investigated the effect of water-sand mixture on the erosion of epoxy and polyurethane coatings. In their studies, they managed the rotational velocity of the mixture from 2 to 10 ms^{-1}, with different sand concentration between 0.5 and 8 kgm^{-3}. Sample weight has been measured to monitor the coating degradation.

In this work, impinging particulate flows were applied on coated samples in a lab-scale impingement chamber. The utilized fluid for the experiments was a 3.5 wt. % NaCl solution with 1 wt. % suspended sand particles. The type of sand particles was industrial rounded quartz with an average diameter size of 390 μm. EIS measurements were conducted to monitor degradation of organic coatings.

3.2. Preparation of particulate fluid and its characteristics

In order to resemble the general condition of oceans, 3.5 wt. % NaCl solution was employed. Multi-purpose rounded quartz sand with the density of $\rho_{sand} = 2.65\ \mathrm{gcm}^{-3}$ was used for the effect of Micro-scale particles on the coatings. A high-resolution microscope (HRX-01 model of HIROX company) was utilized to measure the sizes of 50 random sand samples. The average diameter of the sand particles was 390.2 ± 125.19 μm as shown in Figure 29. The

regular concentration of particles in shallow waters up to 50 *m* depth is between 20 and 50 $mg.l^{-1}$. The installations of offshore wind turbines normally cause an increase in concentration of suspended particles. Therefore, the concentration of 1 wt.% of sand was added to the 3.5 wt. % NaCl solution for experiments. The measured density of the mixture was $\rho_m = 1030.928\ kgm^{-3}$. A Rheometer (TA Instruments) was utilized to measure the dynamic viscosity of the mixture. The temperature was fixed on 25°C, while the shear rate was in the range of 0 to 100 s^{-1}. The applied shear stresses were between 0.01and 0.2 Pa. The dynamic viscosity measurements were conducted five times with the volume of 1.3 mL of the mixture. The measured dynamic viscosities of the mixture varied with respect to the applied shear stresses in the range between $\mu_m = 1.837 \times 10^{-3}$ and 1.749×10^{-3} Pa.s. For the stress analysis, the average dynamic viscosity of $\mu_m = 1.813 \times 10^{-3}$ Pa. s was employed.

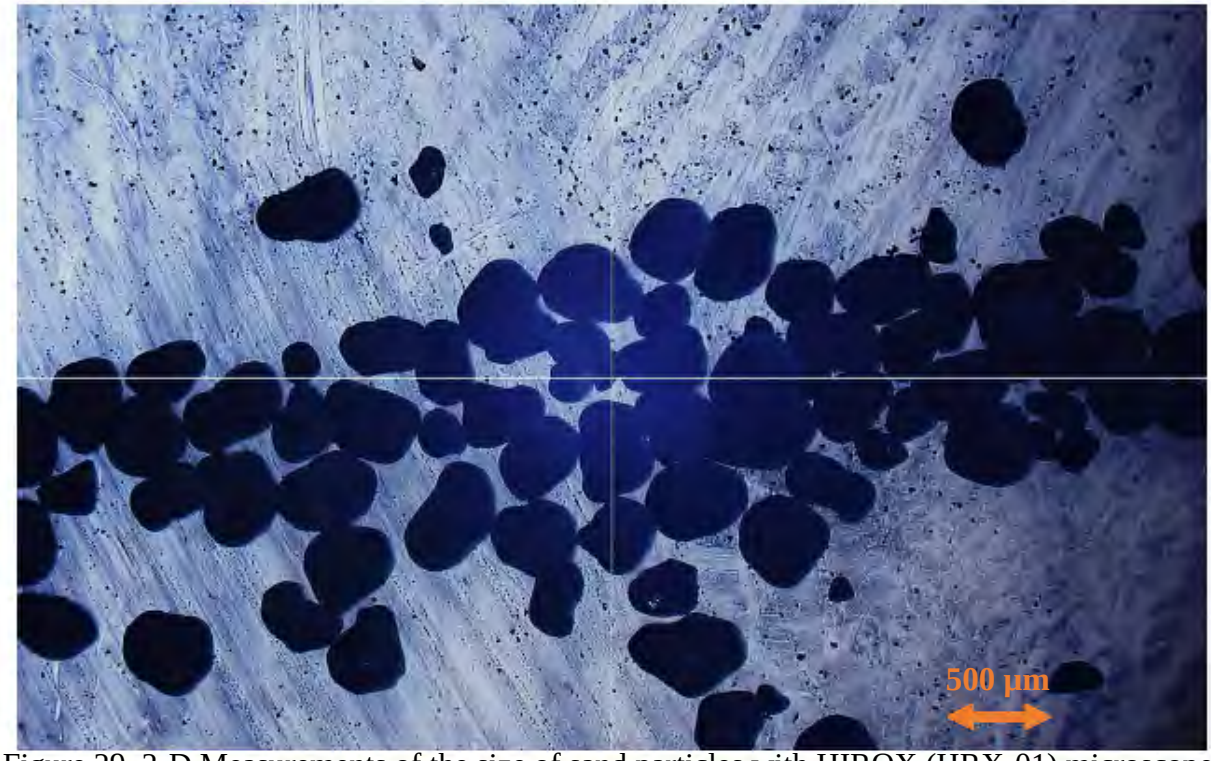

Figure 29. 2-D Measurements of the size of sand particles with HIROX (HRX-01) microscope.

3.3. Flow circulation system and EIS measurements

The circulation system of particulate fluid and the EIS measurement method are exactly the same as the non-particulate impingement flow experiment. However, a magnetic stirrer was employed in the reservoir to constantly resuspend sand particles which accumulated at the bottom of the reservoir (see Figure 6).

3.4. EIS results of sand particulate fluid and the comparison with non-particulate fluid

The epoxy coatings were exposed to two different working fluid of 3.5 w% NaCl solution in addition to the 1 w% sand suspended particles. Three flow rates (Q = 6.31, 12.62 and 18.93 cm^3s^{-1}) were employed for a period of one week. The degradation of the coatings was monitored with EIS. The impedance modulus (Bode plot) and phase angle of the coatings for each applied flow rates are shown in Figure 30. The graphs represent impedance and phase angles measured upon stabilization after the onset of the flow (initial) and those measured daily while the coating sample was kept under the impingement flow. The area of the exposed coatings ($A = 50.24\ cm^2$) was used in the calculation of the impedance modulus for the Bode plot We observe from the Bode plots that all impedance modulus decreases with time as the coatings were submerged in particulate impingement flow.

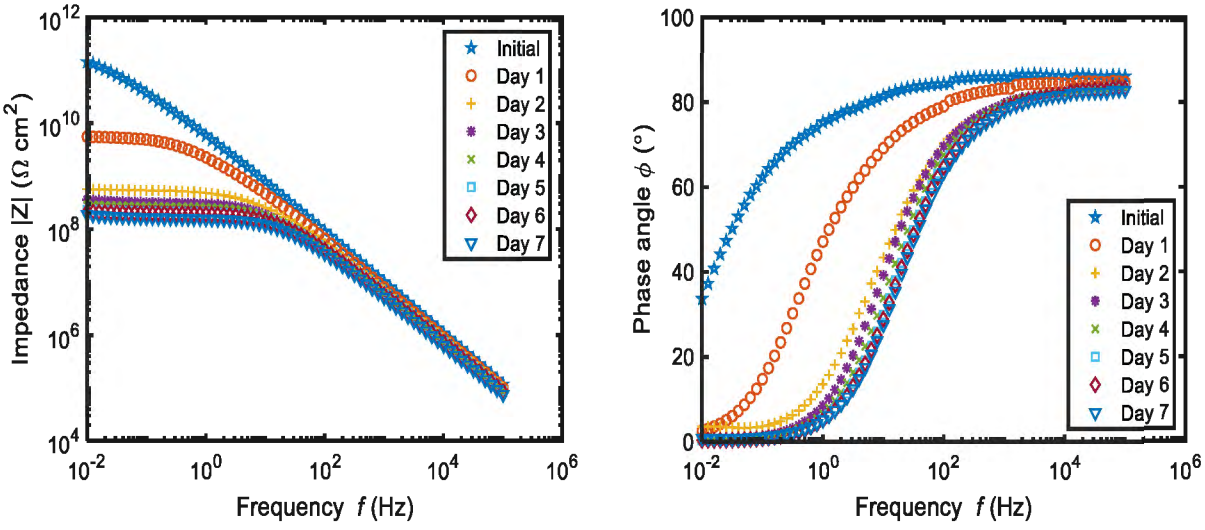

(a)

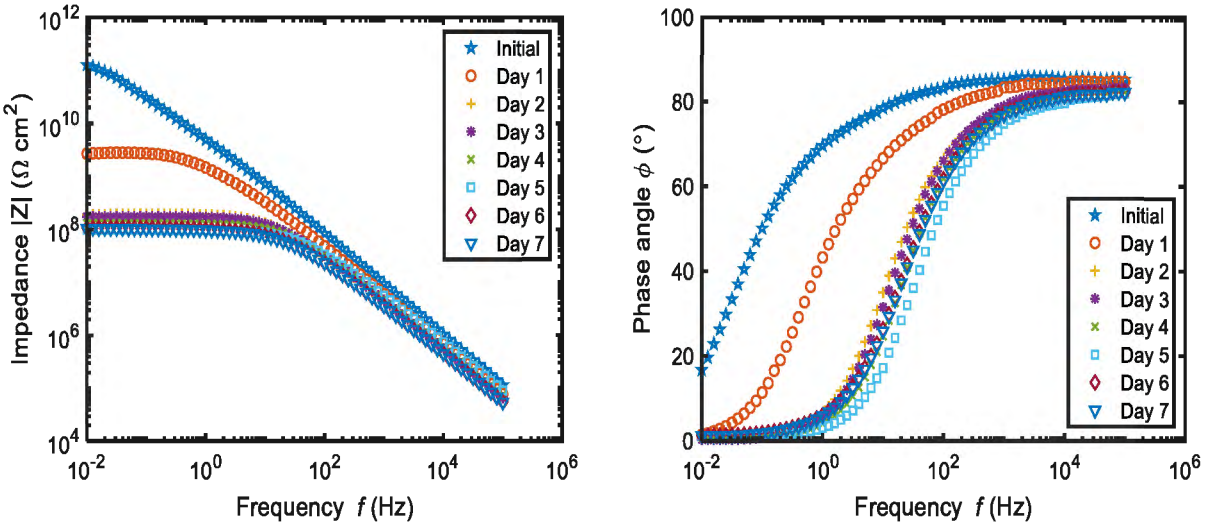

(b)

Figure 30. Impedance modulus and phase angle as a function of the frequency for the coatings exposed to 3.5 wt. % NaCl solution with 1 wt. % added sand particles for (a) Q=6.31 cm^3s^{-1}, (b) Q=12.62 cm^3s^{-1}.

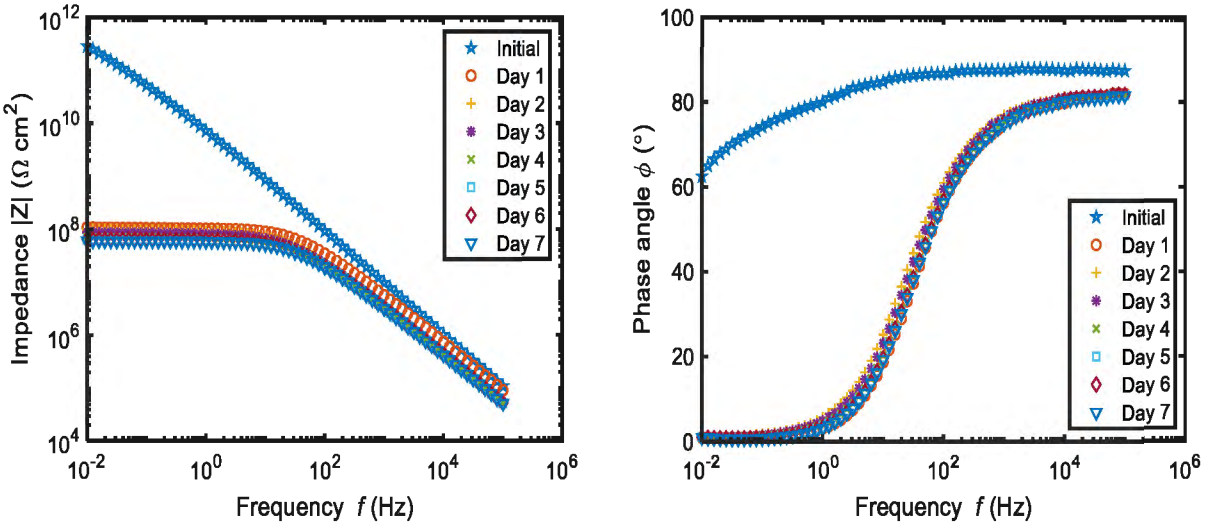

(c)

Figure 30. Impedance modulus and phase angle as a function of the frequency for the coatings exposed to 3.5 wt. % NaCl solution with 1 wt. % added sand particles for (a) Q=6.31 cm^3s^{-1}, (b) Q=12.62 cm^3s^{-1}, and (c) Q=18.93 cm^3s^{-1} (continued).

We plot the low frequency impedance modulus as a function of immersion time in Figure 31. For particulate working fluid, the low frequency impedance modulus of the coatings decreases more drastically for higher flow rates.

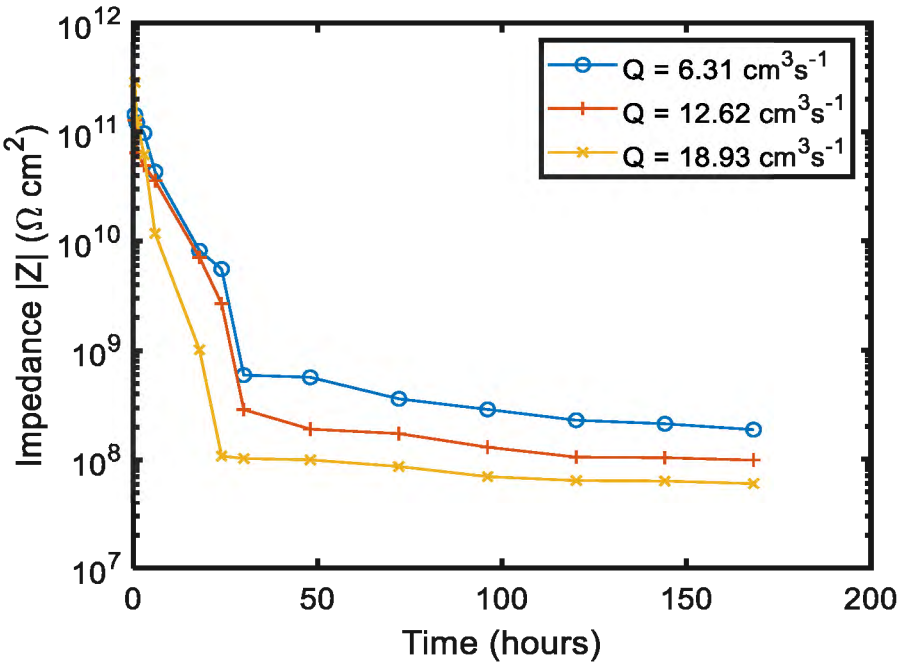

Figure 31. Low-frequency impedance as a function of immersion time at 0.01 Hz for different flow rates for 3.5 wt. % NaCl solution with 1 wt. % sand particles.

To make direct comparison between samples submerged in different working fluids, we plot in Figure 32 the low frequency impedances normalized by the low-frequency impedance modulus at the initial immersion time for both particulate and non-particulate fluids. As shown in Figure 32 (a) where the trends for the lowest applied flow rate (Q = 6.31 cm^3s^{-1}) are plotted, the degradation of the coatings occurred at almost the same rate for both types of fluids, indicating the added sand particles did not have significant influence on the degradation of the coating at low flow rates. For the flow rate of Q = 12.62 cm^3s^{-1}, the added sand particles slightly increased the rate of the coatings' degradation as shown in Figure 13b. The effect of the sand particles was significant after the first 24 hours of the immersion. For the highest flow rate (Q = 18.93 cm^3s^{-1}), the low frequency impedance modulus of the coatings decreased at a noticeable higher rate in the particulate fluid than that in the non-particulate fluid. Overall, as the flow rate increased, the destructive influence of added sand particles was more significant on the coatings.

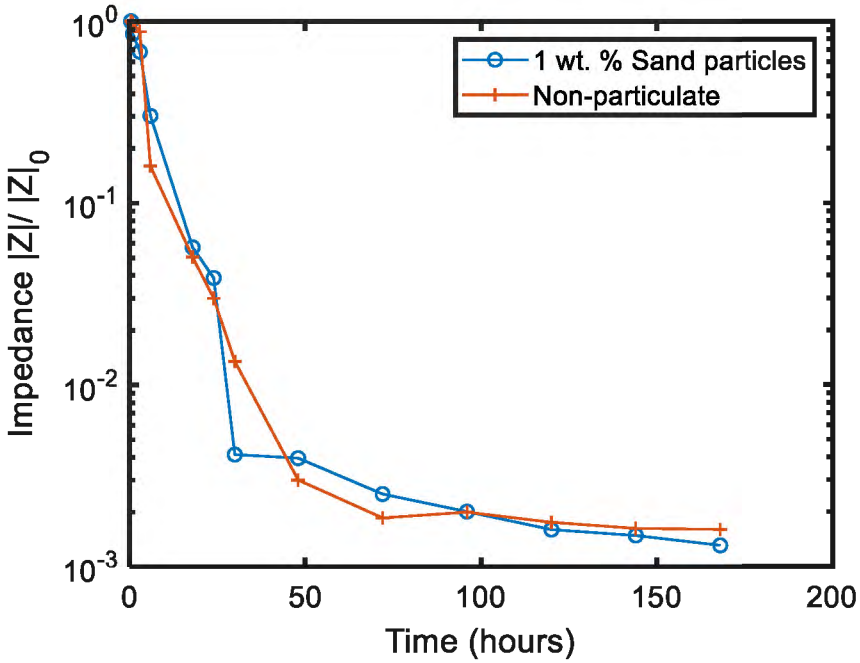

(a) Q = 6.31 cm^3s^{-1}

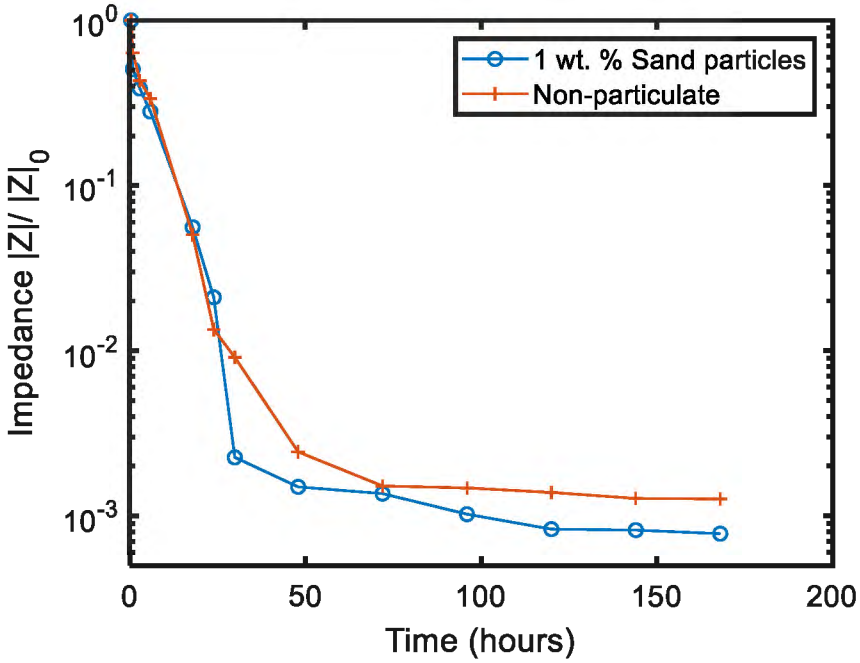

(b) Q = 12.62 cm^3s^{-1}

Figure 32. The comparison between the normalized low-frequency impedance modulus of particulate and non-particulate flow at (a) Q=6.31 cm^3s^{-1}, (b) Q=12.62 cm^3s^{-1}.

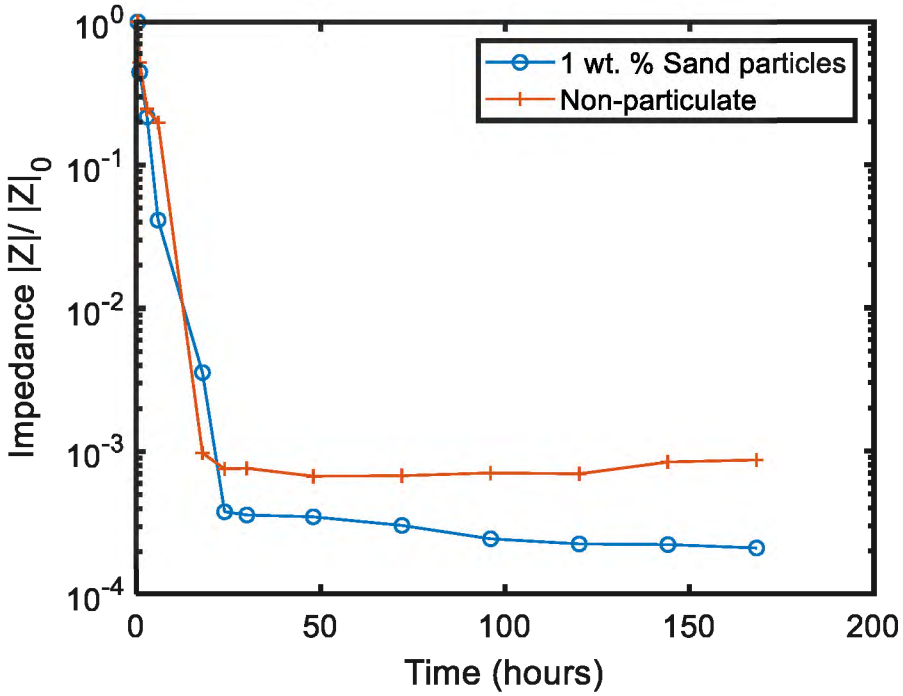

(c) Q = 18.93 cm^3s^{-1}

Figure 32. The comparison between the normalized low-frequency impedance modulus of particulate and non-particulate flow at (a) Q=6.31 cm^3s^{-1}, (b) Q=12.62 cm^3s^{-1}, and (c) Q=18.93 cm^3s^{-1}(continued).

3.5. Equivalent circuit modeling

The equivalent circuit models with constant phase elements (CPE) provided the best fitting to the EIS data as shown in Figure 11 (b). A sample of curve fitting process with Zsimp software is shown in Figure 33. In Figure 33, the Nyquist graph of the third day of coatings exposure to the sand particulate flow with Q = 12.62 cm^3s^{-1} was fitted with the model provided in Figure 33, while the respective χ^2 value was 5.06×10^{-5}.

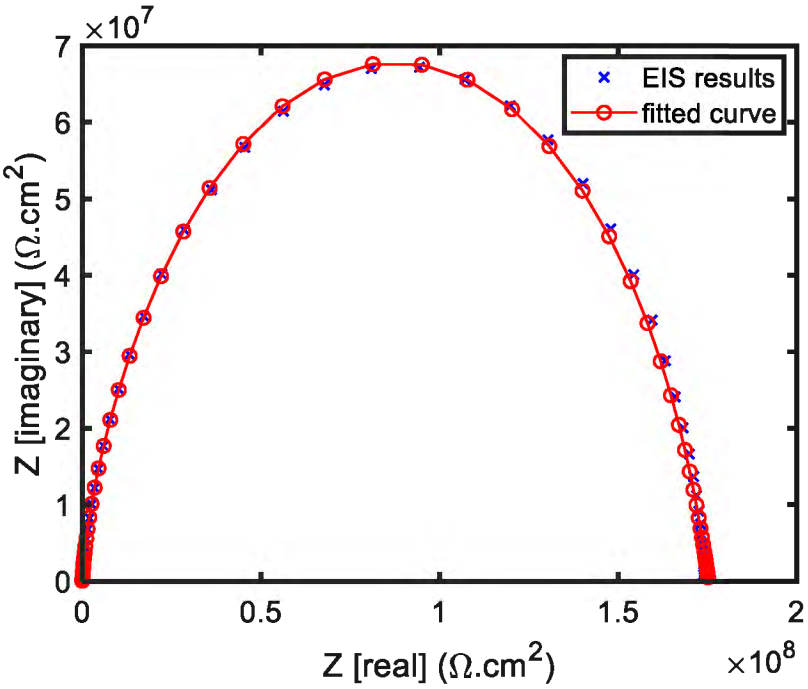

Figure 33. A sample curve fitting of the EIS results with respect to chosen equivalent circuit model: EIS data of day three for the sand particulate flow with Q = 12.62 cm^3s^{-1} modeled as Figure 11 (b) with $\chi^2=5.06\times10^{-5}$.

Based on (*1* 1 and 2, the equivalent coating capacitances (C_c) were calculated with respect to the pore resistances and the double layer capacitances (C_{dl}) were calculated with respect to the charge transfer resistances. The trends of coating capacitances exposed to the sand particulate fluid flows are shown in Figure 34. Considering the graph, the magnitude of coating capacitances increased proportionally to the increase of the inlet flow rates. Moreover, as shown in Figure *35*, the increase rates of the coating capacitances were significantly higher for the sand particulate fluid compared with non-particulate one at each respective applied flow rate. Generally, the coating capacitance indicates the rate (the speed) at which the transformation of ions take place on the outer layer of the coatings. Considering Figure 22 and Figure 34, and the three different stages of the coating failures [99], [100], the homogeneous diffusion of ions took place during the first 48 hours regardless of the fluids' type and the applied flow rates. The approximately constant magnitudes of the coating capacitances after the homogeneous diffusion

period (from *t=48* to *t=168 h*), clearly show that the coatings' condition consistently stood in saturation stage during the rest of experiments. Since we did not observe a sudden increase of one of the coating capacitances during the last days of exposure, it can be concluded that the coating capacitances did not enter the electrochemical reaction stage (complete failure stage). In theory, the electrochemical reaction stage starts, when the water molecules reach the interface of the metal, and then consequently the transfer of ions/electrons take place towards/away from the metal to the corrosive environment. Overall, with respect to the applied flow rates, the more prominent increase of the magnitude of coating capacitance implies that the ion diffusion was enhanced faster and at a higher rate for the highest applied flow rates during the first 48 hours regardless of the type of the fluids. However, the additional sand particle caused even higher rate of ion diffusion, especially for the highest applied flow rate of $Q = 18.93\ cm^3s^{-1}$.

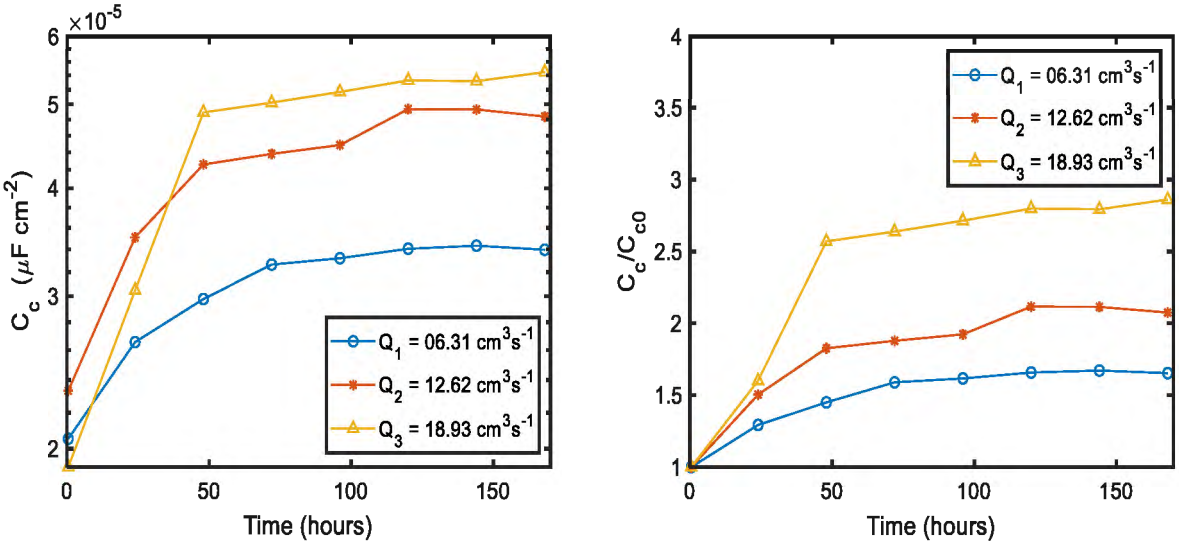

Figure 34. The magnitude and normalized graphs of the coating capacitances (C_c) as a function of immersion time exposed to the three different flow rates of sand-particulate 3.5 wt. % NaCl solution.

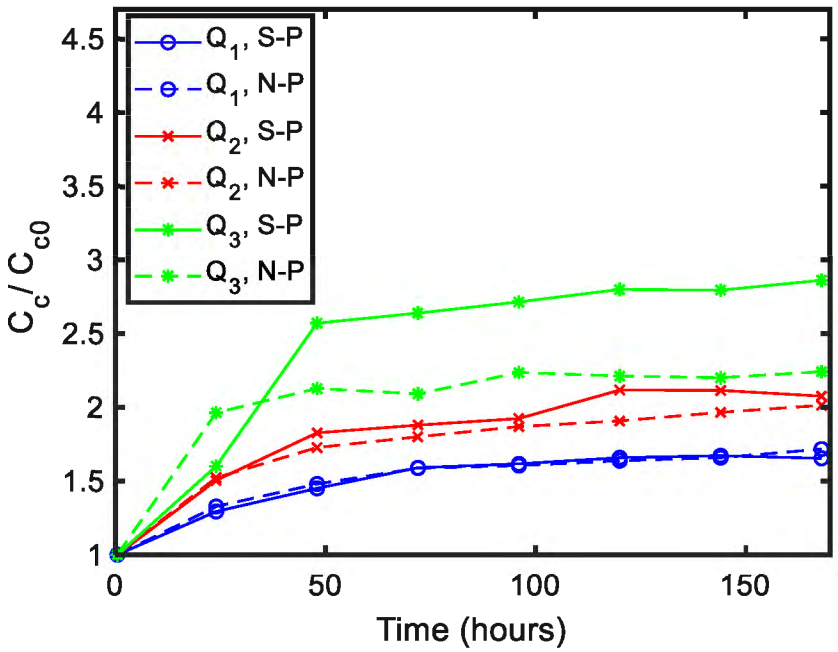

Figure 35. The comparison between the normalized graphs of the coating capacitance (C_c) of the equivalent circuit model as a function of the immersion time for the both non- particulate (N-P) and 1 wt. % sand-particulate (S-P) 3.5 wt.% NaCl solution flows.

The plots of double layer capacitances for the particulate fluid is depicted in Figure 36. The graphs of the both types of fluids (particulate and non-particulate - Figure 23 and Figure 36) show no particular pattern with respect to the applied flow rates. The complexity of the situation at the metal-coating interface is the main reason of such a fluctuating behavior. On one hand, the diffusion of some ions through the few random paths of the coatings, down to the surface of the metal, provide a suitable environment for the start of some electrochemical reactions; however, due to the limitation of the access paths of the free electrons to the electrolyte solutions the formation of anodic and cathodic regions on the surface of the metal is not possible. The curves for the both types of fluids clearly show the inconsistent condition on the metal-coating interface with respect to the ionic concentrations, electrode potentials, and the uncertain condition of the oxide layer of the steel substrates.

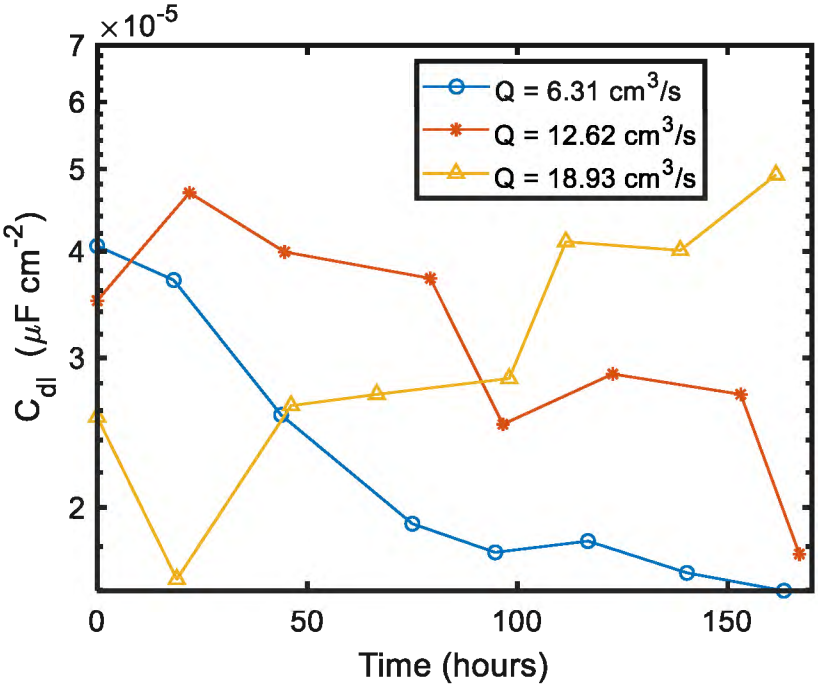

Figure 36. The magnitude of the double layer capacitances (C_{dl}) as a function of immersion time and flow rate for the 3.5 wt % NaCl solution with 1 wt% sand particle.

The reduction pattern of the coatings' pore resistance exposed to the three different flow rates for the sand particulate fluid is shown in Figure *37*. With respect to the normalized graph in Figure *37*, the pore resistance of the coatings decreased at different rates, and the higher flow rates caused higher degradation of the coating (higher rate of the reduction of R_{po}). Figure *38* illustrates the comparison between the normalized graphs of pore resistances for different applied flow rates and for the two utilized types of the fluids. It is obvious that the pore resistance of the coatings decreased at higher rates for sand particulate flow compared with non-particulate one. This indicated that the presence of sand particles in the fluid flows deteriorated the surface of the coatings' more harshly, and therefore, increased the amount of conducting pathways of ions through the coatings. Moreover, the destructive influence of the sand particles increased as the flow rates increased.

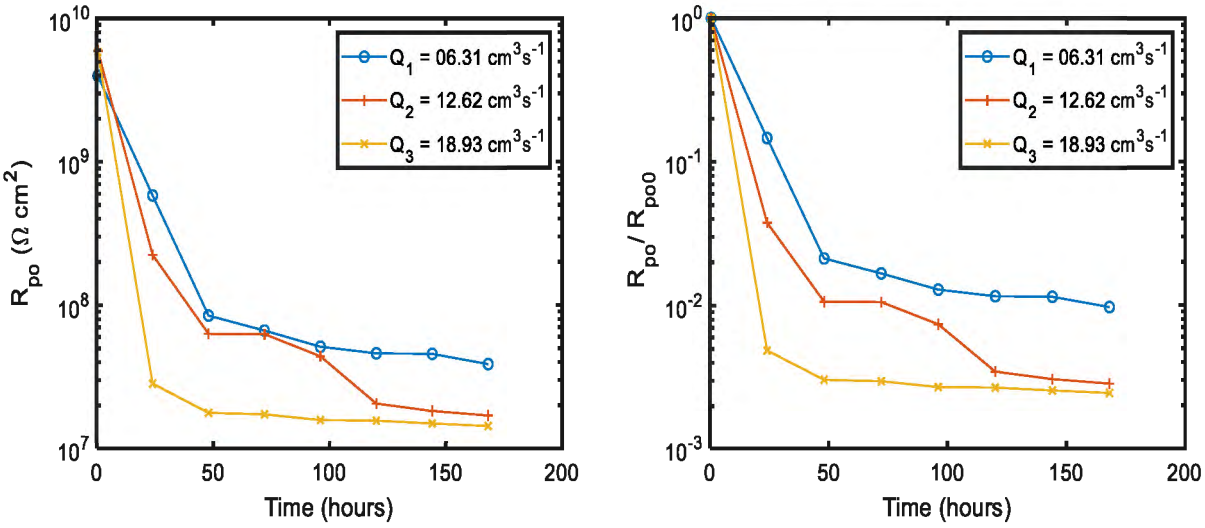

Figure 37. The magnitude and normalized graphs of pore resistance (R_{po}) of the equivalent circuit model as a function of the immersion time for the sand- particulate 3.5 wt.% NaCl solution flow.

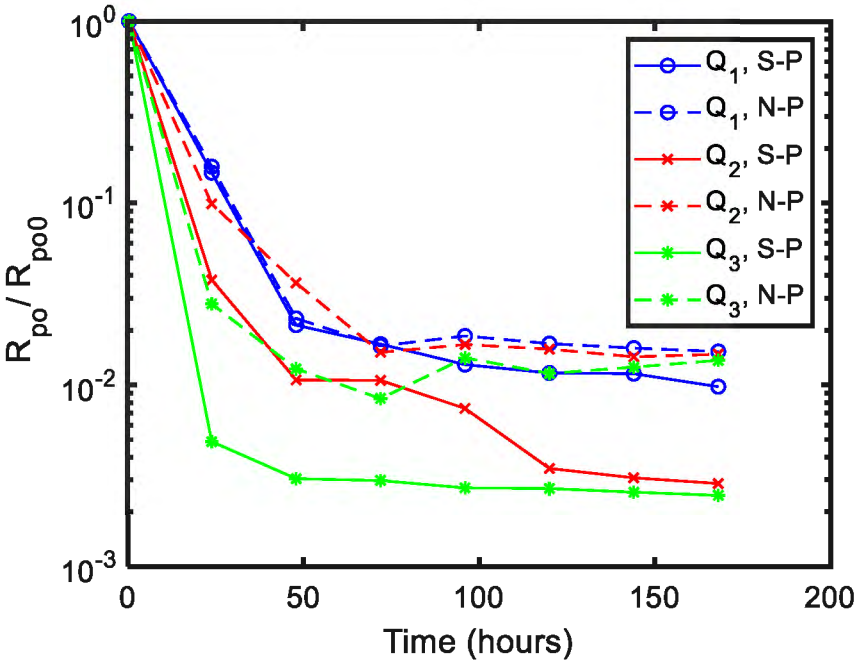

Figure 38. The comparison between the normalized graphs of the pore resistance (R_{po}) of the equivalent circuit model as a function of the immersion time for the both non- particulate (N-P) and 1 wt. % sand-particulate (S-P) 3.5 wt.% NaCl solution flows.

Figure *39* illustrates the charge transfer resistance (R_{ct}) of the equivalent circuit model for sand particulate flow. As shown in Figure 39, regardless of the applied flow rates, the sharp

decline of the charge transfer resistance took place during the first two days of the exposures time. It indicates that the resistance between the coating and metal interface dropped significantly as soon as the first ions passed through the entire thickness of the coatings and reached the interface. However, the charge transfer resistances for all the experiments remained approximately constant to the end of the experiment after the second day of exposure indicating the constant diffusion of electrons toward the coatings from the electrode, and the ions toward the electrode from the upper layer of the coatings. Similar to the trend observed for the decline of pore resistances, in the case of charge transfer resistance, the increase in flow rates caused the higher reduction rates of the charge transfer resistances, while the presence of the sand particles caused even greater reduction rates of the R_{ct} values as shown in Figure 40.

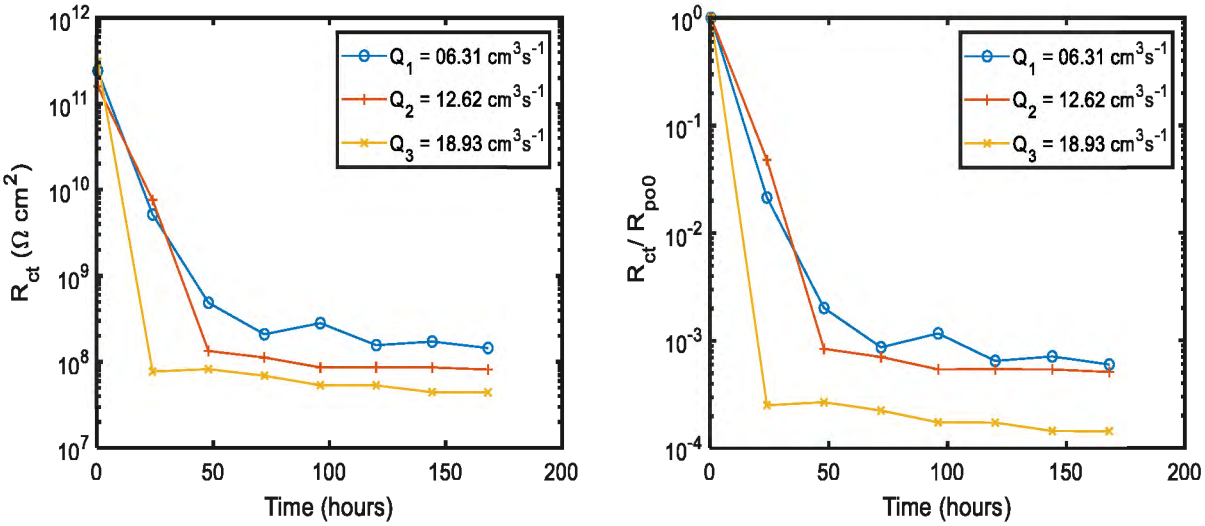

Figure 39. The magnitude and normalized graphs of charge transfer resistance (R_{ct}) of the equivalent circuit model as a function of the immersion time for the sand- particulate 3.5 wt.% NaCl solution flow.

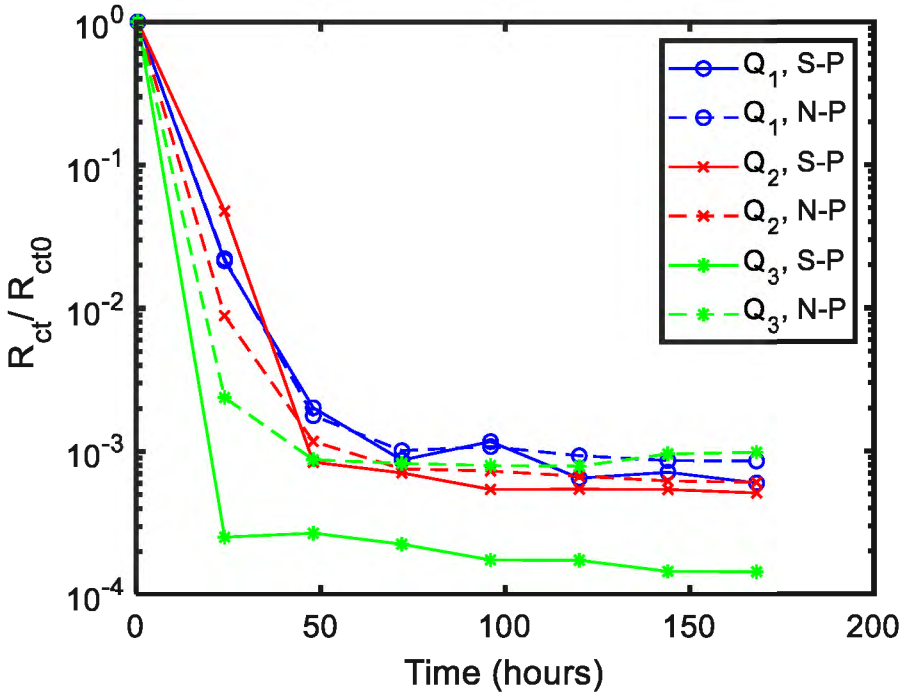

Figure 40. The comparison between the normalized graphs of the charge transfer resistance (R_{ct}) of the equivalent circuit model as a function of the immersion time for the both non- particulate (N-P) and 1 wt. % sand-particulate (S-P) 3.5 wt.% NaCl solution flows.

3.6. Discussion

In this study, the influence of 1 wt. % sand particulate 3.5 wt.% NaCl solution with three different constant impingement flow rates on degradation of epoxy coating was investigated. Then the obtained EIS results of the particulate fluid compared with the EIS results of the non-particulate one. The main research conclusions are as the following:

- For the lowest applied flow rate, $Q_1=6.31\ cm^3s^{-1}$, the influence of sand particles was not significant since the values of compared equivalent circuit elements (C_c, R_{ct}, R_{po}) for both sand particulate and non-particulate fluids were almost the same.
- For $Q_2=12.62\ cm^3s^{-1}$, the comparisons between the low frequency impedance moduli of both types of fluids, in addition to the coating capacitances and pore resistances showed noticeable higher coatings' degradation rates for the sand particulate fluid. The decrease in charge transfer resistances for both fluids took place at almost same

rate. That indicates, for the medium applied flow rate, the additional stresses due to the momentum impacts of sand particles were only effective on the outer layer of coatings and did not cause any difference on the coating and metal interface.

- For $Q_3=18.93\ cm^3s^{-1}$, the compared graphs of low frequency impedance modulus, coating capacitance, pore resistance, and charge transfer resistance showed significant destructive influence of the particle impacts on the coatings.

Overall, it was concluded that for the lowest applied flow rate ($Q_1=6.31\ cm^3s^{-1}$), the additional sand particles did not have any obvious additional destructive influence on the degradation of coatings. For the medium applied flow rate ($Q_2=12.62\ cm^3s^{-1}$), the compared equivalent circuit elements showed that the added sand particles slightly increased the degradation rate of the coatings. For the highest applied flow rate ($Q_3=18.93\ cm^3s^{-1}$), the destructive influence of sand particles was significant, indicating that when the velocity of particulate flow reaches 1 ms^{-1}, the momentum impact of the sand particles plays a vital role in degradation of the organic coatings.

4. DEGRADATION OF EPOXY COATINGS EXPOSED TO CYCLICAL LOADS OF WAVES OF A WAVE TANK

4.1. Introduction

The monopile structures of offshore wind turbines are subjected to cyclic wave and tidal loads, which normally results into corrosion, wear, and ultimately the catastrophic failures due to fatigue loads. The area at which such cyclical loads are dominant is called the wave zone. The cyclical lifting movement formed by the sea surface over time results into tidal currents. Tidal currents are in the horizontal direction perpendicular to the structure of offshore wind structures. The resultant of the attractive force between moon and earth, and the inertial centrifugal force by rotation around a barycenter of the earth and its moon are the driving force of the tidal current. The combination of local wind current, gradient current and tidal current forms the waves in the sea. The dependence of waves on wind speed and its direction, in addition to the pressure on the sea, make the formation of waves unpredictable. As waves are random phenomena, the characteristics and basic parameters of ocean waves observed also have different values that change with time and position. The wave loads are usually simulated as linear irregular waves with theories like Pierson-Moskovitz or JONSWAP [101], [102]. The linear theory can estimate the wave forces acting on offshore platforms with high accuracy when the offshore structures are installed in deep ocean [103]. However, most offshore monopile wind turbines are installed in medium-shallow waters, where nonlinear effects are commonly encountered due to high steepness [104]. For the shallow waters, the Sharma and Dean model [105] is normally utilized which is based on a second order expansion of the potential flow at finite water depths.

The main parameters that define the characteristics of wave include the wave height (H) in m, the wavelength (L) in m, the displacement of the water surface (η) in m, the wave frequency

(ω) in *rad/s*, the amplitude of wave (*a*) in *m*, the depth of water from the free surface (*d*) in *m*, the wave speed (*U*) in ms^{-1}, and the wave period (*T*) in *s*. Figure 41 shows the schematic of the wave parameters for a linear wave.

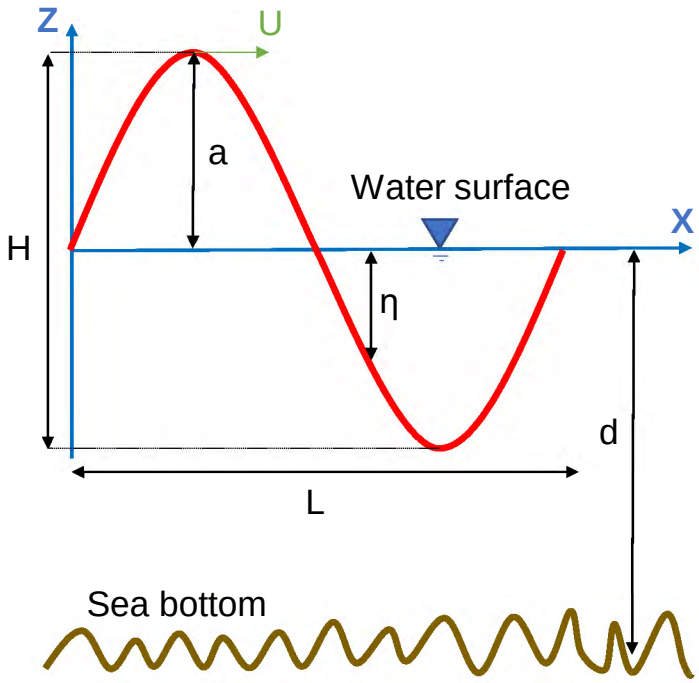

Figure 41. The main parameters of regular ocean waves: the wave height (H) in m, the wavelength (L) in m, the displacement of the water surface (η) in m, , the amplitude of wave (a) in m, the depth of water from the free surface (d).

In a study on the North Sea, the statistical wave data was monitored in the area where the water dept was around 30 m [106]. For the wind speeds between $3\ m/s \leq U_{wind} \leq 25\ m/s$ at *100 m* above the sea level, the respective wave heights were measured to be $0.8\ m \leq H \leq 7.3\ m$, and the wave periods were between $5\ s \leq T \leq 12\ s$ [107]. For strong waves with $T \approx 10\ s$ *and* $H \approx 10\ m$, the respective normal momentum energy on the monopile structures were measured to be between $80\ MJ \leq E \leq 145\ MJ$ [108], [109]. In another case study on a monopile structure with the diameter of *5 m* and the wind speed at around 18 ms^{-1}, the maximum horizontal wave force on the structure was measured as *F = 0.88 MN* [110].

Offshore monopile structures are subjected to cyclic loads of waves which result in fatigue damage, and then lead to the initiation of cracks and eventually failure. The fatigue damage is time consuming, while the failure of the structure takes place at a relatively rapid pace after the initial cracks form and growth on the outer surface of the structure. The steady state tidal currents result in gradual abrasion and corrosion of the structure. There is an interaction between corrosion and fatigue damage. Although both damages can occur simultaneously, generally the abrasion of coatings and water penetration toward the metal surface result in plastic deformation of the metal due to corrosion. Eventually the electrochemical reactions on the metal surface exacerbates the fatigue damage. The magnitude of applied load, the frequency of wave, and the period of the waves identifies the dominant damage type of corrosion-fatigue phenomenon [111]. The impact of wave loads on fatigue damage and cracking of the monopile structures have been studied in several papers [107], [112]–[118]. Ziegler et al. [114], [115] investigated the significance of wave height and mean velocities of free surface on the fatigue Loads on offshore wind turbine structures using Monte Carlo simulation. Their work showed the influence of the water depth and the wave period on the fatigue loads. Schløer et al. [116] showed the vital effect of nonlinearity and steepness of waves on the impulsive structural responses. In another study, Marino et al. [117] concluded that the nonlinearity of waves has a substantial influence on the fatigue loads, especially when the wind turbines are in parked state (the blades are still, and the turbine does not generate electricity). Further, Camp et al. [118] addressed the importance of extreme waves and the nonlinear wave at shallow water for modeling the loads and fatigue damage on offshore wind turbines.

The methods available to protect the generally steel monopile structure against corrosion include cathodic protection (galvanic corrosion), corrosion allowance and formation of passive

layer, and application of multilayer coating systems [6], [13], [14], [27], [53], [119]–[122]. Inhibitive coatings promote passivation of the metal surface and generate protective layers. They are used as a primer coating since the reaction with the steel surface is required. The selection of coatings and their respective applied thickness is very challenging since the monopile structures in tidal and splash zones are exposed to unpredictable waves in addition to the other regular corrosive factors including the Oxygen content of air and water, salt, UV lights, temperature, etc [123]. The on-site corrosion tests are usually conducted on coating systems of offshore wind turbine, where coating samples exposed to the sea water at different locations that were planned for installations of the turbines [6], [54], [124], [125]. However, due to the existence of all corrosive factors, it is impossible to distinguish the individual effect of each corrosive factor on the degradation of the coatings. In recent years, many lab-based flow induced accelerated corrosion tests were conducted. The majority of the lab-based corrosion tests were conducted on uncoated metals [31]–[36], while the degradation of coatings have not received enough attentions until recently [50], [52], [126]–[130].

In this study, to investigate the influence of cyclic loads of waves on degradation of organic coatings, a wave tank was designed and configurated. The wave tank was designed to apply very low to medium range of stresses on the surface of coatings sample. Such stresses help to study the gradual degradation of coatings rather than witnessing the fatigue damage. The velocity of the water flow was measured with Particle Image Velocimetry. Moreover, the Electrochemical Impedance Spectroscopy method was utilized to monitor the deterioration of coatings.

4.2. Wave tank and wave characteristics

The wave tank designed in a way to simulate low frequency tidal waves in ocean conditions. The dimensions of the wave tank were *1524 mm* × *508 mm* ×*508 mm*. As shown in Figure 42, the flap-type paddle was located *178 mm* far from the right wall of the tank, while a wave breaker with the dimensions of *380 mm* × *380 mm* was located at the opposite wall at the other end of the tank. The steel coated samples were located *584 mm* far from the paddle and *382 mm* to the edge of the wave breaker. The tank is filled with 3.5 wt. % NaCl solution to half of its height (*254 mm*). The top edge of the exposed coating area was *20 mm* lower than the free water surface, while the samples have *10 mm* distance to the bottom of the tank.

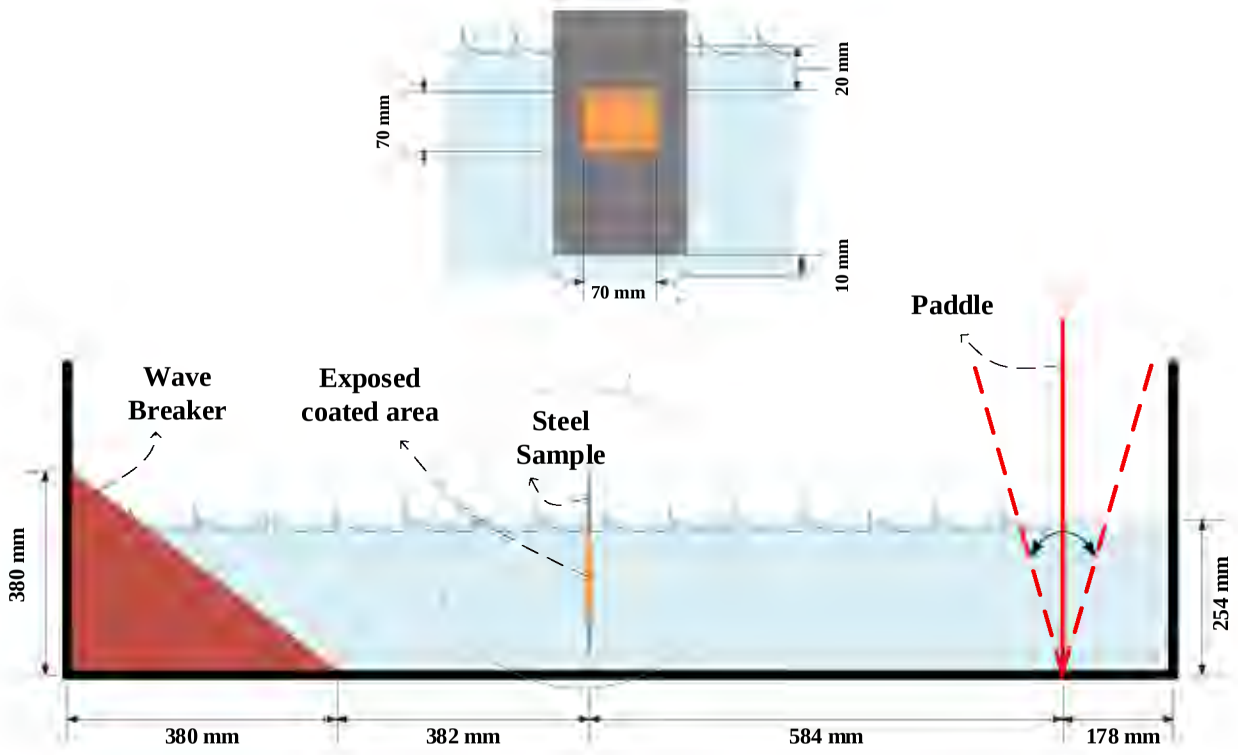

Figure 42. A 2-D schematic of the wave tank.

As shown in Figure 43, the motor is located on a motor holder on top and is powered by an Arduino motor. This motor has a rotor attached to its output shaft with a pin connection to another shaft which is connected to the top portion of the paddle with a pin connection. In this

study, 3 motor speeds (20, 40, and 60 rpm) were considered for each set of corrosion tests. For each test, two coating samples were placed next to each other with a *26 mm* distance between their edges and *89 mm* distance from their other edge to the wall, as shown in Figure 44. The coating samples were exposed to steady-state waves at constant motor speed for one week.

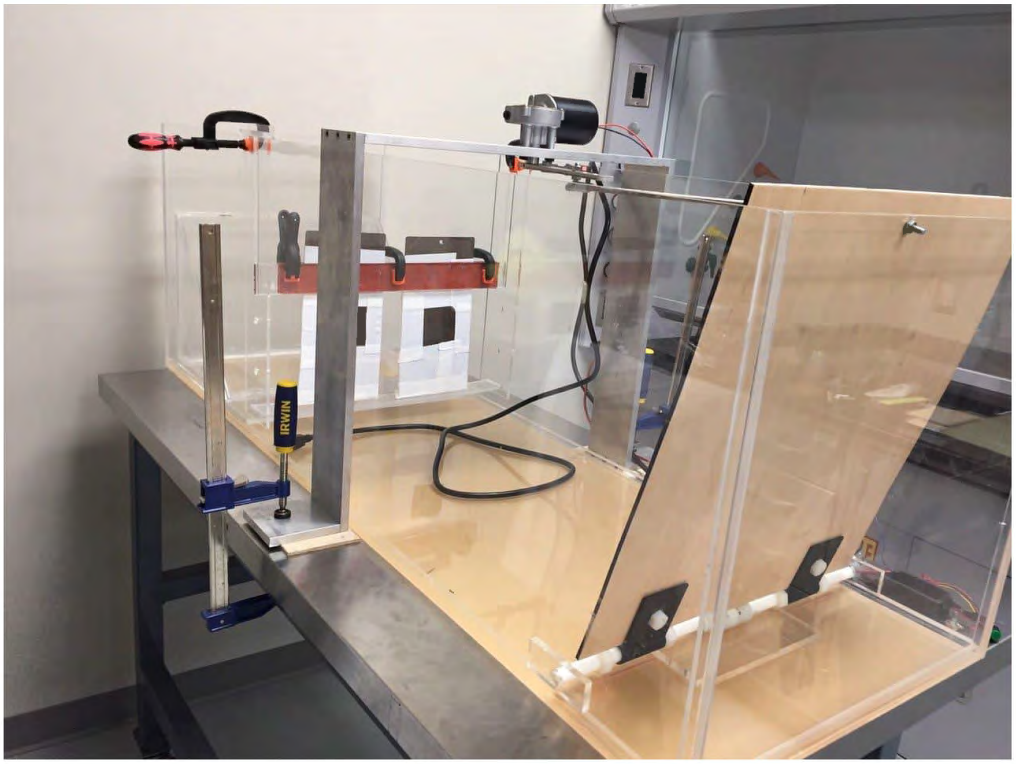

Figure 43. The wave tank.

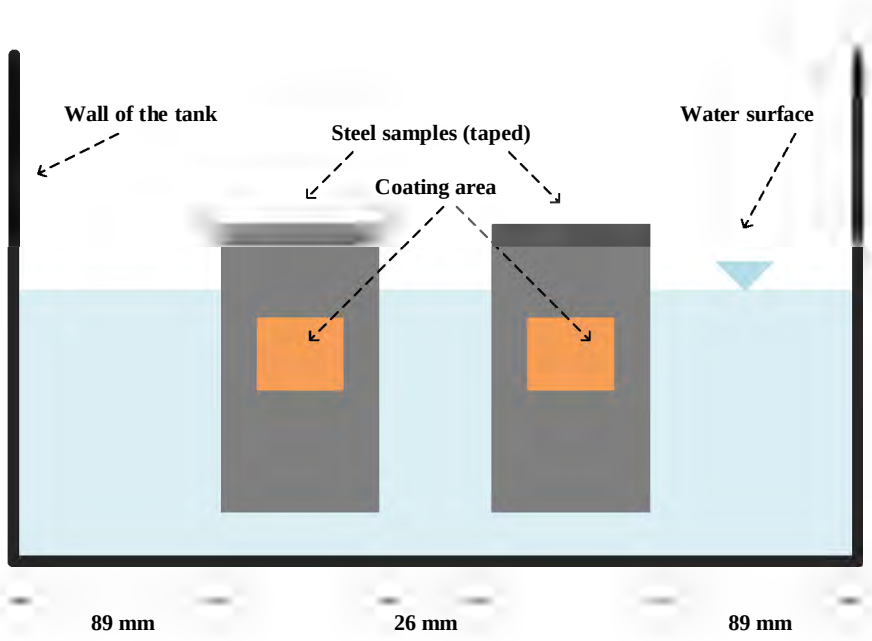

Figure 44. The location of the coating samples inside the wave tank.

The paddle of the wave tank was designed as a flap-type wavemaker where the pendulum movement of the paddle forms the waves in the wave tank (see Figure 45). The length of the paddle is *533.4 mm* (only *245 mm* of the paddle is in water), and its stroke length is *S = 176.4 mm*. The rotation angle from the vertical position of the paddle to the longest distance of its pendulum movement was $\alpha = 19°$.

The governing equation of the flap-type wavemaker was developed by Galvin [131]–[133], which relates the stroke length (*S*) to the wave height (*H*), water depth (*d*), and the wavelength (*L*) (see Figure 45).

$$\frac{H}{S} = 4\left(\frac{\sinh(kd)}{kd}\right)\left(\frac{1 + kd\sinh(kd) - \cosh(kd)}{2kd + \sinh(2kd)}\right) \tag{3}$$

where *k* is the wave number, which can be calculated as the following:

$$k = \frac{2\pi}{L} \tag{4}$$

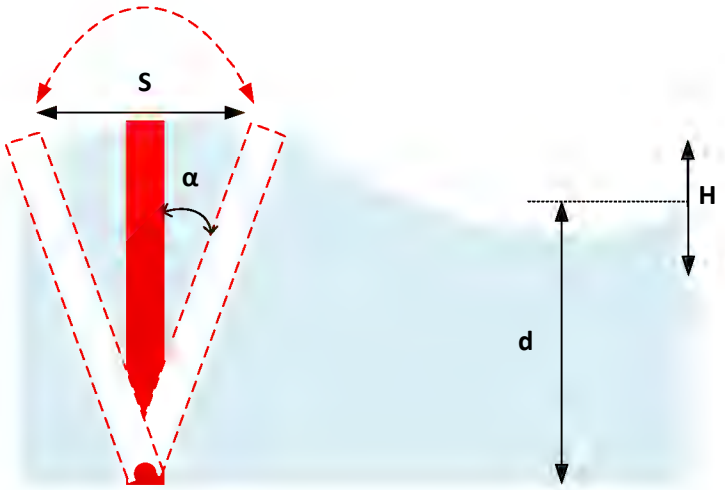

Figure 45. The flap-type wavemaker and its respective parameters, which was utilized in the wave tank.

4.3. Sample preparation

The coating samples are prepared in the same way that was described in section 2.2. In addition, the edged of the samples were applied with an extra layer of coating using dip-coat method. Finally, a waterproof tape was applied all over the samples except for an area of *70 mm* × *70 mm* which was exposed to the flow waves (see Figure 46).

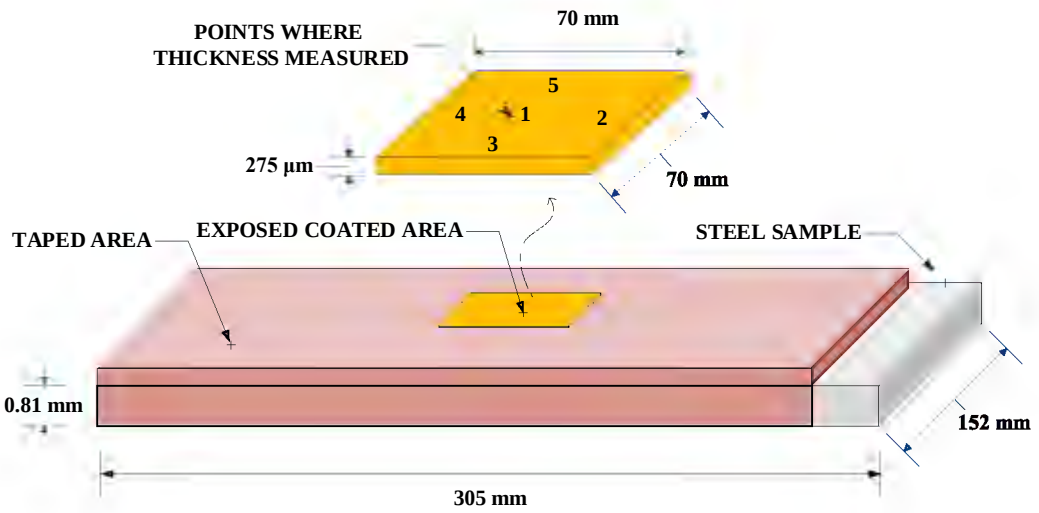

Figure 46. The schematic of the coating samples for wave tank experiments, showing the layers of steel, organic coating, and the applied waterproof tape.

4.4. EIS method

To monitor the process of the degradation of coatings, Electrochemical Impedance Spectroscopy (EIS) method was utilized. In order to collect the EIS data, a reference 600 Potentiostat by Gamry Instruments was employed. In each EIS test, the steel substrates were considered as working electrode while platinum electrodes were used as reference and counter electrodes, while three platinum electrodes were considered as a reference and counter electrodes as shown in Figure 47. The reference electrode was located at the center right in front of the coating samples, while the two counter electrodes located in symmetry on the left and right side of the reference electrode. All the EIS tests were taken over the frequency range of 10^{-2} to 10^{5} *Hz* with ten points per decade using *15 mV AC* perturbation coupled with the open circuit potential. The initial EIS tests were conducted at the beginning of the immersion of coating samples, and the second EIS test was conducted *3* hours after the exposure to the waves. The third and fourth EIS tests were conducted after *12 h* and *24* hours of the exposure time. The rest of the EIS tests were accomplished every *24* hours until the end of the seventh day. During the time that the EIS measurements were conducted (about 35 min for each test), the motor was turned off to minimize the disturbance of attacking waves on the EIS results.

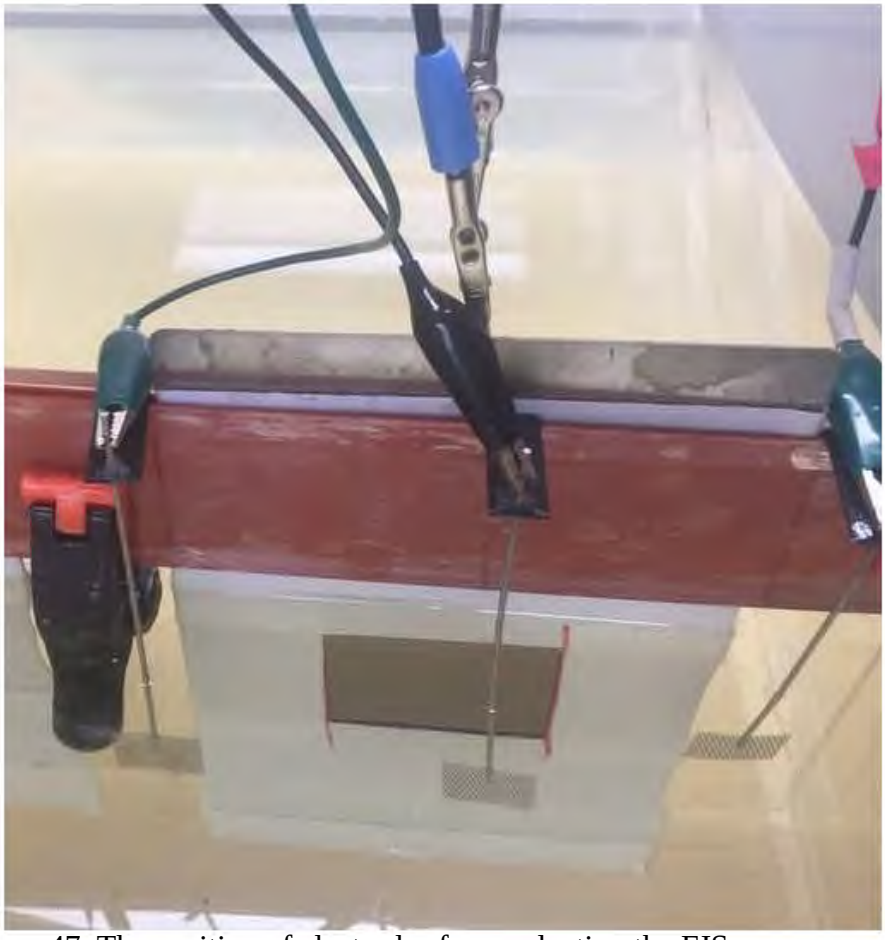

Figure 47. The position of electrodes for conducting the EIS measurements.

4.5. EIS results

The coatings were exposed to three different waves which were produced in the wave tank with three different motor speed, 20, 40, and 60 rpm, for a period of one week. The degradation of the coatings was monitored with EIS. The impedance modulus (Bode plot) and phase angle of the coatings for each applied wave were shown in Figure 48 and Figure 49. The graphs in both figures represent impedance and phase angles measured upon stabilization after the onset of the flow (initial) and those measured daily while the coating sample was kept completely under water. The area of the exposed coatings ($A = 49\ cm^2$) was used in the calculation of the impedance modulus for the Bode plot. We observe from the Bode plots that all impedance modulus decreases with time as the coatings were exposed to the cyclical wave loads.

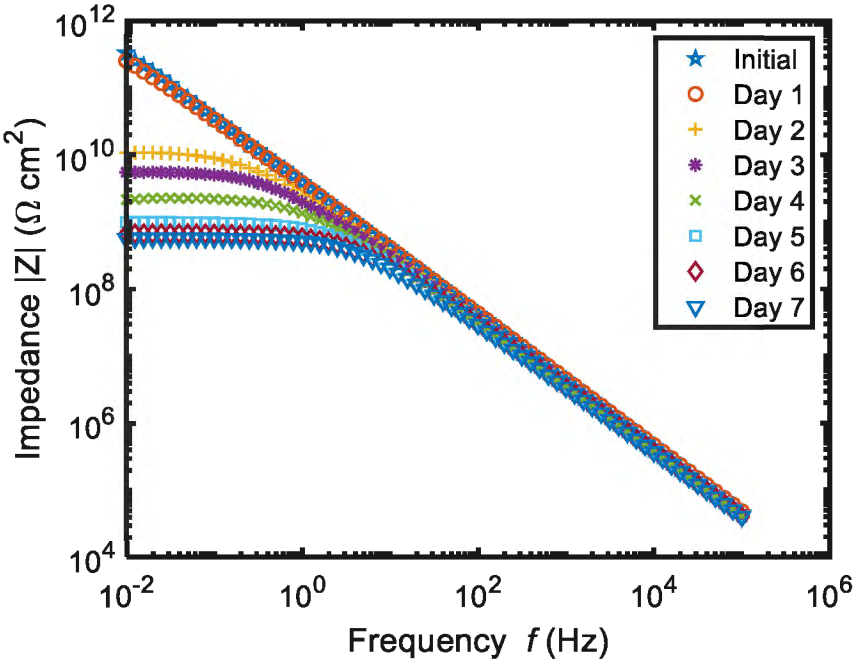

(a) Motor speed (20 rpm)

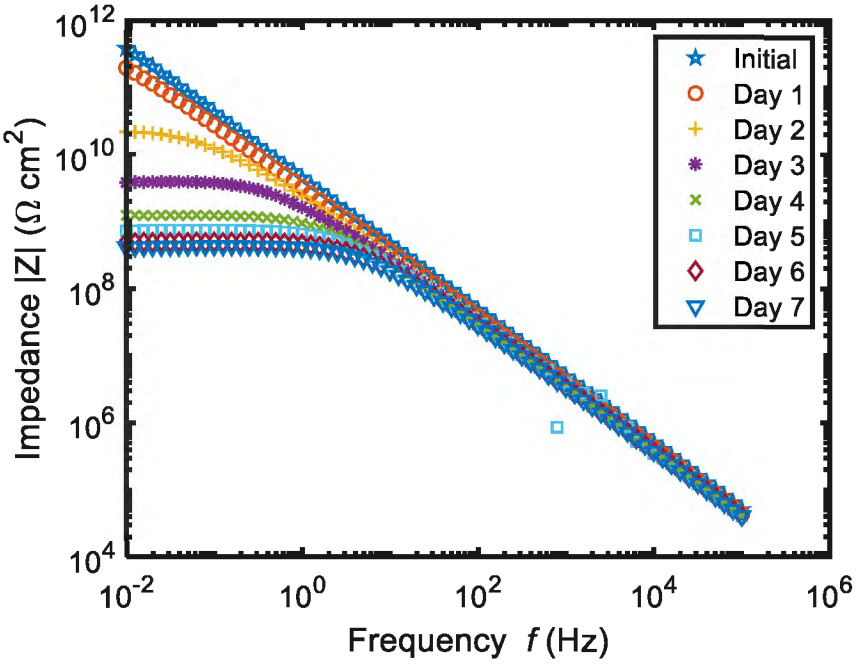

(b) Motor speed (40 rpm)

Figure 48. The impedance modulus of the coating samples exposed to three different cyclical wave loads for a week.

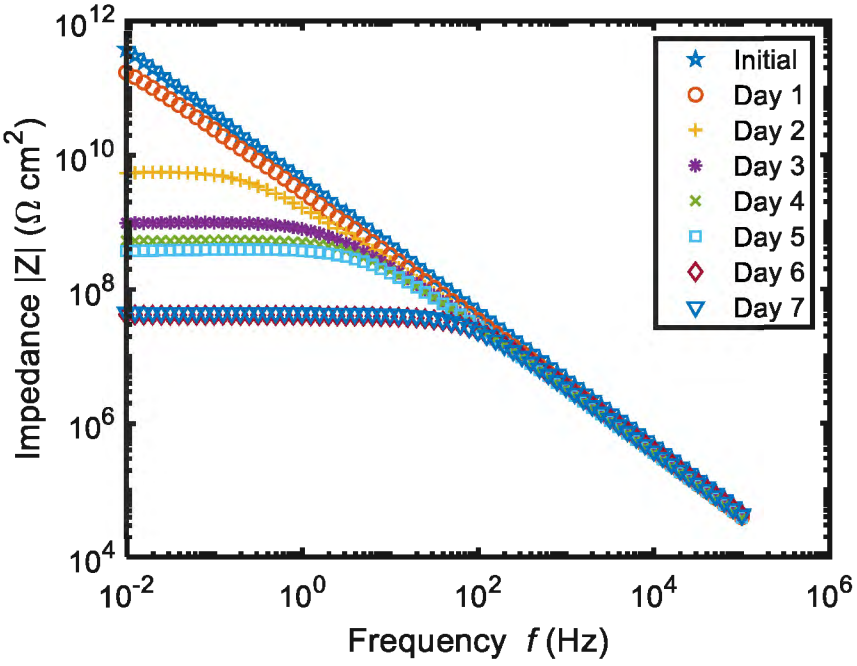

(c) Motor speed (60 rpm)

Figure 48. The impedance modulus of the coating samples exposed to three different cyclical wave loads for a week (continued).

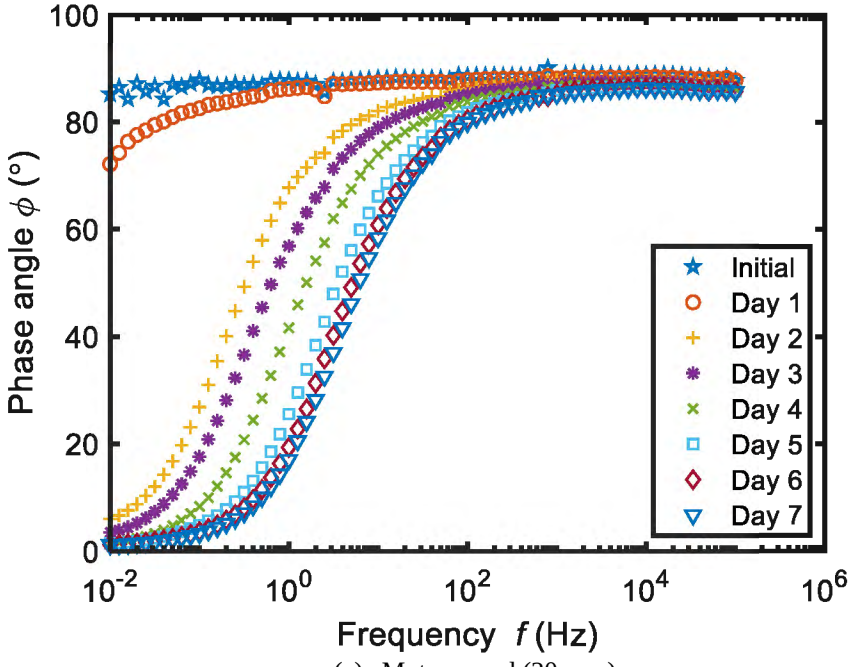

(a) Motor speed (20 rpm)

Figure 49. The phase angles of the coating samples exposed to three different cyclical wave loads for a week.

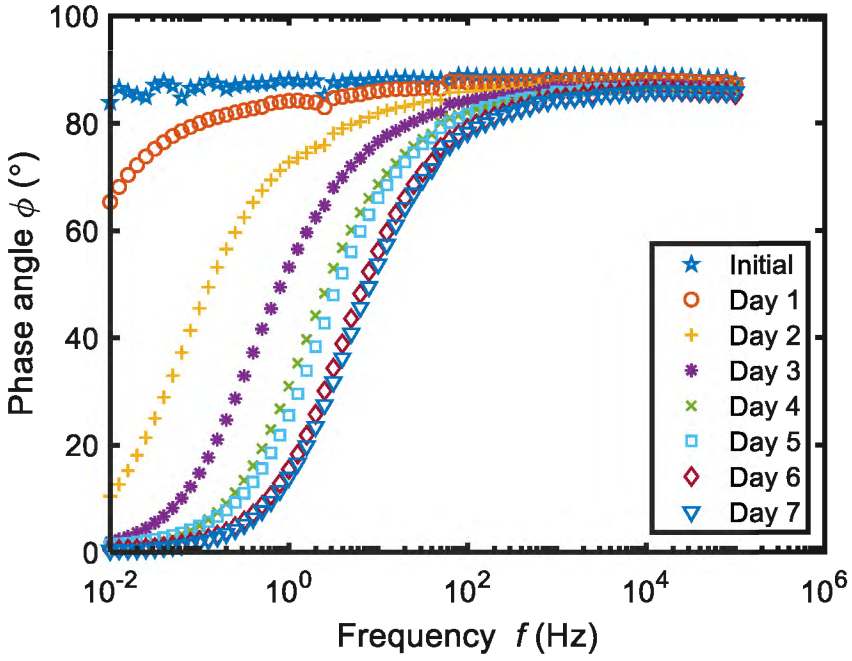

(b) Motor speed (40 rpm)

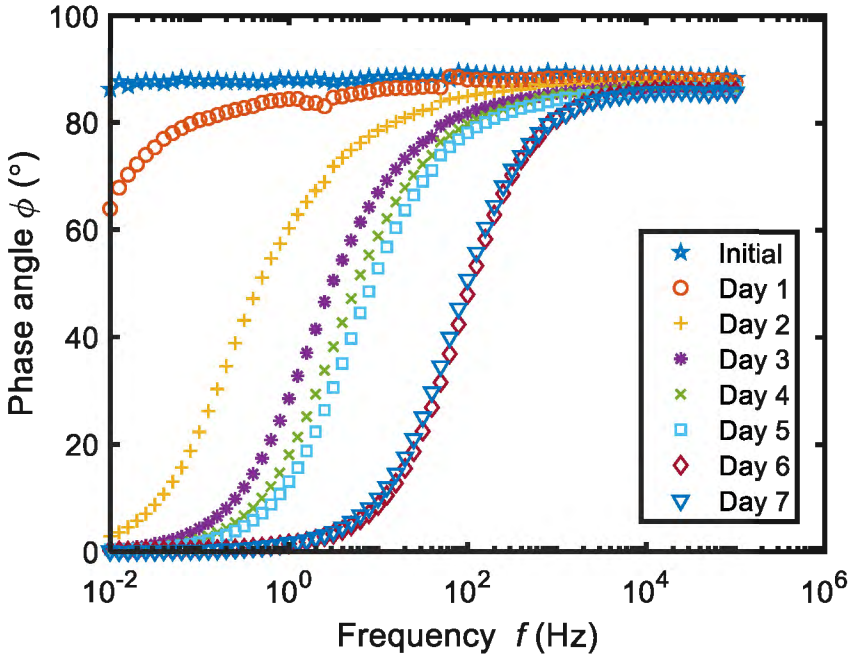

(c) Motor speed (60 rpm)

Figure 49. The phase angles of the coating samples exposed to three different cyclical wave loads for a week (continued).

To make a comparison between the impedance of the samples we plot the low frequency impedances normalized by the low-frequency impedance modulus at the initial immersion time. As shown in Figure 50, the low frequency impedance of the coatings decreased during the week of exposure to waves for all three cases. Moreover, the decreasing rate of impedance was higher for the highest rotational speed of the motor ($\omega_3 = 60\ rpm$) compared to the other two motor speeds. The low frequency graphs show the direct relation between the increase of the cyclic loads and the decrease of the impedance of the coatings (i.e. the degradation of the coatings).

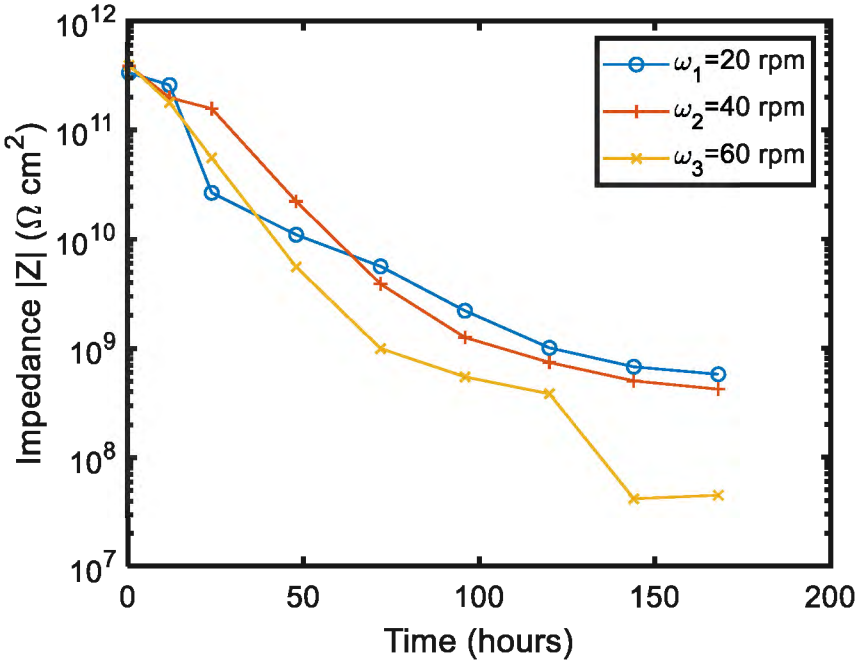

(a)

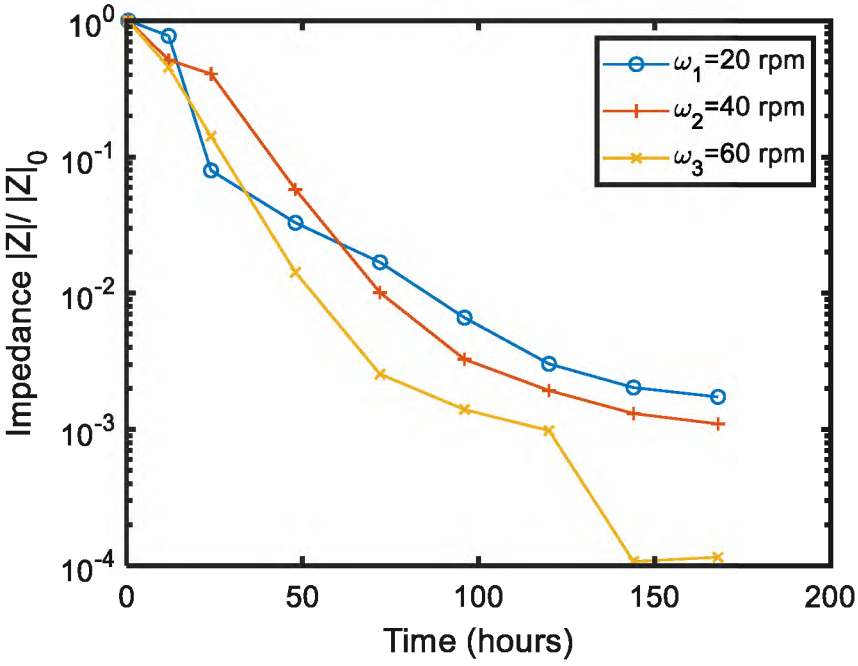

(b)

Figure 50. Low-frequency impedance moduli (a) and their respective normalized graphs (b) as a function of immersion time at 0.01 Hz for different rotational speed of the motor.

4.6. Equivalent circuit modeling

Figure 51 shows the equivalent circuit models that have been used to analyze the EIS data. ZsimpWin3.6 has been employed in the process. The best fitted equivalent circuit model was selected by fitting to the Nyquist graphs of EIS data and the values of χ^2 were compared. Ideally the value of χ^2 should be between 10^{-5} and 10^{-3} to be regarded as an acceptable circuit model. As an example of the model selection, Figure 52 shows a Nyquist diagram of the experimental data of one of the samples that was exposed to the waves with motor speed of $\omega_3 = 60\ rpm$. Figure 52 shows that the equivalent model was fitted the experimental data with $\chi^2 = 1.03\times10^{-4}$.

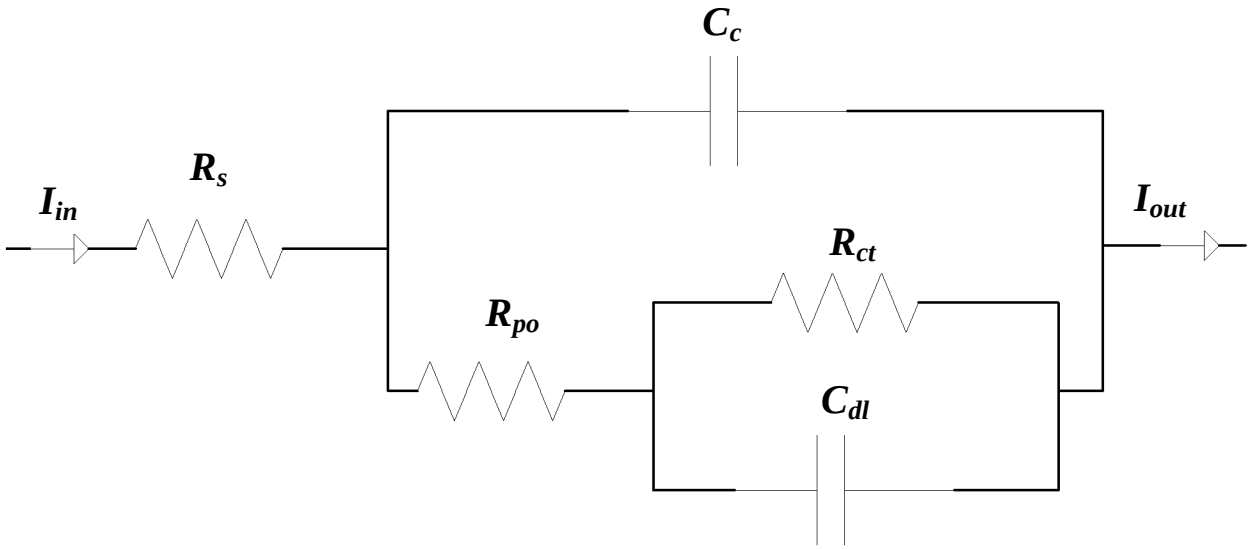

Figure 51. The equivalent circuit models used in analysis. R_s is the solution resistance, R_{ct} is the coating resistance. R_{po} is the resistance of the coating-substrate interface, C_c and C_{dl} are coating capacitance and charge transfer capacitance respectively.

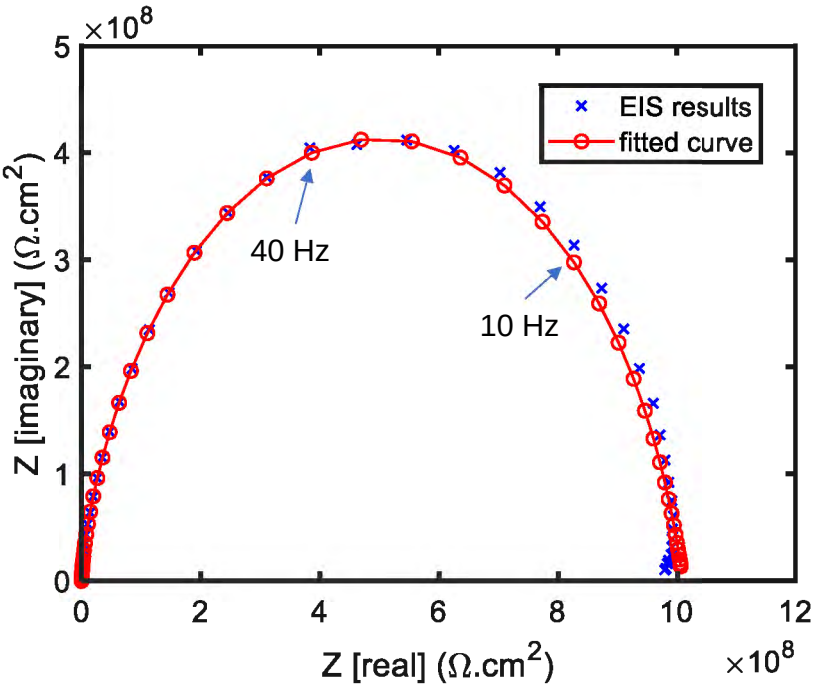

Figure 52. A sample curve fitting of the EIS results with respect to chosen equivalent circuit model: EIS data of day four for the strongest waves with ω_3=60 rpm modeled with $\chi 2=1.06\times10^{-4}$.

Figure 53 (a) shows the behavior of the coating capacitance C_c during the exposure to the waves produced with three different motor speeds. Figure 53 (b) plots the capacitance values normalized by the capacitance at initial immersion for comparison purpose. The coating capacitance increases as immersion time increases. It is also observed that the coating capacitance increases more rapidly for higher wave loads. The phenomenon may be explained by the increased percolation of solution into the coatings promoted by higher flow rates.

We plot the double layer capacitance (C_{dl}) as a function of immersion time in Figure 54 for different wave loads created by three different motor speeds. The value of the double layer capacitance depends on many variables including electrode potential, temperature, ionic concentrations, types of ions, oxide layers, electrode roughness, impurity adsorption, etc. There is no obvious tendency observed with respect to the immersion time and the flow rate, as may be caused by a model artifact.

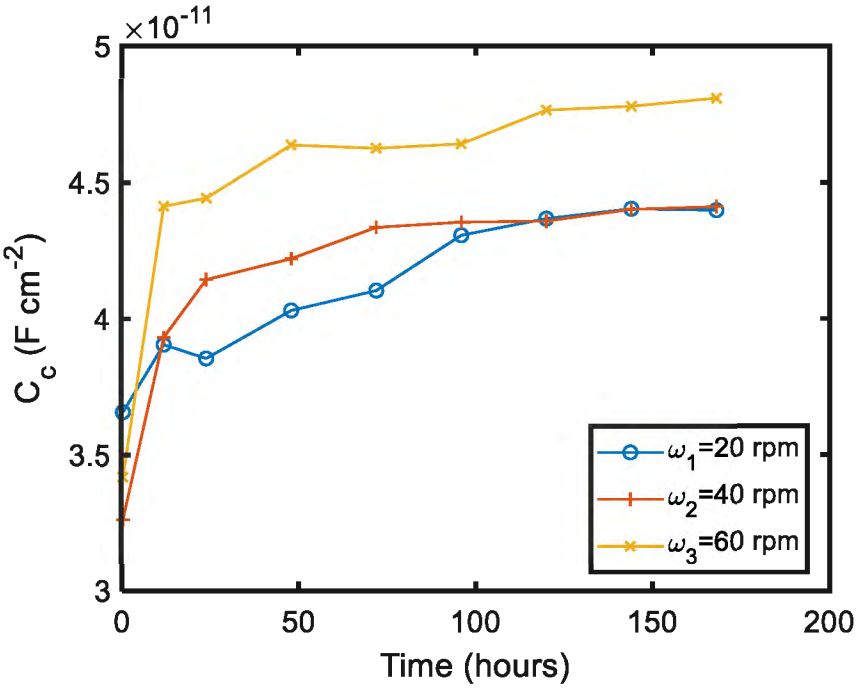

(a)

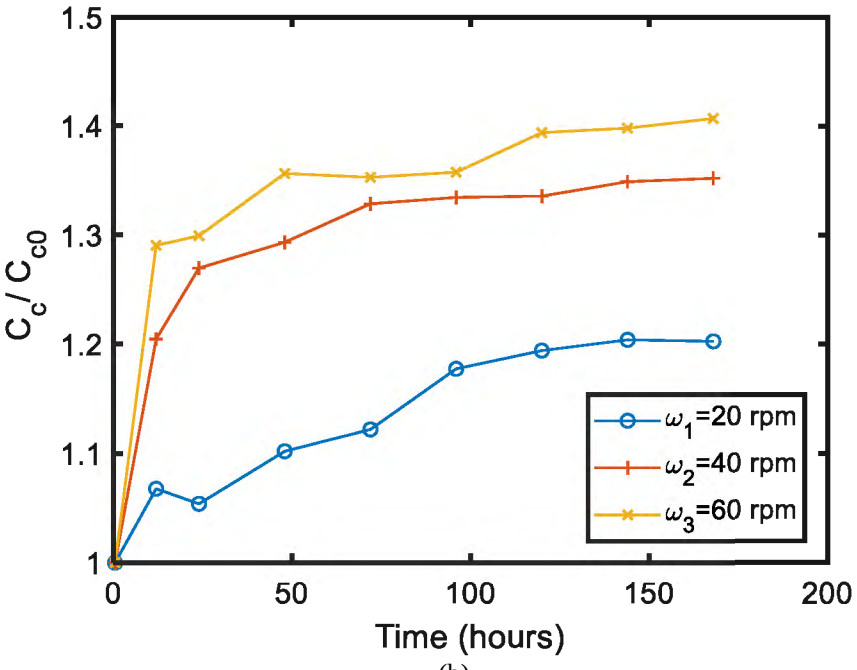

(b)

Figure 53. Coating capacitance (C_c) of the equivalent circuit model as a function of immersion time for the waves produced with three different motor speed: (a) absolute values of capacity in one week, (b) the normalized values of the capacitance.

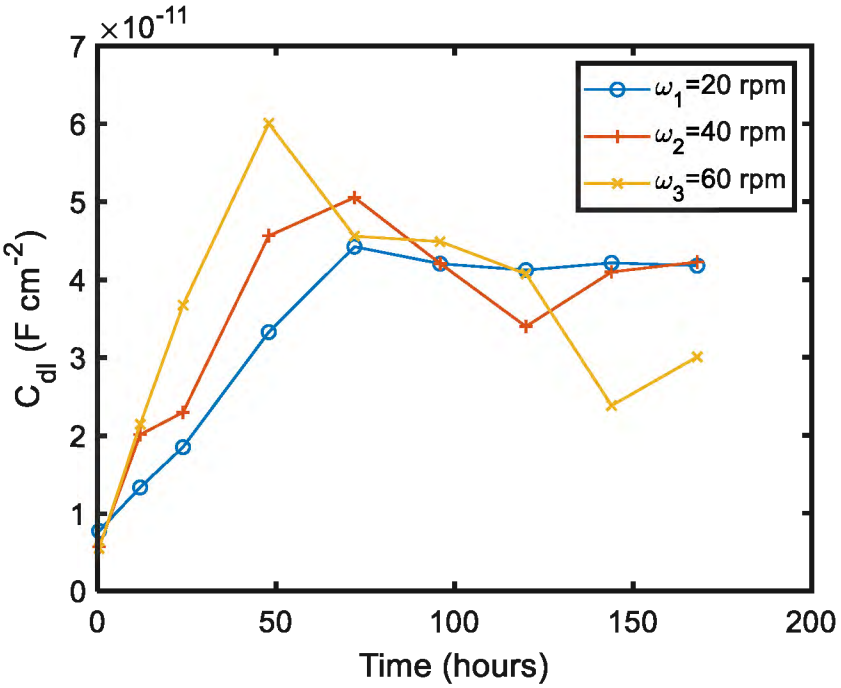

Figure 54. Double layer capacitance (C_{dl}) of the equivalent circuit model as a function of immersion time for three different motor speeds.

Figure 55 shows the pore resistance (R_{PO}) and its normalized value as a function of immersion time. The value of R_{PO} indicates the amount of ion conducting pathways that develop in the coating. The decline of the value of pore resistance indicates the increase in the amount of conducting pathways and the deterioration of the coating's barrier properties against corrosion. The overall trends indicate that the R_{PO} values decrease over time for all samples, and the higher the applied wave load is, the greater decrease R_{PO} value exhibits.

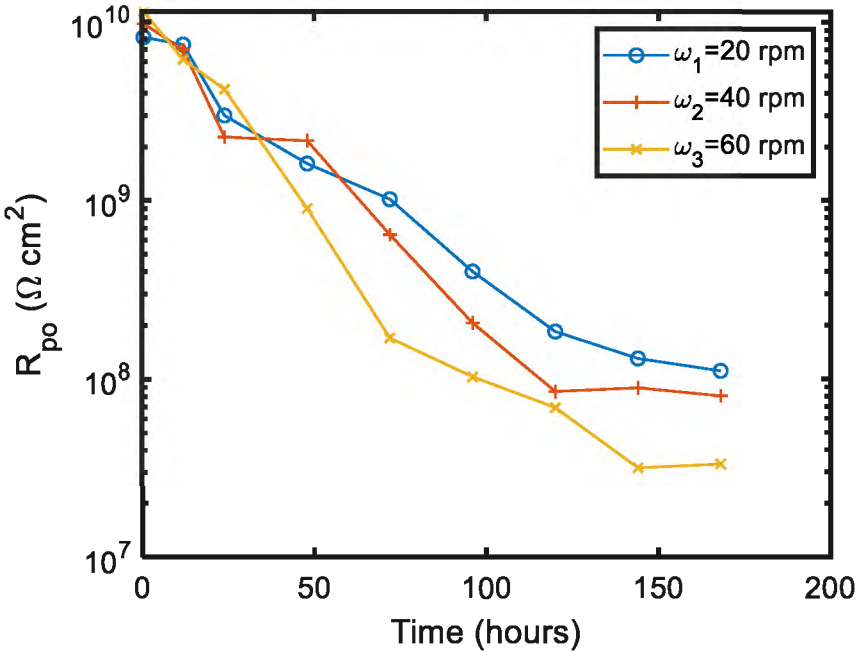

(a)

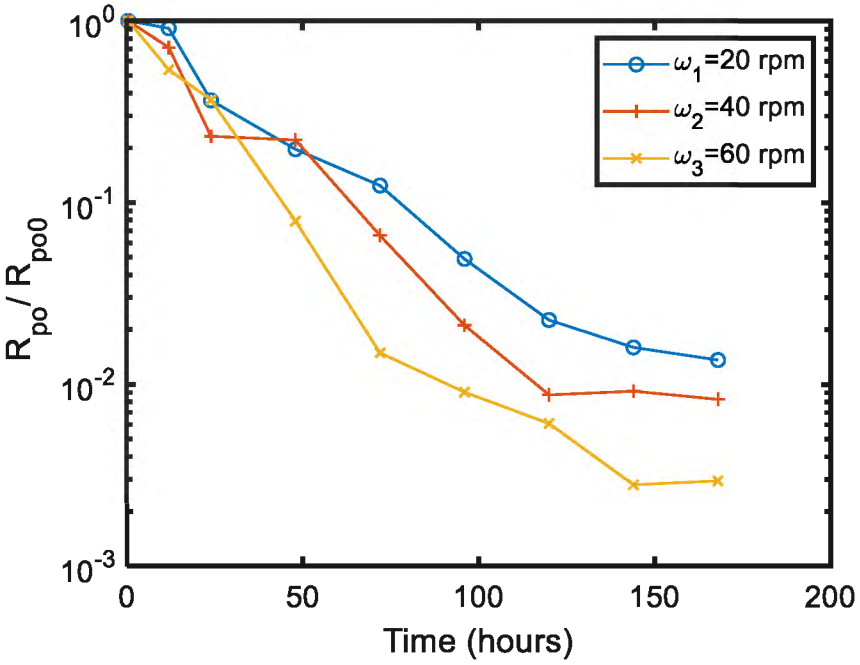

(b)

Figure 55. Pore resistance (Rpo) of the equivalent circuit model as a function of immersion time for the waves produced with three different motor speeds: (a) absolute values of resistance in one week, (b) the normalized values of the resistance.

Figure 56 illustrates the charge transfer resistance (R_{ct}) of the equivalent circuit model as a function of immersion time. When an electrode is polarized, it can cause the current to flow via electrochemical reactions that occur on the electrode surface. The amount of current is controlled by the kinetics of the reactions as well as the diffusion of reactants/products towards/away from the electrode. During immersion, for all samples R_{ct} values decrease as immersion time increases. We observe in Figure *56* that R_{ct} exhibits a more rapid decay for waves created with motor speed of $\omega_3 = 60\ rpm$, owing to a faster diffusion rate promoted by higher flow velocities of the working fluid.

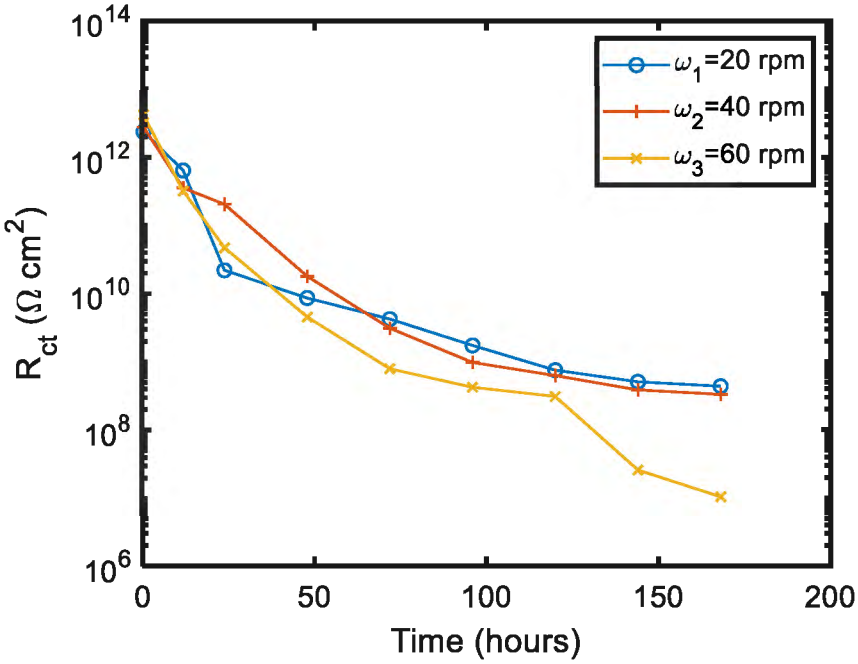

(a)

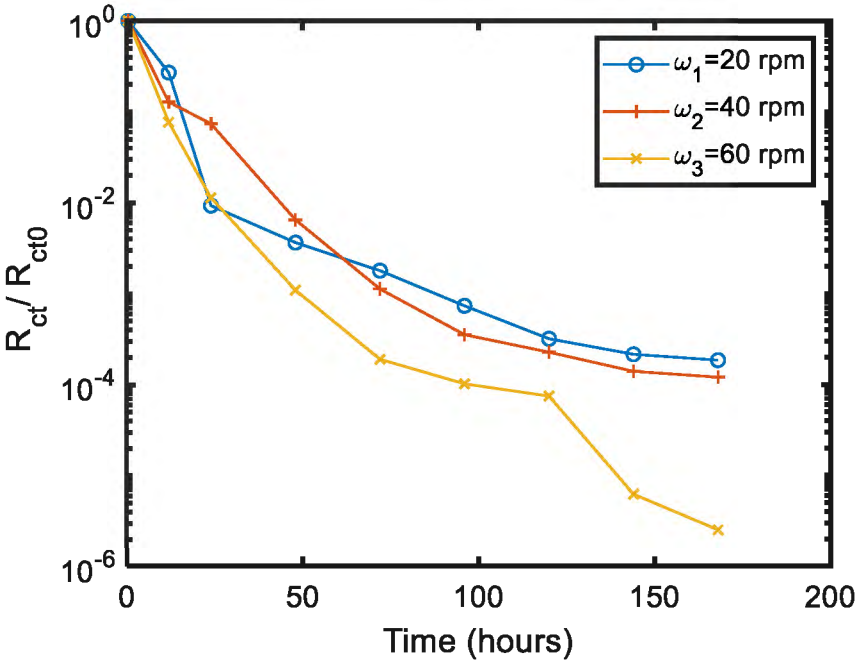

(b)

Figure 56. Charge transfer resistance (R_{ct}) of the equivalent circuit model as a function of immersion time for the waves produced with three different motor speeds: (a) absolute values of resistance in one week, (b) the normalized values of the resistance.

4.7. Topography characterization

The thickness of the coating samples was measured at five points in the square of the exposed coatings to the waves. The mean values for each sample were taken into comparison. Figure 57 shows the values of coating thickness before and after the exposure to the wave loads. We observe that for all the cases, the thickness of the coating slightly increases after the period of the tests. We believe the coating swelling was dominating in this case, which was caused by the solution that percolates through the coating layers. For samples exposed to the higher wave loads, the relative thickness of the coatings increased with higher percentage. The increase rates of the thicknesses were measured as 4.49, 8.8 and 10.2% the lowest to highest motor speeds respectively.

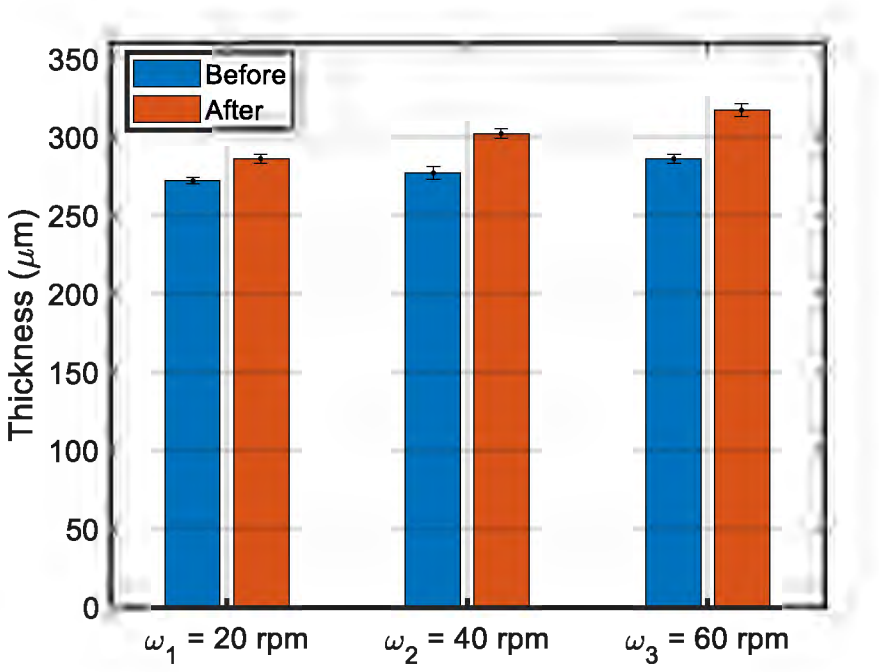

Figure 57. Coating thickness before and after the exposure to wave loads for a week.

4.8. Discussion

This study investigated the degradation behavior of an epoxy coating exposed to wave loads which were generated in a wave tank with three different rotational speed of an electric motor. The analysis of EIS data and equivalent circuit models revealed the changes in coatings' barrier property. We observed that the impedance modulus experiences a more significant decrease after exposure to the higher wave loads. Assisted by equivalent circuit models, we discovered that under the influence of impingement flow, higher wave loads result in a more substantial decrease in polarization resistance and double layer capacitance. The coating capacitance value also shows significant increase as the wave load increases. Those help us to understand that the higher wave loads promote the percolation of working fluids and the transport of the oxygen and ions into coatings. The higher wave loads on the surface of the coating samples causing more water penetration through the outer layer of the coatings. The absorption of the working fluid into the coating causes the swelling process during the time of exposure.

5. CFD AND PIV METHODS

5.1. Introduction

In this study, the applied stresses on the coating samples due to the fluid flow were measured and analyzed. The boundary layer and the applied forces on the surface were considered initially based on theoretical calculations under axisymmetric and steady-state conditions, then the Computational Fluid Dynamics modeling (CFD) was utilized to provide numerical results, and finally the velocity of the fluid measured experimentally by Particle Image Velocimetry (PIV) method to compare and verify the results from the CFD modeling. The analysis of the produced normal and shear stresses by the impingement flow can provide a good correlation to the stresses exerted on the structure of offshore wind turbines in field tests.

For the wave tank, the CFD method was not utilized due to the complexity of the model, and very time expensive calculations of the non-steady state, transient flow. However, the PIV method was conducted to measure the magnitude of the applied cyclical wave loads on the coatings' surfaces.

5.2. CFD modeling of the impingement flow in the chamber

The schematic diagram of the chamber is shown in Figure 58. As shown in Figure *58*, the fluid enters the chamber from a vertical pipe with a diameter of $d = 5\ mm$. The distance between the pipe's outlet and the bottom of the chamber is $75\ mm$. While maintaining the solution level at 90 mm from the bottom of the chamber, the outlet of the pipe is always submerged in the solution. Two exit orifices with the same diameter as the inlet pipe located $10\ mm$ above the bottom of the device, i.e. the surface of the coating sample.

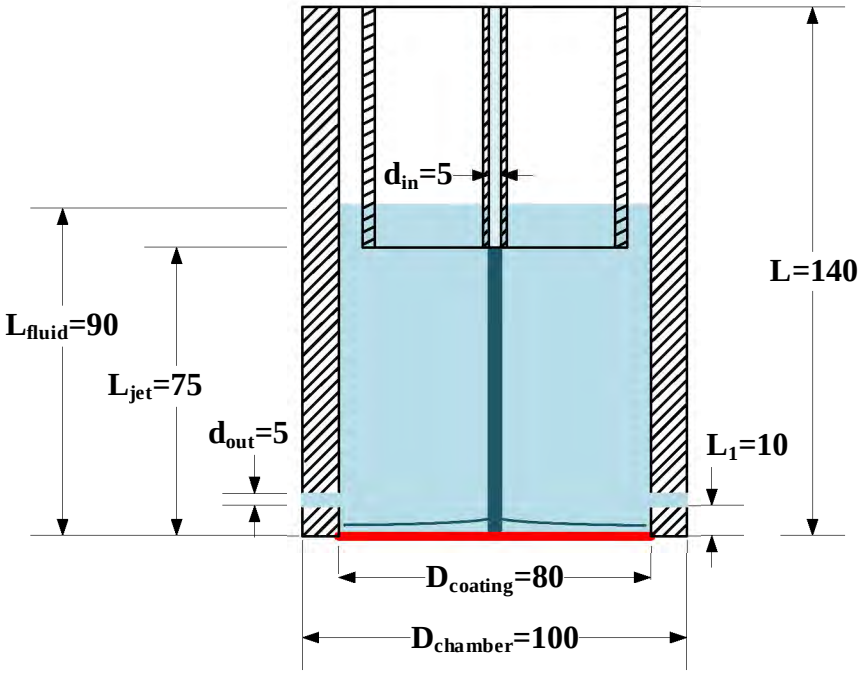

Figure 58. A 2-D schematic model of the impingement flow chamber. All dimensions are in millimeters.

The jet of the fluid forms a vertical stream impacting the surface, and then after hitting the surface, it flows to the side in a direction parallel to the surface of the coated samples. Figure 59 shows the schematic of the jet stream in *y* direction (*i.e.* impingement flow direction) and the formation of symmetric wall jets and the boundary layers in *x* direction, which is parallel to the coating surface.

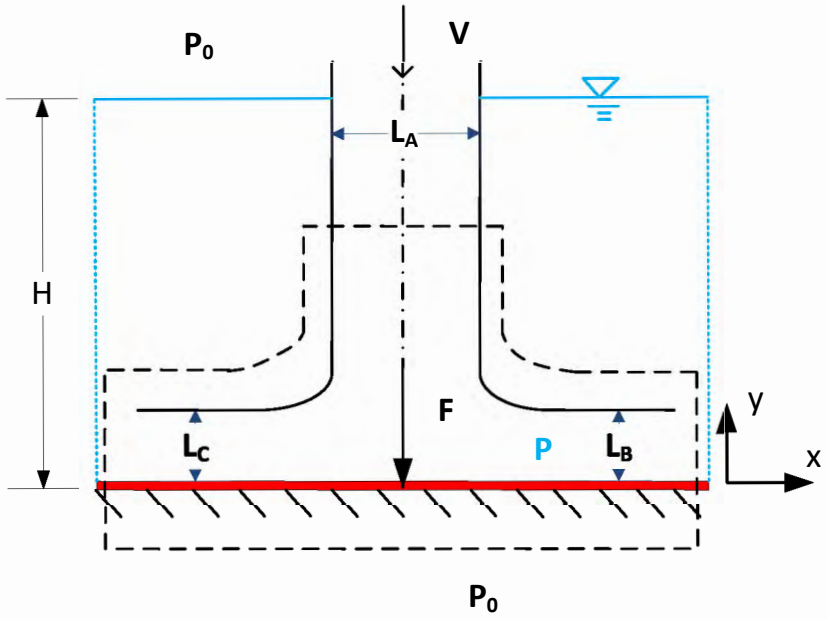

Figure 59. Schematic of the momentum impact of the impingement flow on the coating sample, in addition to the formation of symmetric boundary layer parallel to the surface of the sample in x direction.

Theoretically, the wall shear is zero in the stagnation area, while the axisymmetric boundary layers, which form on the side of the jet stream in *x* direction, cause significant wall shear starting from the maximum values at the locations where the parallel flow to the coated surface forms, and decreases as the flow moves away from the stagnation area. Based on the measurement represented in Figure 58, a three-dimensional model was developed for CFD analysis (using ANSYS CFX) as shown in Figure 60.

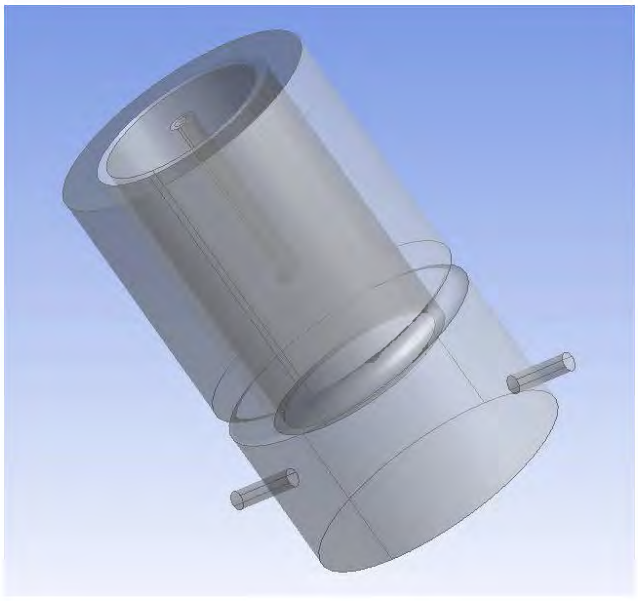

Figure 60. The 3D model of the chamber utilized for CFD analysis.

The combination of body and face sizing meshes were applied on the model. The entire body was meshed with body sizing, while the face sizing applied on the bottom part of the chamber. For the body sizing, a sphere of influence is centered at the centroid of the bottom plate with a radius of 0.06 m (Figure 61). Five different mesh sizes have been employed in our calculation. The computed values for pressure at the center of the coating sample are summarized in Table *2*. The visual comparison between mesh type 1 and 3 is shown in Figure *62*. As we decrease the mesh size, convergence could be observed in the calculated pressure value in Table *2*. Mesh size type 3, 4, and 5 appear to achieve similar results. Due to the relatively lower computational cost, we decided to employ the fourth mesh size shown in Table *2*.

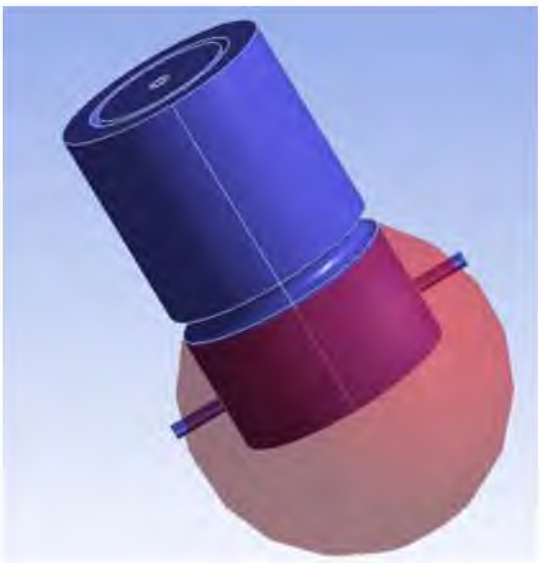

Figure 61. Face and body sizing mesh with sphere centered at the bottom plate of the chamber.

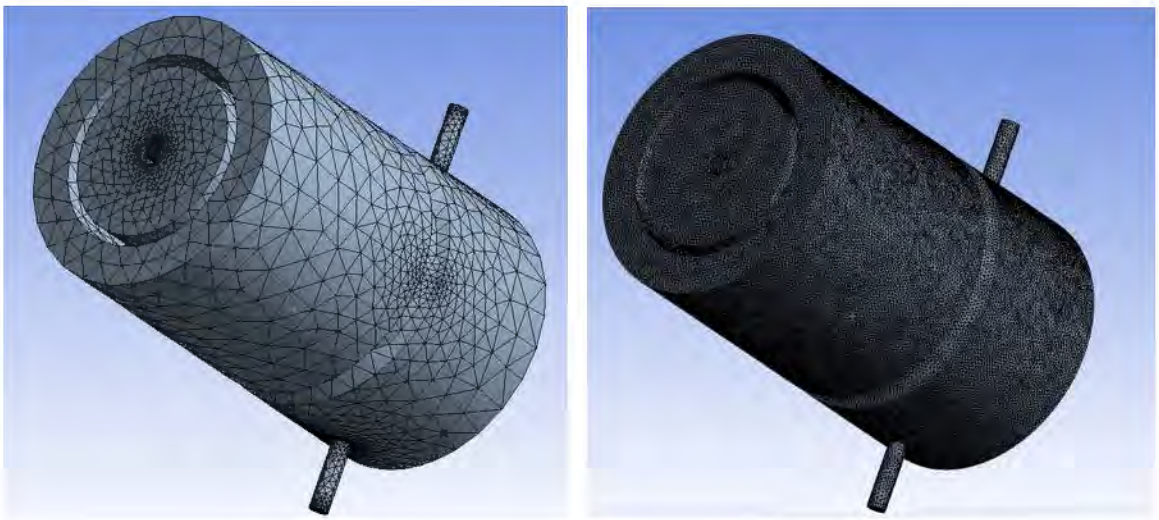

Figure 62. Visual comparison between the mesh type 1 (left) and 3 (right) of Table 2.

Table 2. The data of mesh study for CFD modeling.

Mesh Size Type	Mesh Type	Element Size (*cm*)	Num. of Nodes	Num. of Elements	Max Pressure at the bottom center of the plane (Pa)
1	Face sizing Body sizing	0.01 0.007	6174	3086	-177.302002
2	Face sizing Body sizing	0.001 0.005	2860734	2095392	-92.3851013
3	Face sizing Body sizing	0.003 0.0009	4016009	2942831	-155.943237
4	Face sizing Body sizing	0.001 0.0007	12106652	8892922	-155.3044519
5	Face sizing Body sizing	0.0009 0.0005	27463629	20302236	-156.0044519

The boundary condition at the inlet is defined with 3 different velocities, V = 0.3214, 0.6427, and 0.9641 (ms^{-1}), corresponding to the three different applied flow rates. The boundary condition for the exit orifices was considered as half of the inlet flow rate for each orifice to satisfy the mass conservation. An airhole at top of the chamber keeps the pressure at $P = 1\ atm$ on the water level inside the chamber. At the bottom of the chamber, the applied stresses on the coating surface is determined by the applied inlet velocities. No-slip boundary conditions are applied on other surfaces including the coating surface (see Figure *63*). The working fluid once considered as 3.5 wt. % NaCl solution with the density of $\rho_{3.5\%NaCl} = 1025\ kgm^{-3}$ and dynamic viscosity of $\mu_{3.5\,\%\,NaCl} = 1.2712 \times 10^{-3}\ Pa.s$. For CFD modeling of the sand particulate fluid, the whole mixture was considered as a single-phase flow with a density of $\rho_m = 1030.928\ kgm^{-3}$, and dynamic viscosity of $\mu_m = 1.813 \times 10^{-3}\ Pa.s$. The flow inside the impingement chamber modeled with k-ε turbulence model. The iteration process for solving the nonlinear equations of the turbulent flow was set to converge on 10^{-6}.

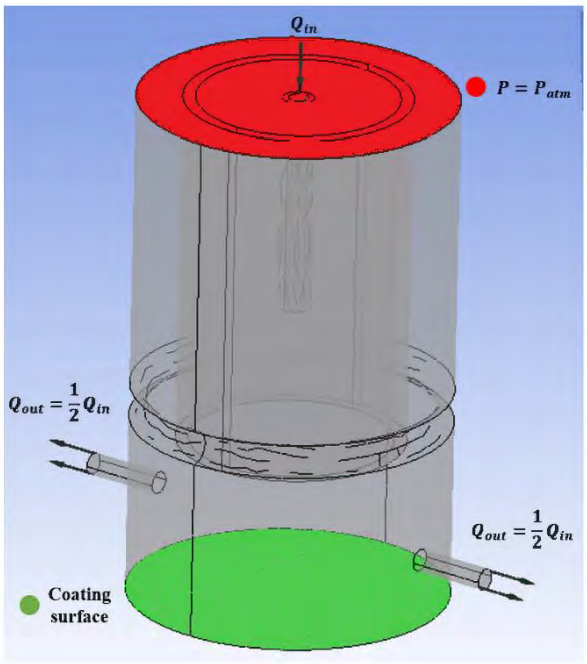

Figure 63. The schematic of the boundary conditions of CFD analysis of the impingement chamber.

5.3. PIV method for the impingement flow chamber

The schematic of the PIV set up for the impingement chamber is shown in Figure 64. Illumination was provided by a double-pulsed Nd:YAG laser (NewWave MiniLase-III) capable of emitting two laser pulses of 100 *mJ* at a wavelength of 532 *nm* with a repetition rate of 15 *Hz*. For 2D PIV, the laser beam was shaped to a laser sheet (thickness <1 *mm*) by using a set of mirrors, spherical and cylindrical lenses. The fluid was seeded with Polyamide particles (HQ Dantec Dynamics) with mean diameter of 20 μm and the density of 1.03 gcm^{-3}. A high-resolution CCD PIV camera with resolution of 1600×1200 pixels and inter frame capability of < 1 μs was set up with its axis perpendicular to the laser sheet for image acquisition [134]. The CCD camera and the Nd:YAG lasers were connected to a programming timing unit (PTU) from LaVision, which controls the timing of the laser illumination and the image acquisition. Instantaneous PIV velocity vectors were obtained by a frame to frame cross-correlation

technique involving successive frames of patterns of particle images in multi-pass interrogation process from window size of 128 × 128 to 32 × 32 pixels. An effective overlap of 75% was employed. The time-averaged quantities were obtained from a cinema sequence of 100 frames of instantaneous velocity fields for each case.

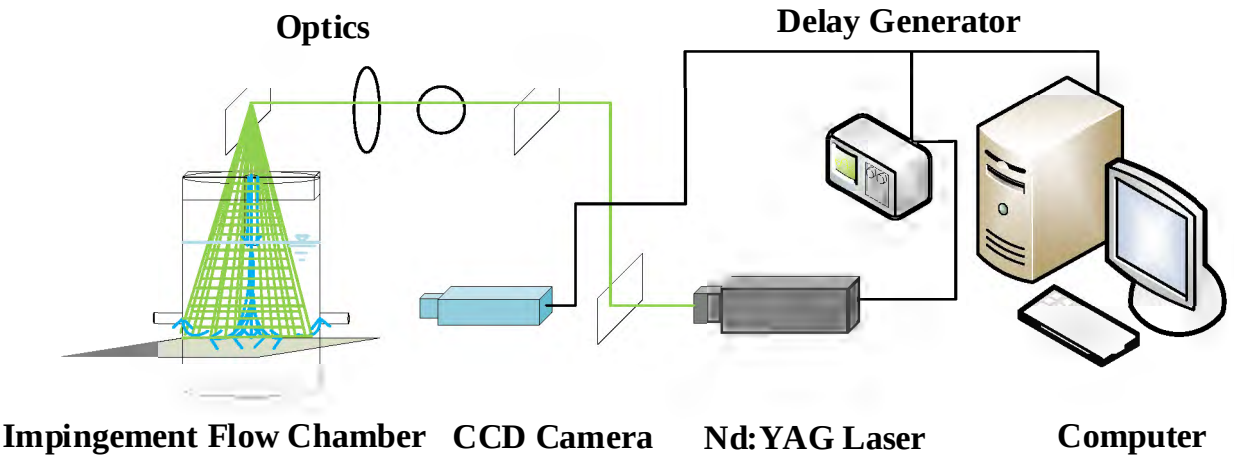

Figure 64. Schematic of the PIV system.

Since it was intended to measure the 2-D velocity components on the surface of the coated samples, the CCD camera was placed 10 *mm* above the surface of the coated sample on the side of the impingement flow chamber, which was not blocked by the exit orifices. In order to avoid the disturbance caused by the flow inside the inlet pipe at the middle and top of the chamber, the center of the mirror is placed 10 *mm* to the left of the center. Therefore, the center of the PIV measurements experienced 10 *mm* of shift from the center of the chamber (see Figure 65). The PIV system installed in the lab is shown in Figure 66.

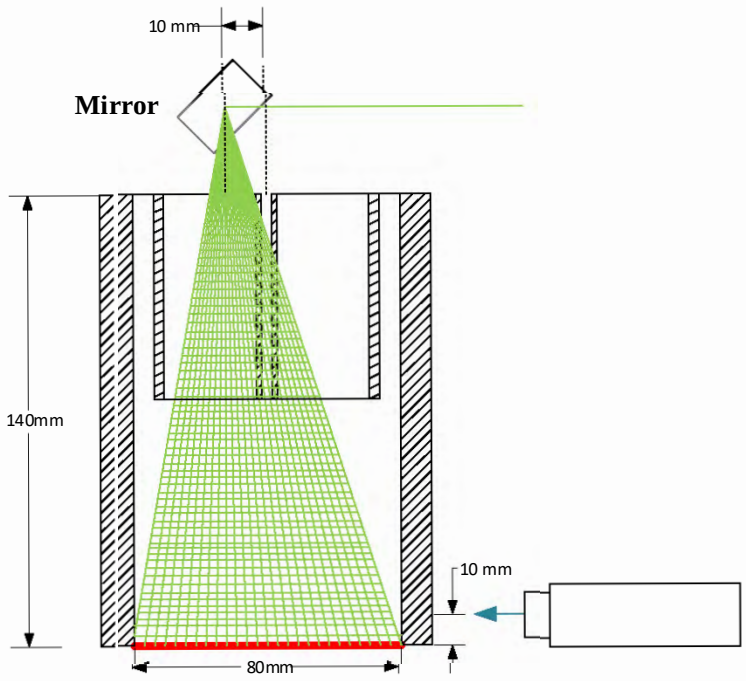

Figure 65. Locations of the CCD camera and the top mirror with respect to the geometry of the impingement flow chamber.

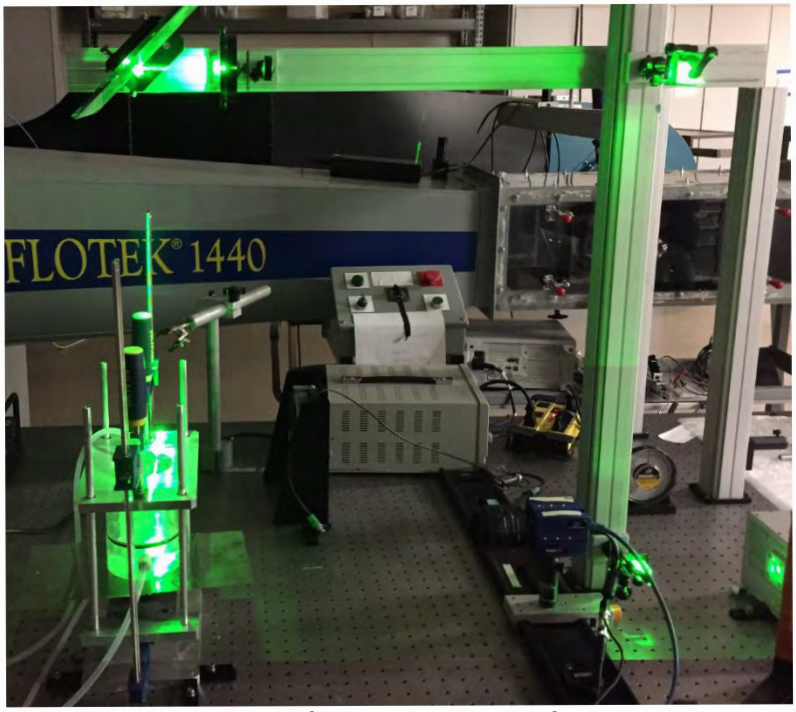

Figure 66. PIV measurement of the impingement flow inside a test chamber.

5.4. CFD and PIV results of the impingement flow chamber

The coatings surface under the jet was mainly subjected to normal stresses resulted from the impingement flow. Beyond the jet area, the shear stresses were dominant since the fluids mainly flowed parallel to the coatings' surfaces toward the exit orifices. Figure 67 shows the streamlines of the CFD simulation inside the impingement chamber for the particulate flow with a flow rate of Q = 18.93 cm^3s^{-1}. In order to compare the magnitude of applied stresses on the surface of the coatings, an imaginary diameter line was considered parallel to the exit orifices (see the yellow line in Figure 67). The magnitude of the velocities, shear, and normal stresses on the specified line were depicted in Figure 68,Figure 69, and Figure 70, respectively. As shown in Figure *68*, the velocities are zero at the center of the coating regardless of the type of the fluids and the inlet flow rates. This indicates that due to the initial assumption of the non-slip wall for the coating's surface, all the kinetic energy of the flows was converted into normal stresses at that point. The maximum velocities appeared at the border of the jet area due to the combination of reflected flows from the coating's surface and the formation of parallel flow to the coating. The velocities then decreased gradually further away from the jet area until it reached zero again at the edge of the chamber. The higher inlet flow rates resulted into higher velocity magnitudes The velocity magnitudes were slightly lower for the sand suspended flow compared to non-particulate flow. The shear stress distribution is plotted in Figure *69*. We observe the magnitude of shear stresses for particulate fluid were higher than non-particulate fluid for all three applied inlet flow rates. as the dynamic viscosity of the particulate fluid was higher than the non-particulate one ($\mu_m = 1.813 \times 10^{-3}\ Pa.s$, $\mu_{3.5\,\%\,NaCl} = 1.2712 \times 10^{-3}\ Pa.s$ at $T = 25°C$). As shown in Figure *70*, the magnitude of normal stresses increased proportionally to the increase of the inlet flow rates. Since the normal stress (σ) is theoretically proportional to the inlet

velocity squared, V^2 [135], by increasing the velocity the normal stress on the surface increases significantly. The magnitude of the normal stresses for sand particulate flows were slightly higher than the non-particulate flows. The differential behavior in velocity and stresses between sand suspended flow and non-particulate flow is resulted from their difference viscosity and density due to the existence of sand particles.

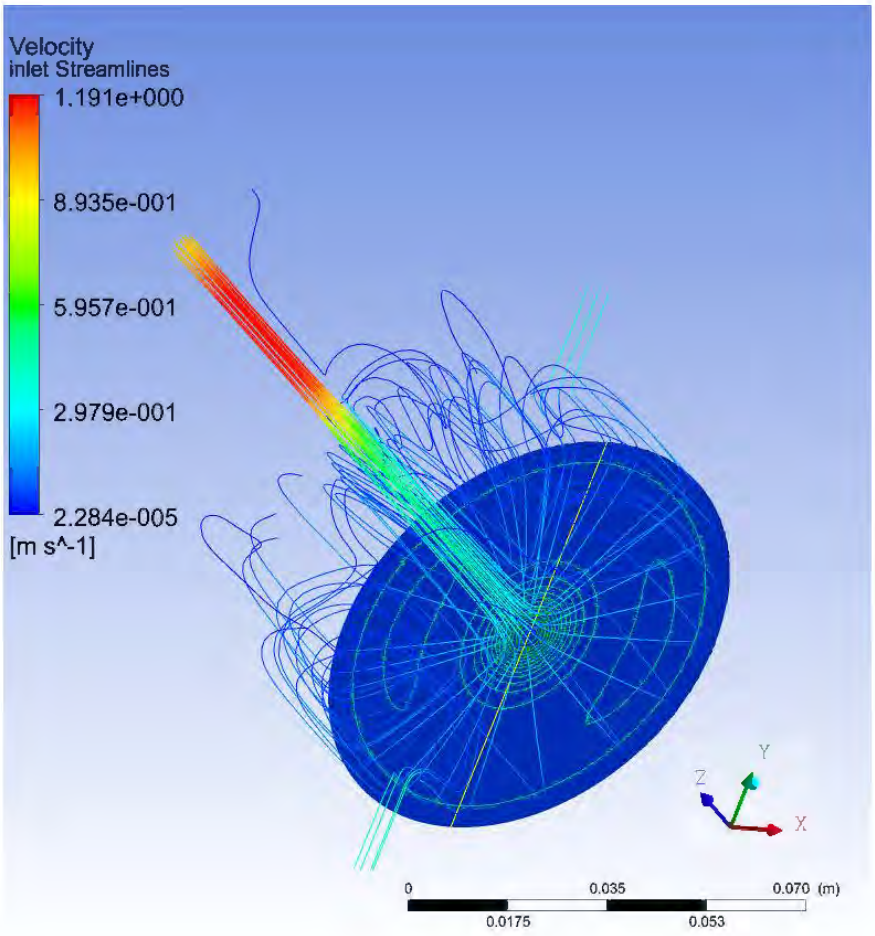

Figure 67. Streamlines of CFD simulation inside the impingement chamber for sand particulate fluid with the inlet flow rate of Q = 18.93 cm^3s^{-1}.

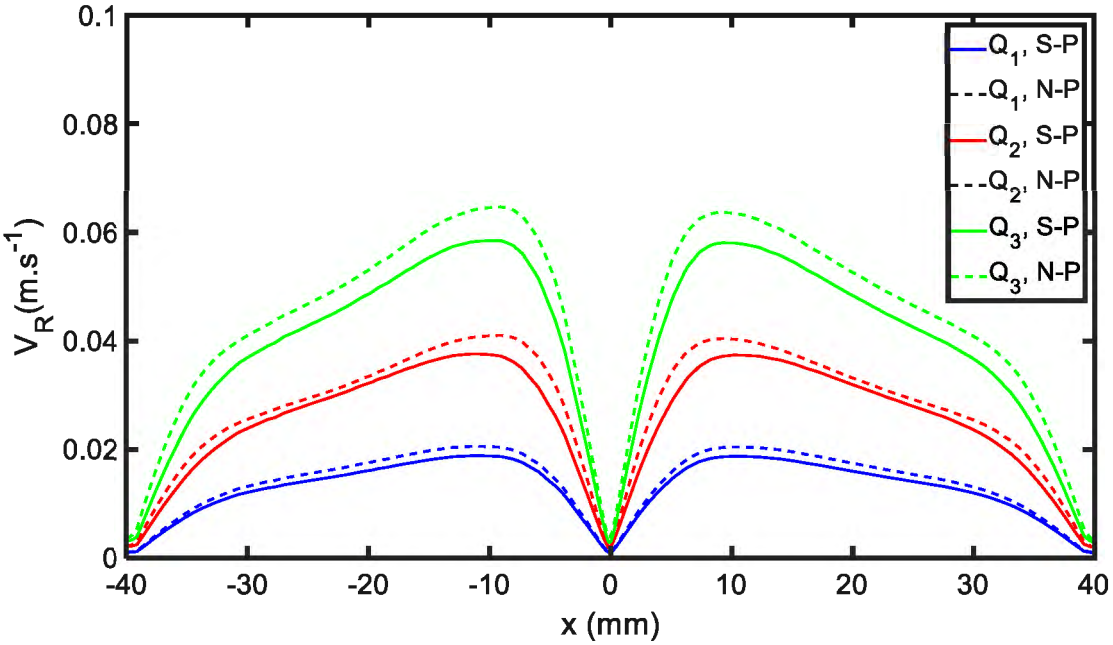

Figure 68. Magnitude of the velocity profile on the centerline of the coating samples with respect to the inlet flow rates of Q_1 = 6.31, Q_2=12.62, Q_3=18.93 cm^3s^{-1} for non-particulate (N-P) and 1 wt. % sand suspended (S-P) electrolyte solution.

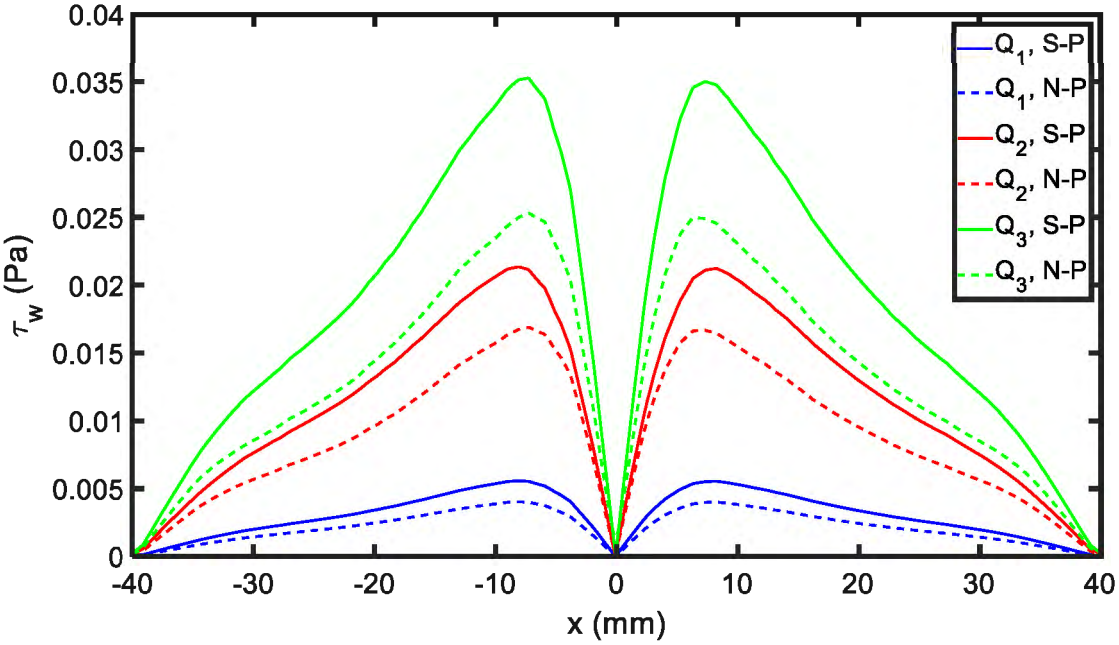

Figure 69. Magnitude of the shear stresses applied on the coating surface due to the inlet flow rates of Q_1 = 6.31, Q_2=12.62, Q_3=18.93 cm^3s^{-1} for non-particulate (N-P) and 1 wt. % sand suspended (S-P) electrolyte solution.

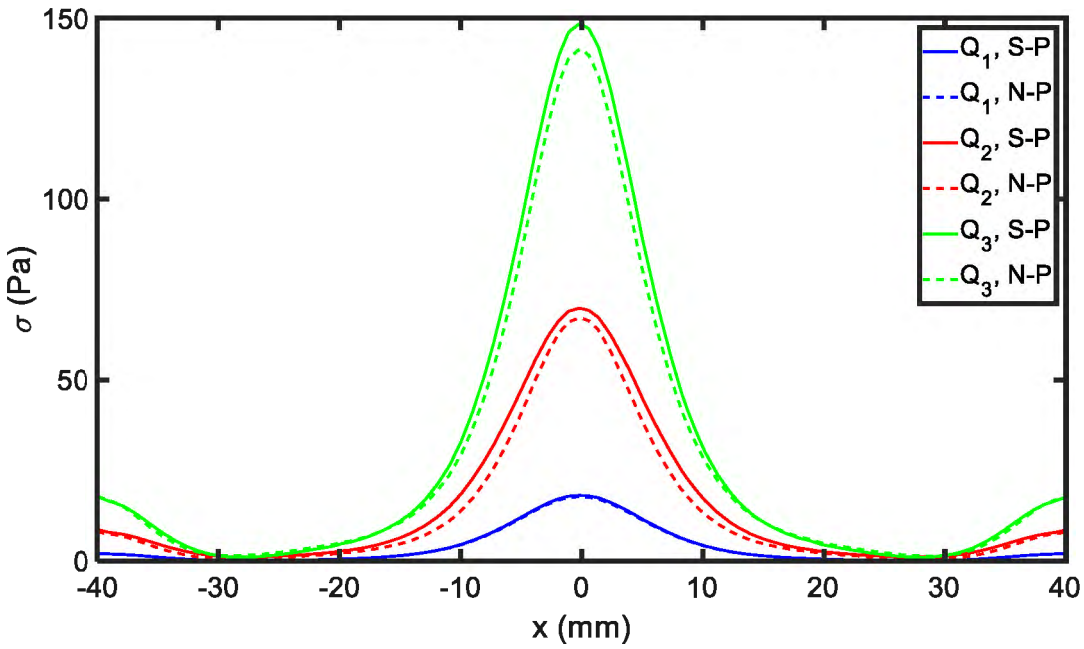

Figure 70. Magnitude of the normal stresses applied on the coating surface due to the inlet flow rates of Q_1 = 6.31, Q_2=12.62, Q_3=18.93 cm^3s^{-1} for non-particulate (N-P) and 1 wt. % sand suspended (S-P) electrolyte solution.

The CFD results were verified for the non-particulate fluid by the experimental particle image velocimetry technique (PIV). The velocity vectors measured by PIV method for the inlet velocity of $V = 0.3214$ cm/s ($Q = 6.31\ cm^3s^{-1}$) are shown in Figure 71 and Figure 72 for its *x*- and *y*-direction components respectively. The bottom line at $y = -10\ mm$ in both figures represent the location of the coating samples, while the CCD camera is lined up with $y = 0$. By comparing the velocity components, we observe that V_y values are dominant in the region within the jet column, while the *x* component velocities (V_x) are dominant near the surface of the coating sample out of the jet column. Moreover, the direction of the vectors near the walls shows how the reflected velocities form and mix with the incoming flow to create a turbulent flow inside the chamber.

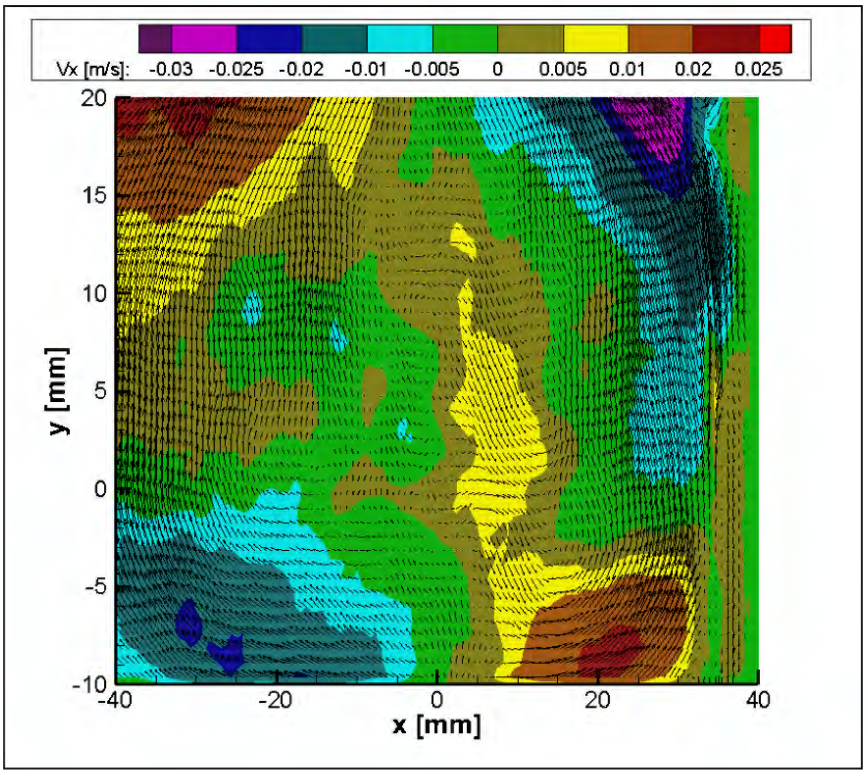

Figure 71. PIV results of the x component of the velocity vector inside the flow chamber for an inlet velocity of V=0.3214 m/s.

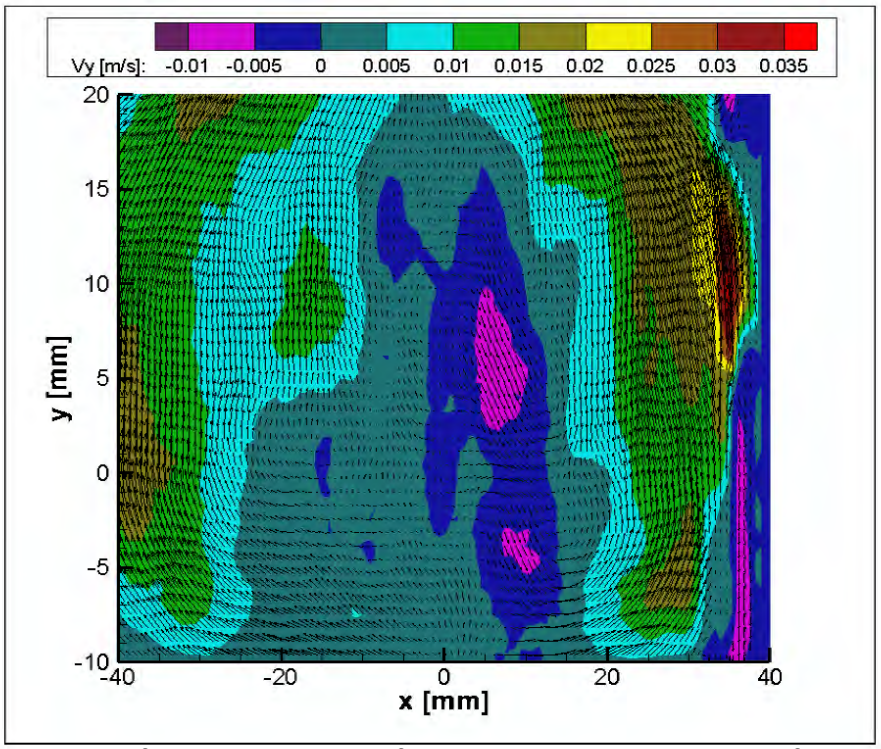

Figure 72. PIV results of the y component of the velocity vector inside the flow chamber for an inlet velocity of V=0.3214 m/s.

In PIV, the camera needs to detect motions of enough particles to report their velocities. However, at the coating surface due to the lack of enough data no velocity was recorded and reported. Since $y = -10\ mm$ is exactly where coating sample is located, no velocity data is available there. The velocity vectors in its vicinity were plotted instead and compared with CFD results. Moreover, theoretically, the coating surface is usually considered as a no-slip boundary; the velocity of fluid at the wall should be zero. The velocity magnitude (V_R) at three heights of ($y = -7.35\ mm, -8.18\ mm, -9.5\ mm$) for different flow rates are shown in Figure 73. The heights were chosen due to the higher number of available data measured by PIV. We could observe in Figure *73*, the obtained values of the velocity magnitudes on all three locations were very close. Moreover, the velocity magnitudes for the case with y=-9.5 mm were every close to the results obtained from CFD modeling (Figure 68). Based on the validation from PIV, the calculated normal and wall shear stresses by CFD modeling were employed to analyze the effect of flow induced stresses on the degradation of coatings.

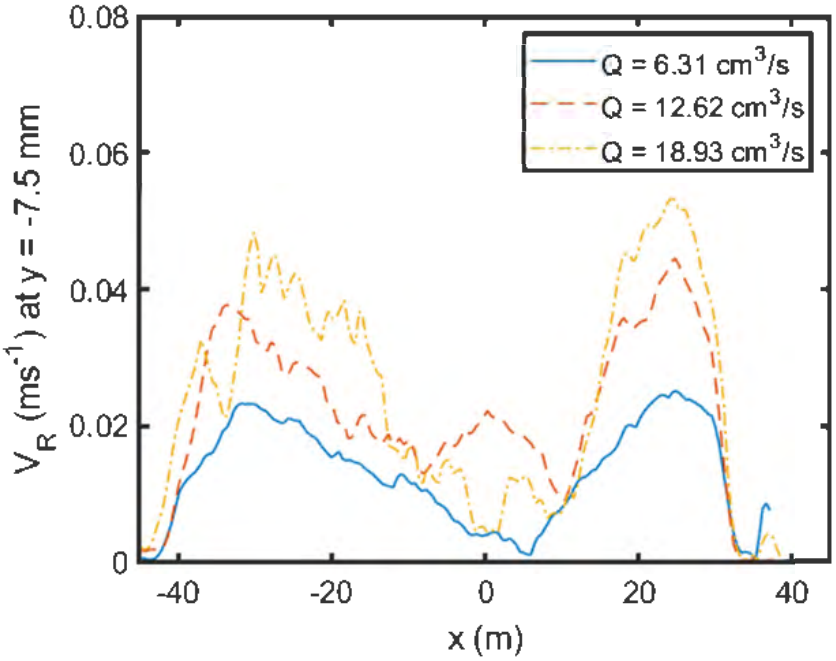

(a)

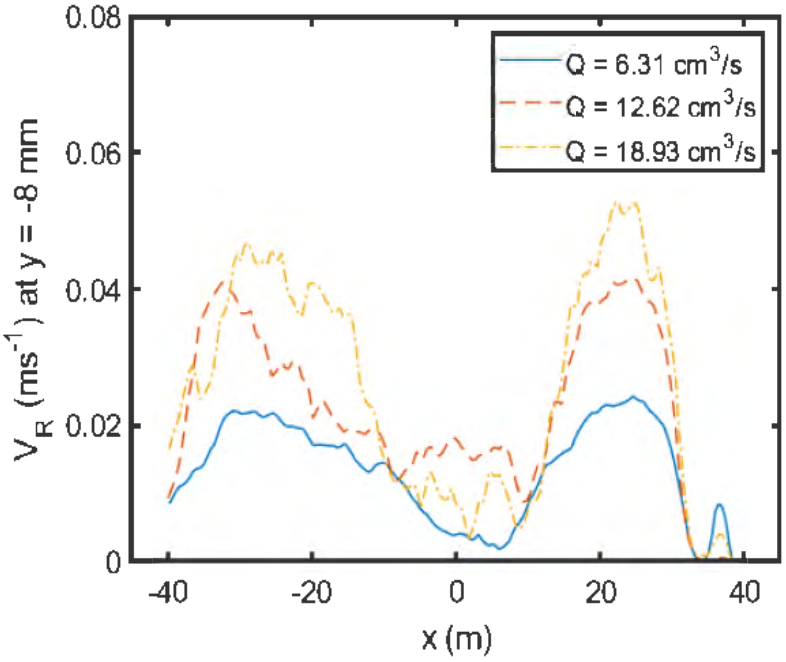

(b)

Figure 73. The magnitude of the velocity at three different heights in PIV measurement for different flow rates.

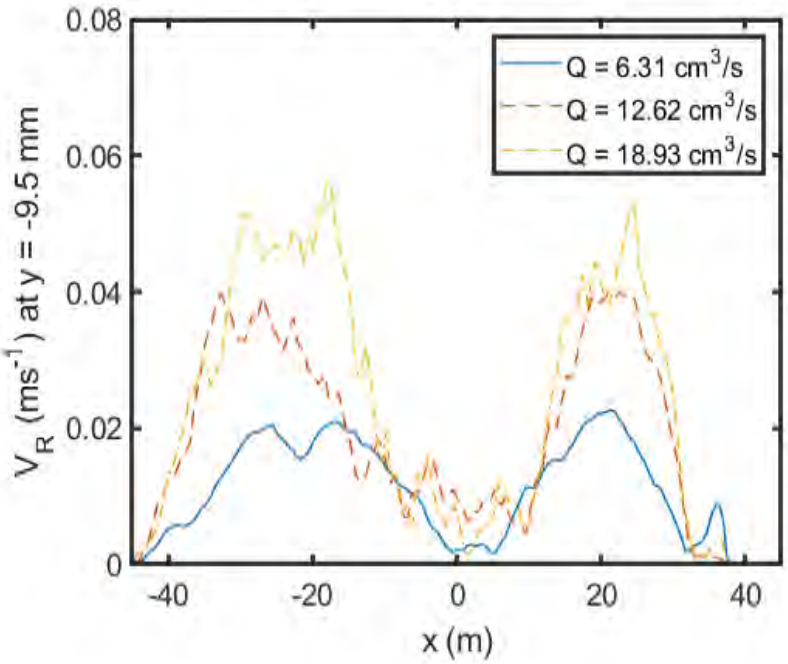

(c)

Figure 73. The magnitude of the velocity at three different heights in PIV measurement for different flow rates (continued).

For verification of the obtained stresses due to the sand particulate fluid, the following analytical procedure was committed:

Assuming a spherical geometry for the sand particles, the following equation represents the kinetic energy of each particle with the liquid flow [90]:

$$E_k = \frac{2}{3}\rho\pi r^3 V^2 \tag{5}$$

where E_k, ρ, R, and V are the kinetic energy, density, radius, and velocity of the particle, respectively. The mean mass of each sand particle was calculated as $m_{sand} = 10^{-4}\ g$, while the mean radius $r = 195\ \mu m$. The velocity of the particles are assumed to approximate the inlet velocity of the fluid, $V = 0.3214, 0.6427,$ and 0.9641 (ms^{-1}). The density of the sand particles was $\rho_{sand} = 2650\ kgm^{-3}$. The kinetic energy of each sand particle with respect to the inlet

velocities was calculated as $E_k = 0.00425, 0.017, \text{and } 0.0383\ \mu J$, respectively. Considering the concentration of sand particles in the fluid (1 wt. %), and the volume of the jet column ($\forall_{jet} = 1.47 \times 10^{-6}\ m^3$), the number of sand particles in the volume of the jet column could be estimated as *n = 151*. Therefore, the total kinetic energy of the sand particles in the jet column for each respective inlet velocity was $nE_k = 0.6418, 2.676, \text{and } 5.783\ \mu J$. Considering the distance between the inlet flow and the surface of the coating (L_{jet} *= 75 mm*), and the jet area on the coating ($A_{jet} = 1.963 \times 10^{-5}\ m^2$), the normal stresses owing to the impact of sand particles in the jet area were $\sigma = 0.44, 1.74, \text{and } 3.93\ Pa$ for each inlet flow velocity respectively. As shown in Figure *70*, the difference between the maximum normal stresses of the particulate and non-particulate fluids were calculated as $\Delta\sigma = \sigma_{particulate} - \sigma_{non-particulate} = 0.41, 2.79, \text{and } 6.7\ Pa$. Although the results from the CFD modeling show deviations from the analytical calculations, by considering all the assumptions for the analytical approach, the CFD results were considered reasonable. Moreover, the only difference between the CFD models of the two types of fluids were the working fluids' densities and dynamic viscosities. Since the CFD results of the non-particulate fluid has been validated by experimental PIV results, the CFD model can be considered reliable for calculating the stresses due to the particulate fluid.

5.5. PIV method of the wave tank

For the cyclic behavior of the waves, a PIV setup was deployed to capture the flow characteristics near the coating samples. The schematics of the PIV setup are shown in Figure *74*. Fundamentally, PIV captures two instances of flow, one after another, separated by a few microseconds, and cross-correlation can be used to determine the displacement of particle ensembles in the flow. Velocity can be determined once displacement and time separation are known for each particle ensemble. It is intended to capture the velocity distribution very close to

the coating sample to obtain the stresses. The coating sample was placed on two sides of the wave tank. As two coating samples were placed at an equal distance from the centerline, the flow characteristics can be assumed to be symmetrical on the two coating samples. Therefore, the PIV experiment was conducted on one sample. A 2D schematic of the setup with detailed dimensions is shown in Figure 42 and Figure 44.

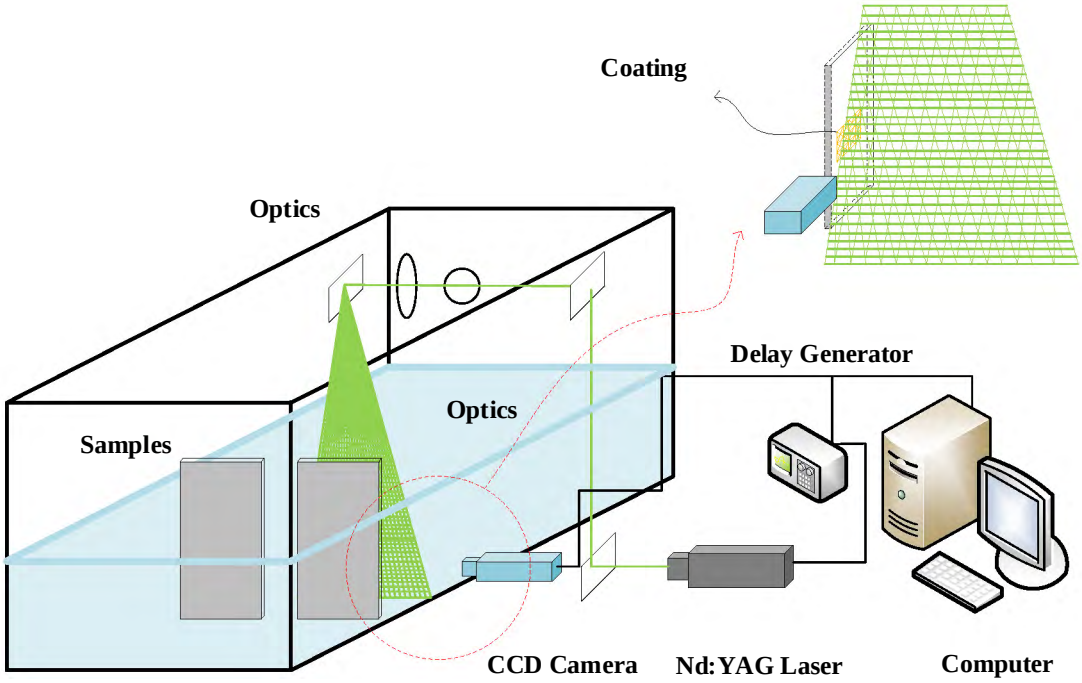

Figure 74. The schematic of PIV set-up on the wave tank.

The center of the one coating sample in the wave tank was illuminated by a double-pulsed Nd:YAG laser emitting two laser pulses of *100 mJ* at a wavelength of *532 nm* with a repetition rate of *15 Hz*. The laser beam can then be shaped to a laser sheet (thickness *<1 mm*) using a set of mirrors and spherical and cylindrical lenses. The water was mixed with Polyamide particles to achieve characteristics diameter of particles approximately equal to *20μm*. It is

visualized by LaVision IMAGER LX 2M cameras with a resolution of *1608×1208* and interframe capability of 200 ns set up with their axis perpendicular to the laser sheet for image acquisition. For the desired flow speed, the time between images taken was set to $\Delta t = 500\ \mu s$. The cameras and the Nd:YAG lasers were connected to a workstation and controlled with a PTU timing unit to control the timing of the laser illumination and the image acquisition. LaVision DaVis 10 software was used to control the imaging parameters and controlled by an external trigger. Note that the LASER was illuminated on top of the coating sample, and the camera was placed in such a way so that the particle displacement can be quantified near the coating sample (see Figure *75*). After capturing two instances, the processing was done from *96×96* to 48×48 pixel cross-correlation. After process total *1000* instantaneous velocity, the average stresses were calculated for each second of measurement which contained 15 frames for each reported stress.

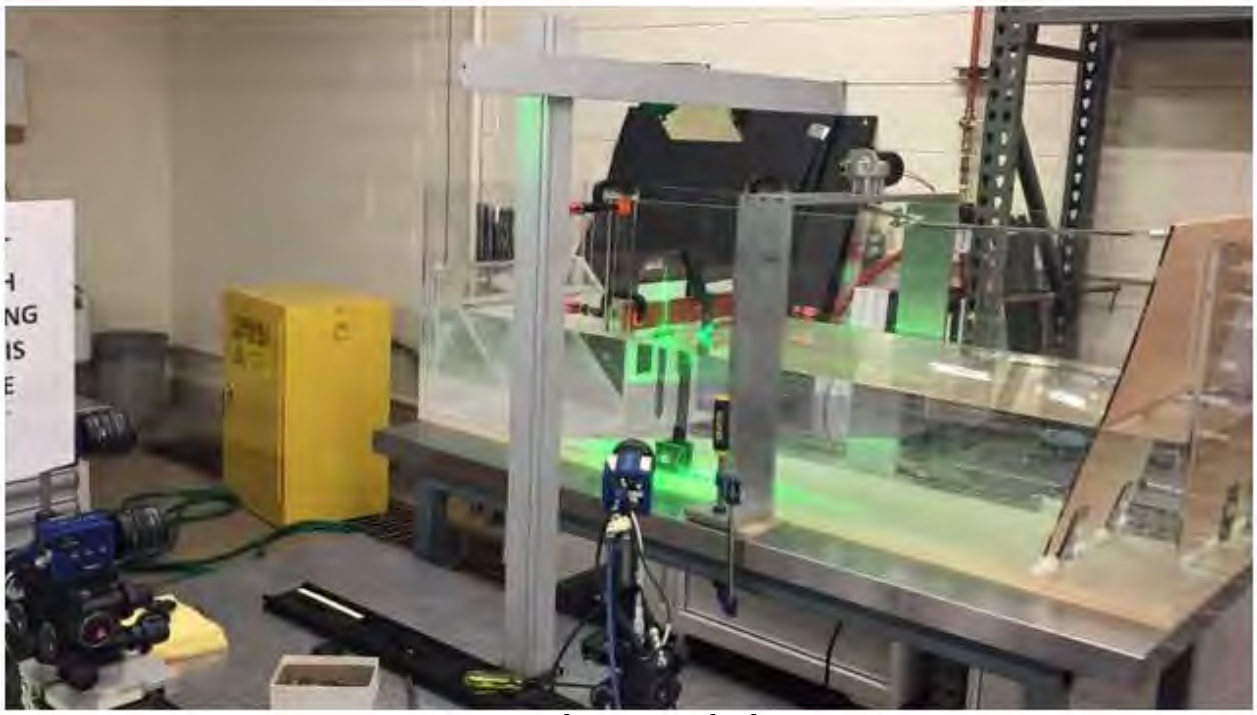

Figure 75. The PIV method set-up.

5.6. PIV results and wave parameters

The celerity of waves (*U*, speed of wave at the crest) was measured with PIV method in the area next to the tip of the paddle at $\alpha = 19°$ for each applied rotational speed of the motor. By assuming that the wave period (*T*) was equal to the time that the paddle completed two strokes, the wave period for each test was also measured. Then from $U = \frac{L}{T}$, the wave length (*L*) was calculated. Finally, from (*3* and (*4*, the wave height (*H*) and wave number (*k*) were calculated. The summary of the wave parameters is shown in Table *3*.

Table 3. The wave parameters in the wave tank with respect to the applied rotational motor speed.

Motor Speed (rpm)	T (s)	S (m)	U (m/s)	L (m)	k	H (m)
20	13.2	0.1764	0.05	0.165	9.52	0.0136
40	6.4	0.1764	0.1	0.165	9.82	0.0139
60	3.4	0.1764	0.15	0.128	12.32	0.0157

The magnitude of velocities with respect to the 2D velocity vectors, one in the direction of the wave, and the other vector in the direction of the water depth, were calculated. The velocity vectors were measured at 1 cm away from the surface of the coatings. By considering the centerline of the coating as *y = 0*, the velocity data were captured from *y = -35 mm* to *y = +35 mm*, covering the *70 mm* height of the exposed coating area. Since each PIV test was conducted for 60 s, the magnitude of velocities with respect to the time, and the location with respect to the height of coatings in depth was depicted. Figure 76, Figure 77, Figure 78 show the velocity magnitudes with respect to the applied rotational speed of the motor. The higher motor speed resulted into higher velocity magnitudes on the surface of the coatings. Moreover, the

maximum velocities were found above the coatings and close to the free surface of water all three cases.

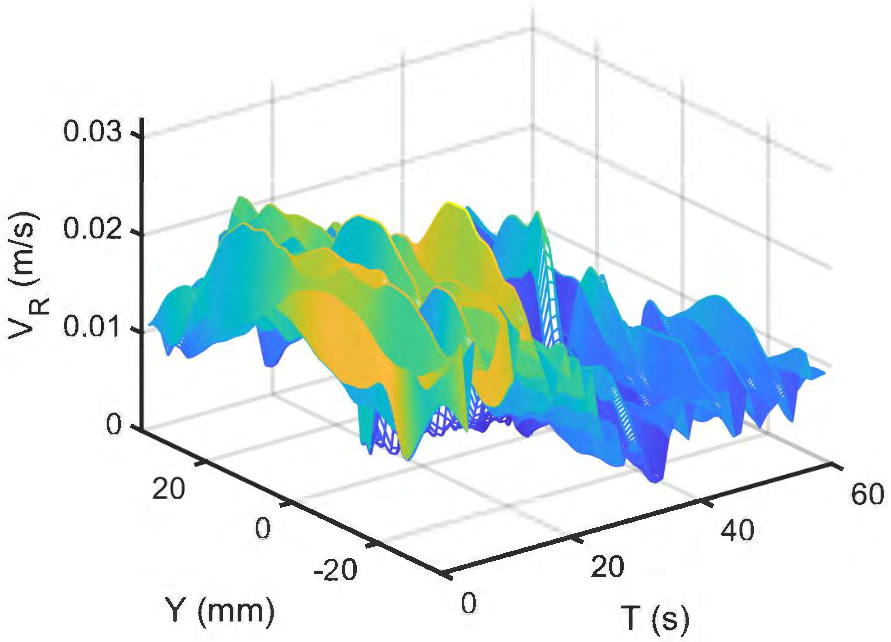

Figure 76. Velocity magnitude near (i.e. 1 cm from) the surface of the coating for 60 s in waves generated with a motor speed of 20 rpm.

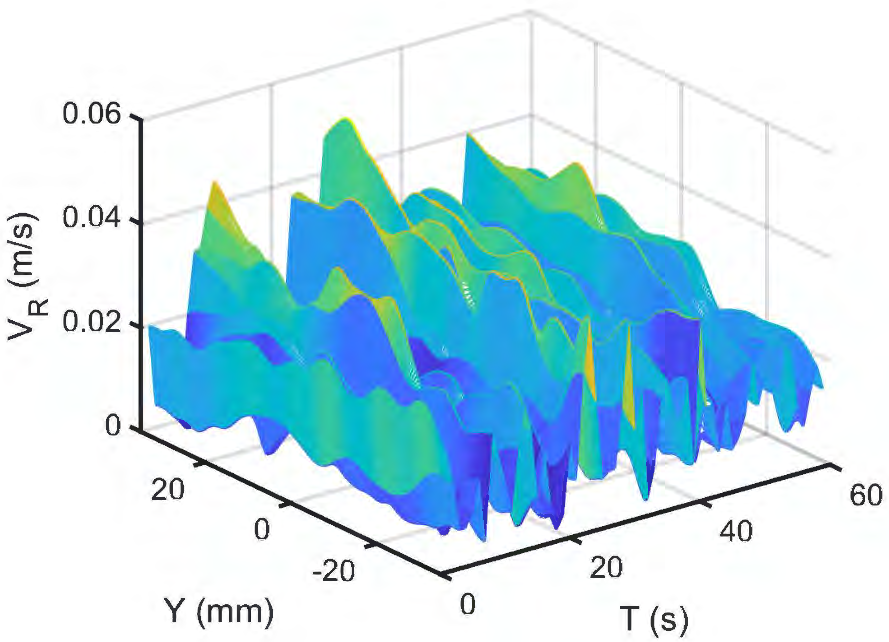

Figure 77. Velocity magnitude near (i.e. 1 cm from) the surface of the coating for 60 s in waves with motor speed of 40 rpm.

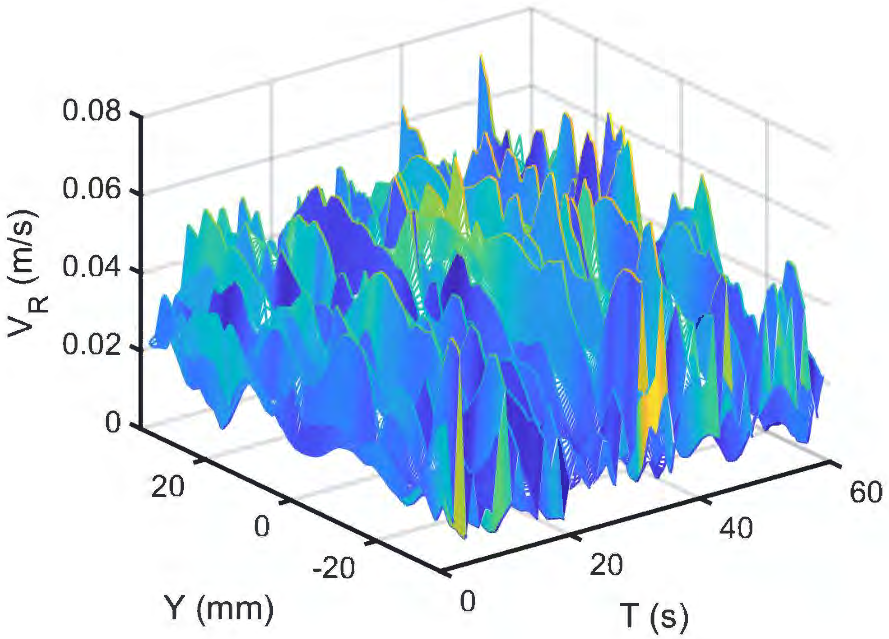

Figure 78. Velocity magnitude near (i.e. 1 cm from) the surface of the coating for 60 s in waves with motor speed of 60 rpm.

The average velocity contours and vectors measured by PIV method for the duration of 60 seconds with different motor rotational speeds of 20, 40 and 60 rpm are shown in Figure 79, Figure 80, and Figure 81, respectively. The location of the coating sample is also shown in the graphs. As expected, the higher motor rotational speeds resulted into higher velocities near the surface of the coating. The standard deviations of the calculated average velocity magnitudes are shown in Figure 82, Figure 83, and Figure 84 for the three speeds. By comparing the average velocity magnitudes and their respective standard deviations, we observe that by increasing the motor speed the turbulence of the fluid flow increased and the variation of measured velocities at every location increased significantly as we increase the motor speed.

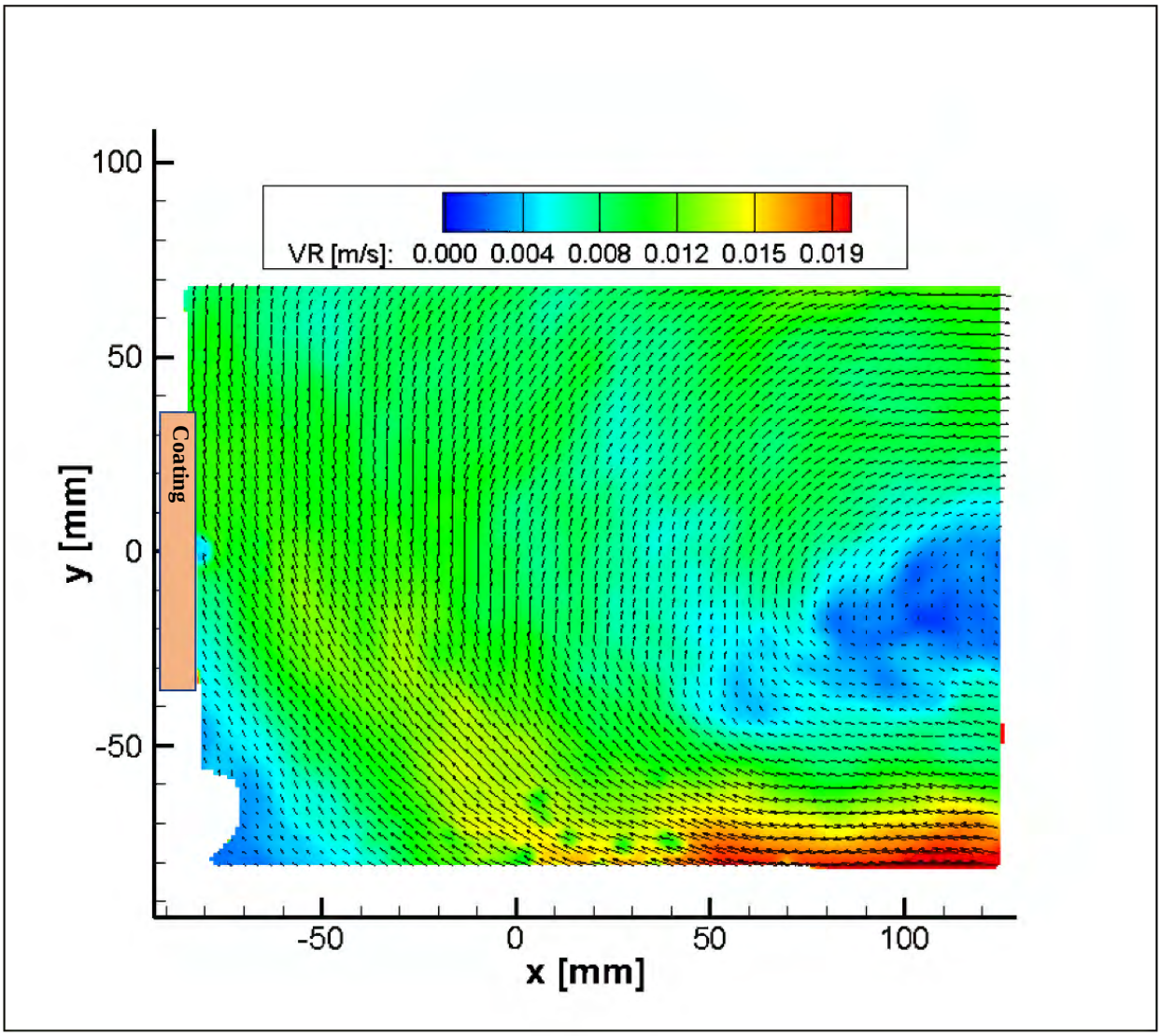

Figure 79. The magnitude and direction of the average flow velocity over a duration of 60 seconds for a motor speed of 20 rpm.

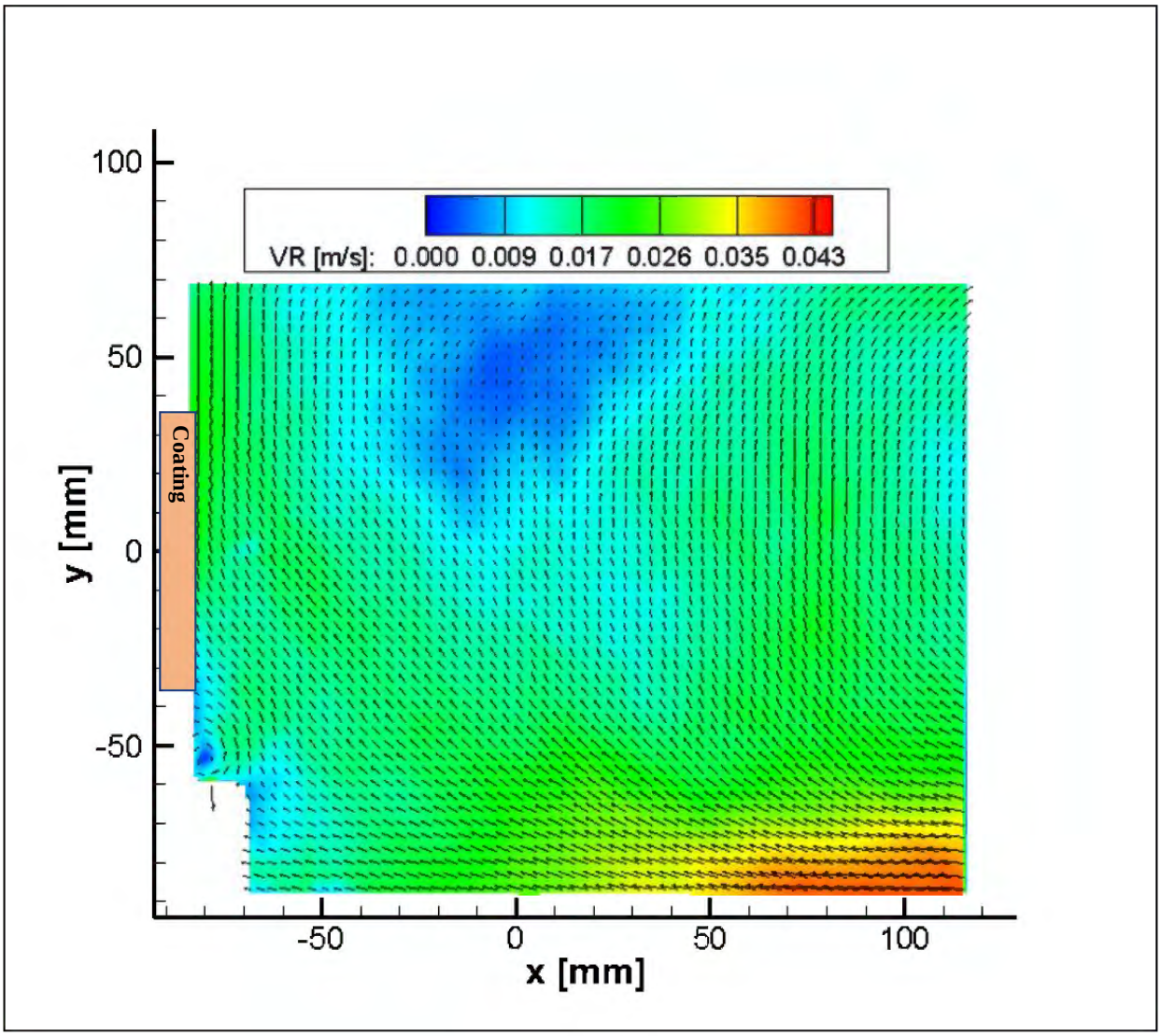

Figure 80. The magnitude and direction of the average flow velocity over a duration of 60 seconds for a motor speed of 40 rpm.

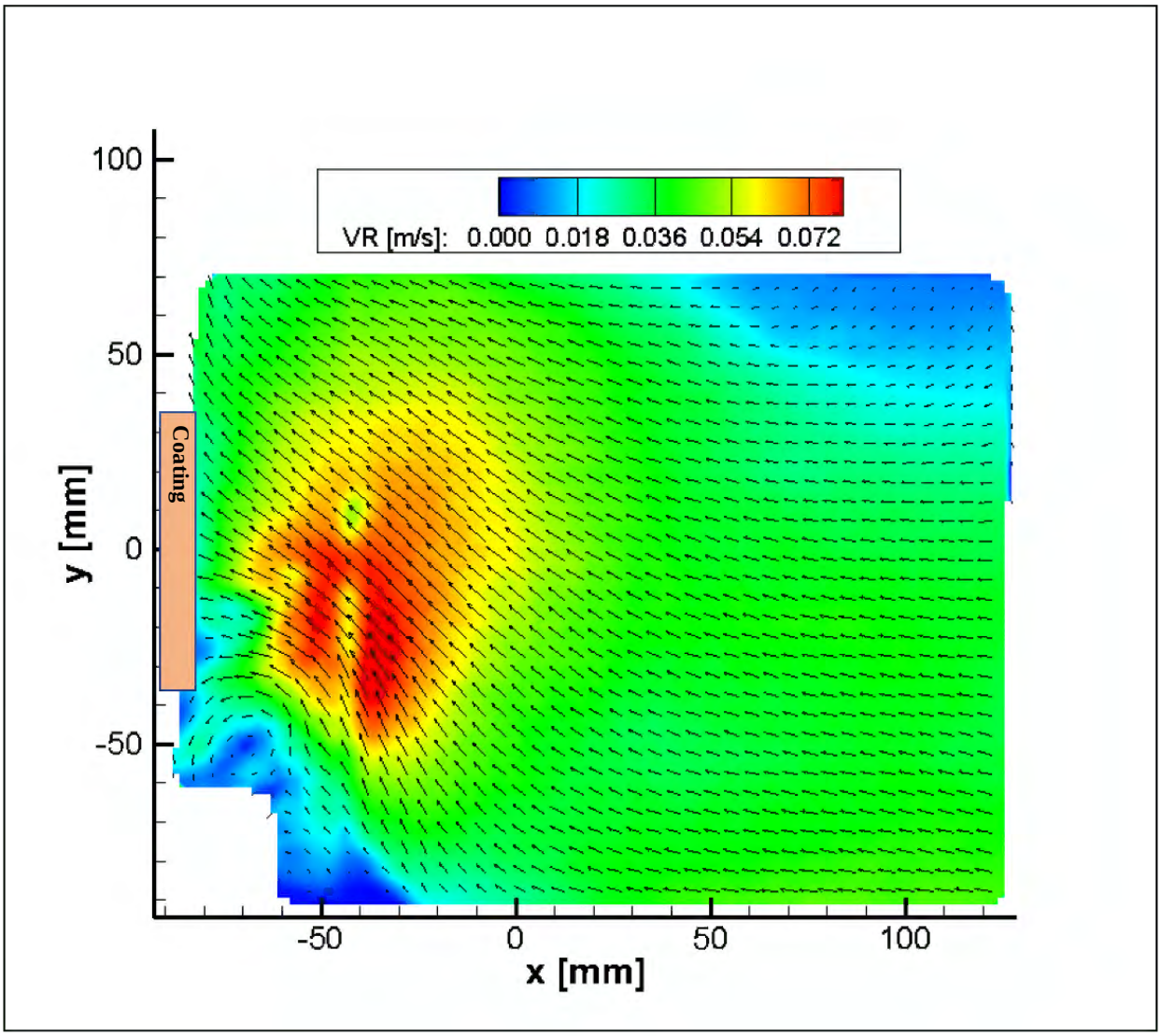

Figure 81 The magnitude and direction of the average flow velocity over a duration of 60 seconds for a motor speed of 60 rpm.

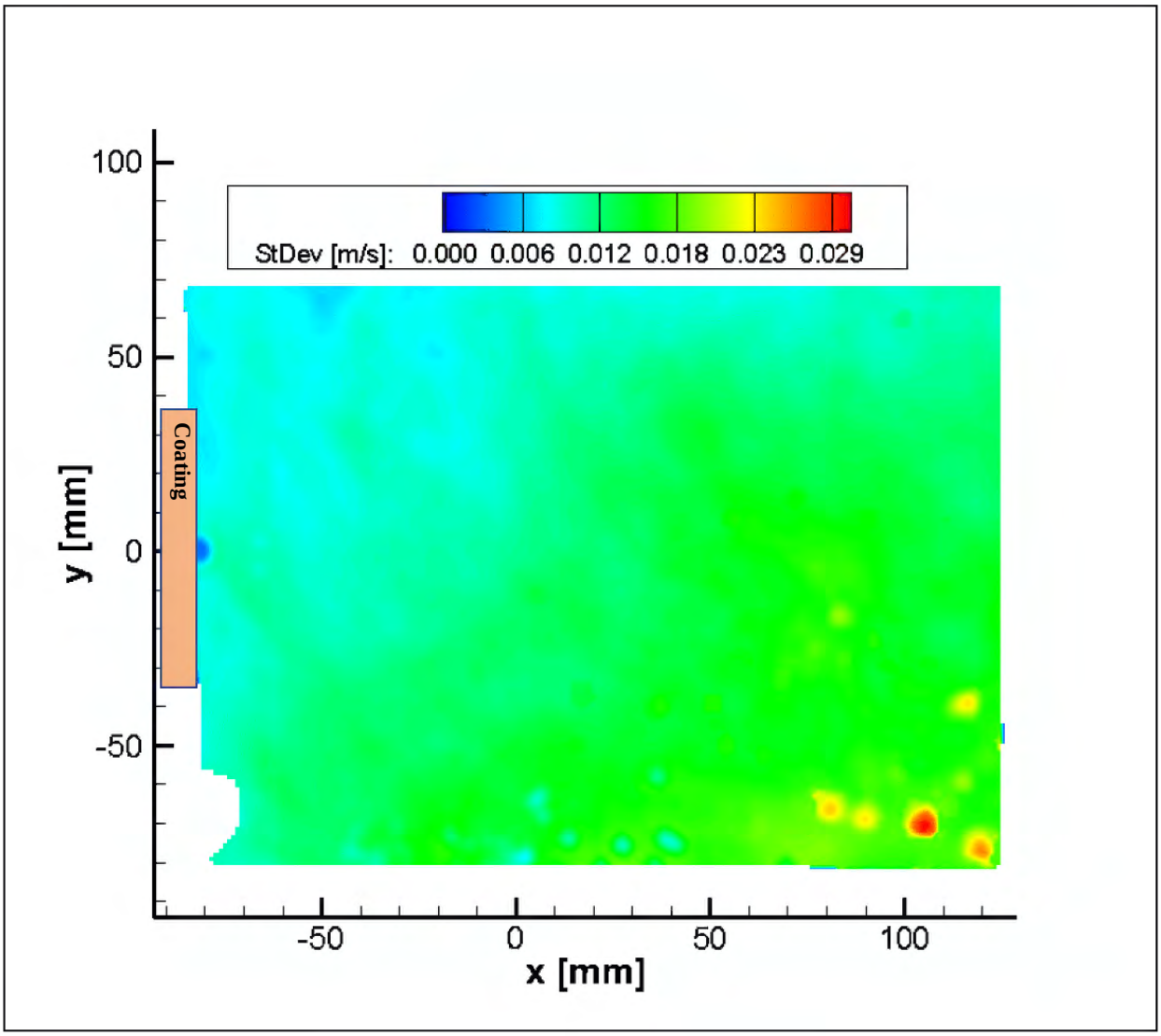

Figure 82. The standard deviation of the velocity magnitude over a duration of 60 seconds for a motor speed of 20 rpm.

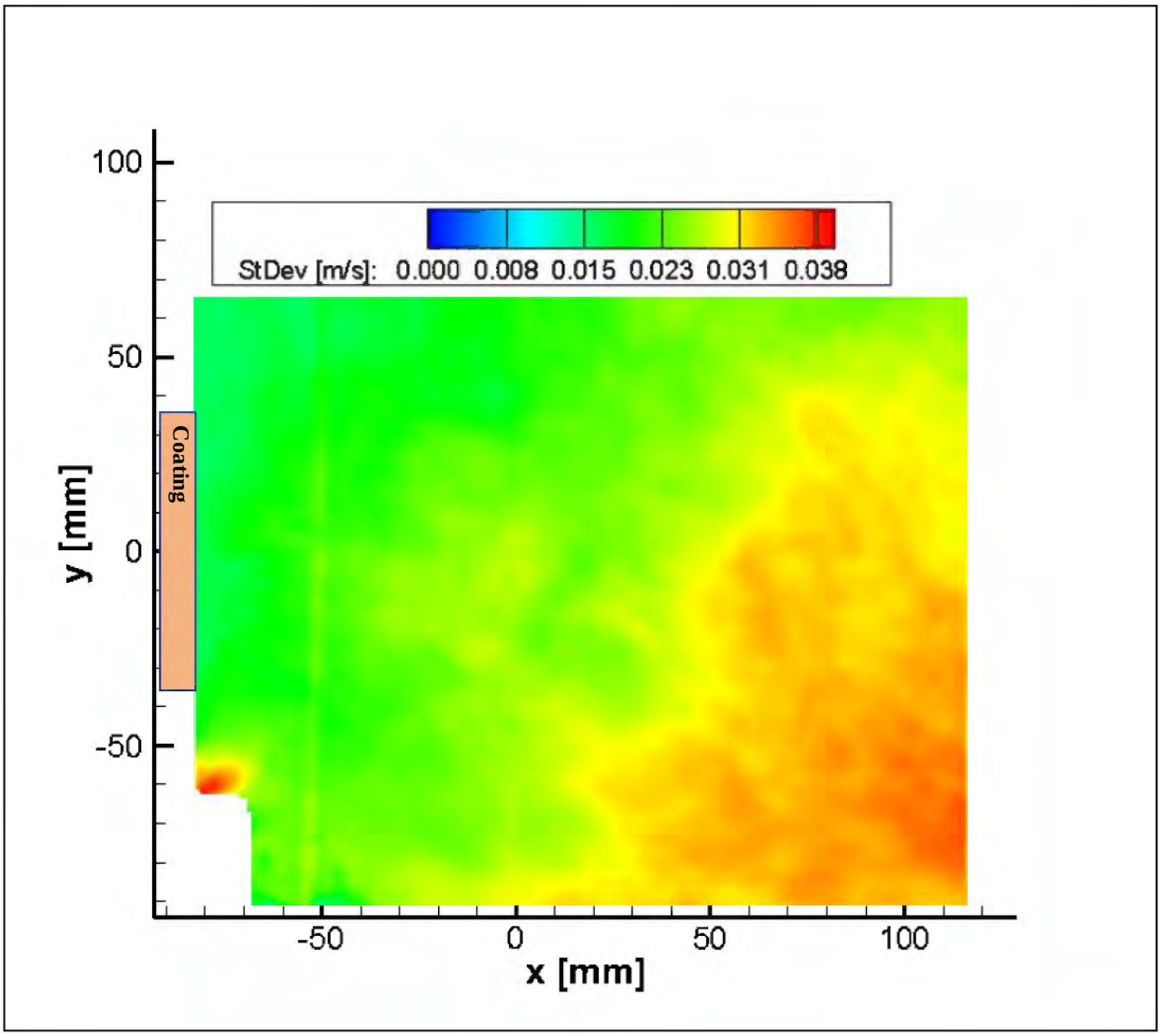

Figure 83. The standard deviation of the velocity magnitude over a duration of 60 seconds for a motor speed of 40 rpm.

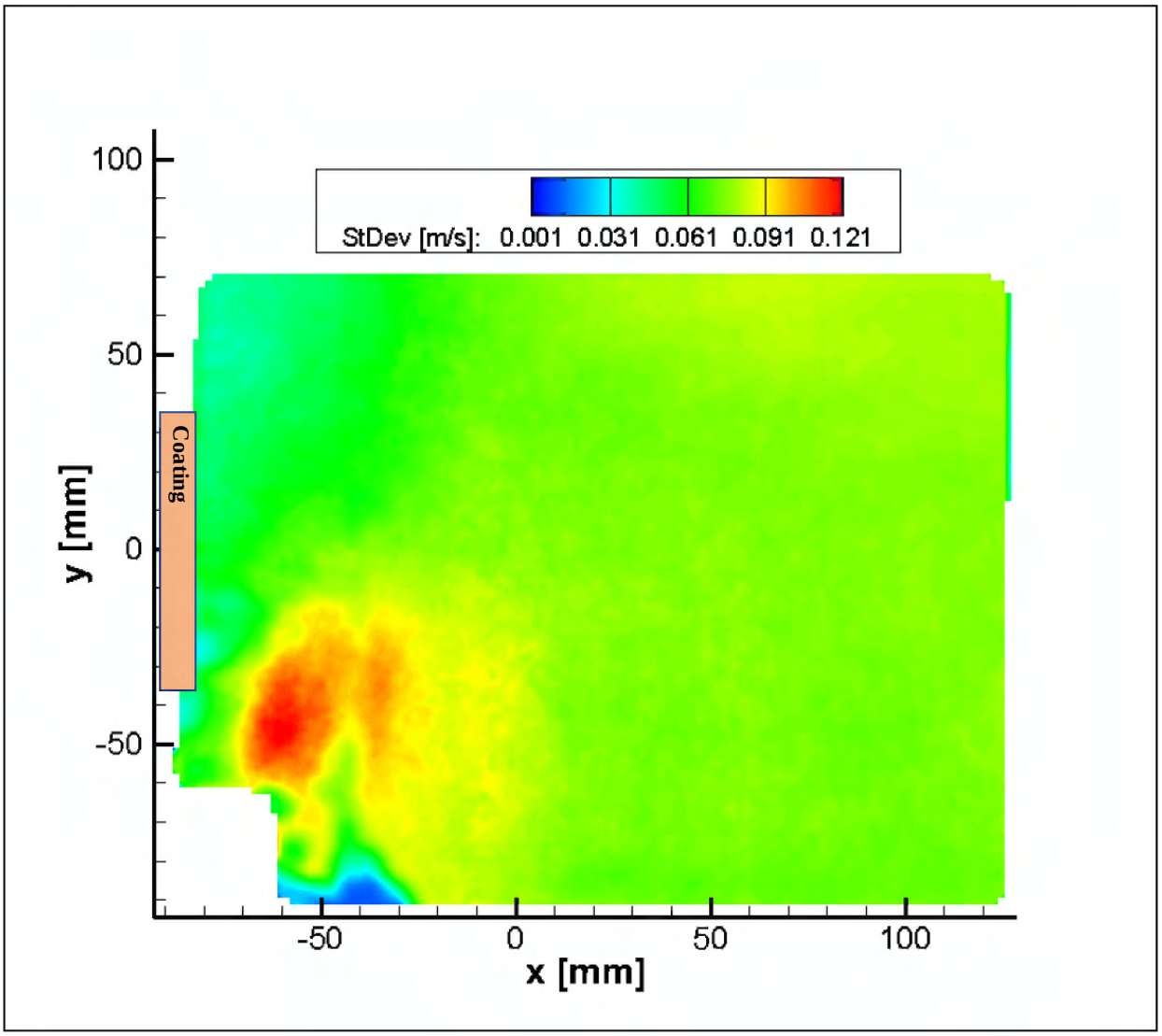

Figure 84. The standard deviation of the velocity magnitude over a duration of 60 seconds for a motor speed of 60 rpm.

To calculate the shear stresses due to the fluid flow on the coatings, the velocity components in y direction (V_y) were considered. The contours and vectors of the average velocity components in y direction are shown in Figure 85, Figure 86, and Figure 87 for three different motor speeds. The average velocity components in y direction at the surface of the coating ($-35\ mm \leq y \leq 35\ mm$) were considered to calculate the shear stress from the following:

$$\tau = \mu \frac{dV_y}{dx} \tag{6}$$

where μ is the dynamic viscosity of the fluid $\mu_{3.5\ w.t.\%\ NaCl} = 1.2712 \times 10^{-3}\ Pa.s$, and dx considered as 1 *mm* since the velocity components in y direction were extracted 1 *mm* far from the surface of the coatings.

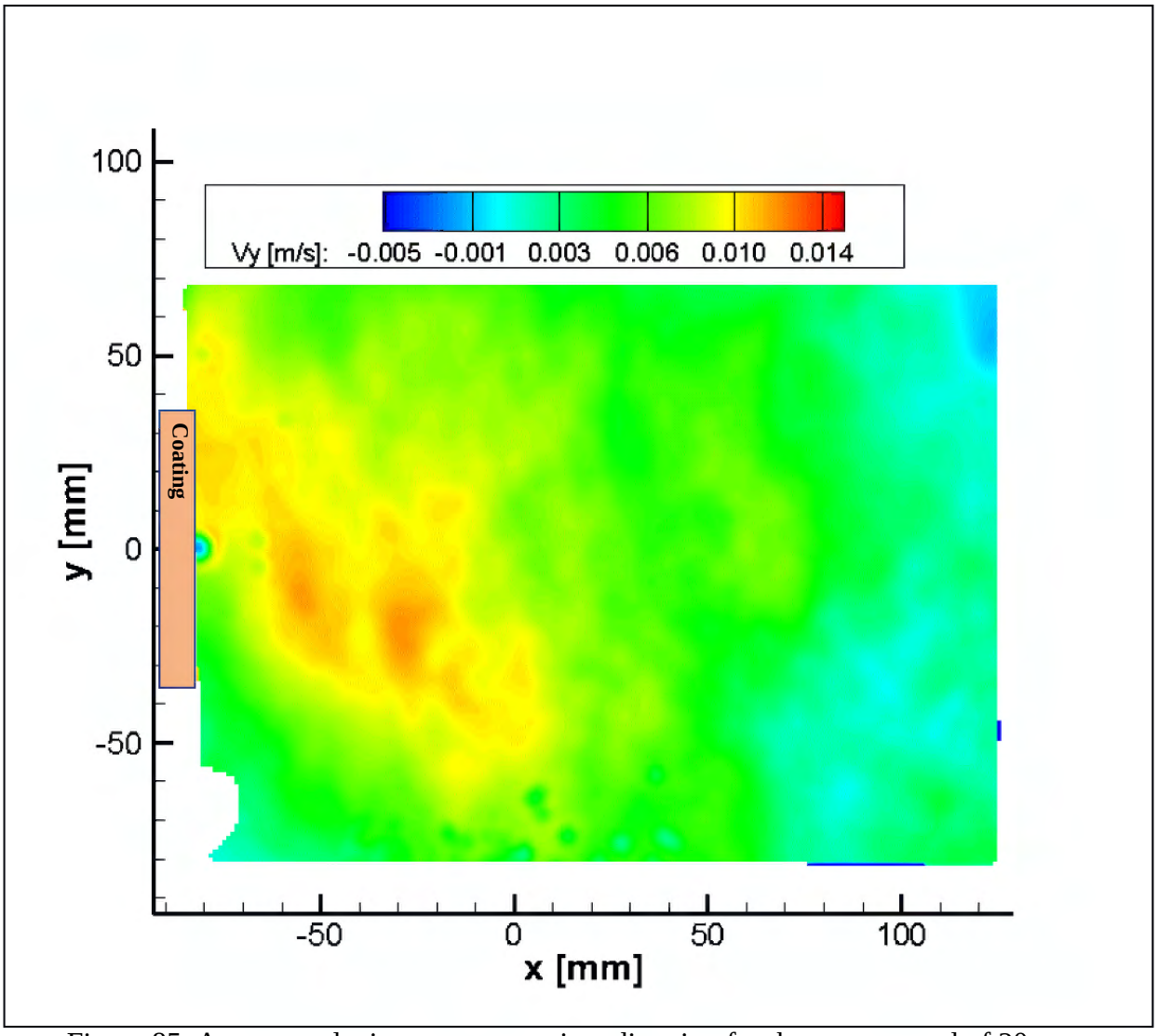

Figure 85. Average velocity components in y direction for the motor speed of 20 rpm.

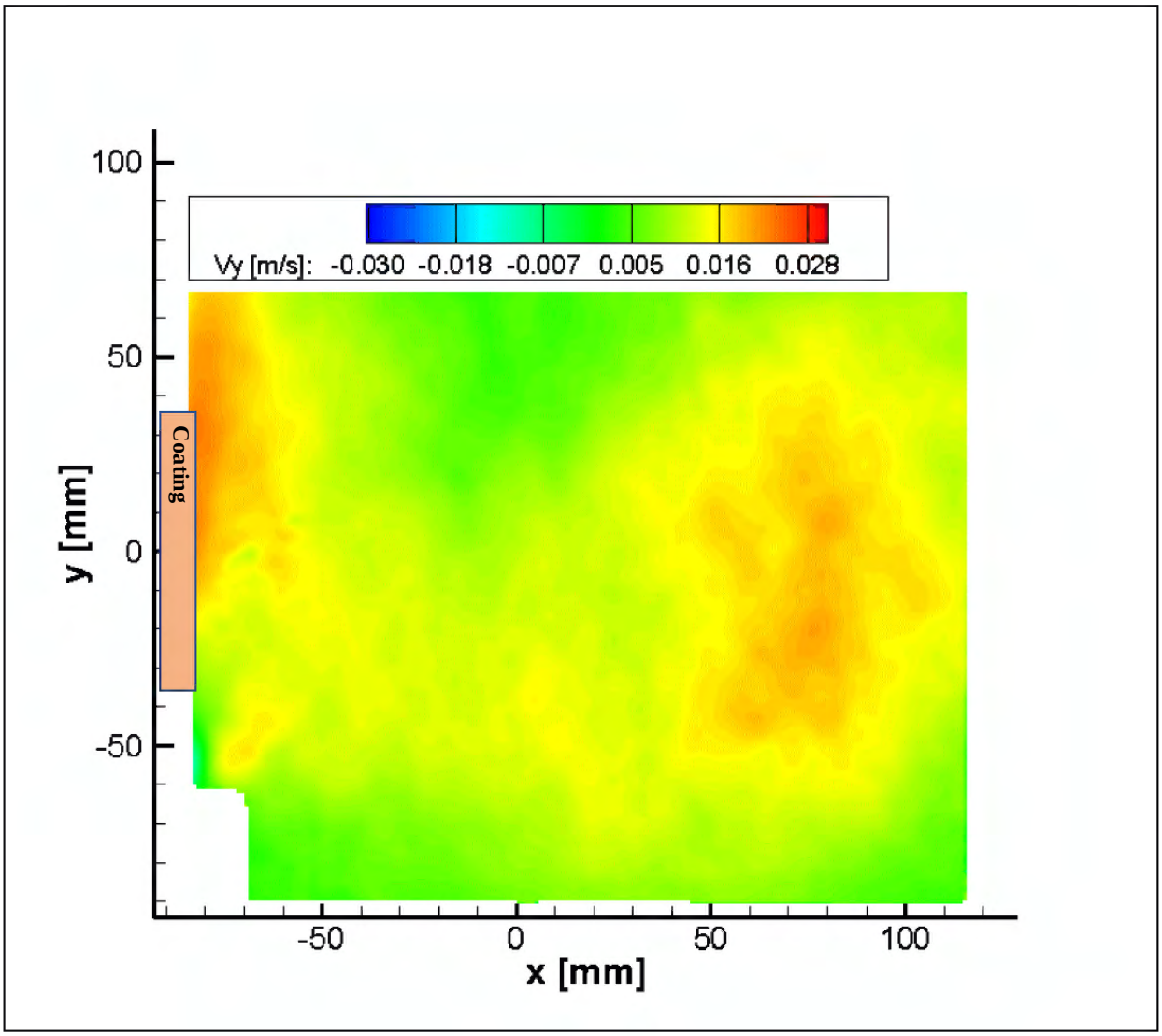

Figure 86. Average velocity components in y direction for the motor speed of 40 rpm.

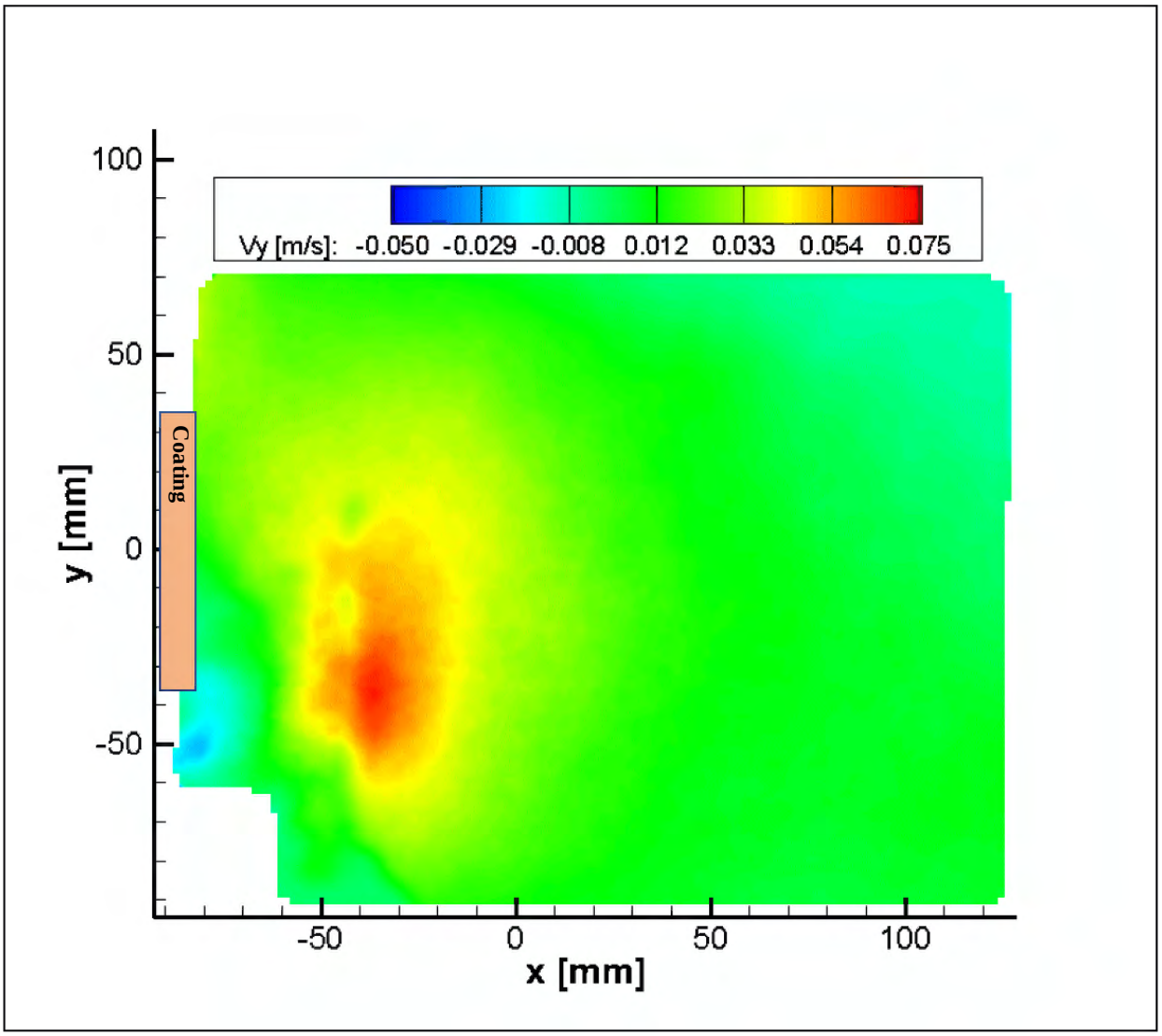

Figure 87. Average velocity components in y direction for the motor speed of 60 rpm.

The calculated shear stresses of the fluid flow on the coatings for the three different motor speeds are shown in Figure 88. In Figure 88, since the flow is turbulent, we do not observe any consistent trend for shear stresses across the coating surfaces. However, the higher applied motor speeds resulted in higher average shear stresses on the surface of the coating.

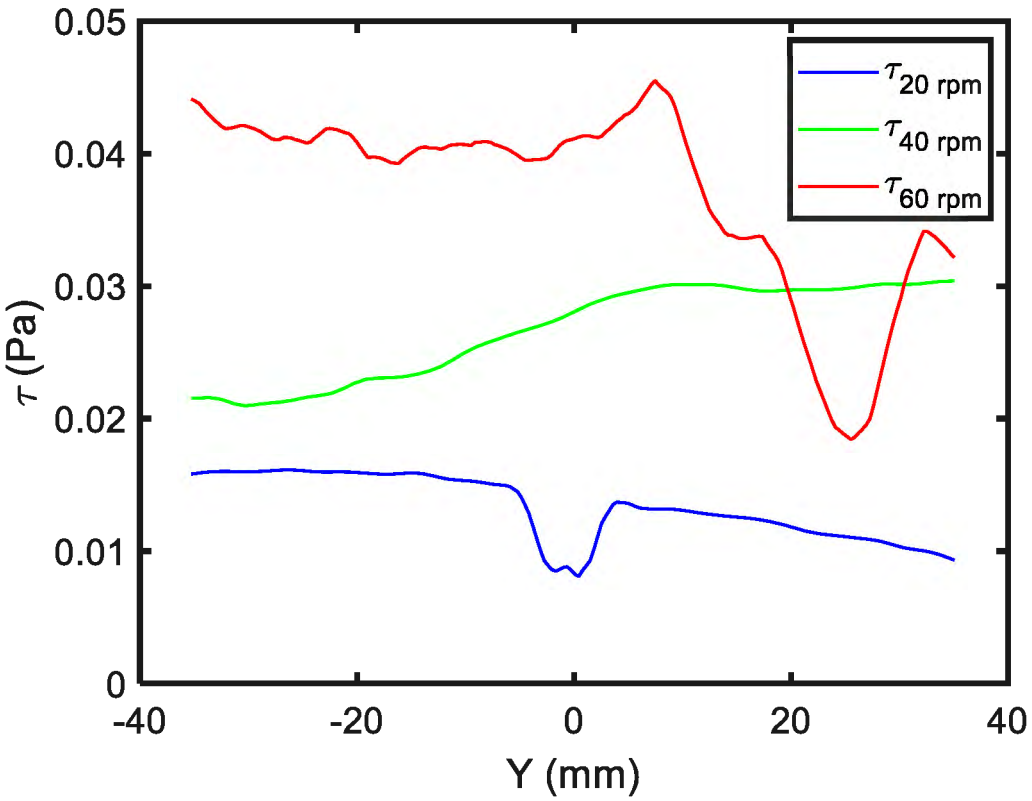

Figure 88. The average shear stresses on the surface of the coatings due to the cyclic loads for three different motor speeds.

The average total stresses on the surface of coatings for the period of 60 seconds are shown in Figure 89. The average total stresses were calculated as the resultant of the average shear stresses and the flow pressure ($\frac{1}{2}\rho V_R^2$) at every point on the coating for the 60 seconds. As shown in Figure 89, the waves showed more tumultuous behavior for the highest applied rotation speed of the motor. The results also show that by doubling the rotational speed of the motor from 20 to 40 rpm, the average stresses increased almost 2 times on the surface of the coatings, while the stresses were 3 times higher for the motor speed of 60 rpm compared with 40 rpm.

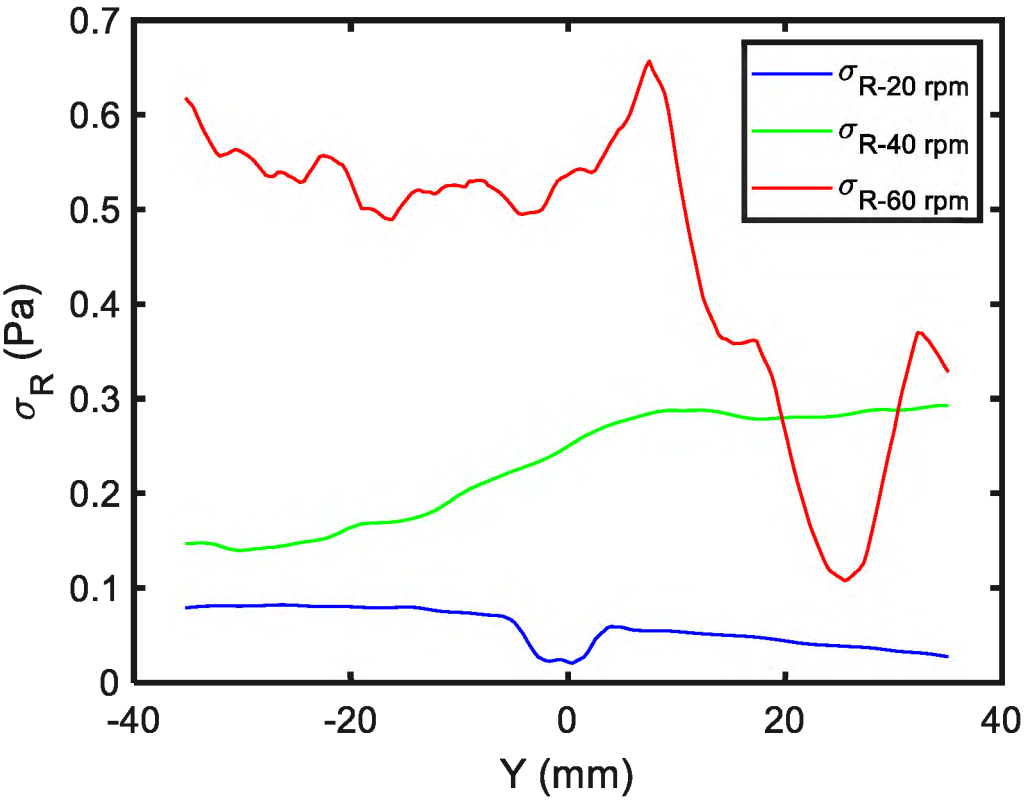

Figure 89. The average total stresses of the cyclic waves on the surface of the coating in the period of 60 s and for the motor rotational speed of 20, 40, and 60 rpm.

6. INFLUENCE OF APPLIED STRESSES ON THE THERMOCHEMICAL PARAMETERS OF THE CORROSION OF COATINGS

6.1. Introduction

After analyzing the EIS results and the applied stresses, a bridge is needed to show the relationship between the stresses and EIS results. To investigate the influence of stresses on physical-chemical properties of coatings, the combination of Eyring theory, the theory of thermal-activated processes, and the thermodynamics of electrochemical reactions were utilized in recent works [136]–[140]. Fredj et al. [136], [137] investigated the influence of stresses caused by loading-unloading-recovery tests on two marine epoxy coatings. Shen et al. [138], [139] suggested a coupled mechanical-oxidation modeling based on chemo-mechanical coupled model with focus on the effect of stresses on diffusion of oxygen in thermal barrier coatings (TBCs). Xu et al. [140] derived new equations based on microscopic thermodynamics, with focus on Gibbs and Helmholtz free energy and entropy imbalances to address the influence of thermal stresses on the chemo-mechanical properties of thermal barrier ceramic coatings.

In this study, we derived some equations based on the theory of thermo-activated processes, thermodynamics, and the thermoelasticity equations to characterize the behavior of organic coatings exposed to impingement flow. The equations relate the exerted stresses on coating samples with activation volume (V_a) and the apparent diffusion coefficient (D) of water in epoxy coatings. Parameters revealing coating properties, such as dielectric constant of the coating (ε_c), volume fraction (ϕ), amount of fluid uptake (M_t), and coatings capacitance (C_c), were obtained and related to the influence of impingement flow and the flow rate.

6.2. Influence of applied stresses on the electrochemical reactions and activation volume of the coatings

The dielectric constant (ε) is a measure of the amount of electric potential energy, in the form of induced polarization that is stored in a given volume of material under the action of an electric field [141]. The change of the relative electric polarizability of a coating during its exposure to a weathering environment could be used to predict coating's degradation or even failure. By defining the dielectric constant as the ratio of the absolute permittivity of a coating to its permittivity in vacuum ((*7*), it has been shown in different studies [49], [99], [141]–[143] that the dielectric constant of a coating increases when water (or other fluids) penetrates beneath the exposed layer of the coating.

The dielectric constant of a typical organic coating ε_c is reported between 2 and 7 [144] and could be expressed in the (*7*,

$$\varepsilon_c = \frac{Cl}{\varepsilon_0} \tag{7}$$

where *C* is the capacitance of the coating film in $\mu F.cm^{-2}$, *l* is the thickness of coating in μm, and ε_0 is the absolute permittivity of vacuum 8.854×10^{-8} $\mu F.cm^{-1}$. The increase of the dielectric constant indicates either the existence of more ions or flux of more electrons through the coatings. The Arrhenius equation ((*8*) provides an empirical relation for calculation of the chemical reactions' rate [145].

$$K = \Gamma e^{\left(\frac{-E_a}{RT}\right)} \tag{8}$$

In equation 8, Γ is the pre-exponential factor, which includes the frequency of molecules' collisions and their orientation. It varies slightly with temperature, and it is often considered constant across small temperature ranges. E_a is the activation energy in $J.mol^{-1}$, *R* is the universal

gas constant (8.3145 $J.mol^{-1}.K^{-1}$), and T is the absolute temperature (K). Eyring theory ((*9*), which was derived based on statistical mechanical justification, is similar to Arrhenius equation[40] with the pre-exponential factor replaced by the product of transmission coefficient (ξ), Boltzmann constant ($k_B = 1.38064852 \times 10^{-23}\, JK^{-1}$), and absolute temperature, divided by the Planck's constant ($h = 6.62607004 \times 10^{-34}\, m^2 kgs^{-1}$) [146]. Moreover, the activation energy was regarded equivalent to the change of the Gibbs free energy ΔG.

$$K = \frac{\xi k_B T}{h} e^{\left(\frac{-\Delta G}{RT}\right)} \tag{9}$$

Based on the theory of thermo-activated processes [58], [136], the dielectric constant can be related to both Eyring theory and Arrhenius equation, which results into the following equation ((*10*):

$$\varepsilon_c = \Gamma\, e^{\left(\frac{-\Delta G}{k_B T}\right)} \tag{10}$$

Considering the thermodynamics relations ($\Delta G = V\Delta P - S\Delta T$ and $V\Delta P = \Delta H - T\Delta S$), and assuming a constant temperature ($\Delta T = 0$), (*10* can be re-written as:

$$\varepsilon_c = \Gamma\, e^{\left(\frac{T\Delta S - \Delta H}{k_B T}\right)} \tag{11}$$

Coating films are viscoelastic materials. The elastic response of the coating is dominant when the applied stress is at a rapid rate, or the temperature is very low (varies for different coating but far less than the room temperature). On the other hand, when the flow applies a relatively small and continuous stresses on the coating, the deformation depends on the viscosity of the material as well as the temperature [147]. The Hooke's law of the theory of elasticity

indicates that the free energy of a body can be considered as a strain tensor. This is valid when the deformation is small, and the expanding free energy is in powers of strain [146].

$$dG = -SdT - ud\sigma \tag{12}$$

$$u = -\left(\frac{\partial G}{\partial \sigma}\right)_T \tag{13}$$

In order to consider the viscoelastic response of the coating, activation volume (V_a) could be considered as a parameter to characterize the deformation process of the coatings. The activation volume expresses the sensitivity of the free energy to charges in the stress, which is a dislocation from a ground equilibrium state to an activated state after the deformation [148]. Switching the activation volume with the strain tensor in (*12* (since $V_a = -\left(\frac{\partial G}{\partial \sigma}\right)_T$) [146], the change in the Gibbs free energy can be related to the product of the activation volume and the change in the applied stresses [136], [137].

$$dG = -SdT - V_a d\sigma \tag{14}$$

Considering (*11* and (*14*, the following equation can be derived in order to calculate the activation volume of the coatings in response to the stresses caused by the three different applied flow rates.

$$\varepsilon_c = \Gamma\, e^{\left(\frac{V_a \Delta\sigma}{k_B T}\right)} \tag{15}$$

Finally, from (*7* and (*15*, the following equation was derived in order to calculate the activation volume.

$$V_a = \frac{k_B T}{\Delta\sigma}\, ln\left(\frac{C_t l_t}{\varepsilon_0 \Gamma}\right) \tag{16}$$

6.3. Influence of the applied stresses on the amount of fluid uptake and diffusion coefficient

The total amount of fluid uptake (M_t) by the coating during the exposure can be calculated from the following equation [141]:

$$M_t = \frac{lA\rho}{\alpha}\left(1 - \frac{C_0}{C_t}\right) \tag{17}$$

$$\alpha = 2.3\ \log \varepsilon_f \tag{18}$$

For *3.5 wt. %* NaCl solution at *T=300 K*, the dielectric constant of the fluid is $\varepsilon_f = 48$ and its density is $\rho = 1.025\ g.cm^{-3}$. The C_0 and C_t values can be obtained from EIS data and *l* and *A* represents the thickness and exposed area of the coatings, respectively. Considering Eq.9a, the amount of water uptake depends on the thickness of the coating. The thickness of the coating could vary during the exposure time due to the initial fluid uptake (swelling of the coating), and then the abrasion of the coating due to shear stresses. However, the mass uptake at equilibrium (M_∞) can be predicted from calculating M_t from (*19*, indicating the ultimate possible amount of fluid that can be absorbed by a film of coating [149].

$$\frac{M_t}{M_\infty} = 1 - \sum_{n=0}^{\infty} \frac{8}{(2n+1)^2\pi^2} exp\left(\frac{-D(2n+1)^2\pi^2 t}{l^2}\right) \tag{19}$$

In (*19*, *t* represents the time, *l* is the thickness of the coating at the mentioned time, and *D* is the diffusion coefficient of the fluid in coating, which can be calculated by the following equation:

$$D = \xi\left(\frac{k_B T}{h}\right) d^2 e^{\left(-\frac{\Delta G}{RT}\right)} \tag{20}$$

where d is the diameter of the penetrant molecules. The average diameter of water molecules is about $d_{water} = 27.5\ nm$, while the average diameter of NaCl is $d_{NaCl} = 185\ nm$. It was assumed that the majority of molecules that penetrate the coatings are water molecules [100], [150]. The change of the Gibbs free energy (ΔG) in (*20* can be related to the applied stresses due to the fluid flow and their respective activation volume like (*15*.

$$D = \xi \left(\frac{k_B T}{h}\right) d^2 e^{\left(\frac{V_a \Delta\sigma}{RT}\right)} \tag{21}$$

Volume fraction (ϕ) is another parameter that provides a better understanding about the amount of fluid absorbed by the coating during the exposure to the fluid flow. Unlike M_t, ϕ does not depend on the thickness of the coating explicitly; therefore, it provides better characterization of the coating.

$$\phi = \frac{\log\left(\frac{C_t}{C_0}\right)}{\log \varepsilon_f} \tag{22}$$

Bellucci et al. [141] suggested an equation which related the amount of fluid uptake to the volume fraction at the time of exposure and their equilibrium values beyond the exposure time.

$$\frac{\phi}{\phi_\infty} = \frac{M_t}{M_\infty} = \frac{\log C_t - \log C_0}{\log C_\infty - \log C_0} \tag{23}$$

Considering (*23*, by calculating M_t, M_∞, and ϕ values from (*17*, (*19*, and (*22*, respectively, the equilibrium value of volume fraction (ϕ_∞) and capacitance (C_∞) of the coating can be calculated.

6.4. Theoretical analysis of water uptake for coatings exposed to the impingement flow of 3.5 wt. % NaCl

Based on theory, when water diffuses in polymeric coatings, the coating capacitance could look like the graph presented in Figure *90* [100]. Hinderliter et al. [99] and Yang et al. [100] divided the period of water diffusion into three stages of homogeneous diffusion, saturation stage and electrochemical reaction. Based on Figure *90*, the coating capacitance increases from the beginning of the exposure to the saturation time (t_s). Then the coating capacitance remains almost constant until the formation of double electrode layer starts. Beyond that point, the capacitance increases steadily as the electrochemical reaction occurs as water reaches the coating-metal interface. Comparing Figure *22* and Figure *90*, we could observe that our experiment fulfilled the first two theoretical stages for all flow rates; however, it is not clear whether the experiments reached the time when the electrochemical reactions took place on the metal-coating interface. Therefore, we calculate the equilibrium volume fraction (ϕ_∞), amount of fluid uptake (M_∞), and coating capacitance (C_∞) based on theory (from (*19* and (*23*) and then compare those with the experimental results obtained on $t = 168\ h$.

The values of the dielectric constants of the coating samples before the exposure to the flow and at $t = 24\ h$ are calculated using (*7* and summarized in Table *4*. The initial values of coatings' dielectric constants were in the same range that was reported in different studies for the epoxy coatings [144]. The application of the higher flow rates resulted in higher dielectric constant values after the first day. The results showed that by increasing the flow rates, the electric potential of the coating increased, which indicated the higher applied flow rates causes more water penetration to the coatings.

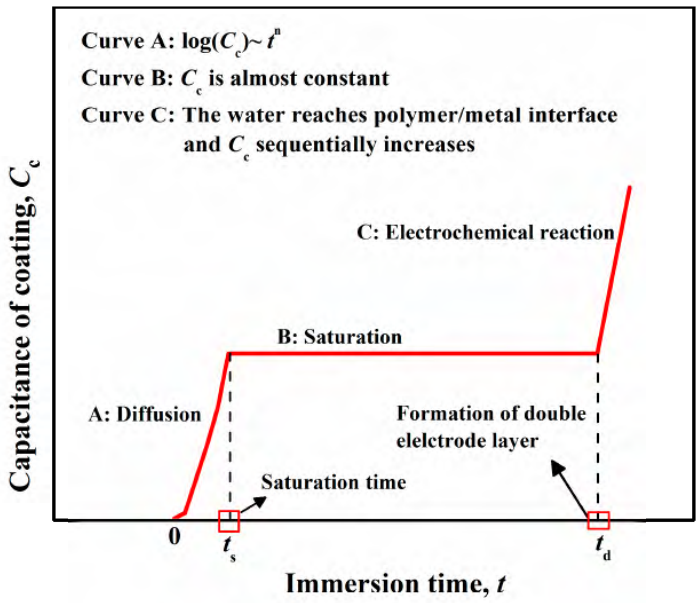

Figure 90. Change of the coating capacitance with respect to the water diffusion. This figure is taken from Ref [100] with permission.

Table 4. The initial and final dielectric constant of coated samples for the coatings that exposed to 3.5 wt. % NaCl solution at different applied flow rates.

Q (cm^3s^{-1})	V (ms^{-1})	$\varepsilon_{c,i}$	$\varepsilon_{c,t=24h}$
6.31	0.3214	5.58 ± 0.021	8.73 ± 0.054
12.62	0.6427	6.52 ± 0.050	10.15 ± 0.116
18.93	0.9641	6.25 ± 0.087	12.81 ± 0.096

The activation volume of the coatings with respect to the applied stresses resulted from different flow rates were calculated from (*16*, where the stress difference ($\Delta\sigma$) was considered as the maximum normal stress exerted by the impingement flow since $\Delta\sigma = \sigma_{max} - \sigma_0 = \sigma_{max}$ where $\sigma_0 = 0$. For the intact coating (at $t = 0\ s$), the applied stresses were zero ($\sigma_0 = \Delta\sigma = 0$); therefore, from (*15* the pre-exponential factor of the Arrhenius equation is equal to the dielectric constant of the intact coating ($\Gamma = \varepsilon_{c,i}$). At the center of the coated samples (in the domain of $-5\ mm < x \leq 5\ mm$), the normal stresses were dominant, while for the rest of the

areas, the shear stresses were dominant. Figure *91* shows the profile of activation volume resulted from the normal stress on coating surface under the flow jet area (i.e. stagnation zone), shear stress in the surrounding area on the coating surface, and total stress on the entire exposed area. The higher applied stresses lead to lower values of the activation volumes.

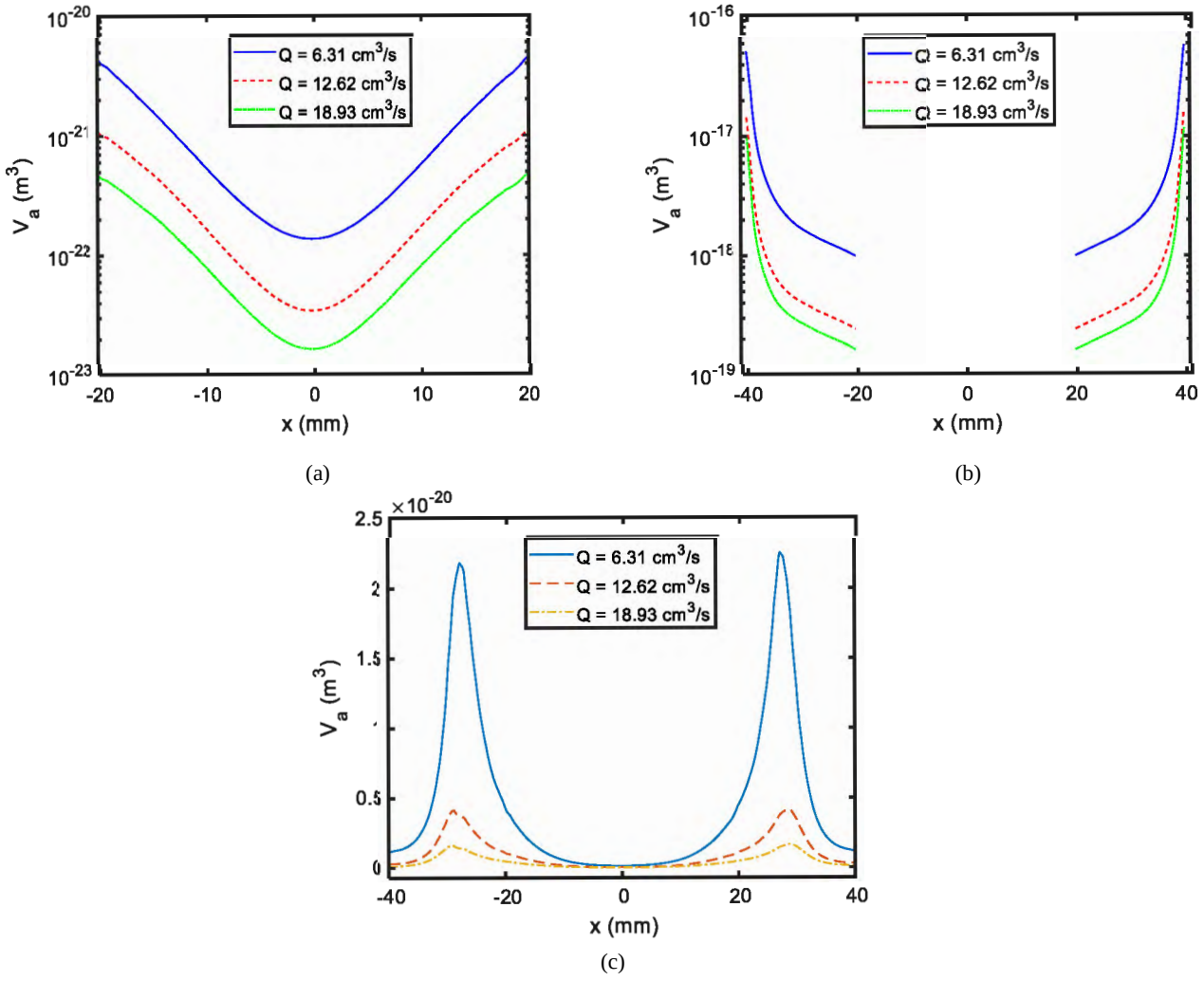

Figure 91. The calculated activation volume of coatings calculated via (a) normal stresses on coating surface under the flow jet area at the center (b) shear stresses on off-center area of coatings under laminar flow region, and (c) total stress over the entire exposed coating surface.

With the V_a values known, the apparent diffusion coefficient of water in coatings in different surface areas for the applied flow rates was calculated from (*21*. The transmission coefficient employed in (*21*, can be calculated using (*8* and (*9*,

$$\xi = \frac{\Gamma h}{k_B T} \tag{24}$$

We also showed that the pre-exponential factor of the Arrhenius equation ((*8*) is equal to the dielectric constant of the intact coating. Therefore, (*21* could be reduced to the following equation:

$$D = \varepsilon_{c,i} d^2 e^{\left(\frac{V_a \Delta\sigma}{RT}\right)} \tag{25}$$

The apparent diffusion coefficients calculated using data for different flow rates are summarized in Table *5*. The fact that the higher applied flow rates resulted in higher calculated values for the apparent diffusion coefficient indicates the convection from the bulk flow promotes the percolation of the water into the coatings. The total amount of fluid uptake (M_t) and the volume fraction (ϕ) of the coatings after a day (24 h) and a week (168 h) of exposure to the applied flow rates were calculated with (17 and (22, respectively, and summarized in Table *5*.

Table 5. The calculated diffusion coefficient, total fluid uptake, and volume fraction of coatings exposed to different flow rates inside an impingement flow chamber.

$Q\ (cm^3 s^{-1})$	$D\ (m^2 s^{-1})$	$M_{t=24\ h}\ (g)$	$M_{t=168\ h}\ (g)$	$\phi_{t=24\ h}$	$\phi_{t=168\ h}$
6.31	4.32×10^{-15}	0.112	0.157	0.116	0.174
12.62	4.91×10^{-15}	0.118	0.162	0.114	0.187
18.93	4.94×10^{-15}	0.146	0.131	0.185	0.216

In order to calculate the amount of water uptake at $t = 24h$, it was assumed that the thickness of the coating remained constant during the first 24 hours of experiment. The obtained results indicate that the amount of $M_{t=24h}$ and $\phi_{t=24\ h}$ were almost the same for the two lowest applied flow rates, while both parameters increased for Q = 18.93 $cm^3 s^{-1}$. The higher applied

flow rates resulted in higher momentum of water impacting the surface of the coated sample, and consequently resulted in relatively larger amount of water percolating through coating layers. By using (*19* and (*23*, the equilibrium values of water uptake, volume fraction, and coating capacitance (M_∞, ϕ_∞,and C_∞) were predicted based on their values at $t = 24\ h$. Figure 92, Figure *93*, and Figure *94* show the comparison between the predicted equilibrium values of the mentioned parameters and their respective values at *t= 24 h* and *t= 168 h*.

In order to calculate $M_{t=168\ h}$, the measured thickness values of the coatings after one week of the submersion were employed, which is an estimation as the thickness may vary during the submersion. As shown in Table *5*.

Table *5*, the amount of water uptake ($M_{t=168\ h}$) in coating samples are relatively smaller for the highest applied flow rate. Initially, due to the percolation of fluid the thickness of the coating increases, i.e. swelling, and the fluid was trapped between in coating layers. Then, due to the abrasive influence of higher flow rates, the top layer of the coating was removed, and the trapped fluid released back to the surrounding environment as illustrated in Figure *95*. Thus, the calculated water uptake at *t=168 h* for the highest flow rate Q = 18.93 cm^3s^{-1} was lower than the other two flow rates. In contrast, as shown in Figure *92*, the M_∞value predicted based on data from 24 hours of immersion increases as we increase of the applied flow rates. This is due to the discount of the abrasive effects of fluid flow in long-term immersion.

As shown in Figure *93* and Figure *94*, the volume fraction ($\phi_{t=168\ h}$), and coating capacitance ($C_{t=168\ h}$) of the coatings increased monotonically with the increase of the applied flow rates, suggesting the destructive effects of the fluid flow to the coatings increases as flow rate increases.

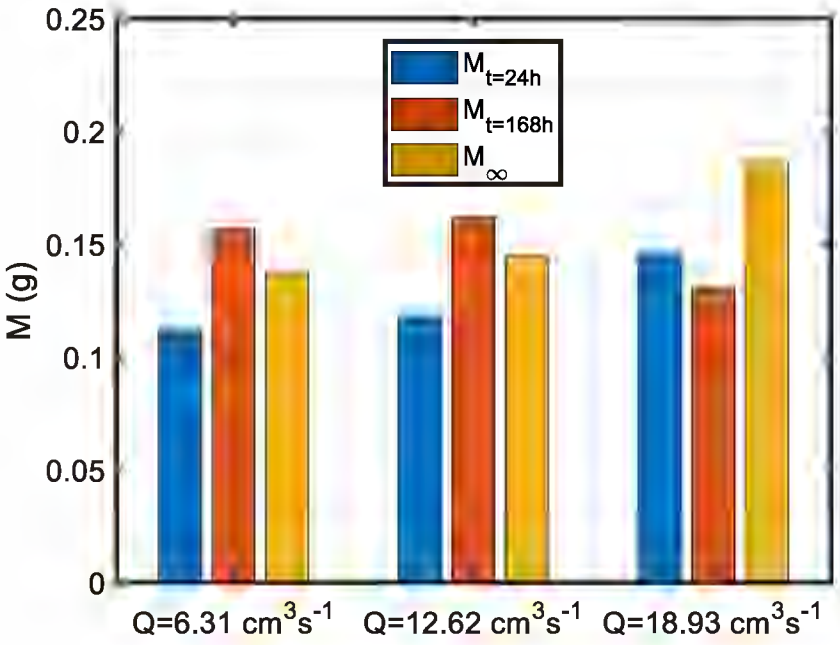

Figure 92. The predicted equilibrium water uptake of the coated samples is compared with the water uptake after a day, and a week of exposure to three different flow rates.

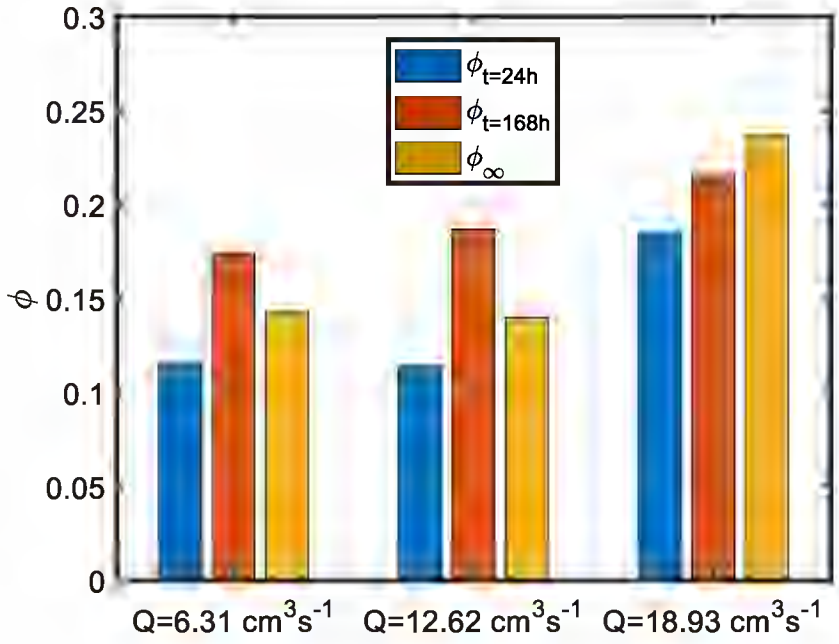

Figure 93. The predicted equilibrium volume fraction of the coated samples is compared with the ones after a day, and a week of exposure to the three different applied flow rates.

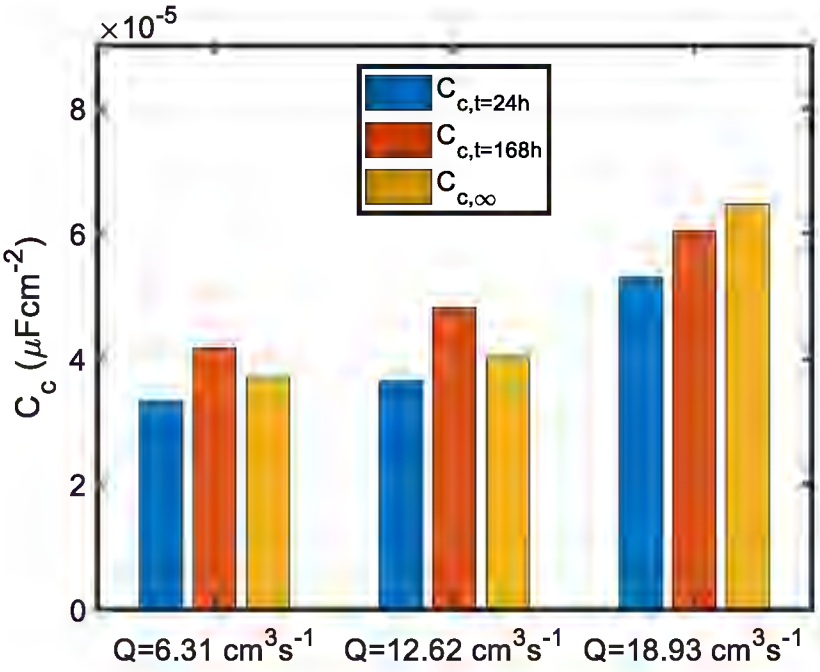

Figure 94. The predicted equilibrium coating capacitance is compared with the coating capacitance after one day, and a week of exposure to the three different flow rates.

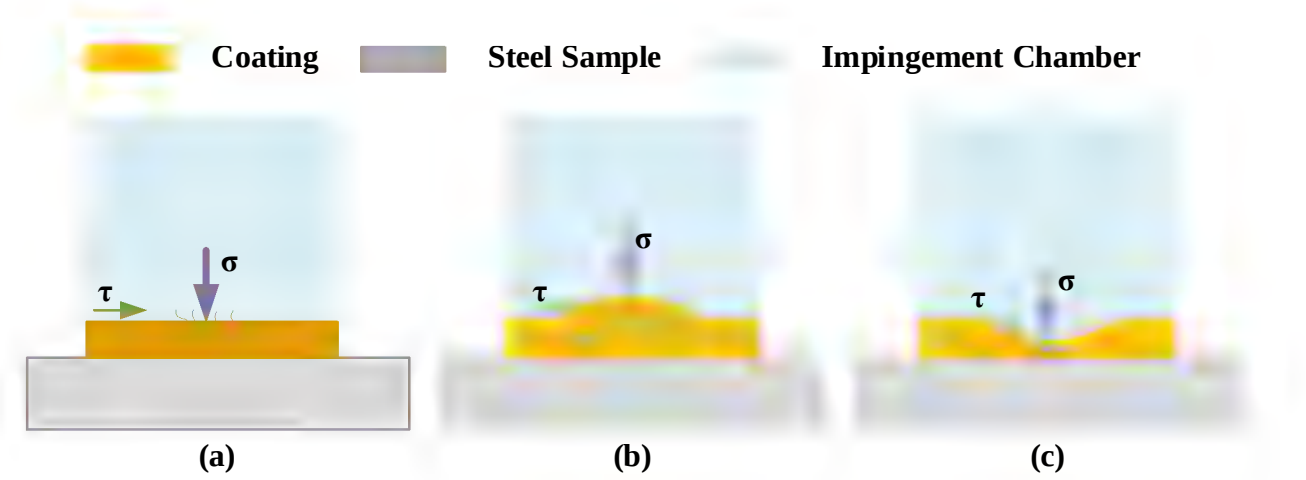

Figure 95. Schematic not to scale) The process of water percolation and coating's behavior owing to the exposure to high flow rates: (a) Water molecules diffuse through the micro-pores of the coating; (b) Water molecules occupy some space of the coating and causes the swelling of the coating; (c) Due to continuously applied fluid stresses, the top thin layer of the coating is removed, and some trapped water is released back to the environment.

The predicted values of water uptake, volume fraction, and coating capacitance (M_∞, ϕ_∞,and C_∞) at equilibrium for each applied flow rate were obtained based on theoretical equations ((*19* and (*23*), which are valid for ideal Fickian diffusion using Fick's law. Philippe et

al. [49] showed the diffusion of water from an aqueous electrolyte into organic coatings could be considered ideal for a very short time of exposure. Bouvet et. al. [151] showed the initial stage of water diffusion – from *t = 0* to t_s in Figure *90*, can be considered as the result of the ideal Fick's law. For our current study, a comparison between the graph of coating capacitances (Figure *22*) and the theoretical behavior of coating capacitances (Figure *90*) shows that in an estimation of the first 24 hours of each experiment the diffusion of water follows Fick's law. Moreover, Miwa et. al. [152] and Ghojavand et. al. [153] concluded that the ideal Fick's law could be employed when the ratio of the actual water uptake and the water uptake at equilibrium is less than 60% ($^{M_t}/_{M_\infty} < 0.6$). In our current study, using (*19*, the calculated ratio of $^{M_{t=24}}/_{M_\infty}$ are 0.4962, 0.4981, and 0.5740 for the applied flow rates of $Q = 6.31, 12.62,$ and $18.93\ cm^3s^{-1}$, respectively. These values are less than the afore-mentioned limit of 0.6.

As shown in Figure *92*, Figure *93*, and Figure *94*, the amount of water uptakes, volume fraction and coating capacitance at 168 hours for $Q = 6.31$ and $12.62\ cm^3s^{-1}$ surpass the corresponding predicted equilibrium values, while for $Q = 18.93\ cm^3s^{-1}$, the predicted equilibrium values are greater than those based on data collected at 168 hours. The observation could be explained as follows. Referring to Figure *90*, after immersion our coating samples may have all passed the saturation period and entered the electrochemical reaction region, meaning that the predicted equilibrium values underestimate the coating's water uptake for long-term immersion. For samples exposed to the highest applied flow rate, however, the abrasion effect from the fluid flow due to the high stresses induced a significant reduction in the coating thickness. Therefore, the predicted values which are based on the coating's initial thickness become greater than the values from actual long-term immersion.

Moreover, the apparent diffusion coefficient of water is highly dependent on the polymer structure of the coatings, the thickness, participant materials, and temperature etc. [154], [155]. Although the current values of *D* showed a slight increase with the increase of the applied flow rates, the increment was negligible. The equilibrium values of volume fraction of absorbed fluid, on the other hand, exhibited a significant difference as the flow rate changed. The results indicated that the rate of water diffusion was not affected notably by the increase of impingement flow rate (or applied stresses), but the increase in the stresses incurred by the elevated flow rate resulted in a larger amount of water in coatings and potentially shortened the service lifetime of coatings against corrosion.

6.5. Comparison between the electrochemical parameters of the coatings exposed to the impingement flow of a 3.5 wt.% NaCl solution with and without 1 wt.% sand particles

The average thickness values of the coatings before and after each experiment are shown in Figure *96*. The coating thickness increased by 5.8% for the lowest applied flow rate (Q_1 = *6.31* cm^3s^{-1}) of the non-particulate fluid. The thickness increased due to the swelling of the coating film because of fluid uptake. For the similar flow rate of the sand particulate fluid, the thickness decreased about 1.2 % after the experiment, indicating that the sand particles eroded the outer surface of the coating's film. For the higher applied flow rates, regardless of the type of the fluid, the thickness of the coating decreased after the immersion. However, the erosions of the coatings were higher for particulate fluid compared with non-particulate one. For Q_2 = *12.62* cm^3s^{-1}, the thickness decreased by 1.8 % for non-particulate fluid, while it decreased by 2.7 % for the particulate fluid. The trend was the same for the highest applied flow rate (Q_3 = *18.93* cm^3s^{-1}), as the thickness decreased 19% for the non-particulate fluid compared with 20 % decrease for the particulate fluid. Zeng et al. [98] concluded that the abrasion amount of the organic coatings

was exponentially correlated with sand flow velocities; however, in their study, the minimum applied velocity was 2 ms^{-1}, and they measured the abrasion for the velocities up to 10 ms^{-1}. In the underwater zone of offshore wind structures, such high velocities do not exist [7]. As it is shown in the current study, for the regular velocities (between 0.3 and 1 ms^{-1}) in the underwater zone, the abrasion amounts due to the sand flows were almost 1 to 2 % higher for all applied flow rates compared with non-particulate fluid flow. Moreover, the abrasion amount increased from 1 to 2 % for the lowest applied flow rate to almost 20% for highest applied flow rate regardless of the fluid type.

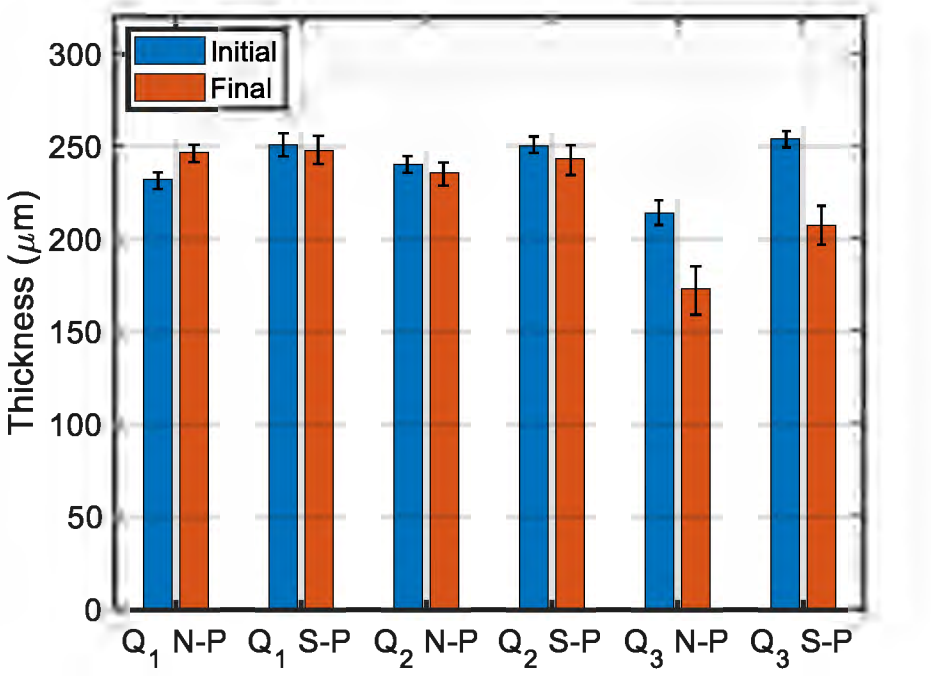

Figure 96. The thickness of the coatings before the experiments (initial) and after the experiments (final) exposed to non-particulate (NP) and 1 wt. % sand particulate (P) 3.5 wt. % NaCl solution at three different applied flow rates of Q1 = 6.31, Q2 = 12.62, and Q_3 = 18.93 cm^3s^{-1}.

The penetration of the electrolyte fluid into the coating increases the dielectric constant of the coating sample since the relative electric polarizability of a coating increases during the time of immersion. In order to calculate the initial dielectric constant of the coating, the initial

coatings' capacitance and the thickness of the coatings before immersions were considered. The activation volume for both fluids' type and three different applied stresses are shown in Figure *97*. The lower the applied flow rates, the higher the value of the activation volume; therefore, V_a values were higher for non-particulate fluids compared with particulate one.

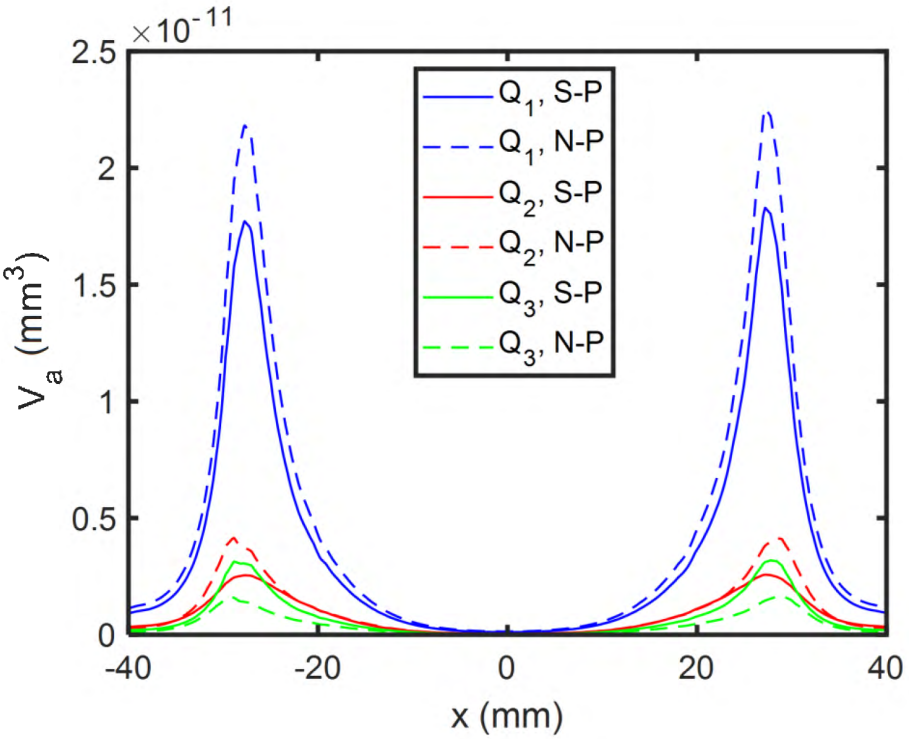

Figure 97. The activation volume of the coatings exposed to non-particulate (N-P) and 1 wt. % sand particulate (S-P) 3.5 wt. % NaCl solution at different flow rates calculated via total stress on exposed coating surface.

Figure 98 shows the amount of fluid uptake by the coatings during the period of experiments. As it is shown, for the non-particulate fluid, the amount of fluid uptake increased as the flow rate doubled from 6.31 to 12.62 cm^3s^{-1}, but the fluid uptake decreased significantly when the highest applied flow rate applied on the coating. The trend was not the same for the sand particulate fluid, as the amount of water uptake increased proportionally to the increase of applied flow rates. The reasons for such difference in the trends of obtained results, are the involvement of coatings' thickness and the use of coating capacitances in calculation M_t values. As shown in Figure *35*, the higher applied flow rates resulted into higher coating capacitances,

which implied the higher rate of ions (fluid) diffusion across the coatings. On the other hand, the higher applied flow rates caused the higher abrasion amount and consequently the thickness of the coatings decreased with the increase of the applied flow rates. Considering the two factors, for the non-particulate fluid, the abrasion amount became substantially higher (decrease of thickness) for the highest flow rates; therefore, the total amount of fluid uptake was less for highest applied flow rate compared with the lower flow rates. In the case of sand particulate fluid, the abrasion amount was maintained at around a similar level while the transport of the fluid into the coatings are highly promoted by the higher flow rates. This resulted in an increased amount of fluid uptake as the flow rate increases.

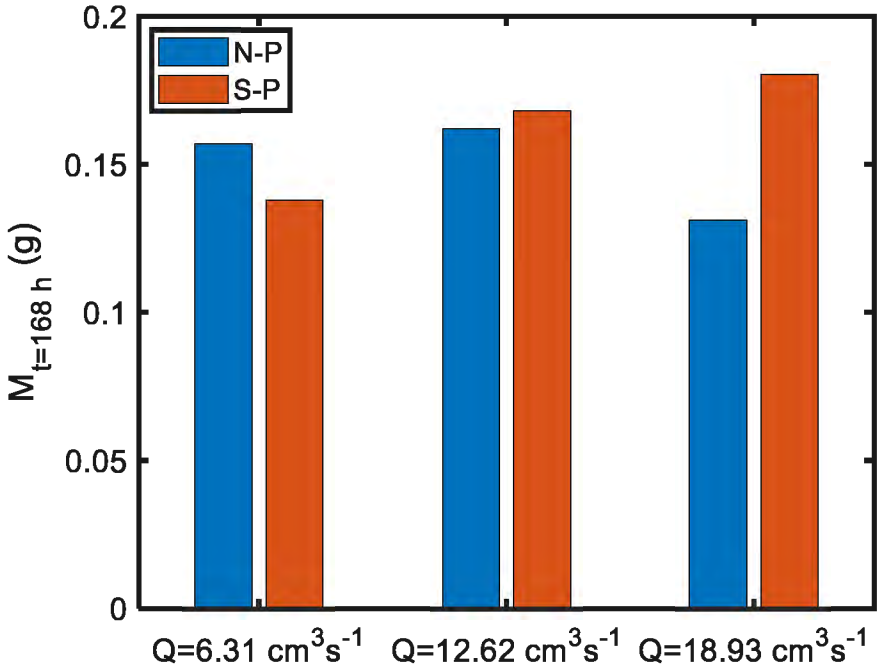

Figure 98. The amount of fluid uptake by the coatings exposed to non-particulate and 1 wt. % sand particulate 3.5 wt. % NaCl solution at three different flow rates.

Owing to the dependence of water uptake values on both the abrasion amounts and diffusion rates, the water uptake may not provide a clear picture of the influence of different applied flow rates on the degradation of the coatings.

Figure 99 shows the volume fraction values of the coatings exposed to the three different applied flow rates of both fluids. The volume fraction of fluid in the coating sample increased monotonically with the increase of the applied flow rates for both fluids. Moreover, except for the lowest applied flow rate, the fluid volume fraction was higher for the coatings exposed to the particulate fluid compared with non-particulate one. For the lowest applied flow rate, the compared values of both the amount of fluid uptake and the volume fraction showed that adding sand particles to the fluid did not influence the amount of fluid percolates into the coatings but resulted in higher fluid abrasion.

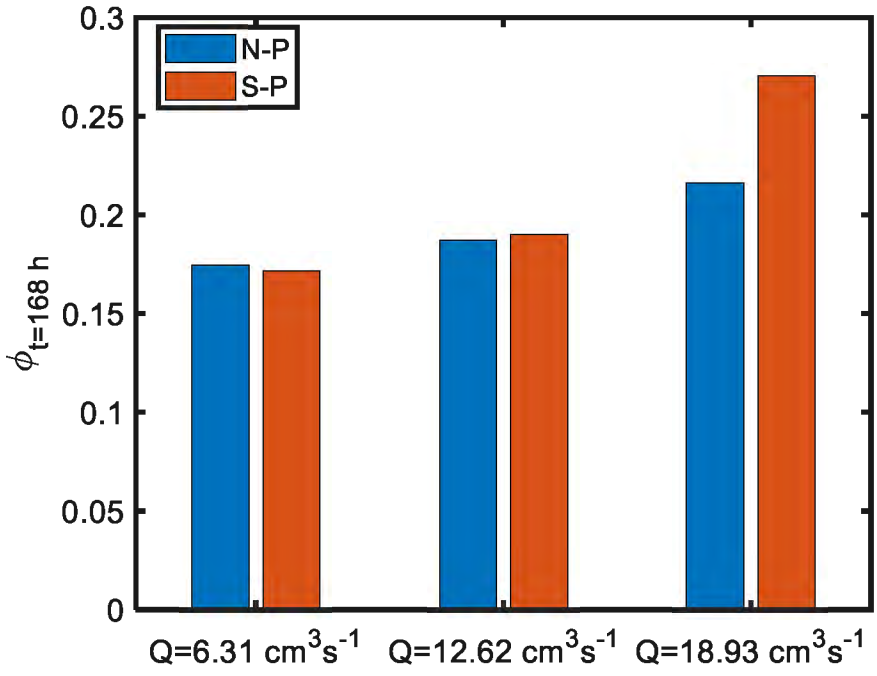

Figure 99. The volume fraction of the coatings exposed to non-particulate and 1 wt. % sand particulate 3.5 wt. % NaCl solution at three different flow rates.

The change of volume fraction with respect to the Reynolds number of the fluid flow inside the inlet pipe of the impingement flow chamber is shown in Figure 100 for both non-particulate and sand-particulate fluids. The increase of the inlet fluid flow increases the value of Reynolds number for constant inner diameter of the inlet pipe. The increase of the Reynolds number is proportional to the increase of the volume fraction due to the increase of the water penetration into the coatings.

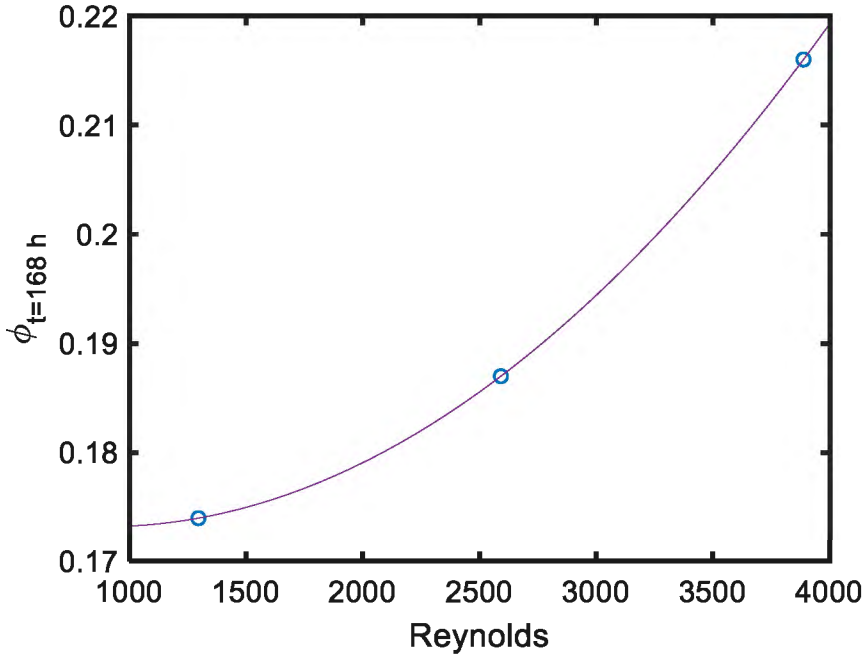

(a) Non-particulate 3.5 wt.% NaCl solution

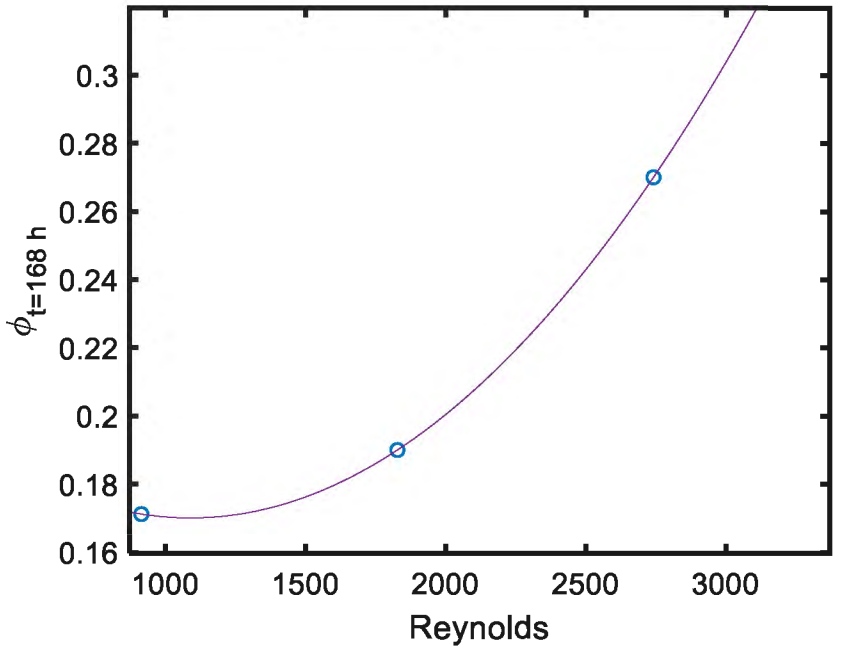

(b) 1 wt.% sand-particulate added to 3.5 wt.% NaCl solution

Figure 100. The change of volume fraction with respect to the Reynolds number of the fluid flow inside the inlet pipe of the impingement flow chamber.

6.6. Electrochemical parameters for the coatings exposed to the wave loads

Figure 101 shows the values of coating thickness before and after the exposure to the wave loads. We observe that for all the cases, the thickness of the coating slightly increases after the period of the tests. We believe the coating swelling was dominating in this case, which was caused by the solution that percolates through the coating layers. For samples exposed to the higher wave loads, the relative thickness of the coatings increased with higher percentage. The increase rates of the thicknesses were measured as 4.49, 8.8 and 10.2% the lowest to highest motor speeds respectively.

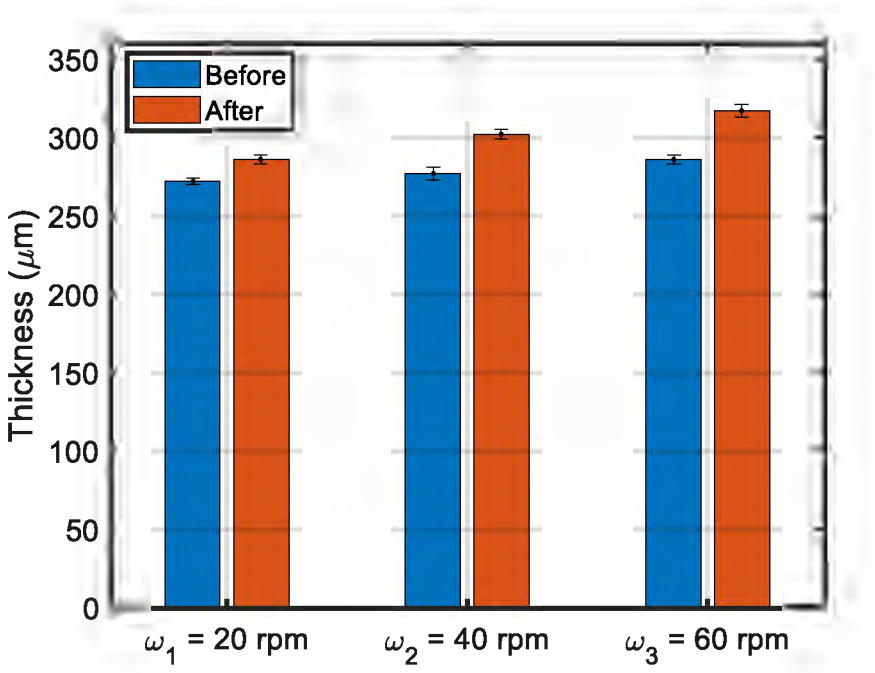

Figure 101. Coating thickness before and after the exposure to wave loads for a week.

The activation volume profiles for the average of three different applied stresses on the surface of the coatings are shown in Figure 102. The lower the applied flow rates, the higher the value of the activation volume s; therefore, V_a values were higher for waves generated with motor speed of $\omega_1 = 20\,rpm$, compared with the other two higher wave loads.

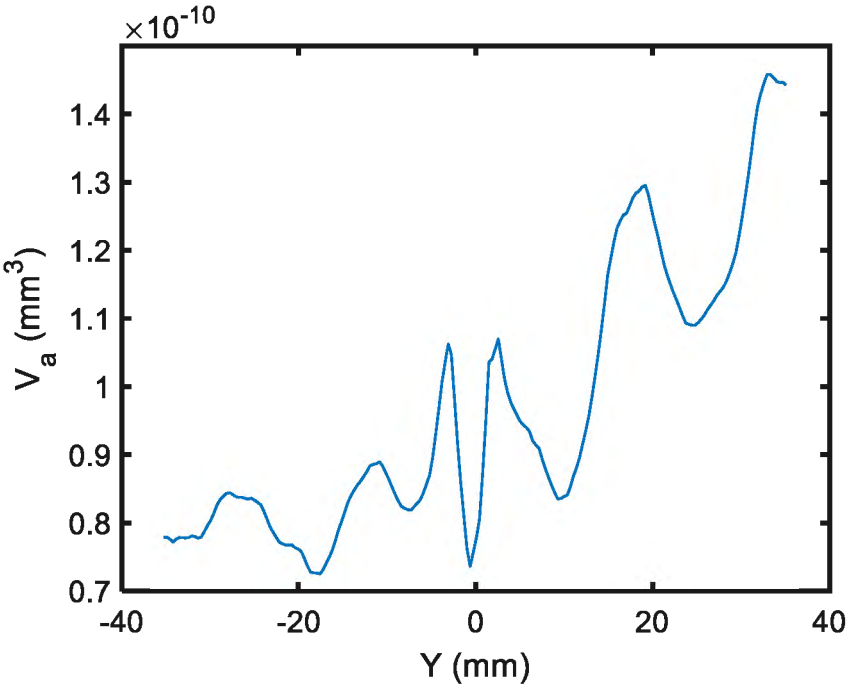

(a) $\omega_1 = 20$ rpm

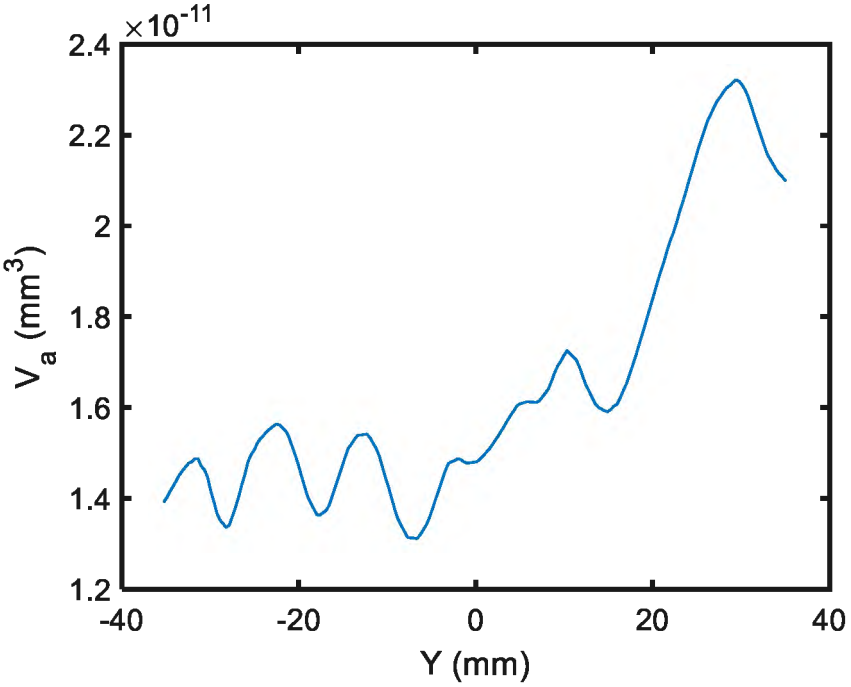

(b) $\omega_2 = 40$ rpm

Figure 102. The activation volume of the coatings exposed to different wave loads calculated via average stresses over exposed coating surface.

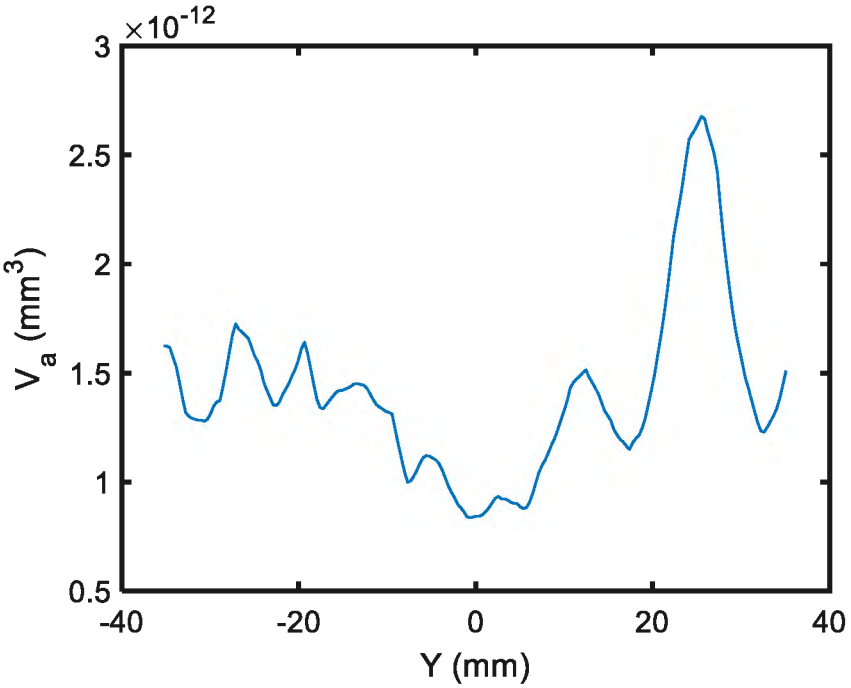

(c) $\omega_3 = 60$ rpm

Figure 102. The activation volume of the coatings exposed to different wave loads calculated via average stresses over exposed coating surface (continued).

During the immersion time, the electrolyte fluid diffuses into the coatings causing the wetness and ultimately failure of the coating when the ions and electrons paths form between the metal substrate and the corrosive environment. Figure 103 shows the amount of fluid uptake by the coatings during the period of experiments. The increase of wave loads resulted into more water percolation through the coatings, and consequently increases the amount of water uptake through the inner layers of the coatings. The applied stresses were not strong enough to cause abrasion of the coatings and reentrance of the captured fluid in the coatings back to the surroundings. Figure 104 shows the volume fraction of the coatings exposed to the three different applied flow rates of both fluids. The fluid volume fraction increased monotonically to the increase of the applied wave loads.

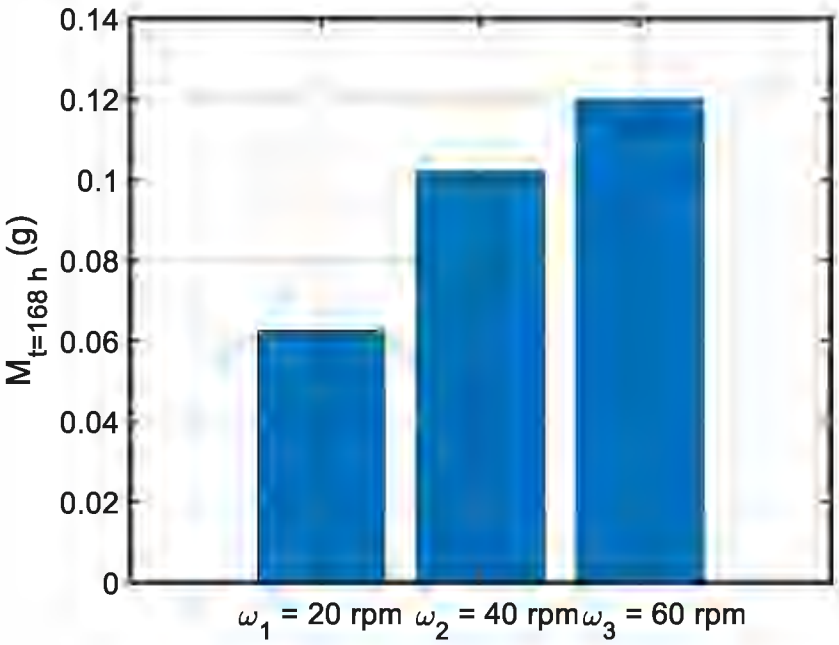

Figure 103. The amount of fluid uptake by the coatings exposed to three different wave loads.

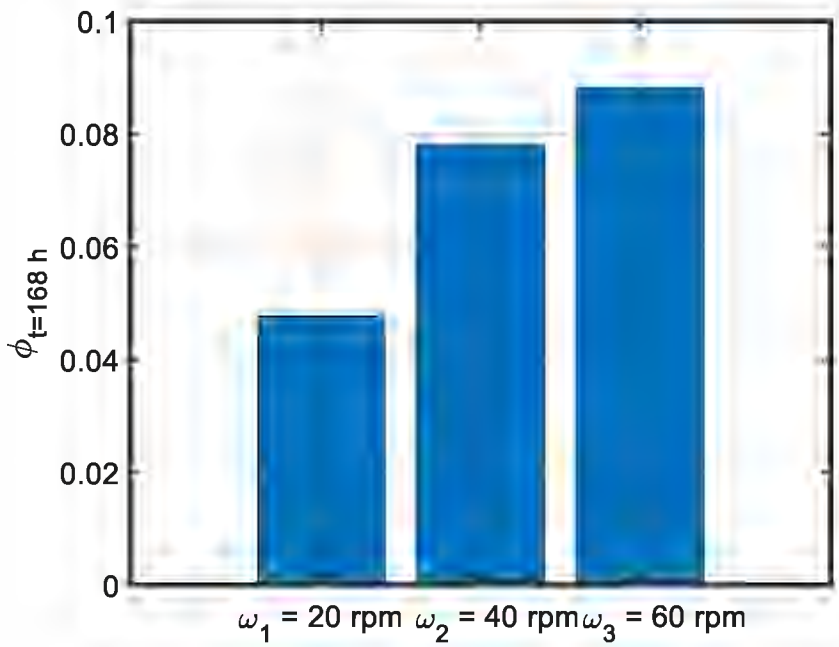

Figure 104. The fluid volume fraction in the coatings when exposed to three different wave loads.

In order to provide a quantitative comparison between the applied waves on the coatings with the respective change in volume fraction of the coatings, the Froude number is calculated from the following:

$$Fr = \frac{U}{\sqrt{gD_h}} \tag{26}$$

where D_h is the cross-section area of the flow by the top width of the flow, which is equal to the depth of the water in tank (0.254 m) and U is the celerity velocity. As shown in the increase of the Froude number is proportional to the increase of the volume fraction due to the increase of the water penetration into the coatings.

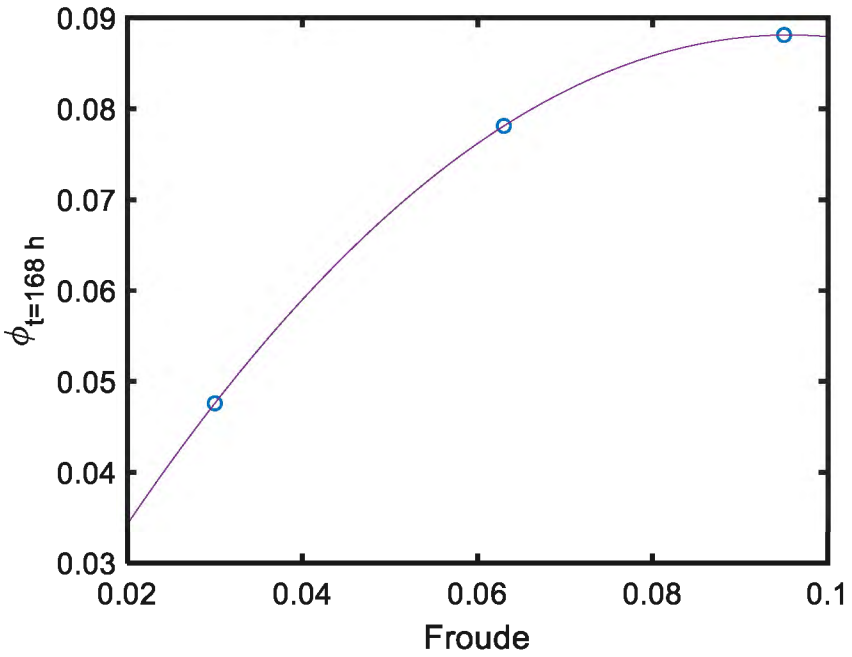

Figure 105. The change of volume fraction of the coatings with respect to the Froude number of the applied waves.

6.7. Discussion

6.7.1. Impingement flow experiments

The fluid abrasion on the coatings occurred proportionally to the increase of the flow rates for the samples exposed to both sand particulate and non-particulate fluids, while for the lowest applied flow rate of the non-particulate fluid, the thickness of the coating increased after the exposure due to swelling effect. The low shear stresses corresponding to low flow rates is not sufficient for the removal of the swollen coatings.

For the lowest applied flow rate, $Q_1=6.31\ cm^3s^{-1}$, thickness of the coating increased for the non-particulate fluid due to the stored fluid uptake beneath the outer layer of the coating; for the particulate fluid, the additional sand provided enough shear stresses to remove the swollen layer of coatings.

For $Q_2=12.62\ cm^3s^{-1}$, the amount of fluid uptakes, and volume fractions of fluid in the coatings were slightly higher for coatings exposed to the sand particulate fluid.

For $Q_3=18.93\ cm^3s^{-1}$, the compared values of fluid uptakes and volume fractions showed that the fluid transport rate was higher for coatings exposed to the sand particulate fluid.

Due to the dependence of the fluid uptake on the final thickness of the coatings, the increase of the applied flow rates did not consequently increase the amount of the fluid uptake; however, the volume fraction values increased monotonically to the increase of the applied flow rates for both fluid types. The increase of the volume fraction was higher for the sand particulate fluid at Q_2 and Q_3 flow rates, indicating the additional applied stresses due to the impact of sand particles provided more paths on the coatings' surface for fluid transport.

The obtained values of M_∞, ϕ_∞,and C_∞ provide an estimation of the influence of applied stresses on the degradation of the coatings. The trends of all parameters show the increase in

permittivity with increase of the applied stresses. The required energy for weakening the bonds of outer layer of coatings were provided by the applied stresses, which resulted into decreasing the activation volume of the coating; consequently, the apparent diffusion coefficient of coatings increased which led to higher amount of water uptake and the volume fraction of absorbed fluid.

Overall, it was concluded that for the lowest applied flow rate ($Q_1=6.31\ cm^3s^{-1}$), the destructive influence of the added sand particles appeared after the first three days of exposure through the final days of experiment. As the flow rate increased, the influence of sand particles became more imminent at the beginning of the exposure, and the compared elements of equivalent circuit model showed broader difference between the particulate and non-particulate fluids. The added sand particles caused abrasion of the coatings regardless of the applied flow rate. For the highest applied flow rate ($Q_3=18.93\ cm^3s^{-1}$), the destructive influence of sand particles was significant, indicating that when the velocity of particulate flow reaches 1 ms^{-1} (the common velocity of water currents in the underwater zone with depth of 30 m), the momentum impact of the sand particles plays a vital role in degradation of the organic coatings.

6.7.2. Wave tank experiment

The increase in the magnitude of the wave loads have a direct effect on the increase in the amount of water uptake and volume fraction. Since all the applied stresses due to the cyclical loads were not strong enough to cause any sort of abrasion, the increase of wave loads only resulted in the increase of water penetration into the coatings. The irregular non-homogeneous wave loads resulted into irregular activation volume over the entire surface of the coatings. However, by increasing the applied stresses, the activation volume decreased proportionally, showing the direct dependence of the coatings' degradation on the applied stresses.

7. CONCLUSIONS

In this study, the effect of applied stresses due to water flow in the underwater zone of epoxy coated monopile wind turbine structures were modeled and analyzed. CFD modeling and experimental PIV measurements were used to derive the magnitudes of the shear and normal stresses. Employing EIS data and the equivalent circuit modelling of coatings, characteristics of the coatings (ε_c, ϕ_t, and M_t) were calculated. By utilizing the thermo-activated theory, thermodynamics relations, thermal elasticity laws, and the Fick's laws, the influence of the applied stresses on the degradation process of the coatings were investigated. The conclusions based on the obtained results are as follows.

In the underwater zone of the wind turbine, the normal stress dominates the total stress created by impingement flow as its magnitude is about 5000 times of that of the shear stress. However, the shear stress is the main cause for the abrasion of the top layers of coatings. Higher applied stresses result in lower values of the activation volumes. Higher flow rates do not affect the apparent diffusion coefficient of water in coatings significantly; however, it increases the volume fraction and coating capacitance substantially. This indicates that the rate of water uptake within the coating layers is almost independent on the flow rate of the applied fluid flow, but the total volume percentage of water in the coating is promoted by the increased flow rate. For high flow rates, despite of the elevated volume percentage of the water in the coating due to higher stresses, the total amount of water uptake decreases over time. This is due to the reduced coating thickness caused by the significant abrasion brought by high fluid shear. In this study, the effect of applied stresses due to the water flow in the underwater zone of epoxy coated monopile wind turbine structures were modeled and analyzed.

We also concluded that the higher applied stresses resulted in lower values of the activation volumes.

- The higher applied flow rates did not change the apparent diffusion coefficient significantly; however, it increased the volume fraction and coating capacitance strongly. That indicates that the rate of water uptake did not change much with the rise of the applied flow rate, but the rate of water penetration into the lower layers of coating increased with the higher applied flow rates.

  Higher applied flow rates result in higher shear stresses, which increase the rate of coatings' abrasion. The higher abrasion rate resulted in the lower amount of water uptake (M_t) due to the removal of coating top layers.
- If the applied stresses on the coatings are not strong enough, the stresses only cause more water penetration without experiencing any significant abrasion. This results in the increase in the coating thickness as the applied stresses increase due to swelling. Such phenomena were observed for the coatings exposed to the waves or low-flow-rate impingement flow.

The equilibrium values of water uptake (M_∞), volume fraction (ϕ_∞), and the coating capacitance (C_∞) with respect to the different flow rates predicted the ultimate condition of coating exposed to constant applied stresses until the time of complete failure.

REFERENCES

[1] S. R. Loss, T. Will, and P. P. Marra, “Refining Estimates of Bird Collision and Electrocution Mortality at Power Lines in the United States,” PLOS ONE, vol. 9, no. 7, p. e101565, Jul. 2014, doi: 10.1371/journal.pone.0101565.

[2] S.-P. Breton and G. Moe, “Status, plans and technologies for offshore wind turbines in Europe and North America,” Renew. Energy, vol. 34, no. 3, pp. 646–654, Mar. 2009, doi: 10.1016/j.renene.2008.05.040.

[3] “Reports - World Forum Offshore Wind (WFO) Global,” WFO-Global. https://wfo-global.org/reports/ (accessed Feb. 15, 2022).

[4] International Energy Agency, “Offshore Wind Outlook 2019: World Energy Outlook Special Report,” Offshore Wind, p. 98, 2019.

[5] T. Stehly, P. Beiter, and P. Duffy, “2019 Cost of Wind Energy Review,” Natl. Renew. Energy Lab., p. 86, 2020.

[6] S. J. Price and R. B. Figueira, “Corrosion Protection Systems and Fatigue Corrosion in Offshore Wind Structures: Current Status and Future Perspectives,” Coatings, vol. 7, no. 2, Art. no. 2, Feb. 2017, doi: 10.3390/coatings7020025.

[7] A. Arapogianni and J. Moccia, “Wind in our Sails- The coming of Europe’s Offshore Wind Energy Industry,” Eur. Wind Energy Assoc., p. 93, 2011.

[8] D. Frick and M. Achmus, “An experimental study on the parameters affecting the cyclic lateral response of monopiles for offshore wind turbines in sand,” Soils Found., vol. 60, no. 6, pp. 1570–1587, Dec. 2020, doi: 10.1016/j.sandf.2020.10.004.

[9] S. Hallowell, A. T. Myers, and S. R. Arwade, “Variability of breaking wave characteristics and impact loads on offshore wind turbines supported by monopiles,” Wind Energy, vol. 19, no. 2, pp. 301–312, 2016, doi: 10.1002/we.1833.

[10] W. Popko et al., “Offshore Code Comparison Collaboration Continuation (OC4), Phase 1 - Results of Coupled Simulations of an Offshore Wind Turbine With Jacket Support Structure,” presented at the The Twenty-second International Offshore and Polar Engineering Conference, Jun. 2012. Accessed: Feb. 02, 2022. [Online]. Available: https://onepetro.org/ISOPEIOPEC/proceedings/ISOPE12/All-ISOPE12/ISOPE-I-12-117/12497

[11] E. Lozano-Minguez, A. J. Kolios, and F. P. Brennan, “Multi-criteria assessment of offshore wind turbine support structures,” Renew. Energy, vol. 36, no. 11, pp. 2831–2837, Nov. 2011, doi: 10.1016/j.renene.2011.04.020.

[12] A. W. Momber, P. Plagemann, and V. Stenzel, “Performance and integrity of protective coating systems for offshore wind power structures after three years under offshore site conditions,” Renew. Energy, vol. 74, pp. 606–617, Feb. 2015, doi: 10.1016/j.renene.2014.08.047.

[13] A. W. Momber and T. Marquardt, “Protective coatings for offshore wind energy devices (OWEAs): a review,” J. Coat. Technol. Res., vol. 15, no. 1, pp. 13–40, Jan. 2018, doi: 10.1007/s11998-017-9979-5.

[14] A. Momber, “Corrosion and corrosion protection of support structures for offshore wind energy devices (OWEA),” Mater. Corros., vol. 62, no. 5, pp. 391–404, 2011, doi: 10.1002/maco.201005691.

[15] O. Adedipe, F. Brennan, and A. Kolios, “Review of corrosion fatigue in offshore structures: Present status and challenges in the offshore wind sector,” Renew. Sustain. Energy Rev., vol. 61, pp. 141–154, Aug. 2016, doi: 10.1016/j.rser.2016.02.017.

[16] 14:00-17:00, “ISO 12944-5:2019,” ISO. https://www.iso.org/cms/render/live/en/sites/isoorg/contents/data/standard/07/77/77795.html (accessed Feb. 13, 2022).

[17] A. W. Momber, “Quantitative performance assessment of corrosion protection systems for offshore wind power transmission platforms,” Renew. Energy, vol. 94, pp. 314–327, Aug. 2016, doi: 10.1016/j.renene.2016.03.059.

[18] B. Eker and E. Yuksel, “Solutions to corrosion caused by agricultural chemicals,” Trakia J Sci, vol. 3, Jan. 2005.

[19] V. M. Bakaleinikov, Y. N. Shekhter, Z. S. Erukhimovich, N. L. Eniseiskii, and A. E. Severnyi, “Protection of agricultural machinery roller chains from corrosion and wear,” Prot. Met., vol. 25, no. 6, 1989, Accessed: Feb. 15, 2022. [Online]. Available: https://www.elibrary.ru/item.asp?id=31093688

[20] P. R. Roberge, Corrosion Engineering: Principles and Practice, 1st edition. McGraw Hill, 2008.

[21] I. T. Kim and Y. Itoh, “Accelerated exposure tests as evaluation tool for estimating life of organic coatings on steel bridges,” Corros. Eng. Sci. Technol., vol. 42, no. 3, pp. 242–252, Sep. 2007, doi: 10.1179/174327807X214833.

[22] The Chemistry and Physics of Coatings. 2004. doi: 10.1039/9781847558206.

[23] J. N. Murray, L. D. Stephenson, and A. Kumar, “Electrochemical and physical evaluations of coil coatings on metal-coated steels for roofing applications,” Prog. Org. Coat., vol. 47, no. 2, pp. 136–146, Aug. 2003, doi: 10.1016/S0300-9440(03)00114-0.

[24] Protective Organic Coatings. 2015. doi: 10.31399/asm.hb.v05b.9781627081726.

[25] O. Ø. Knudsen and A. Forsgren, Corrosion Control Through Organic Coatings. Boca Raton: CRC Press, 2017. doi: 10.1201/9781315153186.

[26] DONG Energy et al., Danish offshore wind: key environmental issues. Copenhagen: Published by DONG Energy, Vattenfall, the Danish Energy Authority and the Danish Forest and Nature Agency, 2006.

[27] L. Lichtenstein, “DNV GL standard harmonization Recommended Practice on corrosion protection of offshore wind farms,” 2015, vol. 2015-January, pp. 659–663.

[28] “DNV-OS-J101: Design of Offshore Wind Turbine Structures,” p. 214, 2013.

[29] 14:00-17:00, “ISO 20340:2009,” ISO. https://www.iso.org/cms/render/live/en/sites/isoorg/contents/data/standard/04/41/44180.html (accessed Feb. 13, 2022).

[30] “Surface preparation and protective coating | standard.no.” https://www.standard.no/en/sectors/energi-og-klima/petroleum/norsok-standard-categories/m-material/m-5014/ (accessed Feb. 13, 2022).

[31] J. Cheng, Z. Li, N. Zhang, Y. Dou, and L. Cui, “Experimental Study on Erosion–Corrosion of TP140 Casing Steel and 13Cr Tubing Steel in Gas–Solid and Liquid–Solid Jet Flows Containing 2 wt % NaCl,” Materials, vol. 12, no. 3, Art. no. 3, Jan. 2019, doi: 10.3390/ma12030358.

[32] H. Meng, X. Hu, and A. Neville, “A systematic erosion–corrosion study of two stainless steels in marine conditions via experimental design,” Wear, vol. 1–6, no. 263, pp. 355–362, 2007, doi: 10.1016/j.wear.2006.12.007.

[33] Z. B. Zheng, Y. G. Zheng, X. Zhou, S. Y. He, W. H. Sun, and J. Q. Wang, “Determination of the critical flow velocities for erosion–corrosion of passive materials under impingement by NaCl solution containing sand,” Corros. Sci., vol. 88, pp. 187–196, Nov. 2014, doi: 10.1016/j.corsci.2014.07.043.

[34] J. A. Wharton and R. J. K. Wood, “Influence of flow conditions on the corrosion of AISI 304L stainless steel,” Wear, vol. 256, no. 5, pp. 525–536, Mar. 2004, doi: 10.1016/S0043-1648(03)00562-3.

[35] A. D. Mercer and E. A. Lumbard, “The corrosion of mild steel in water.,” Br Corros J, vol. 30, no. 1, Art. no. 1, 1995.

[36] R. E. Melchers and R. Jeffrey, “Influence of Water Velocity on Marine Immersion Corrosion of Mild Steel,” Corrosion, vol. 60, no. 01, Jan. 2004.

[37] H. Hornberger, S. Virtanen, and A. R. Boccaccini, “Biomedical coatings on magnesium alloys – A review,” Acta Biomater., vol. 8, no. 7, pp. 2442–2455, Jul. 2012, doi: 10.1016/j.actbio.2012.04.012.

[38] K. Bazaka, M. V. Jacob, R. J. Crawford, and E. P. Ivanova, “Plasma-assisted surface modification of organic biopolymers to prevent bacterial attachment,” Acta Biomater., vol. 7, no. 5, pp. 2015–2028, May 2011, doi: 10.1016/j.actbio.2010.12.024.

[39] E. McCafferty, Introduction to Corrosion Science. New York, NY: Springer New York, 2010. doi: 10.1007/978-1-4419-0455-3.

[40] E. Heitz, “Mechanistically based prevention strategies of flow-induced corrosion,” Electrochimica Acta, vol. 41, no. 4, pp. 503–509, Mar. 1996, doi: 10.1016/0013-4686(95)00336-3.

[41] S. P. Neill, “Introduction to Ocean Renewable Energy,” in Reference Module in Earth Systems and Environmental Sciences, Elsevier, 2021. doi: 10.1016/B978-0-12-819727-1.00081-9.

[42] A. Momber, P. Plagemann, V. Stenzel, and M. Schneider, “Investigating Corrosion Protection of Offshore Wind Towers,” undefined, 2008, Accessed: Feb. 13, 2022. [Online]. Available: https://www.semanticscholar.org/paper/Investigating-Corrosion-Protection-of-Offshore-Wind-Momber-Plagemann/59c350f088d0dc854d33f04e961eb2efdf5e9c33

[43] M. Delucchi and G. Cerisola, “Influence of organic coatings on the stability of macrodefect-free cements exposed to water,” Constr. Build. Mater., vol. 15, pp. 351–359, Oct. 2001, doi: 10.1016/S0950-0618(01)00010-1.

[44] Y. Hamlaoui, L. Tifouti, and F. Pedraza, “On the corrosion resistance of porous electroplated zinc coatings in different corrosive media,” Corros. Sci., vol. 52, no. 6, pp. 1883–1888, Jun. 2010, doi: 10.1016/j.corsci.2010.02.024.

[45] Q. Zhou and Y. Wang, “Comparisons of clear coating degradation in NaCl solution and pure water,” Prog. Org. Coat., vol. 76, p. 1674, Nov. 2013, doi: 10.1016/j.porgcoat.2013.07.018.

[46] W.-G. Ji, J.-M. Hu, L. Liu, J.-Q. Zhang, and C.-N. Cao, “Water uptake of epoxy coatings modified with γ-APS silane monomer,” Prog. Org. Coat., vol. 57, no. 4, pp. 439–443, Dec. 2006, doi: 10.1016/j.porgcoat.2006.09.025.

[47] T. Nguyen, E. Byrd, D. Bentz, and C. Lint, “In situ measurement of water at the organic coating/substrate interface,” Prog. Org. Coat., vol. 27, no. 1, pp. 181–193, Jan. 1996, doi: 10.1016/0300-9440(95)00535-8.

[48] C. S. Jeffcoate and G. P. Bierwagen, “Initial Studies of Electrochemical Comparison of Coating Performance in Flowing versus Stationary Electrolyte,” in Organic Coatings for Corrosion Control, vol. 689, 0 vols., American Chemical Society, 1998, pp. 151–160. doi: 10.1021/bk-1998-0689.ch012.

[49] L. V. S. Philippe, S. B. Lyon, C. Sammon, and J. Yarwood, “Validation of electrochemical impedance measurements for water sorption into epoxy coatings using gravimetry and infra-red spectroscopy,” Corros. Sci., vol. 50, no. 3, pp. 887–896, Mar. 2008, doi: 10.1016/j.corsci.2007.09.008.

[50] Y. Wang and G. Bierwagen, “A new acceleration factor for the testing of corrosion protective coatings: Flow-induced coating degradation,” J. Coat. Technol. Res., vol. 6, pp. 429–436, Nov. 2009, doi: 10.1007/s11998-008-9161-1.

[51] Q. Zhou, Y. Wang, and G. Bierwagen, “Influence of the composition of working fluids on flow-accelerated organic coating degradation: Deionized water versus electrolyte solution,” Corros. Sci., vol. 55, pp. 97–106, Feb. 2012, doi: 10.1016/j.corsci.2011.10.006.

[52] Q. Zhou, Y. Wang, and G. P. Bierwagen, “Flow accelerated degradation of organic clear coat: The effect of fluid shear,” Electrochimica Acta, vol. 142, pp. 25–33, Oct. 2014, doi: 10.1016/j.electacta.2014.07.082.

[53] C. Erdogan and G. Swain, “Conceptual Sacrificial Anode Cathodic Protection Design for offshore wind monopiles,” Ocean Eng., vol. 235, p. 109339, Sep. 2021, doi: 10.1016/j.oceaneng.2021.109339.

[54] A. Momber, T. Marquardt, S. Buchbach, and P. Plagemann, “The corrosion protection performance of repair coatings for offshore wind power constructions after long-term splash zone site exposure,” Mater. Corros., Oct. 2021, doi: 10.1002/maco.202112864.

[55] “Aluminum & Steel Test Panels | Q-PANEL Test Substrates | Q-Lab.” https://www.q-lab.com/products/q-panel-standard-substrates/q-panels (accessed Feb. 15, 2022).

[56] S. Varvara et al., “Propolis as a green corrosion inhibitor for bronze in weakly acidic solution,” Appl. Surf. Sci., vol. 426, pp. 1100–1112, Dec. 2017, doi: 10.1016/j.apsusc.2017.07.230.

[57] N. Wang, C. Li, L. Yang, Y. Zhou, W. Zhu, and C. Y. Cai, “Experimental testing and FEM calculation of impedance spectra of thermal barrier coatings: Effect of measuring conditions,” Corros. Sci., vol. 107, Feb. 2016, doi: 10.1016/j.corsci.2016.02.029.

[58] J. R. Macdonald et al., Impedance Spectroscopy: Theory, Experiment, and Applications, Third Edition. 2018.

[59] H. Tian, W. Li, K. Cao, and B. Hou, “Potent inhibition of copper corrosion in neutral chloride media by novel non-toxic thiadiazole derivatives,” Corros. Sci., vol. 73, pp. 281–291, Aug. 2013, doi: 10.1016/j.corsci.2013.04.017.

[60] S. R. Taylor, “22 - The Role of Intrinsic Defects in the Protective Behavior of Organic Coatings,” in Handbook of Environmental Degradation of Materials (Second Edition), M. Kutz, Ed. Oxford: William Andrew Publishing, 2012, pp. 655–672. doi: 10.1016/B978-1-4377-3455-3.00022-5.

[61] P. P. Newton and P. S. Liss, “Particles in the oceans (and other natural waters),” Sci. Prog. 1933-, vol. 74, no. 1 (293), pp. 91–114, 1990.

[62] D. L. Osmond et al., “WATERSHEDSS: A DECISION SUPPORT SYSTEM FOR WATERSHED-SCALE NONPOINT SOURCE WATER QUALITY PROBLEMS1,” JAWRA J. Am. Water Resour. Assoc., vol. 33, no. 2, pp. 327–341, Apr. 1997, doi: 10.1111/j.1752-1688.1997.tb03513.x.

[63] W. Hu, “Dry weight and cell density of individual algal and cyanobacterial cells for algae research and development,” Thesis, University of Missouri--Columbia, 2014. Accessed: Jul. 29, 2021. [Online]. Available: https://mospace.umsystem.edu/xmlui/handle/10355/46477

[64] J. C. Winterwerp and C. Kranenburg, Fine Sediment Dynamics in the Marine Environment, 1st ed., vol. 5. Elsevier Science, 2002.

[65] R. Forster, “The effect of monopile-induced turbulence on local suspended sediment pattern around UK wind farms,” Rep. Univ. Hull Rep. Crown Estate, p. 88, 2018.

[66] L. Håkanson, “The relationship between salinity, suspended particulate matter and water clarity in aquatic systems,” Ecol. Res., vol. 21, no. 1, pp. 75–90, Jan. 2006, doi: 10.1007/s11284-005-0098-x.

[67] Q. Vanhellemont and K. Ruddick, “Turbid wakes associated with offshore wind turbines observed with Landsat 8,” Remote Sens. Environ., vol. 145, pp. 105–115, Apr. 2014, doi: 10.1016/j.rse.2014.01.009.

[68] M. Baeye and M. Fettweis, “In situ observations of suspended particulate matter plumes at an offshore wind farm, southern North Sea,” Geo-Mar. Lett., vol. 35, no. 4, pp. 247–255, Aug. 2015, doi: 10.1007/s00367-015-0404-8.

[69] P. A. English et al., “Improving Efficiencies of National Environmental Policy Act Documentation for Offshore Wind Facilities - Case Studies Report,” Rep. Fugro EMU, no. BOEM 2017-026, p. 296, Mar. 2017.

[70] S. Horwath, J. Hassrick, R. Grismala, and E. Diller, “Comparison of Environmental Effects from Different Offshore Wind Turbine Foundations,” Rep. ICF Int. Rep. ICF Int., no. OCS Study BOEM 2020-041, p. 53, Aug. 2020.

[71] J. B. Zu, G. T. Burstein, and I. M. Hutchings, “A comparative study of the slurry erosion and free-fall particle erosion of aluminium,” Wear, vol. 149, no. 1–2, pp. 73–84, Sep. 1991, doi: 10.1016/0043-1648(91)90365-2.

[72] D. G. Rickerby and N. H. Macmillan, “On the oblique impact of a rigid sphere against a rigid-plastic solid,” Int. J. Mech. Sci., vol. 22, no. 8, pp. 491–494, Jan. 1980, doi: 10.1016/0020-7403(80)90004-1.

[73] I. M. Hutchings, R. E. Winter, J. E. Field, and D. Tabor, “Solid particle erosion of metals: the removal of surface material by spherical projectiles,” Proc. R. Soc. Lond. Math. Phys. Sci., vol. 348, no. 1654, pp. 379–392, Mar. 1976, doi: 10.1098/rspa.1976.0044.

[74] A. Neville, T. Hodgkiess, and J. T. Dallas, “A study of the erosion-corrosion behaviour of engineering steels for marine pumping applications,” Wear, vol. 186–187, pp. 497–507, Aug. 1995, doi: 10.1016/0043-1648(95)07145-8.

[75] Y. Li, G. T. Burstein, and I. M. Hutchings, “The influence of corrosion on the erosion of aluminium by aqueous silica slurries,” Wear, vol. 186–187, pp. 515–522, Aug. 1995, doi: 10.1016/0043-1648(95)07181-4.

[76] Y. I. Oka, H. Ohnogi, T. Hosokawa, and M. Matsumura, “The impact angle dependence of erosion damage caused by solid particle impact,” Wear, vol. 203–204, pp. 573–579, Mar. 1997, doi: 10.1016/S0043-1648(96)07430-3.

[77] G. T. Burstein and K. Sasaki, “The birth of corrosion pits as stimulated by slurry erosion,” Corros. Sci., vol. 42, no. 5, pp. 841–860, May 2000, doi: 10.1016/S0010-938X(99)00100-6.

[78] J. B. Zu, I. M. Hutchings, and G. T. Burstein, “Design of a slurry erosion test rig,” Wear, vol. 140, no. 2, pp. 331–344, Nov. 1990, doi: 10.1016/0043-1648(90)90093-P.

[79] A. Neville, M. Reyes, and H. Xu, “Examining corrosion effects and corrosion/erosion interactions on metallic materials in aqueous slurries,” Tribol. Int., vol. 35, no. 10, pp. 643–650, Oct. 2002, doi: 10.1016/S0301-679X(02)00055-5.

[80] B. T. Lu, J. L. Luo, F. Mohammadi, K. Wang, and X. M. Wan, “Correlation between repassivation kinetics and corrosion rate over a passive surface in flowing slurry,” Electrochimica Acta, vol. 53, no. 23, pp. 7022–7031, Oct. 2008, doi: 10.1016/j.electacta.2008.02.083.

[81] B. T. Lu, J. L. Luo, H. X. Guo, and L. C. Mao, “Erosion-enhanced corrosion of carbon steel at passive state,” Corros. Sci., vol. 53, no. 1, pp. 432–440, Jan. 2011, doi: 10.1016/j.corsci.2010.09.054.

[82] B. T. Lu, L. C. Mao, and J. L. Luo, “Hydrodynamic effects on erosion-enhanced corrosion of stainless steel in aqueous slurries,” Electrochimica Acta, vol. 56, no. 1, pp. 85–92, Dec. 2010, doi: 10.1016/j.electacta.2010.09.047.

[83] M. M. Stack, N. Corlett, and S. Turgoose, “Some thoughts on modelling the effects of oxygen and particle concentration on the erosion–corrosion of steels in aqueous slurries,” Wear, vol. 255, no. 1, pp. 225–236, Aug. 2003, doi: 10.1016/S0043-1648(03)00205-9.

[84] X. Jiang, Y. G. Zheng, and W. Ke, “Effect of flow velocity and entrained sand on inhibition performances of two inhibitors for CO2 corrosion of N80 steel in 3% NaCl solution,” Corros. Sci., vol. 47, no. 11, pp. 2636–2658, Nov. 2005, doi: 10.1016/j.corsci.2004.11.012.

[85] L. Niu and Y. F. Cheng, “Erosion–corrosion of aluminium alloys in ethylene glycol–water solutions in absence and presence of sand particles,” Corros. Eng. Sci. Technol., vol. 44, no. 5, pp. 389–393, Oct. 2009, doi: 10.1179/174327808X310024.

[86] Y. Zhao, F. Zhou, J. Yao, S. Dong, and N. Li, “Erosion–corrosion behavior and corrosion resistance of AISI 316 stainless steel in flow jet impingement,” Wear, vol. 328–329, pp. 464–474, Apr. 2015, doi: 10.1016/j.wear.2015.03.017.

[87] Y. Xu and M. Y. Tan, “Probing the initiation and propagation processes of flow accelerated corrosion and erosion corrosion under simulated turbulent flow conditions,” Corros. Sci., vol. 151, pp. 163–174, May 2019, doi: 10.1016/j.corsci.2019.01.028.

[88] M. J. Matthewson, “Axi-symmetric contact on thin compliant coatings,” J. Mech. Phys. Solids, vol. 29, no. 2, pp. 89–113, Apr. 1981, doi: 10.1016/0022-5096(81)90018-1.

[89] K. V. Pool, C. K. H. Dharan, and I. Finnie, “Erosive wear of composite materials,” Wear, vol. 107, no. 1, pp. 1–12, Jan. 1986, doi: 10.1016/0043-1648(86)90043-8.

[90] R. J. K. Wood, “The sand erosion performance of coatings,” Mater. Des., vol. 20, no. 4, pp. 179–191, Aug. 1999, doi: 10.1016/S0261-3069(99)00024-2.

[91] K. S. Tan, J. A. Wharton, and R. J. K. Wood, “Solid particle erosion–corrosion behaviour of a novel HVOF nickel aluminium bronze coating for marine applications—correlation between mass loss and electrochemical measurements,” Wear, vol. 258, no. 1, pp. 629–640, Jan. 2005, doi: 10.1016/j.wear.2004.02.019.

[92] M. Papini and J. K. Spelt, “Indentation-induced buckling of organic coatings part II: measurements with impacting particles,” Int. J. Mech. Sci., vol. 40, no. 10, pp. 1061–1068, Oct. 1998, doi: 10.1016/S0020-7403(98)00018-6.

[93] M. Papini and J. K. Spelt, “The plowing erosion of organic coatings by spherical particles,” Wear, vol. 222, no. 1, pp. 38–48, Nov. 1998, doi: 10.1016/S0043-1648(98)00274-9.

[94] M. Papini and J. K. Spelt, “Organic coating removal by particle impact,” Wear, vol. 213, no. 1, pp. 185–199, Dec. 1997, doi: 10.1016/S0043-1648(97)00062-8.

[95] B. Zouari and M. Touratier, “Simulation of organic coating removal by particle impact,” Wear, vol. 253, no. 3, pp. 488–497, Aug. 2002, doi: 10.1016/S0043-1648(02)00141-2.

[96] R. Kaundal, “Role of Process Variables on the Solid Particle Erosion of Polymer Composites: A Critical Review,” Silicon, vol. 1, no. 6, pp. 5–20, 2014, doi: 10.1007/s12633-013-9166-y.

[97] A. P. Harsha and S. K. Jha, “Erosive wear studies of epoxy-based composites at normal incidence,” Wear, vol. 265, no. 7, pp. 1129–1135, Sep. 2008, doi: 10.1016/j.wear.2008.03.003.

[98] L. Zeng, M. Liu, L. Wu, C. Zhou, and E. Abi, “Erosion characteristics of viscoelastic anticorrosive coatings for steel structures under sand flow,” Constr. Build. Mater., vol. 258, p. 120360, Oct. 2020, doi: 10.1016/j.conbuildmat.2020.120360.

[99] B. R. Hinderliter, K. N. Allahar, G. P. Bierwagen, D. E. Tallman, and S. G. Croll, “Water sorption and diffusional properties of a cured epoxy resin measured using alternating ionic liquids/aqueous electrolytes in electrochemical impedance spectroscopy,” J. Coat. Technol. Res., vol. 5, no. 4, pp. 431–438, Dec. 2008, doi: 10.1007/s11998-008-9107-7.

[100] C. Yang, X. Xing, Z. Li, and S. Zhang, “A Comprehensive Review on Water Diffusion in Polymers Focusing on the Polymer–Metal Interface Combination,” Polymers, vol. 12, no. 1, Art. no. 1, Jan. 2020, doi: 10.3390/polym12010138.

[101] W. J. Pierson Jr. and L. Moskowitz, “A proposed spectral form for fully developed wind seas based on the similarity theory of S. A. Kitaigorodskii,” J. Geophys. Res. 1896-1977, vol. 69, no. 24, pp. 5181–5190, 1964, doi: 10.1029/JZ069i024p05181.

[102] D. E. Hasselmann, M. Dunckel, and J. A. Ewing, “Directional Wave Spectra Observed during JONSWAP 1973,” J. Phys. Oceanogr., vol. 10, no. 8, pp. 1264–1280, Aug. 1980, doi: 10.1175/1520-0485(1980)010<1264:DWSODJ>2.0.CO;2.

[103] T. Moan, X. Y. Zheng, and S. T. Quek, “Frequency-domain analysis of non-linear wave effects on offshore platform responses,” Int. J. Non-Linear Mech., vol. 42, no. 3, pp. 555–565, Apr. 2007, doi: 10.1016/j.ijnonlinmec.2006.08.006.

[104] H. F. Veldkamp and J. van der Tempel, “Influence of wave modelling on the prediction of fatigue for offshore wind turbines,” Wind Energy, vol. 8, no. 1, pp. 49–65, 2005, doi: 10.1002/we.138.

[105] J. N. SHARMA, “Development and Evaluation of a Procedure for Simulating a Random Directional Second-Order Sea Surface and Associated Wave Forces.,” Ph.D., University of Delaware, United States -- Delaware. Accessed: Feb. 02, 2022. [Online]. Available: https://www.proquest.com/docview/302935280/citation/4A672856B2284B48PQ/1

[106] K. E. Mittendorf, “Joint Description Methods of Wind and Waves for the Design of Offshore Wind Turbines,” Mar. Technol. Soc. J., vol. 43, no. 3, pp. 23–33, Aug. 2009, doi: 10.4031/MTSJ.43.3.2.

[107] L. Colone, A. Natarajan, and N. Dimitrov, “Impact of turbulence induced loads and wave kinematic models on fatigue reliability estimates of offshore wind turbine monopiles,” Ocean Eng., vol. 155, pp. 295–309, May 2018, doi: 10.1016/j.oceaneng.2018.02.045.

[108] L. Suja-Thauvin, J. R. Krokstad, E. E. Bachynski, and E.-J. de Ridder, “Experimental results of a multimode monopile offshore wind turbine support structure subjected to steep and breaking irregular waves,” Ocean Eng., vol. 146, pp. 339–351, Dec. 2017, doi: 10.1016/j.oceaneng.2017.09.024.

[109] L. Suja-Thauvin, J. R. Krokstad, and E. E. Bachynski, “Critical assessment of non-linear hydrodynamic load models for a fully flexible monopile offshore wind turbine,” Ocean Eng., vol. 164, pp. 87–104, Sep. 2018, doi: 10.1016/j.oceaneng.2018.06.027.

[110] B. K. Gupta and D. Basu, “Offshore wind turbine monopile foundations: Design perspectives,” Ocean Eng., vol. 213, p. 107514, Oct. 2020, doi: 10.1016/j.oceaneng.2020.107514.

[111] A. Mehmanparast and A. Vidament, “An accelerated corrosion-fatigue testing methodology for offshore wind applications,” Eng. Struct., vol. 240, p. 112414, Aug. 2021, doi: 10.1016/j.engstruct.2021.112414.

[112] V. Zernov, L. Fradkin, and P. Mudge, “Guided waves in a monopile of an offshore wind turbine,” Ultrasonics, vol. 51, no. 1, pp. 57–64, Jan. 2011, doi: 10.1016/j.ultras.2010.05.008.

[113] B. Yeter and Y. Garbatov, “Structural integrity assessment of fixed support structures for offshore wind turbines: A review,” Ocean Eng., vol. 244, p. 110271, Jan. 2022, doi: 10.1016/j.oceaneng.2021.110271.

[114] L. Ziegler, S. Voormeeren, S. Schafhirt, and M. Muskulus, “Sensitivity of Wave Fatigue Loads on Offshore Wind Turbines under Varying Site Conditions,” Energy Procedia, vol. 80, pp. 193–200, Jan. 2015, doi: 10.1016/j.egypro.2015.11.422.

[115] L. Ziegler, S. Schafhirt, M. Scheu, and M. Muskulus, “Effect of Load Sequence and Weather Seasonality on Fatigue Crack Growth for Monopile-based Offshore Wind Turbines,” Energy Procedia, vol. 94, pp. 115–123, Sep. 2016, doi: 10.1016/j.egypro.2016.09.204.

[116] S. Schløer, H. Bredmose, H. Bingham, and T. Larsen, “Effects From Fully Nonlinear Irregular Wave Forcing on the Fatigue Life of an Offshore Wind Turbine and its Monopile Foundation,” Jul. 2012, vol. 7. doi: 10.1115/OMAE2012-83477.

[117] E. Marino, A. Giusti, and L. Manuel, “Offshore wind turbine fatigue loads: The influence of alternative wave modeling for different turbulent and mean winds,” Renew. Energy, vol. 102, pp. 157–169, Mar. 2017, doi: 10.1016/j.renene.2016.10.023.

[118] T. Camp et al., “Design methods for offshore wind turbines at exposed sites,” Proc. 3rd Int. Conf. Mar. Renew. Energy Marec 2004, pp. 171–179, 2004.

[119] B. B. Jensen, “Specifying corrosion protection for the offshore wind turbine industry,” NACE - Int. Corros. Conf. Ser., vol. 3, pp. 1936–1946, 2017.

[120] C. G. Munger, “Corrosion prevention by protective coatings,” Jan. 1985, Accessed: Feb. 05, 2022. [Online]. Available: https://www.osti.gov/biblio/5498670

[121] P. A. Sørensen, S. Kiil, K. Dam-Johansen, and C. E. Weinell, “Anticorrosive coatings: a review,” J. Coat. Technol. Res., vol. 6, no. 2, pp. 135–176, Jun. 2009, doi: 10.1007/s11998-008-9144-2.

[122] C. E. Weinell, A. R. Black, T. Mathiesen, and P. K. Nielsen, “New developments in coatings for extended lifetime for offshore wind structures,” NACE - Int. Corros. Conf. Ser., vol. 1, pp. 68–80, 2017.

[123] K. Sunday and F. Brennan, “A review of offshore wind monopiles structural design achievements and challenges,” Ocean Eng., vol. 235, p. 109409, Sep. 2021, doi: 10.1016/j.oceaneng.2021.109409.

[124] A. Momber and D. Brün, “The use of sensor data for the monitoring of corrosion processes on offshore wind power structures,” Jun. 2021.

[125] A. Momber, A. Krenz, and S. Buchbach, “The corrosion of carbon steel under delaminating repair coatings after long-term marine splash zone exposure,” Mater. Corros., Jan. 2022, doi: 10.1002/maco.202112942.

[126] A. Vedadi et al., “Degradation of epoxy coatings exposed to impingement flow,” J. Coat. Technol. Res., vol. 18, no. 4, pp. 1153–1164, Jul. 2021, doi: 10.1007/s11998-021-00472-2.

[127] A. Vedadi, M. S. Parvej, X. Wang, and Y. Wang, “Comparison of Epoxy Coating Degradations Under Impingement Flow and Stationary Immersion,” presented at the ASME 2020 International Mechanical Engineering Congress and Exposition, Feb. 2021. doi: 10.1115/IMECE2020-24274.

[128] Q. Zhou and Y. Wang, “Comparisons of clear coating degradation in NaCl solution and pure water,” Prog. Org. Coat., vol. 76, no. 11, pp. 1674–1682, Nov. 2013, doi: 10.1016/j.porgcoat.2013.07.018.

[129] Q. Zhou, Y. Wang, and G. P. Bierwagen, “Influence of the composition of working fluids on flow-accelerated organic coating degradation: Deionized water versus electrolyte solution,” Corros. Sci., vol. 55, pp. 97–106, Feb. 2012, doi: 10.1016/j.corsci.2011.10.006.

[130] N. Wang, C. Li, L. Yang, Y. Zhou, W. Zhu, and C. Cai, “Experimental testing and FEM calculation of impedance spectra of thermal barrier coatings: Effect of measuring conditions,” Corros. Sci., vol. 107, pp. 155–171, Jun. 2016, doi: 10.1016/j.corsci.2016.02.029.

[131] C. J. Galvin, Wave-height Prediction for Wave Generators in Shallow Water. Coastal Engineering Research Center, 1964.

[132] F. M. Marques Machado, A. M. Gameiro Lopes, and A. D. Ferreira, “Numerical simulation of regular waves: Optimization of a numerical wave tank,” Ocean Eng., vol. 170, pp. 89–99, Dec. 2018, doi: 10.1016/j.oceaneng.2018.10.002.

[133] W. Muharini, N. Karjanto, and G. Klopman, “Linear theory for single and double flap wavemakers,” J. Indones. Math. Soc. JIMS, vol. 12, Jan. 2006.

[134] M. Raffel, C. E. Willert, S. T. Wereley, and J. Kompenhans, Particle Image Velocimetry: A Practical Guide, 2nd ed. 2007 edition. Berlin Heidelberg: Springer, 2014.

[135] F. Durst, Fluid Mechanics: An Introduction to the Theory of Fluid Flows, 2008th edition. Berlin: Springer, 2008.

[136] N. Fredj, S. Cohendoz, X. Feaugas, and S. Touzain, “Ageing of marine coating in natural and artificial seawater under mechanical stresses,” Prog. Org. Coat., vol. 74, no. 2, pp. 391–399, Jun. 2012, doi: 10.1016/j.porgcoat.2011.10.002.

[137] N. Fredj, S. Cohendoz, X. Feaugas, and S. Touzain, “Effect of mechanical stresses on marine organic coating ageing approached by EIS measurements,” Prog. Org. Coat., vol. 72, no. 3, pp. 260–268, Nov. 2011, doi: 10.1016/j.porgcoat.2011.04.014.

[138] Q. Shen, S. Z. Li, L. Yang, Y. C. Zhou, Y. G. Wei, and T. Yuan, “Coupled mechanical-oxidation modeling during oxidation of thermal barrier coatings,” Comput. Mater. Sci., vol. 154, pp. 538–546, Nov. 2018, doi: 10.1016/j.commatsci.2018.08.017.

[139] Q. Shen, Y. Li, Y. Zhou, Y. Wei, and Z. Wang, “Effects of growth stress in finite-deformation thermally grown oxide on failure mechanism of thermal barrier coatings,” 2017, doi: 10.1016/J.MECHMAT.2017.08.011.

[140] G. N. Xu, L. Yang, Y. C. Zhou, Z. P. Pi, and W. Zhu, “A chemo-thermo-mechanically constitutive theory for thermal barrier coatings under CMAS infiltration and corrosion,” J. Mech. Phys. Solids, vol. 133, p. 103710, Dec. 2019, doi: 10.1016/j.jmps.2019.103710.

[141] F. Bellucci and L. Nicodemo, “Water Transport in Organic Coatings,” Corrosion, vol. 49, no. 3, pp. 235–247, Mar. 1993, doi: 10.5006/1.3316044.

[142] A. Miszczyk and K. Darowicki, “Water uptake in protective organic coatings and its reflection in measured coating impedance,” Prog. Org. Coat., vol. 124, pp. 296–302, Nov. 2018, doi: 10.1016/j.porgcoat.2018.03.002.

[143] O. A. Stafford, B. R. Hinderliter, and S. G. Croll, “Electrochemical impedance spectroscopy response of water uptake in organic coatings by finite element methods,”

Electrochimica Acta, vol. 52, no. 3, pp. 1339–1348, Nov. 2006, doi: 10.1016/j.electacta.2006.07.047.

[144] "EIS of Organic Coatings-Paints: Electrochemical Impedance Spectroscopy." https://www.gamry.com/application-notes/EIS/eis-of-organic-coatings-and-paints/ (accessed Feb. 13, 2022).

[145] Solutions for CHEMISTRY: The Molecular Nature of Matter and Change 2016 9th by Martin S. Silberberg, Patricia G. Amateis | Book solutions | Numerade. Accessed: Feb. 13, 2022. [Online]. Available: https://www.numerade.com/books/chemistry-the-molecular-nature-of-matter-and-change-2016-9th/?gclid=CjwKCAiA9aKQBhBREiwAyGP5lUwa8sbMduSs09NWZF82fhyBi0yYG3DP_81oASAgV9WMNp9IzSu5wBoCJQUQAvD_BwE

[146] Theory of Elasticity: Course of Theoretical Physics: 7 3rd.

[147] Z. W. W. Jr, F. N. Jones, S. P. Pappas, and D. A. Wicks, Organic Coatings: Science and Technology, 3rd edition. Hoboken, N.J: Wiley-Interscience, 2007.

[148] A. Sarkar and J. K. Chakravartty, "Activation Volume and Density of Mobile Dislocations in Plastically Deforming Zr-1pctSn-1pctNb-0.1pctFe Alloy," Metall. Mater. Trans. A, vol. 46, no. 12, pp. 5638–5643, Dec. 2015, doi: 10.1007/s11661-015-3153-4.

[149] J. Comyn, Polymer permeability, 0 edition. London ; New York: Elsevier Applied Science Publishers, 1985.

[150] J. M. Hu, J. Q. Zhang, and C. N. Cao, "Determination of water uptake and diffusion of Cl− ion in epoxy primer on aluminum alloys in NaCl solution by electrochemical impedance spectroscopy," Prog. Org. Coat., vol. 46, no. 4, pp. 273–279, Jun. 2003, doi: 10.1016/S0300-9440(03)00010-9.

[151] G. Bouvet, D. NGUYEN DANG, S. Cohendoz, F. Xavier, S. Mallarino, and S. Touzain, "Impact of polar groups concentration and free volume on water sorption in model epoxy free films and coatings," Prog. Org. Coat., Jan. 2016, doi: 10.1016/j.porgcoat.2015.12.011.

[152] T. Miwa, Y. Takeshita, A. Ishii, and T. Sawada, "Simulation of water absorption and desorption behavior for anti-corrosion coatings in existing and new accelerated corrosion tests," Prog. Org. Coat., vol. 120, pp. 71–78, Jul. 2018, doi: 10.1016/j.porgcoat.2018.02.031.

[153] S. Ghojavand, R. Arefinia, and H. Sahrayi, "On the diffusion phenomenon of solvent within polymeric coatings: Development of a new model," Prog. Org. Coat., vol. 97, pp. 301–306, Aug. 2016, doi: 10.1016/j.porgcoat.2016.04.011.

[154] L. De Rosa, T. Monetta, and F. Bellucci, "Moisture Uptake in Organic Coatings Monitored with EIS," Mater. Sci. Forum, vol. 289–292, pp. 315–326, 1998, doi: 10.4028/www.scientific.net/MSF.289-292.315.

[155] S. Duval, Y. Camberlin, M. Glotin, M. Keddam, F. Ropital, and H. Takenouti, "Characterisation of organic coatings in sour media and influence of polymer structure on corrosion performance," Prog. Org. Coat., vol. 39, no. 1, pp. 15–22, Aug. 2000, doi: 10.1016/S0300-9440(00)00094-1.